



TECHNISCHE
UNIVERSITÄT
DARMSTADT

ULB

Synthesis and investigation of hybrid nanomaterials for photocatalytic and spectroanalytical applications

Okeil, Sherif
(2020)

DOI (TUprints): <https://doi.org/10.25534/tuprints-00012581>

Lizenz:



CC-BY-SA 4.0 International - Creative Commons, Attribution Share-alike

Publikationstyp: Ph.D. Thesis

Fachbereich: 07 Department of Chemistry

Quelle des Originals: <https://tuprints.ulb.tu-darmstadt.de/12581>

Synthesis and investigation of hybrid nanomaterials for photocatalytic and spectroanalytical applications

Dissertation

M.Sc. Sherif Mahmoud El-Sayed Okeil Ibrahim

Fachbereich Chemie | März 2020



TECHNISCHE
UNIVERSITÄT
DARMSTADT

Fachbereich Anorganische Chemie
Eduard-Zintl-Institut für Anorganische
und Physikalische Chemie

Synthesis and investigation of hybrid nanomaterials for photocatalytic and spectroanalytical applications

vom Fachbereich Chemie

der Technischen Universität Darmstadt

zur Erlangung des Grades

Doctor rerum naturalium (Dr. rer. nat.)

Dissertation

von **Sherif Mahmoud El-Sayed Okeil Ibrahim, M. Sc.**

Erstgutachter : Prof. Dr. rer. nat. Jörg J. Schneider

Zweitgutachter: Prof. Dr. Wolfgang Ensinger

Darmstadt 2020

Okeil, Sherif: **Synthesis and investigation of hybrid nanomaterials for photocatalytic and spectroanalytical applications**

Synthese und Untersuchungen von Hybrid-Nanomaterialien für photokatalytische und spektroanalytische Anwendungen

Darmstadt, Technische Universität Darmstadt

Jahr der Veröffentlichung der Dissertation auf TUpriints: 2020

Tag der Einreichung: 27.04.2020

Tag der mündlichen Prüfung: 06.07.2020

Veröffentlicht unter der Lizenz CC BY-SA 4.0 International

Printed and/or published with the support of the German Academic Exchange Service

Erklärung A

Sherif Mahmoud El-Sayed Okeil Ibrahim

Datum 16.03.2020

Siemensstraße 3

64289 Darmstadt

Erklärung

Ich erkläre hiermit, dass ich meine Dissertation selbstständig und nur mit den angegebenen Hilfsmitteln angefertigt und noch keinen Promotionsversuch unternommen habe.

Sherif Okeil

Erklärung B

Erklärung der Übereinstimmung

Sherif Mahmoud El-Sayed Okeil Ibrahim

Datum 16.03.2020

Siemensstraße 3

64289 Darmstadt

Erklärung

Ich erkläre hiermit, dass die elektronische Version der Doktorarbeit mit der schriftlichen Version übereinstimmt. Die elektronische Version liegt dem Prüfungssekretariat vor.

Sherif Okeil

Erklärung C

Erklärung zum Eigenanteil an den Veröffentlichungen

Sherif Mahmoud El-Sayed Okeil Ibrahim

Datum 16.03.2020

Siemensstraße 3

64289 Darmstadt

Im Folgenden ist aufgelistet, mit welchem Anteil ich an den Veröffentlichungen beteiligt war.

Publikationsliste

Wissenschaftliche Artikel als Erstautor und Teil der vorliegenden Arbeit

1. Mein Anteil an der folgenden Veröffentlichung beträgt 75%.

S. Okeil, J. Krausmann, I. Dönges, S. Pflieger, J. Engstler, J. J. Schneider, ZnS/ZnO@CNT and ZnS@CNT nanocomposites by gas phase conversion of ZnO@CNT. A systematic study of their photocatalytic properties. *Dalton Transactions* **2017**, 46 (16), 5189-5201.

2. Mein Anteil an der folgenden Veröffentlichung beträgt 90%.

S. Okeil, J. J. Schneider, Controlling surface morphology and sensitivity of granular and porous silver films for surface-enhanced Raman scattering, SERS. *Beilstein Journal of Nanotechnology* **2018**, 9 (1), 2813-2831.

3. Mein Anteil an der folgenden Veröffentlichung beträgt 65%.

S. Okeil, S. Yadav, M. Bruns, A. Zintler, L. Molina-Luna, J. J. Schneider, Photothermal catalytic properties of layered titanium chalcogenide nanomaterials. *Dalton Transactions* **2020**, 49 (4), 1032-1047.

4. Mein Anteil an der folgenden Veröffentlichung beträgt 65% (eingereicht zur Begutachtung am 20. Januar 2020).

S. Okeil, M. Pashchanka, S. Heinschke, M. Bruns, J. J. Schneider, Silver sputtered barrier-type anodic aluminum oxide derived from iodine-based oxoacid electrolytes as efficient SERS substrates. Evidence for a combined physical and chemical enhancement effect. *Journal of Physical Chemistry C* **2020**, in review.

Wissenschaftliche Artikel aus Kooperationen und nicht in dieser Arbeit enthalten

1. Mein Anteil an der folgenden Veröffentlichung beträgt 30%.

D. J. Babu, T. Herdt, **S. Okeil**, M. Bruns, R. Staudt, J. J. Schneider, Bud type carbon nanohorns: materials for high pressure CO₂ capture and Li-ion storage. *Journal of Materials Chemistry A* **2016** 4 (37), 14267-14275.

2. Mein Anteil an der folgenden Veröffentlichung beträgt 30%.

D. Puthusseri, D. J. Babu, **S. Okeil**, J. J. Schneider, Gas adsorption capacity in an all carbon nanomaterial composed of carbon nanohorns and vertically aligned carbon nanotubes. *Physical Chemistry Chemical Physics* **2017**, 19 (38), 26265-26271.

3. Mein Anteil an der folgenden Veröffentlichung beträgt 30%.

D. J. Babu, D. Puthusseri, F. G. Kühl, **S. Okeil**, M. Bruns, M. Hampe, Jörg J. Schneider, SO₂ gas adsorption on carbon nanomaterials: a comparative study. *Beilstein Journal of Nanotechnology* **2018** 9 (1), 1782-1792.

4. Mein Anteil an der folgenden Veröffentlichung beträgt 50% (wird noch zur Begutachtung eingereicht).

M. Pashchanka, **S. Okeil**, J. J. Schneider, Long-range hexagonal pore ordering as a key for the control of SERS substrate efficiency in porous alumina. *To be submitted*.

Sherif Okeil

Erklärung D

Erklärung zur Begutachtung der Veröffentlichungen

Referent: Prof. Dr. Jörg J. Schneider

Korreferent: Prof. Dr. Wolfgang Ensinger

Darmstadt, 16.03.2020

Weder Referent (Prof. Dr. Jörg J. Schneider) noch Korreferent (Prof. Dr. Wolfgang Ensinger) der vorliegenden kumulativen Doktorarbeit waren an der Begutachtung nachstehender Veröffentlichungen beteiligt:

1. **S. Okeil**, J. Krausmann, I. Dönges, S. Pflieger, J. Engstler, J. J. Schneider, ZnS/ZnO@CNT and ZnS@CNT nanocomposites by gas phase conversion of ZnO@CNT. A systematic study of their photocatalytic properties. *Dalton Transactions* **2017**, 46 (16), 5189-5201.

2. **S. Okeil**, J. J. Schneider, Controlling surface morphology and sensitivity of granular and porous silver films for surface-enhanced Raman scattering, SERS. *Beilstein Journal of Nanotechnology* **2018**, 9 (1), 2813-2831.

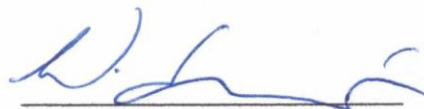
3. **S. Okeil**, S. Yadav, M. Bruns, A. Zintler, L. Molina-Luna, J. J. Schneider, Photothermal catalytic properties of layered titanium chalcogenide nanomaterials. *Dalton Transactions* **2020**, 49 (4), 1032-1047.

4. **S. Okeil**, M. Pashchanka, S. Heinschke, M. Bruns, J. J. Schneider, Silver sputtered barrier-type anodic aluminum oxide derived from iodine-based oxoacid electrolytes as efficient SERS substrates. Evidence for a combined physical and chemical enhancement effect. *Journal of Physical Chemistry C* **2020**, in review.



Referent

(Prof. Dr. Jörg J. Schneider)



Korreferent

(Prof. Dr. Wolfgang Ensinger)

ACKNOWLEDGEMENTS

I express my sincere gratitude towards **Prof. Dr. Jörg J. Schneider** for his mentorship and his continuous support during the period of my Ph.D. work and especially in the last phase of finally submitting the complete thesis. His constant follow up, his interesting suggestions and guidance enabled the successful completion of this work. I could learn from him a lot on a personal and scientific level.

I deeply thank **Dr. Mikhail Pashchanka** and **Dr. Sandeep Yadav** for enabling me to collaborate with them in interesting work areas which was fruitful and resulted in publications presented in this thesis. I am also indebted to **Dr. Jörg Engstler** for TEM analysis as well as several interesting scientific discussions which always took me steps further. I would also thank **M.Sc. Silvio Heinschke** for several XRD and ellipsometry measurements as well as **Dr. Rudolf Hoffmann** and **M.Sc. Thorsten Bies** for TGA analysis. his constant scientific insights into the material analysis and characterizations.

Scientific discussions with **Dr. Michael Bruns** regarding XPS investigations and **Tobias Weingärtner** for the Auger electron spectroscopic measurements is gratefully acknowledged. I would also like to express my sincere thanks to the Egyptian Ministry of Higher Education (**MoHE**) and German Academic Exchange Service (**DAAD**) for funding me through the German-Egyptian Research Scholarship (**GERLS**) program for the first three and half years of my Ph.D. work.

I am grateful to my recent and former coworkers **Dr. Mathias Nowotny**, **Dr. Deepu J. Babu**, **Dr. Peter Krauß**, **Dr. Tim Herdt**, **Dr. Tobias Wombacher**, **Dr. Shawn Sanctis**, **M.Sc. Jan Krausmann**, **M.Sc. Inga Dönges**, **M.Sc. Daniel Deckenbach**, **Dipl.-Ing Ildiko Balog** and **Ute Schmidt** for creating a nice and relaxed personal and scientific atmosphere as well as for constant support during the Ph.D. I especially thank **M.Sc. Nico Koslowski**, **Dr. Jonathan Stott** and **M.Tech. Saurabh Bopte** for the nice lunch break times we had together.

I express my deepest gratitude towards my family especially my beloved mother **Azza Hamed Shaker**, my sister **Nariman Okeil** and my brother **M.Sc. Hesham Okeil** for their unwavering support and ongoing encouragement during the course of this PhD. My fiancée and future wife **M.Sc. Bassant Elbardisy** also supported me with love in the final stressful period of my Ph.D. thesis. I hope I have not overlooked anyone but if I have, it is certainly not for the lack of appreciation.

Abstract

This thesis is divided into two parts where the first part of the thesis deals with the design and synthesis of heterostructures for efficient photocatalysis e.g. for water remediation while the second part deals with the design of effective substrates suitable for sensitive surface-enhanced Raman scattering (SERS) analysis. Investigating different hybrid nanomaterials which can serve as efficient photocatalysts, the wide band gap semiconductors ZnO and ZnS have been combined with vertically aligned carbon nanotubes (VACNTs) to form ZnO@CNT and ZnS@CNT nanocomposite heterostructures which are able to make use not only from the ultraviolet (UV) region of light but from most of the solar spectrum. Through atomic layer deposition (ALD) ZnO nanoparticles are directly deposited on VACNTs which could be converted in a gas phase sulfidation process to ZnS@CNT nanocomposites. Depending on the gas phase conversion temperature different ZnS/ZnO@CNT, sphalerite-based ZnS@CNT and wurtzite-based ZnS@CNT nanocomposites could be obtained where at high conversion temperatures defects could be even induced in the ZnS nanoparticles. This study revealed that wurtzite-based ZnS@CNT nanocomposites with induced defects show the highest photocatalytic activity towards the degradation of methyl orange which was used as model pollutant under simulated sunlight.

Furthermore, the photocatalytic properties of two-dimensional titanium chalcogenides have been investigated. These materials possess in contrast to traditional titanium dioxide a small band gap and a layered structure which is advantageous for photocatalytic applications. The different titanium chalcogenides were prepared by a chemical vapor transport method whereby tuning of the ratio of the starting elements and the reaction temperature a series of different titanium chalcogenides (TiS₃, TiS₂, TiS, TiSe₂ and TiTe) could be synthesized. The investigation of titanium sulfides, TiS₃ and TiS which is defect-rich TiS₂ showed promising results concerning their photocatalytic activity. Non-stoichiometric titanium disulfide shows a large number of defects which are responsible for a high photocatalytic and thermocatalytic activity. Excellent recyclability of these materials was also found and was attributed to the spontaneous formation of titanium sulfide/titanium oxide heterostructures due to the surface oxidation with time further increasing the photocatalytic activity of the material.

New approaches for the preparation of efficient SERS substrates with high enhancement factors were investigated as they are crucial for trace analysis e.g. of bioactive compounds. First, a

facile plasma-assisted approach for the preparation of SERS substrates has been developed. Different plasma treatments using different plasma gases and different parameters have been investigated on thin transparent silver films of 10 nm thickness and thick non-transparent silver films of 200 nm thickness. Hydrogen, nitrogen and argon plasma were found to increase the surface roughness of these sputtered silver films, thus increasing their SERS enhancement factors significantly. Subsequent oxidation-reduction plasma treatment of the 200 nm thick silver sputtered films through oxidation with oxygen plasma followed by reduction with either hydrogen, nitrogen or argon plasma enabled the formation of complex three-dimensional porous silver films showing high SERS enhancement factors.

Finally, aluminum/anodic aluminum oxide/silver (Al/AAO/Ag) substrates have been investigated to elucidate the different factors which could increase the SERS response obtained from such substrates. It was found that a possible chemical enhancement from iodine species introduced in barrier-type anodic aluminum oxide by iodine oxoacid electrolytes could effectively increase the SERS enhancement factors of these substrates compared to other dense barrier-type anodic aluminum oxides obtained from citrate buffer and porous anodic aluminum oxide (PAOX) films. These findings could be valuable for the preparation of more effective SERS substrates based on Al/AAO/Ag thin layer compositions.

Kurzfassung

Diese Arbeit gliedert sich in zwei Teile. Der erste Teil befasst sich mit dem Design und der Synthese von Heterostrukturen für eine effiziente Photokatalyse. Der zweite Teil befasst sich mit dem Design neuartiger Substrate für die empfindliche, oberflächenverstärkte Raman-Streuungsanalyse (SERS). Während der Untersuchung verschiedener Hybrid-Nanomaterialien, die als effiziente Photokatalysatoren dienen können, wurden die Halbleiter ZnO und ZnS, die breite Bandlücken besitzen, mit vertikal ausgerichteten Kohlenstoffnanoröhren (VACNTs) kombiniert. Dadurch konnten ZnO@CNT und ZnS@CNT Nanokomposit-Heterostrukturen gebildet werden, die nicht nur den ultravioletten Bereich des Lichts, sondern nahezu das gesamte Sonnenspektrum ausnutzen. Durch Atomlagenabscheidung konnten ZnO-Nanopartikel direkt auf VACNTs abgeschieden werden, die in einem Gasphasensulfidierungsprozess in ZnS@CNT-Nanokomposite umgewandelt werden. Abhängig von der Gasphasenumwandlungstemperatur konnten unterschiedliche ZnS/ZnO@CNT, Sphalerit-basierte ZnS@CNT und Wurtzit-basierte ZnS@CNT-Nanokomposite hergestellt werden, wobei bei hohen Umwandlungstemperaturen gezielt Defekte in den ZnS-Nanopartikeln induziert werden konnten. Die Studie ergab, dass ZnS@CNT-Nanokomposite auf Wurtzitbasis mit induzierten Defekten die höchste photokatalytische Aktivität im Abbau von Methylorange als Modellschadstoff unter simuliertem Sonnenlicht aufweisen.

Darüber hinaus wurden die photokatalytischen Eigenschaften zweidimensionaler Titanchalkogenide untersucht. Diese Materialien besitzen im Gegensatz zu Titandioxid eine kleine Bandlücke und eine Schichtstruktur, die für photokatalytische Anwendungen vorteilhaft sind. Die verschiedenen Titan-Chalkogenide wurden durch eine chemische Transportreaktion hergestellt, bei dem durch Abstimmung des Verhältnisses der Ausgangselemente und der Reaktionstemperatur eine Reihe verschiedener Titan-Chalkogenide (TiS_3 , TiS_2 , TiS , TiSe_2 und TiTe) synthetisiert werden konnten. Nichtstöchiometrisches Titandisulfid zeigt eine große Anzahl von Defekten, die für eine hohe photokatalytische und thermokatalytische Aktivität verantwortlich sind. Diese Materialien besitzen die Eigenschaft einer spontanen Bildung von Titansulfid/Titanoxid-Heterostrukturen aufgrund einer selektiven Oberflächenoxidation, wodurch die photokatalytische Aktivität des Materials weiter erhöht werden kann.

Des Weiteren wurden neue Ansätze zur Herstellung effizienter SERS-Substrate mit hohen Verstärkungsfaktoren untersucht, da sie für die Spurenanalyse, z.B. von bioaktiven

Verbindungen von Interesse sind. Zunächst wurde ein einfacher Ansatz beruhend auf Plasmabehandlung zur Herstellung von SERS-Substraten entwickelt. Verschiedene Plasmabehandlungen unter Verwendung verschiedener Plasmagase und verschiedener Prozessparameter wurden an dünnen transparenten Silberfilmen mit einer Dicke von 10 nm und dicken nicht transparenten Silberfilmen mit einer Dicke von 200 nm untersucht. Es wurde festgestellt, dass Wasserstoff-, Stickstoff- und Argonplasma die Oberflächenrauheit dieser gesputterten Silberfilme erhöht und somit ihre SERS-Verstärkungsfaktoren signifikant gesteigert werden können. Eine kombinierte Oxidations-Reduktions-Plasmabehandlung der 200 nm dicken silbergesputterten Filme durch Oxidation mit Sauerstoffplasma und anschließende Reduktion mit Wasserstoff-, Stickstoff- oder Argonplasma ermöglichte die Bildung komplexer dreidimensionaler poröser Silberfilme mit hohen SERS-Verstärkungsfaktoren.

Zusätzlich wurden Substrate mit Kompositstruktur aus Aluminium/anodischem Aluminiumoxid/Silber (Al/AAO/Ag) synthetisiert und untersucht, um die verschiedenen Faktoren, die Einfluss auf die resultierende SERS-Verstärkung haben, aufzuklären. Dabei zeigte sich, dass eine mögliche chemische Verstärkung durch Iodspezies, die in anodischen Aluminiumoxid vom Barrier-Typ durch Iodoxosäure-Elektrolyte eingeführt wurden, die SERS-Verstärkungsfaktoren dieser Substrate im Vergleich zu anderen anodischen Aluminiumoxiden hergestellt mittels eines Citratpuffers sowie auch von porösem anodischen Aluminiumoxid Filmen (PAOX) deutlich erhöht. Diese Erkenntnisse könnten zukünftig für die Herstellung neuartiger effektiver SERS-Substrate auf der Basis von Al/AAO/Ag-Dünnschichten wertvoll sein.

List of Abbreviations

AAO	anodic aluminum oxide
AEF	analytical enhancement factor
AFM	atomic force microscopy
ALD	atomic layer deposition
c	speed of light
CB	conduction band
CBM	conduction band minimum
CCD	charge-coupled device
CM	chemical enhancement mechanism
CNTs	carbon nanotubes
C _{RS}	analyte concentrations used in normal Raman
C _{SERS}	analyte concentrations used in SERS
DNA	deoxyribonucleic acid
E	potential
e	elementary charge
EBL	electron beam lithography
E _F	Fermi energy level
EF	enhancement factor
E _g	band gap
E _{inc}	magnitude of the electric field of the incident electromagnetic radiation
EM	electromagnetic enhancement mechanism
ε'	real part of the dielectric function
ε''	imaginary part of the dielectric function
ε(ω)	dielectric function
ε ₀	permittivity of vacuum
ε _M	permittivity of medium
g-C ₃ N ₄	graphitic carbon nitride
HOMO	highest occupied molecular orbital
HRTEM	high resolution transmission electron microscopy

I_0	intensity of incident radiation
IERS	interference-enhanced Raman scattering
I_{inc}	field intensity of the incident electromagnetic radiation
I_R	Raman signal intensity
I_{SERS}	SERS intensity
IUPAC	International Union of Pure and Applied Chemistry
k	imaginary part of refractive index
LSP	localized surface plasmon
LSPR	localized surface plasmon resonance
LUMO	lowest unoccupied molecular orbital
m	effective mass of the electron
MFONs	metal film over nanospheres
N	number of scattering molecules
n	density of free electrons
n	real part of refractive index
NHE	normal hydrogen electrode
NIR	near-infrared
N_{RS}	number of molecules contributing to the scattering in conventional Raman
N_{SERS}	number of molecules contributing to the scattering in SERS
NSL	nanosphere lithography
O_{int}	oxygen interstitials
PANI	Polyaniline
PAOX	porous anodic aluminum oxide
Q	quality factor
rf	radio frequency
ROS	reactive oxygen species
SEM	scanning electron microscopy
SERRS	surface-enhanced resonant Raman scattering
SERS	surface-enhanced Raman scattering
SPP	surface plasmon polariton
TEM	transmission electron microscopy

TERS	tip-enhanced Raman spectroscopy
THF	tetrahydrofuran
Ti _{int}	titanium interstitials
UV	ultraviolet
VACNTs	vertically aligned carbon nanotubes
VB	valence band
VBM	valence band maximum
Vis	visible
V _o	oxygen vacancy
V _{Ti}	titanium vacancy
α	molecular polarizability
γ	damping factor
λ	wavelength
λ_p	critical wavelength
ν_M	frequency difference of vibrational energy states
σ_{abs}	absorption cross-section
σ_{sca}	scattering cross-section
ω	angular frequency
ω_{inc}	frequency of incident electromagnetic radiation
ω_p	plasma frequency
ω_s	frequency of scattered radiation

Table of contents

1 Introduction and theoretical background	1
1.1 Hybrid nanomaterial photocatalysts for environmental remediation	1
1.1.1 Motivation and aim of this work	1
1.1.2 Fundamentals of photocatalysis	3
1.1.3 Traditional photocatalysts and modifications for improvement of photocatalytic efficiency	8
1.1.4 Synthesis of nanoparticle-carbon nanotube nanocomposites	19
1.1.5 Defect engineering for photocatalysis	24
1.1.6 Photocatalysis with two-dimensional materials	27
1.2 Plasmonic nanomaterials for optical analyte detection using surface-enhanced Raman Spectroscopy (SERS)	30
1.2.1 Motivation and aim of this work	30
1.2.2 Understanding the Raman scattering phenomena	31
1.2.3 Raman spectroscopy	33
1.2.4 Emergence of Surface-enhanced Raman scattering (SERS)	33
1.2.5 Explanation of the properties of metals and surface plasmons	34
1.2.6 Effect of surface roughness, hot spots and geometry	41
1.2.7 Mechanisms involved in SERS enhancement	44
1.2.8 Calculation of SERS enhancement factor	46
1.2.9 SERS substrates	47
1.2.9.1 Plasma-assisted surface roughening	49
1.2.9.2 Anodized aluminum oxide as platform for SERS applications	52
2 Organization of the cumulative part of this dissertation	57
2.1 ZnS/ZnO@CNT and ZnS@CNT nanocomposites by gas phase conversion of ZnO@CNT. A systematic study of their photocatalytic properties	58
2.2 Photothermal catalytic properties of layered titanium chalcogenide nanomaterials	72
2.3 Controlling surface morphology and sensitivity of granular and porous silver films for surface-enhanced Raman scattering, SERS	90
2.4 SERS enhancement of silver functionalized dense anodic aluminum oxide derived from iodine-based oxoacid electrolytes. Evidence for a combined physical and chemical enhancement effect.	110
3 Summary	143
4 Conclusion and outlook	145
5 Appendix	146
6 References	149
7 Curriculum Vitae	164

1 Introduction and theoretical background

The thesis is divided into two main parts, where the first focuses on the design of effective photocatalytic hybrid nanomaterials for water remediation while the second focuses on the design and preparation of sensitive surface-enhanced Raman scattering (SERS) substrates for trace analysis. In each part the motivation of the work is given followed by an explanation of the underlying theories for the performed work as well as the current state of art in the respective research areas are presented.

Photocatalysis and plasmonics, although appearing to be two completely different areas of research, they can be connected at some points which will be shown throughout this thesis work. In the first part of the thesis new hybrid nanomaterial photocatalysts will be studied, in a second part plasmonic materials which offer high sensitivity for spectroscopic detection of analytes using the SERS effect are in the center. However, on one hand, plasmonic materials can increase the photocatalytic activity of photocatalysts if appropriately combined, on the other hand these plasmonic materials can serve as analysis platform based on surface-enhanced Raman scattering (SERS) with a self-cleaning ability where the measured analyte is removed through photocatalysis. These general concepts and the underlying science for photocatalysis and SERS will be presented in the following.

1.1 Hybrid nanomaterial photocatalysts for environmental remediation

1.1.1 Motivation and aim of this work

Photocatalysis for water remediation offers an interesting and environmentally friendly approach to remove organic pollutants from water with the aid of renewable solar energy. A wide variety of photocatalysts have been developed in literature but still the search for effective photocatalysts is ongoing.

Hybrid nanomaterials or heterostructure nanocomposites present a category of interesting photocatalysts as they usually enable the use of not only the ultraviolet (UV) light but from most of the solar radiation. Furthermore, such a nanocomposite enables efficient charge separation by increasing the recombination time due to the spatial separation of the photo-induced charge carriers which usually represents a challenge for single component nanomaterials. In literature, there is a wide range of different nanocomposites which have been synthesized to serve as efficient photocatalysts like nanoparticle-graphene,¹ nanoparticle-polymer,² nanoparticle-carbon powder,³ metal/semiconductor,⁴ graphitic carbon nitride (g-C₃N₄)/graphene oxide,⁵

nanoparticle-graphene oxide⁶ and nanoparticle-carbon nanotube nanocomposites⁷ to name just a few. As our group is specialized in the synthesis of vertically aligned carbon nanotubes (VACNTs) as shown in **Figure 1**, it would be interesting to take it as a basis for the synthesis of semiconductor nanoparticle@CNT heterostructure nanocomposites and to test these for their photocatalytic properties. These nanocomposites show several advantages over traditional single photocatalysts e.g. titanium dioxide TiO₂. On top, it is known that CNTs possess high adsorptive capacities which would enable to remove pollutants or their degradates also through adsorption which makes these semiconductor nanoparticle@CNT nanocomposites interesting.

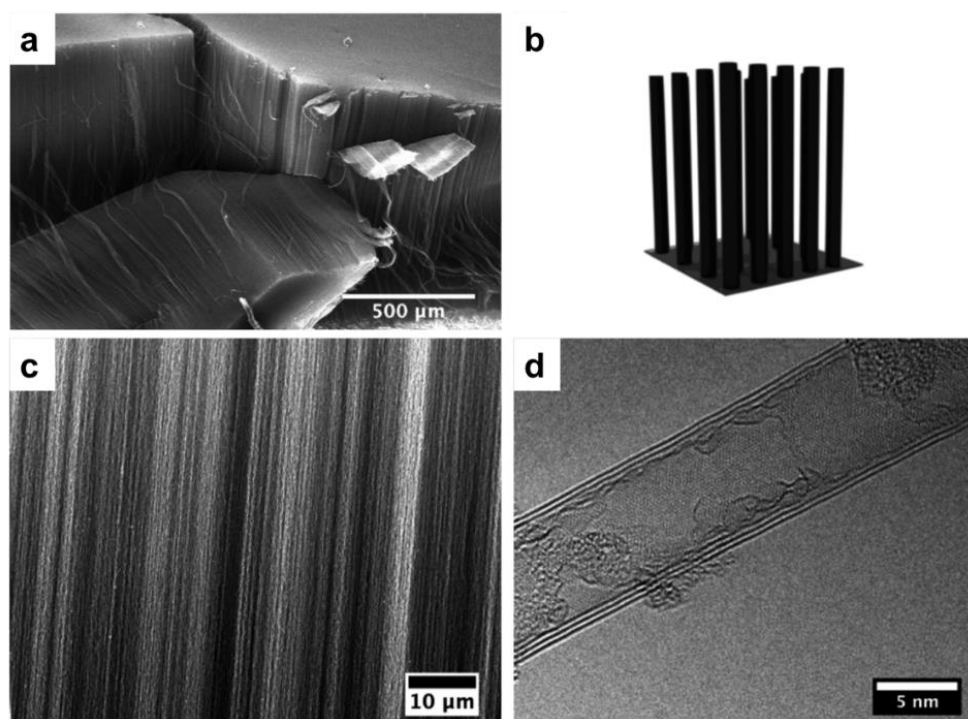


Figure 1 (a) SEM image of as-prepared VACNTs showing the vertical alignment to the substrate. (b) Schematic showing the concept of VACNTs where CNTs are aligned perpendicular to the substrate as observed in (a). (c) SEM showing a close-up of the VACNTs where the parallel alignment of the CNTs can be clearly seen. (d) TEM image of a single CNT isolated from the VACNT structure. Adapted with permission from Ref. ⁸, © 2017 WILEY-VCH Verlag GmbH & Co. KGaA, Weinheim.

The work with VACNTs would also enable the preparation of nanocomposites already fixed to a substrate in an ordered manner which could then be integrated into devices which would help to photocatalytically clean wastewater without the need to add a separation step to separate the photocatalyst from the water. Till now such nanocomposites have been prepared in literature through wet chemical techniques which would not be suitable in the case of VACNTs as these ordered structures would become deteriorated. Therefore, it is important to develop

new techniques enabling the homogenous coverage of VACNTs with semiconductor nanoparticles without the destruction of their ordered arrangement. For that especially gas phase deposition would be appropriate and as the distance between the CNTs in the VACNT forest usually is very small it is important to employ gas phase deposition techniques which are able to infiltrate the VACNT structure without depositions forming nanoparticles at the periphery of the VACNT structure blocking the further infiltration of the inner part of these 3D structures.

Atomic layer deposition (ALD) represents a gas phase deposition technique which enables precise control over the process of deposition of nanomaterials as thin layers or particles on top of a structured substrate. This would thus provide a new approach for the synthesis of [nanoparticle@CNT] nanocomposites which would combine photocatalytic active materials with high surface area flexible substrates.

Along another avenue of research, it was the intention to study titanium chalcogenides (chalcogenide = S, Se, Te). Titanium dioxide represents a traditional model photocatalyst suffers from the drawback of only absorbing UV light due to its wide band gap. It is known that titanium sulfides, selenides and tellurides possess small band gaps enabling them to make use of most of the solar spectrum. Besides, these materials exhibit layered structures which are advantageous for photocatalytic applications. Due to the strong affinity of titanium for oxygen the surface of such titanium chalcogenides (sulfides, selenides or tellurides) can even be easily oxidized forming titanium chalcogenide/titanium oxide core/shell heterostructures which would represent two-dimensional heterostructures representing an interesting category for photocatalytic hybrid materials.

In the following, the state of art of different photocatalyst materials and the synthesis of these materials is presented.

1.1.2 Fundamentals of photocatalysis

An increased interest is arising in the design of new efficient photocatalysts and the improvement of existing photocatalysts.^{9,10} According to the International Union of Pure and Applied Chemistry (IUPAC) photocatalysis the process where a chemical reaction is induced and accelerated by the use of semiconductor and light.¹¹

The electronic structure of semiconductors can be described as follows: semiconductors possess an electron filled valence band (VB) and an unoccupied conduction band (CB) which are

separated by a band gap where the presence of electrons is prohibited (**Figure 2**).¹² Not every semiconductor is suitable for photocatalysis. The band gap of a semiconductor can be **direct band gap** or an **indirect band gap**. In a direct band gap the momentum of an electron does not to be changed upon excitation from the valence band to the conduction band while in an indirect band gap the electron needs to absorb energy and also change its momentum in order to be excited to the conduction band. For that, the electron has to interact with a photon of appropriate energy and interact with a phonon (i.e. lattice vibration) at the same time. As the probability of the simultaneous interaction of an electron with a phonon is rather low and the overall process is slow, such semiconductors with an indirect band gap form much less excitons and are therefore not efficient as photocatalysts.^{13,14}

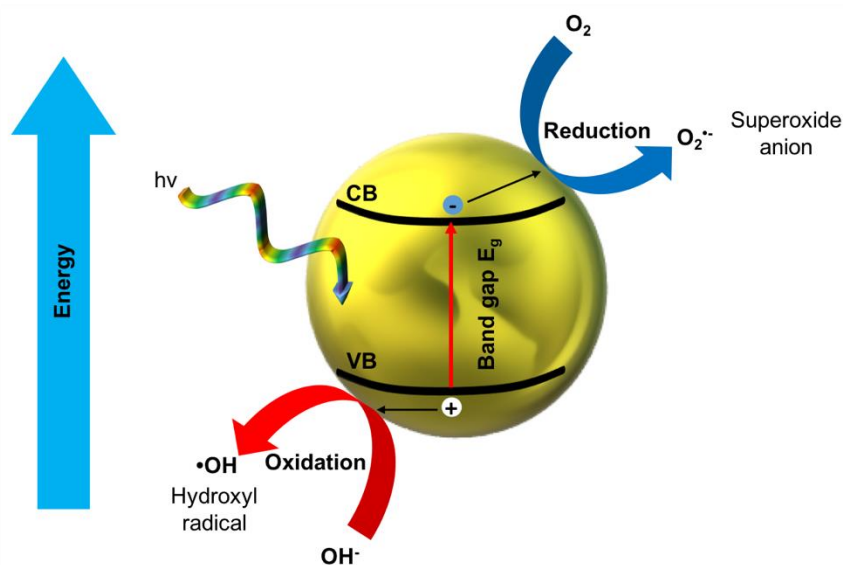
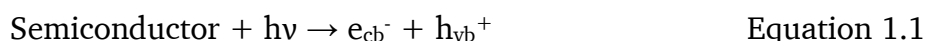


Figure 2 Schematic showing the processes taking place during photocatalysis upon absorption of light by a semiconductor nanoparticle for water remediation. Electrons from the valence band (VB) are excited to the conduction band (CB) forming an electron-hole pair which is then involved in redox reactions forming radicals.

Upon absorption of light having the appropriate energy required to overcome the semiconductor direct bandgap, electrons from the valence band are elevated into the conduction band leaving a hole behind forming an electron-hole pair, also known as exciton, as shown in **Figure 2**.¹⁴ The formed electron hole-pair is then involved in the formation of different reactive oxygen species (ROS), mainly superoxide anions $O_2^{\bullet-}$ and hydroxyl radicals $\bullet OH$ which are able to destroy organic materials and even kill pathogens in water enabling effective water remediation.^{15,16} The formed exciton can be destroyed through recombination of the electron and hole usually under generation of heat without being involved in any redox reactions. The photo-induced charge carrier recombination can occur in the bulk, known as bulk recombination, or at the

surface, known as surface recombination.¹⁷ Thus, mainly semiconductors with a direct band gap are appropriate for photocatalytic applications, but it is not only important to consider the exciton generation but also the lifetime of the formed exciton is of considerable interest. An extended lifetime of the exciton is very important to make the charge carriers available for subsequent chemical reactions.¹⁴

Equations 1.1-1.7 demonstrate the general reactions taking place during photocatalysis showing the different types of ROS radicals formed which then attack the organic molecules.^{15,18} When the semiconductor is excited electrons from the valence band move to the conduction band leaving a hole behind (Equation 1.1). If the formed charge carriers do not recombine in the bulk and reach the surface of the semiconductor they can react with oxygen and water thus providing reactive oxygen species for further reactions. Electrons from the conduction band are transferred to oxygen forming a superoxide anion radical $O_2^{\bullet-}$ (Equation 1.2). Holes from the valence band will be filled with electrons from water molecules resulting in the formation of hydroxyl radicals $\bullet OH$ (Equation 1.3). Hydroxyl radicals can combine to form hydrogen peroxide (Equation 1.4) which can further react with another superoxide radical (Equation 1.5). Superoxide anion radical can further react to hydroperoxyl radicals (Equation 1.6). The formed radicals can then attack organic compounds in various ways to decompose it to carbon dioxide and water in the ideal case as shown in equation 1.7.



For any redox reaction it should be considered that the redox potential of the electron acceptor is more positive than the conduction band and that the redox potential of the electron donor is more negative than the valence band as shown in **Figure 3a**. Thus, the semiconductor photocatalyst is only suitable for a specific redox reaction if the redox potential lies within its band gap. **Figure 3b** shows different common semiconductors with their band gaps and their band edge potentials and energies showing the position of the important redox potentials for the redox pairs involved in degradation of organics during water remediation ($\bullet OH/H_2O$ and

$O_2/O_2^{\cdot-}$) as well as the redox pairs involved in water splitting (O_2/H_2O and H_2/H_2O). The redox potential for the formation of hydroxyl radicals is $E_0(\cdot OH/H_2O) = 2.8$ V versus the normal hydrogen electrode (NHE) and the redox potential for the formation of superoxide anion radicals is $E_0(O_2/O_2^{\cdot-}) = -0.28$ V versus NHE. Thus, for the formation of hydroxyl radicals the valence band of the semiconductor must be more positive than 2.8 V and for the formation of superoxide anion radicals the conduction band of the semiconductor has to be more negative than -0.28 V to enable the electrons excited to the conduction band to reduce the oxygen.^{19,20}

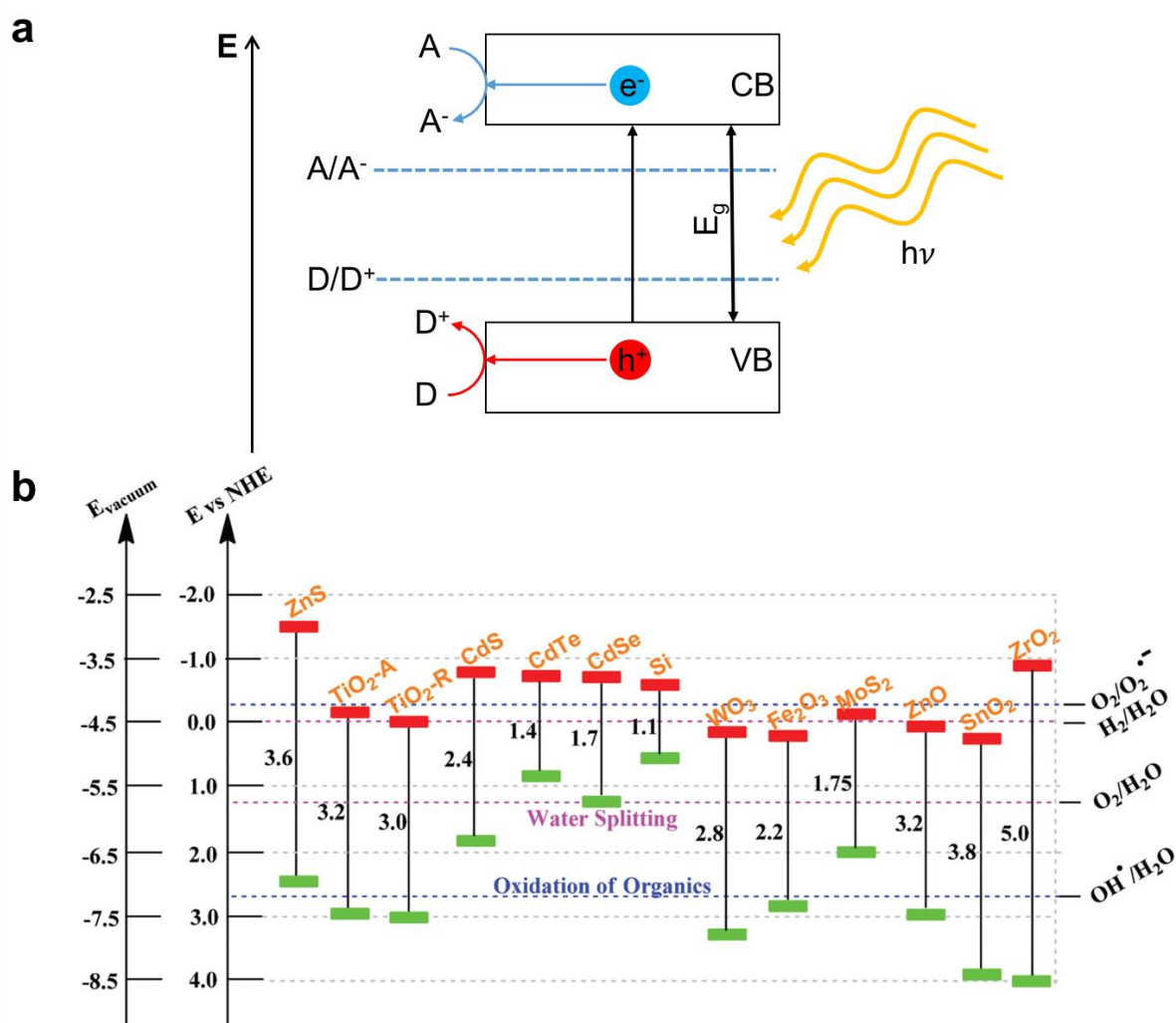


Figure 3 (a) Schematic showing the position of the redox potential of the electron acceptor (A) and electron donor (D) relative to the potential (E) of the valence band (VB) and conduction band (CB) of a semiconductor with the band gap E_g . (b) Band edge energies and band gap of different common semiconductors relative to the vacuum and to the normal hydrogen electrode (NHE) showing their position relative to the redox potentials of ($\cdot OH/H_2O$) and ($O_2/O_2^{\cdot-}$) redox pairs which are important for water remediation as well as the redox potentials of (O_2/H_2O) and (H_2/H_2O) redox pairs which are important for water splitting. Adapted with permission from Ref. ²⁰, © 2015 Royal Society of Chemistry.

Besides to the position and size of the band gap there are also a number of other factors which affect the quality of the photocatalyst of specific chemical composition. Usually crystal impurities and low crystallinity or crystal imperfections in the bulk or at the surface act as charge traps favoring the charge recombination, thus decreasing the lifetime of the photo-induced charge carriers. With decreasing particle size the amount of crystal imperfections and charge traps decrease resulting in more efficient photocatalysts.²¹ Furthermore, the probability of bulk recombination of the photo-induced charge carriers decreases as they reach the surface more quickly.^{14,21} A smaller particle size has also the advantage of a higher specific surface area which gives the possibility of interacting with a huge number of molecules during the photocatalytic process.¹⁴ On the other hand, a smaller particle size of a semiconductor also results in an increase in the band gap shifting the light absorption to the UV portion of the light spectrum which is known as the quantum size effect.²²⁻²⁴ Another factor concerning the structure of the material is the presence of a layered structure. Materials with a layered structure show a good charge separation and correspondingly excellent photocatalytic activity which makes the design and synthesis of layered materials attractive for photocatalytic applications.^{14,25}

An ideal semiconductor photocatalyst should have the following properties:^{10,26}

1. The material should be photoactive i.e. absorption of light should result in exciton formation.
2. The material should be able to absorb and make use of most of the solar radiation. Solar radiation consists of about 3 % UV, 44 % visible light and 53 % infrared radiation as shown in **Figure 4**.²⁷ Thus, it is important that the material is able to utilize the visible radiation of the sunlight.
3. The lifetime of the formed exciton should be long enough enabling the transport of the photo-induced charge carriers to the semiconductor-liquid interface where the redox reactions take place.
4. The photocatalyst should be chemically stable and inert as well as biologically inert.
5. The photocatalyst should be photostable i.e. it should be stable towards photo-corrosion.
6. It should be inexpensive and nontoxic.

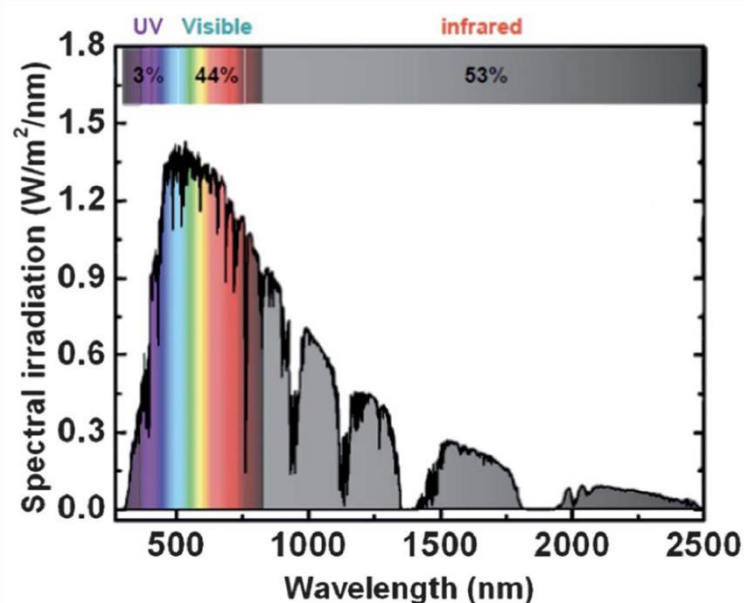


Figure 4 Spectral distribution of the solar light showing the intensities and percentages of UV, visible and infrared radiation. Adapted with permission from Ref. ²⁷, © 2012 Royal Society of Chemistry.

Titanium dioxide has emerged as model photocatalyst on which extensive research has been performed as it has several characteristics of a good photocatalyst.^{28–30} Thus, in order to understand and get an insight into the problems and challenges in the field of photocatalysis and photocatalyst design, it is crucial to take a look on the research performed on the traditional model photocatalyst titanium dioxide. Approaches which were developed for the increase of the photocatalytic activity of TiO₂ have been also used for other wide band gap semiconductors which are interesting candidates for photocatalysis such as ZnO and ZnS.

1.1.3 Traditional photocatalysts and modifications for improvement of photocatalytic efficiency

Titanium dioxide is the most investigated photocatalyst due to its advantages of high photocatalytic efficiency, non-toxicity, stability and low cost.³¹ But still it suffers from the major drawback that it only absorbs light in the ultraviolet range due to its wide band gap (3.2 eV for anatase and 3.0 eV for rutile phase).³¹ Thus, a large part of the solar radiation is left without use. Therefore, several approaches for modification of TiO₂ have been investigated in order to enable full use of the solar spectrum:

- **Metal ion doping and non-metal doping:** Doping with various metals and non-metals has been performed in literature and has been referred to as band-gap engineering.³² In order to achieve a visible light response for wide band gap semiconductors like TiO₂,

ZnO, ZnS, etc. a narrowing of the band gap is required either through the elevation of the level of the valence band, through the lowering of the level of the conduction band or through the insertion of mid-gap states.³¹ But it is still important to ensure that the redox potential of the reactions of interest still lie within the modified band gap. Metal doping has been performed in literature for the different wide band gap semiconductors (TiO₂, ZnO and ZnS) with metals ions as Cr³⁺,^{33,34} Fe³⁺,³⁵⁻³⁹ Mg²⁺,⁴⁰ Cu²⁺,⁴¹ Mn²⁺,⁴² Nd³⁺,⁴³ Sm³⁺,⁴⁴ Gd³⁺,⁴⁵ and other rare earth metal ions.⁴⁶ Although still some controversy about the exact role of the doped metal ion exists, it is suggested that the doped metal ions form some localized states below the conduction band minimum resulting in band gap narrowing (**Figure 5a**).⁴⁷ On the other hand, it was also found that these localized impurity states introduced through metal doping have the problem of thermal instability and sometimes act as charge carrier recombination centers which affects the photocatalytic activity.⁴⁸ Modifications through non-metal doping have been also extensively performed and studied in literature with non-metals like boron, carbon, phosphorous, sulfur, iodine and especially nitrogen which partially substitute oxygen in case of metal oxides resulting in the formation of localized states above the valence band and leading to a band gap narrowing (**Figure 5b**).^{29,49-56} N-doped ZnS also showed increased stability towards photocorrosion which shows that non-metal doping can have also a positive effect on the stability of photocatalysts.⁵⁵

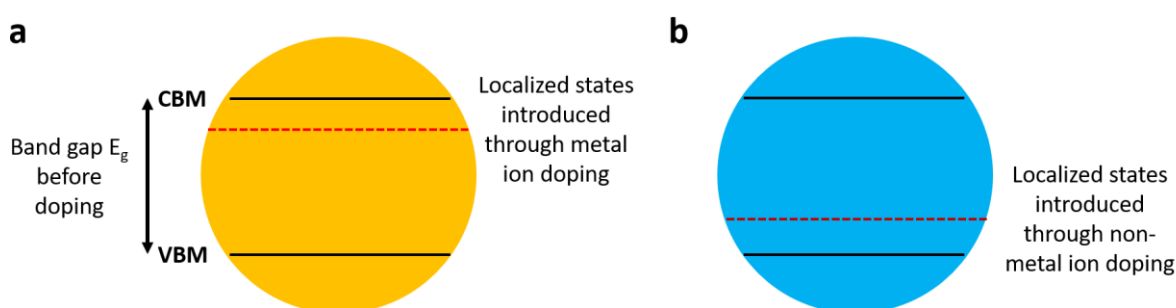


Figure 5 Schematic showing the localized states which could be introduced in the band gap through (a) metal ion doping and (b) non-metal ion doping resulting in a narrowing of the band gap enabling visible light absorption in case of wide band gap semiconductors like TiO₂. VBM is the valence band maximum and CBM is the conduction band minimum.

- **Dye sensitization:** Dyes which can be physisorbed on the surface of semiconductor photocatalysts can help in semiconductor sensitization towards visible light. Dyes can be physisorbed through the formation of weak van der Waals interactions and absorb visible

light which excites their electrons from the HOMO to LUMO which can be further transferred to the conduction band of the wide band gap semiconductor giving it the ability to produce the required radicals for pollutant degradation.^{56,57} As the dye sensitization of the semiconductor depends on the adsorption of the dye on the semiconductor surface a pH adjustment can introduce a charge on the surface of the semiconductor and depending on the charge of the dye the adsorption can be increased for more efficient sensitization.⁵⁸ Different dyes have been used to sensitize wide band gap semiconductors, especially TiO₂, for visible light photocatalysis like acid red 44,⁵⁸ eosin Y,⁵⁹ 8-hydroxyquinoline,⁶⁰ methylene blue,⁶¹ and reactive red dye 198.⁶² The problem of dye sensitized semiconductors for photocatalysis is their stability as desorption of the dye results in a loss of the visible light photocatalytic activity and pollution. Thus, some methods were introduced for the chemical fixation of the sensitizing dye molecules on the surface of the semiconductor.⁵⁹

- **Partial reduction or hydrogenation (Black TiO₂):** The first synthesis of black TiO₂ was performed by Chen et al. in 2011 through the treatment of pure white TiO₂ with hydrogen under high pressure (20 bar) at 200°C for 5 days which resulted in a black TiO₂ powder (**Figure 6a**).⁶³ A black powder indicates instantly the absorption of visible light which results in the black color appearance representing a successful extension of the absorption range of TiO₂ to the visible light. Investigation of the underlying cause for the efficient band gap reduction to about 1.54 eV which extended the absorption not only to the visible but also to the near infrared region revealed a hydrogenation of the outer surface of the TiO₂ nanoparticles forming a disordered shell layer (**Figure 6b-d**). The dramatic reduction of the band gap was attributed to the hydrogenation which resulted in the formation of mid-gap states consequently elevating the valence band edge. These engineered disorders also act as traps for the trapping of charge carriers thus preventing their rapid recombination.⁶³ Due to the high activity of black TiO₂, it quickly became a research hot spot for environmental nanoscience where different methods for its synthesis have been developed.⁶⁴⁻⁷⁰

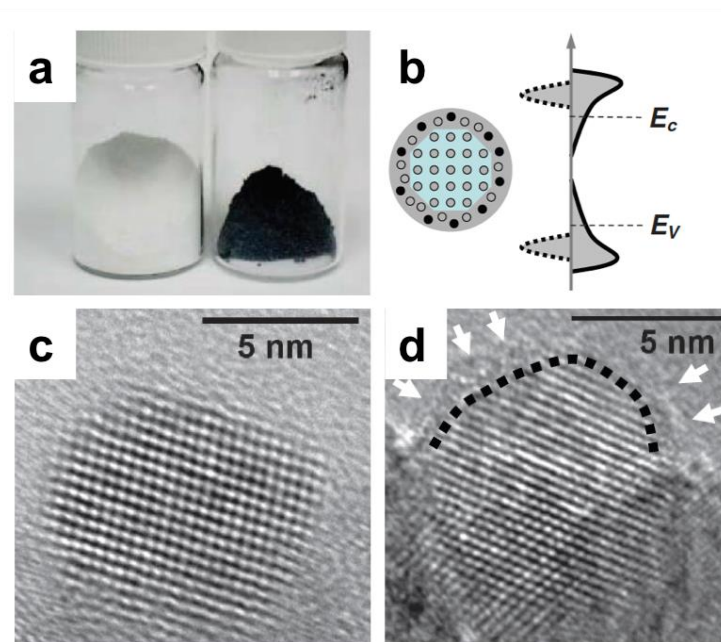


Figure 6 (a) Photograph showing a comparison of TiO_2 powder before (white) and after (black) high pressure hydrogenation, (b) Schematic showing the structure of black TiO_2 which consists of an outer disordered shell layer (grey) and an inner highly crystalline core (cyan). Besides the valence band (E_v) and conduction band (E_c) for unmodified white TiO_2 (on the left) and black TiO_2 (on the right) are illustrated showing the tailing of these bands resulting in the dramatic decrease of the band gap. (c) HRTEM image of unmodified white TiO_2 showing the high crystallinity of the TiO_2 before hydrogenation. (d) HRTEM image of black TiO_2 formed after hydrogenation showing the outer disordered shell and the inner crystalline core. The curved dotted line outlines the interface between the disordered shell and the crystalline core for clarification. Adapted with permission from Ref. ⁶³, © 2011 American Association for the Advancement of Science.

Another direction is the design of composite materials which enable the use of the full solar spectrum and at the same time enable spatial separation of the formed electron-hole pairs which increases the lifetime of the exciton making the charge carriers available for the subsequent redox reactions. Through combining different materials, it is possible to achieve synergistic effects and to make use of the advantages of each material. There have been different material composites used for photocatalysis which can be categorized in:

a) **Semiconductor-semiconductor composites:** Semiconductors can be combined forming a heterojunction to increase the ability of charge separation. There are different types of possible heterojunctions between semiconductors depending on the band alignments namely type I (straddling gap), type II (staggered gap) and type III (broken gap) heterojunctions (**Figure 7**).⁷¹⁻⁷³

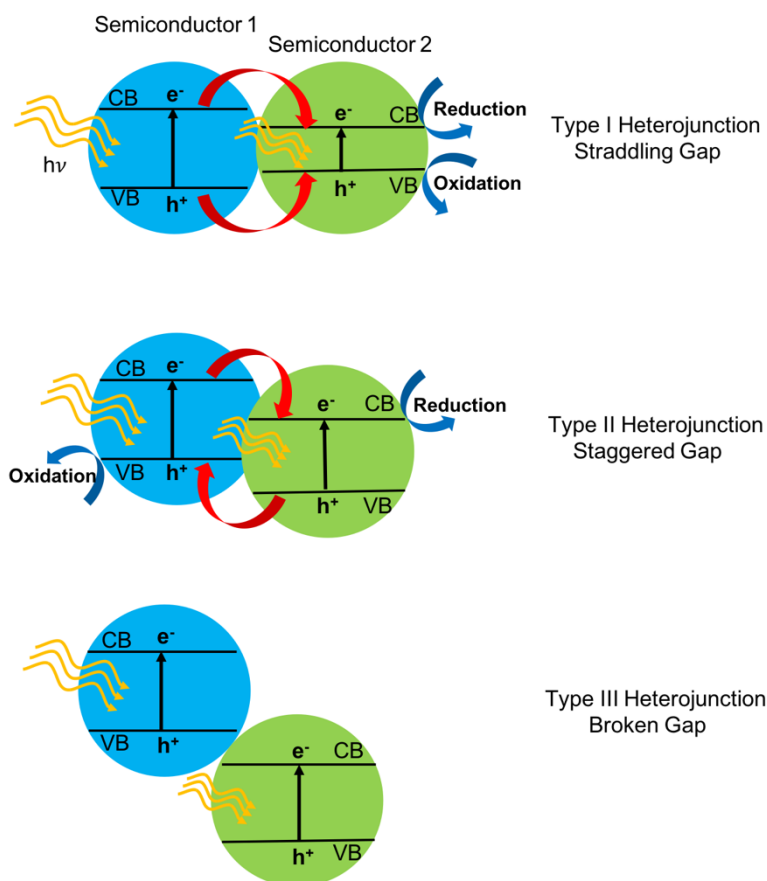


Figure 7 Schematic showing the different types of heterojunctions which can be formed between two semiconductors depending on their relative band alignments and the resulting electron-hole separation behavior upon light excitation.

In case of type I heterojunction with the straddling gap, the valence and conduction band of one semiconductor lies within the band gap of the other semiconductor (**Figure 7**, top). This results upon light excitation that both the photo-induced electrons and holes of the wide gap semiconductor flow to the conduction band and valence band of the narrow gap semiconductor, respectively. Thus, there is no spatial separation of the photo-induced charge carriers as the oxidation and reduction reactions take place on the same semiconductor. At the same time the overall redox ability of the composite photocatalyst is reduced as the reactions take place on the semiconductor with lower redox potential.⁷² In case of type II heterojunction with the staggered gap, the conduction band as well as the valence band of the second semiconductor lie beneath the corresponding conduction and valence bands of the first semiconductor (**Figure 7**, middle). Upon light excitation, this results in a net flow of the photo-induced holes to the valence band with more negative potential present in semiconductor 1 and a flow of the photo-induced electrons to the conduction band with the more positive potential present in semiconductor 2.

Overall an efficient spatial separation of the formed electron-hole pair can be achieved which is highly advantageous for efficient photocatalysis but on the other hand this also results in an overall decrease for the redox ability similar to type I heterostructures.^{27,72,74–76} Type III heterojunctions with the broken gap are an extreme form of the staggered gap where the band gaps of both semiconductors do not overlap at all (**Figure 7**, bottom). In this case a transfer of photo-generated holes or electrons is not possible between the semiconductors resulting in no efficient charge separation.⁷² Accordingly, type II heterojunctions appear to be the appropriate choice for the design of efficient photocatalysts due to the efficient charge separation. In literature, several type II heterojunction photocatalysts have been designed with high photocatalytic activities. For example, Yu et al. synthesized a CdS-TiO₂ nanocomposite through a microemulsion-mediated solvothermal method showing a 8 times increased photocatalytic activity in the degradation of methylene blue under UV-Vis light compared to CdS alone.⁷⁷ Furthermore, SnO₂/TiO₂ composite films were prepared by Zhou et al. via electrophoretic deposition on conductive glass substrates and subsequent calcination in air at different temperatures. The composite samples showed high photocatalytic activity in the decomposition of Rhodamine B under UV-light where especially the sample calcined at 400°C showed the highest photocatalytic activity. This was attributed to the optimal crystallinity of the samples which further reduced possible recombination centers besides the rapid and effective charge separation achieved through the composite film.⁷⁸ SnO₂ has been also combined with TiO₂ by Wang et al. in form of nanofiber heterostructures where SnO₂ nanoparticles were grown through a hydrothermal method on the surface of previously electrospun TiO₂ nanofibers (**Figure 8a, b**). The nanocomposite was compared to bare TiO₂ nanofibers and showed a 2.5 times increase in the photocatalytic activity in Rhodamine B decomposition under UV light due to the more efficient charge separation and suppressed charge recombination in the heterostructure.⁷⁹ In order to make use of visible light Shang et al. prepared a three-dimensional hierarchical heterostructure of Bi₂WO₆/TiO₂ through an electrospinning-assisted route which was able to effectively degrade acetaldehyde in air and Rhodamine B in water.⁸⁰ The nanocomposite formed a three-dimensional network of TiO₂ nanofibers with Bi₂WO₆ platelets grown aslant on the surface of the TiO₂ nanofibers (**Figure 8c, d**) thus producing a mesh with high surface area and efficient charge separation for visible light photocatalysis. The observed increase in photocatalytic activity achieved a 5-fold increase in comparison to Bi₂WO₆ alone for the degradation of Rhodamine B under visible light where the photocatalytic activity of TiO₂

alone under visible light can be ignored which shows the synergistic effect achieved by the nanocomposite due to the type II heterojunction formed.⁸⁰

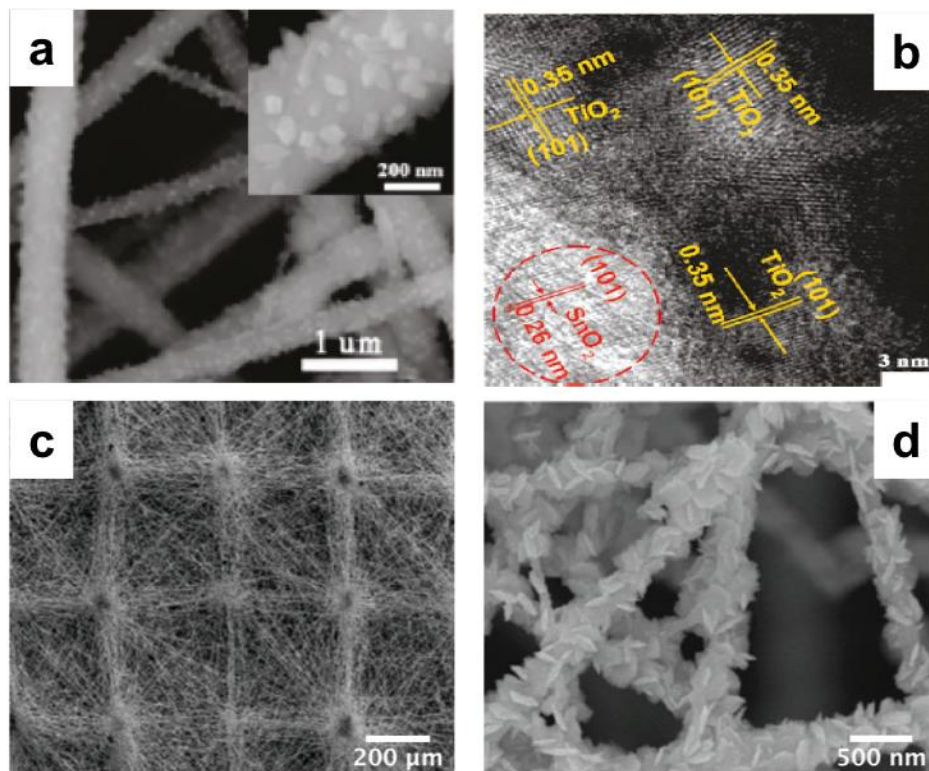


Figure 8 (a) SEM of TiO₂ nanofibers with SnO₂ nanoparticles on the nanofiber surface and (b) HRTEM of the SnO₂-TiO₂ heterojunction region showing the attachment of SnO₂ nanoparticles to TiO₂ nanofibers. Adapted with permission from Ref. ⁷⁹, © 2009 American Chemical Society. (c) SEM image showing an overview of the three-dimensional hierarchical Bi₂WO₆/TiO₂ structure prepared through electrospinning procedure and (d) SEM image with increased magnification showing a close-up of the detailed structure of the nanocomposite where Bi₂WO₆ platelets are grown aslant on TiO₂ nanofibers. Adapted with permission from Ref. ⁸⁰, © 2009 American Chemical Society.

Also, type II heterojunctions could be achieved with different phases of the same semiconductor as it is the case with anatase and rutile phases of TiO₂.⁸¹⁻⁸³ From **Figure 3b** it is obvious that the valence and conduction band of anatase TiO₂ is shifted to more negative potential in comparison with the corresponding valence and conduction bands of rutile TiO₂. Thus, a composite consisting of these two TiO₂ phases will form a type II heterojunction what makes the commercial Degussa P25 so special as it consists of a mixture of anatase and rutile TiO₂ phases in a ratio of about 3:1.⁸⁴

For further enhancement of the spatial separation of the photo-induced charge carrier as well as increasing the rate of charge separation to further suppress charge recombination p-n

heterojunctions have been developed. Here, a p-type and n-type semiconductor are used in the composite material. When p-type and n-type semiconductors are in contact electrons diffuse from the n-type semiconductor to the p-type semiconductor interface and holes diffuse from the p-type semiconductor to the n-type semiconductor interface to equilibrate the Fermi energy levels E_F resulting in a space charge region forming an intrinsic electric field at the p-n heterojunction (**Figure 9**).^{72,75} The formed internal electric field is an additional driving force for the efficient spatial charge separation. Thus, after light irradiation the photo-induced electrons flow from the conduction band of the p-type semiconductor to the conduction band of the n-type semiconductor due to the band alignment as well as due to electrostatic attraction through the internal electric field formed at the p-n heterojunction. The same applies to the flow of photo-induced holes in opposite direction from the valence band of n-type semiconductor to the valence band of p-type semiconductor.⁷⁵ For example, Yu et al. prepared NiO/TiO₂ p-n junction flowerlike composites by a hydrothermal method followed by calcination at 400°C and showed that their photocatalytic activity is superior to TiO₂ or NiO alone. The increased activity was explained by the formation of a p-n junction between NiO and TiO₂ resulting in an efficient charge separation.⁸⁵

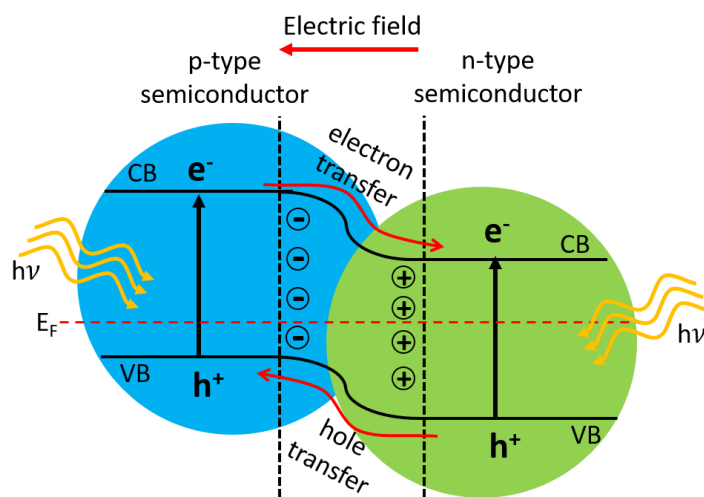


Figure 9 Schematic showing the processes occurring in a semiconductor nanocomposite composed of a p-type and n-type semiconductor forming a p-n heterojunction.

b) Semiconductor-metal nanocomposites: Semiconductor-metal nanocomposites have been used for the design of efficient photocatalysts as these nanocomposites offer two main advantages^{26,74,86,87}:

1. The fast and efficient charge separation due to the conductivity of metals and the formation of Schottky barrier at the semiconductor-metal interface which promotes spatial charge separation upon light irradiation and suppressing charge recombination.⁸⁸
2. The spectrum of light absorption is extended to the visible light due to the plasmonic properties of metals (especially noble metals like gold and silver).

Furthermore, the noble metals such as platinum act as co-catalysts in the system forming active centers for chemical reactions to take place on with lower activation energies than on the semiconductor.²⁶ Different semiconductor-metal nanocomposites have been synthesized in literature and proved enhanced photocatalytic efficiency in the degradation of different dyes and pollutants as phenol,⁸⁹ methyl orange⁹⁰ and rhodamine B.^{91,92} A plasmonic Au/TiO₂ nanocomposite photocatalyst which consists of titania with embedded gold nanoparticles of 0.5% loading showed a three times increased activity in phenol degradation compared to TiO₂ alone.⁸⁹

c) Semiconductor-polymer composites: Semiconductors were also combined with polymers to enhance the photocatalytic activity and to act as matrix for embedding photocatalyst nanoparticles.⁹³ The main benefit of using polymers especially of an extended π -conjugated system is the ability of visible light absorption thus sensitizing wide band gap semiconductors like TiO₂ for visible light.⁹⁴ Zhang et al. prepared a TiO₂-Polyaniline (TiO₂-PANI) nanocomposite where the polyaniline formed a thin layer around TiO₂ nanoparticles.⁹⁵ The formed semiconductor-polymer nanocomposite showed an increased UV light photocatalytic activity in methylene blue and Rhodamine B degradation compared to bare TiO₂. Additionally, the nanocomposite also showed a visible light photocatalytic activity, thus overcoming one important disadvantage of bare TiO₂ which is only active under UV irradiation. Investigation of the underlying mechanism revealed that upon UV light irradiation electrons are excited in the TiO₂ nanoparticles to the conduction band leaving holes behind in the valence band. As PANI is a good conductor for holes, the holes are transferred to the HOMO of PANI as it lies above the valence band of TiO₂, thus resulting in a spatial charge separation and suppressing the charge recombination (**Figure 10a**). This is reflected as a synergistic effect in the photocatalytic activity of the nanocomposite under UV irradiation. Upon visible light irradiation which cannot excite the electrons in TiO₂, the electrons are excited in PANI from π to π^* and due to the relative position of the π^* orbital to the conduction band of TiO₂ electrons

are transferred to the conduction band of TiO_2 reducing adsorbed oxygen and resulting in active radical species for pollutant degradation giving the nanocomposite its visible light photocatalytic activity (**Figure 10b**).⁹⁵ Zhu et al. prepared polythiophene/ TiO_2 composites which showed efficient photocatalytic degradation of methyl orange under UV and visible light irradiation. Also an increased adsorption efficiency of the nanocomposite compared to each component alone was observed which is further beneficial for the pollutant removal beside the photocatalytic activity.⁹⁶ Other composites include sulfonated polyaniline@ TiO_2 for the degradation methylene blue and brilliant blue dyes under visible light irradiation,⁹⁴ chitosan-g-poly(acrylamide)/ZnS nanocomposite for the degradation of methyl orange and congo red under simulated solar radiation,⁹⁷ and polythiophene/mesoporous SrTiO_3 nanocomposites for the degradation of methylene blue under visible light.⁹⁸

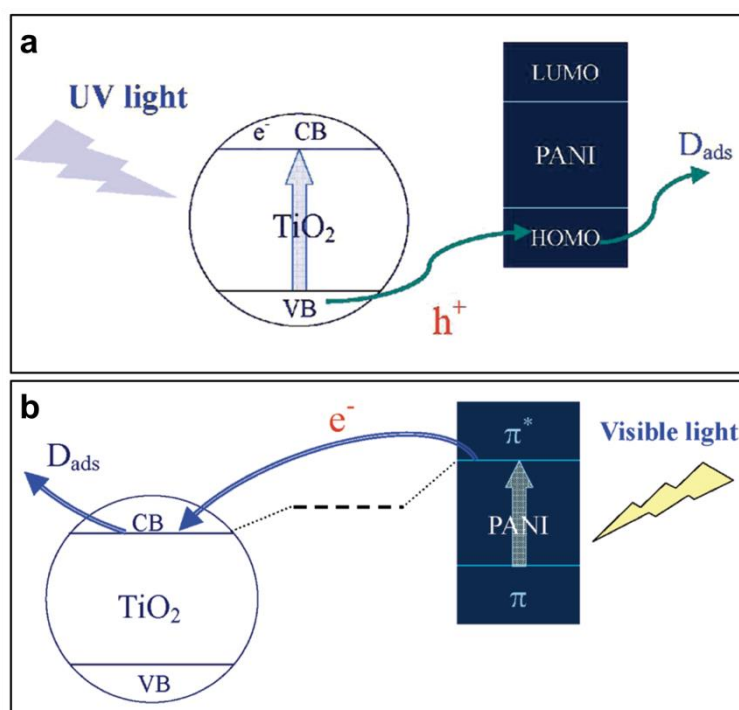


Figure 10 Schematic showing the possible mechanism resulting in the photocatalytic activity of the TiO_2 -PANI nanocomposite upon (a) UV light and (b) visible light irradiation. Adapted with permission from Ref. ⁹⁵, © 2008 American Chemical Society.

d) Semiconductor-carbon composites: Various work has been also performed on the combination of different semiconductors with different carbon forms as carbon nanotubes (CNTs), graphene, reduced graphene oxide, activated carbon and carbon dots which has been nicely reviewed in several review articles.^{73,75,99–104}

Carbon nanotubes, especially multi-walled CNTs, which possess metallic character have been proved very effective in photocatalytic applications upon formation of heterostructures with different wide band gap semiconductors as TiO_2 ,^{7,105–109} ZnO ^{110–113} and ZnS .^{114–119} Heterostructures of semiconductors with CNTs possess several advantages showing the uniqueness of these nanocomposites:

1. CNTs with metallic character form a Schottky barrier junction upon contact with the semiconductor as it is known for semiconductor-metal junctions. This is very beneficial for the rapid and efficient charge separation upon irradiation and it increases the recombination time of the photo-induced charge carriers.⁷⁵
2. CNTs also possess a high electron storage capacity which enables an easy electron transfer to the CNTs which in turn has a positive effect on the charge carrier separation retarding their recombination and resulting in a spatial separation of the photo-induced charge carriers.²⁴
3. CNTs are capable to absorb light till the infrared region thus extending the light absorption for the semiconductor-CNT nanocomposite making the use of most sunlight.¹¹⁷
4. CNTs are known for their high specific surface area which give the CNTs a high adsorption capacity. Thus, pollutants are not only removed through degradation but also through efficient adsorption from the surrounding medium which is especially important for non-organic pollutants not being accessible through photocatalytic degradation.^{120–}

123

The proposed mechanism for the dual action of semiconductor-CNT heterostructure nanocomposites can be found in **Figure 11**. For wide band gap semiconductors (e.g. TiO_2 , ZnO and ZnS) which can only absorb UV light, an electro-hole separation takes place upon UV light irradiation. Due to the good electron conductivity of CNTs the electrons from the conduction band of the excited semiconductor easily migrates to the CNT which is also enhanced by the formed Schottky barrier resulting in an efficient spatial charge separation.^{24,75,104} In case of longer wavelengths (i.e. visible and infrared light) which cannot be absorbed by the semiconductor, this light is absorbed by the electron-rich CNTs resulting in electron excitation which are then injected into the conduction band of the attached semiconductor resulting in an electron-deficiency in the CNTs which is compensated through back-transfer from the valence band of the semiconductor leaving a hole behind. Like this,

CNTs act as a photosensitizer for wide band gap towards visible and even infrared light.^{124–}

127

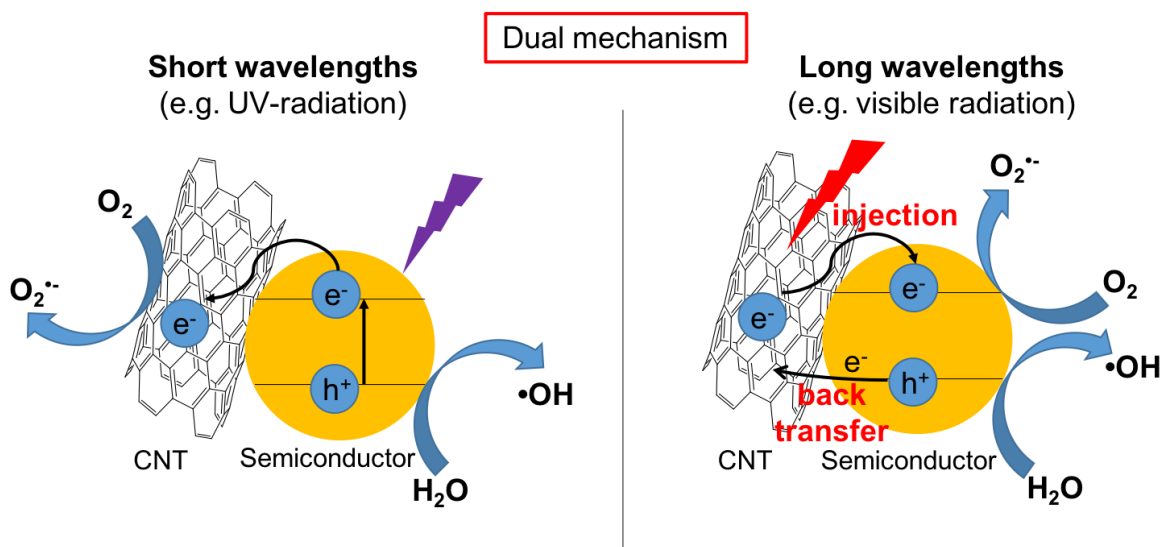


Figure 11 Schematic showing the possible mechanism involved in the photocatalytic activity of semiconductor-CNT nanocomposites where a dual mechanism enables the use of most of the solar spectrum.

After discussing the advantages of semiconductor-carbon nanocomposites and as in the following work presented in the cumulative part we focused on the synthesis of semiconductor nanoparticle-CNT nanocomposites, it is important to present the different approaches for synthesis of different nanoparticle-CNT nanocomposites found in literature.

1.1.4 Synthesis of nanoparticle-carbon nanotube nanocomposites

In literature different synthesis methods and approaches for the preparation of nanoparticle-CNT heterostructure nanocomposites exist which can be broadly divided into three categories¹²⁸:

1. Covalent attachment of nanoparticles through organic linker molecules to functionalized CNTs. This requires a surface functionalization of the CNTs which could alter its electronic properties. But this approach offers the advantages of controlling the synthesis of the nanoparticles separately without the influence of CNTs on the nucleation and growth of the nanoparticles, the firm attachment of the nanoparticles to the CNTs preventing their detachment even under extensive washing and finally a controlled attachment position of the nanoparticles depending on the placement of the organic linker molecules on the CNTs enabling a homogenous distribution of the particles on the walls of CNTs.¹²⁸ The most widely distributed covalent approach is the oxidation of the

-
- CNTs so that the walls carry acid functionalities which are then coupled to the synthesized nanoparticles through carbodiimide coupling.^{129,130}
2. Noncovalent attachment of nanoparticles through noncovalent interactions like van der Waals interactions to CNTs. As in case of covalent attachment the sp^2 hybridization of some carbon atoms gets converted to sp^3 which disrupts the electronic structure of CNTs the noncovalent functionalization will offer the advantage of not changing the carbon hybridization, thus being a non-destructive approach maintaining the electronic integrity of CNTs.¹²⁸ Different approaches for non-covalent attachment have been developed including attachment through electrostatic interactions where the CNTs are wrapped with a polymer (polymer wrapping) or covered with a polyelectrolyte or surfactant to produce a surface charge to which the nanoparticles of opposite charge are attached.^{131,132} Other approaches are direct hydrophobic interaction or π - π interactions of nanoparticles capped with hydrophobic molecules with the walls of the CNTs.¹³³⁻¹³⁵ But still depending on the interactions used for the noncovalent attachment these nanocomposites are more prone to nanoparticle detachment when compared to the covalent approach. Furthermore, a direct electron transfer between the CNTs and the nanoparticles could be problematic due to the absence of a direct contact between the CNTs and the nanoparticles.
 3. Direct deposition of the nanoparticles on the walls of CNTs through in situ formation of the nanoparticles in presence of CNTs. In this case, the precursors for the formation of the nanoparticles are added to a CNT suspension and are allowed to react resulting in a direct nucleation of the nanoparticles on the CNT walls.¹³⁶⁻¹³⁸ This enables a direct and intimate contact between the nanoparticle and the CNT which is beneficial for any electron transfer processes.

While TiO₂-CNT nanocomposites have been synthesized much in literature^{7,108} and applied for photocatalysis, there are only a few reports about ZnS-CNT nanocomposites and their use as photocatalysts.¹¹⁴⁻¹¹⁹ Feng et al. synthesized ZnS-CNT nanocomposite through a hydrothermal route where aqueous solutions of Zn(NO₃)₂ and Na₂S were added to previously nitric acid treated CNTs and allowed to react. The obtained ZnS-CNT nanocomposite (**Figure 12a**) was tested for its photocatalytic activity towards the degradation of methylene blue under UV irradiation where the ZnS-CNT nanocomposite showed an increased activity degrading the dye in 35 min instead of 80 min needed in case of ZnS nanoparticles.¹¹⁴ Wu et al. prepared ZnS-

CNT nanocomposites through a microwave-assisted method where nitric acid treated CNTs were mixed with zinc acetate and thioacetamide as Zn and S precursors, respectively followed by microwave refluxing for 15 min. The resulting nanocomposite (**Figure 12b**) was tested for its photocatalytic activity towards methyl orange degradation under UV light.¹¹⁵ Fang et al. synthesized ZnS-CNT nanocomposites through a photochemical methods where previously prepared amorphous carbon nanotubes were mixed with zinc acetate and thioacetamide. Then the mixture was exposed to UV light with a wavelength of 365 nm for different reaction times. The resulting nanocomposites (**Figure 12c**) were tested for their photocatalytic activity towards the degradation of eosin, methylene blue and methyl red under UV irradiation.¹¹⁶

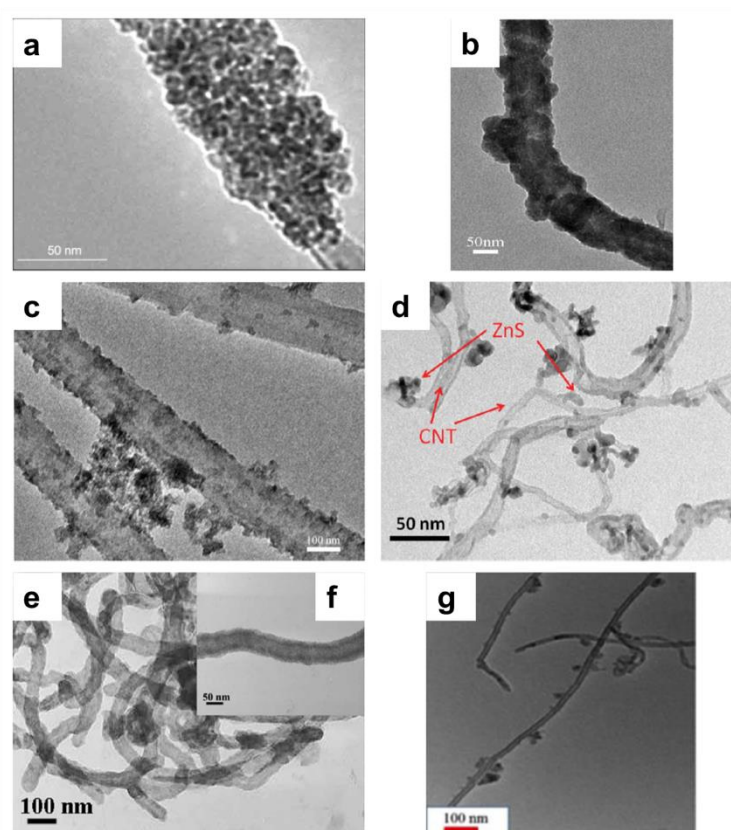


Figure 12 TEM images for different ZnS-CNT nanocomposites prepared in different literature work through (a) a hydrothermal route by Feng et al. (Adapted with permission from Ref. ¹¹⁴, © 2008 Institute of Coal Chemistry, Chinese Academy of Sciences. Published by Elsevier B.V.), (b) a microwave-assisted route by Wu et al. (Adapted with permission from Ref. ¹¹⁵, © 2008 American Chemical Society), (c) a photochemical method by Fang et al. (Adapted with permission from Ref. ¹¹⁶, © 2011 Springer Nature), (d) an ultrasonication-assisted route by Meng et al. (Adapted with permission from Ref. ¹¹⁷, © 2015 Taylor & Francis Group, LLC), (e) and (f) an ultrasonic-assisted route in organic media by Tang et al. (Adapted with permission from Ref. ¹¹⁸, © 2017 Springer Nature), (g) a co-precipitation method for the production of manganese doped ZnS-CNT by Sharifi et al. (Adapted with permission from Ref. ¹¹⁹, © 2019 Elsevier).

Meng et al. prepared ZnS-CNT nanocomposites through an ultrasonication route where previously oxidized CNTs were mixed with ZnCl_2 and Na_2S aqueous solutions followed by ultrasonication for 7 h and a final heat treatment of the dried product at 300°C . The obtained dark greenish ZnS-CNT nanocomposite (**Figure 12d**) was tested for the photocatalytic degradation of methylene blue under visible light irradiation.¹¹⁷ Another ultrasonic-assisted synthesis of ZnS-CNT nanocomposites was performed by Tang et al. where CNTs were dispersed together with ZnCl_2 and elemental sulfur in tetrahydrofuran (THF) through ultrasonication, followed by the dropwise addition of a NaBH_4 solution in THF with further ultrasonication for 30 min. The resulting nanocomposite (**Figure 12e** and **12f**) was tested for its photocatalytic activity in degrading methyl orange under visible light where the nanocomposite showed improved activity compared to ZnS nanoparticles alone.¹¹⁸ Sharifi et al. prepared manganese doped ZnS-CNT nanocomposite through a simple co-precipitation method where acid functionalized CNTs were mixed with aqueous solutions of zinc acetate and manganese acetate to which Na_2S was added dropwise and allowed to react at 100°C for 1 h. The resulting nanocomposite (**Figure 12g**) was tested for its photocatalytic performance towards the degradation of acid red 18 and methylene blue under UV irradiation.¹¹⁹

The previous discussion shows that in literature mainly wet chemical approaches are used for the preparation of nanoparticle-CNT nanocomposites. One reason for the use of wet chemical approaches is the use of powdered CNTs which can be easily suspended in different solvents. Coating of powdered CNT samples with semiconductor nanoparticles using gas phase deposition techniques would not be possible as this would not result in a homogenous coating of the CNTs. On the contrary, the use of ordered vertically aligned CNTs (VACNTs) forests would enable a gas phase deposition of semiconductor nanoparticles as all sides of the CNTs will be equally exposed to the reaction gas. The gas phase deposition of nanoparticles on VACNTs would enable direct contact between the semiconductor nanoparticles and the CNTs without any linker molecules or modification of the CNT walls which would facilitate the electron transfer between the semiconductor nanoparticles and the CNTs which would make such an approach attractive. In order to achieve homogenous coating of the VACNT forest, it is important to use a gas phase deposition technique which enables precise control of the deposition in order to prevent clogging of the outer surfaces of the VACNT forest which would leave the interior of the VACNT forest without nanoparticles. Atomic layer deposition (ALD)

offers such an interesting synthetic approach for the controlled production of semiconductor-CNT nanocomposites.

ALD depends on the principle of self-limiting surface reactions which enable a precise control of the deposition process. Simply, the process consists of consecutive cycles where each cycle consists of two subsequent half-reactions. During each half-reaction the precursor gas is allowed to react with the surface followed by the removal of excess unreacted precursor gas and any gaseous by-products before the next precursor enters into the reaction chamber. Thus, an ALD cycle for the deposition of binary semiconductors such as TiO₂, ZnO or ZnS consists of four steps: first precursor pulse (usually a precursor of the metal), inert gas purge, second precursor pulse (usually water in case of metal oxides) and again an inert gas purge (**Figure 13a**). This cycle can be repeated several times thus forming the material layer by layer with precise thickness control.^{139–141} Due the precise control offered by the ALD process which also enables good coating of high aspect ratio substrates,^{142,143} it rapidly gained popularity and was used for the effective coating of vertically aligned CNT forests by different semiconductors to form semiconductor-CNT heterostructures (**Figure 13b**) which are applicable for various applications including photocatalysis as discussed above.^{144–150}

The use of ALD for nanoparticle deposition on CNTs enables direct contact of the nanoparticles with the CNTs without the use of any linker molecules which is beneficial for electron transfer to take place between the semiconductor nanoparticles and the CNTs. Upon exposure of the vertically aligned CNTs with the precursor gas adsorption takes place especially on defective parts on the CNT wall thus resulting in an island growth which results in the formation of nanoparticles for a small cycle number and their size can be tuned with the number of cycles.^{144–146} Increasing the cycle number results in a closed layer due to the coalescence of neighboring crystals.¹⁴⁸ Acauan et al. showed that coating of a forest of nitrogen doped CNTs and oxidized plasma-treated CNTs resulted in a more uniform and complete coverage with TiO₂ compared to a pristine forest of vertically aligned CNTs which has been ascribed to the increased distribution of defects or more precisely carbon-heteroatom bonds.¹⁴⁹ This shows the possibility of the controlled formation of different semiconductor-CNT heterostructure nanocomposites which can be used for efficient photocatalytic applications.

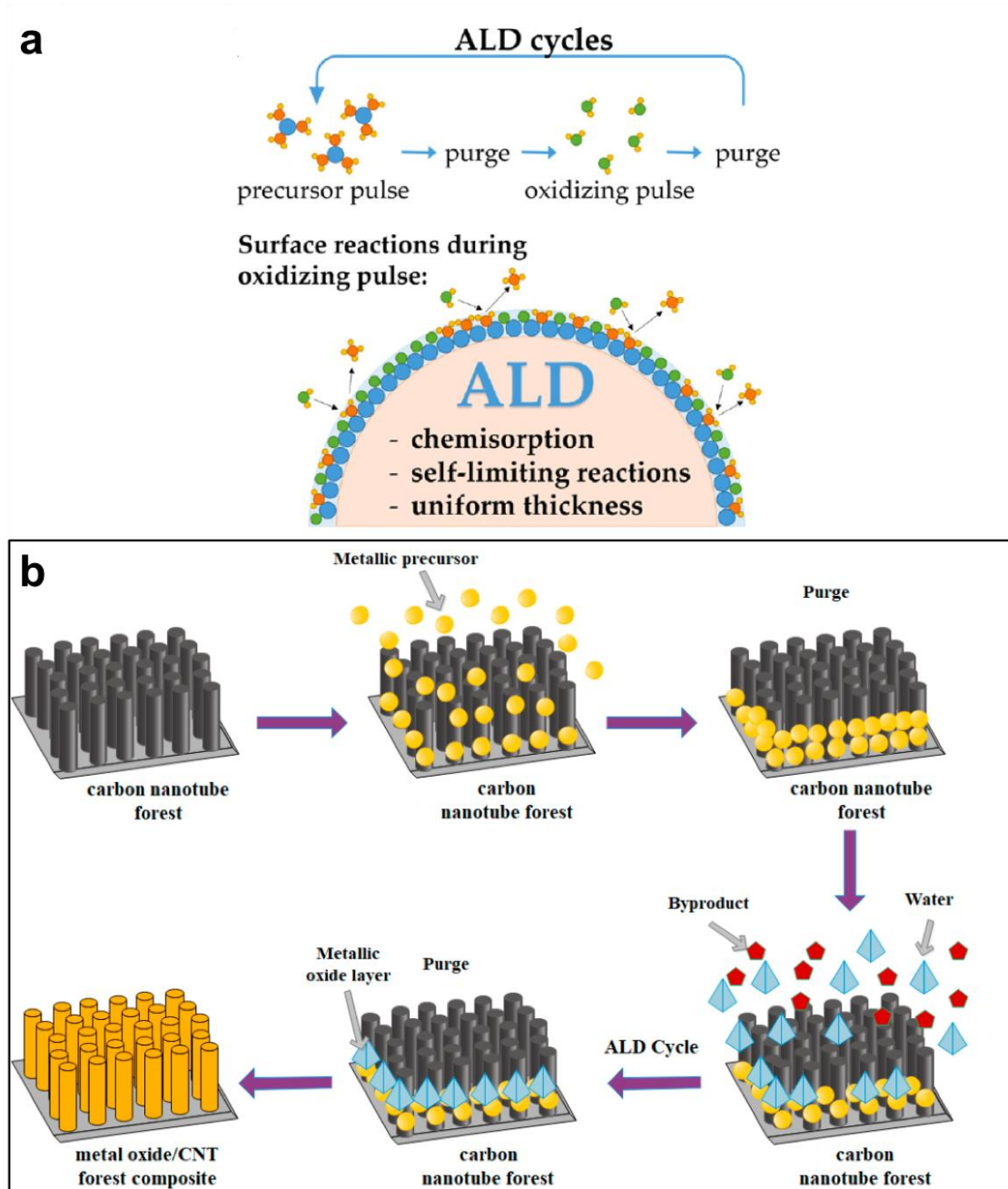


Figure 13 (a) Schematic illustrating the general steps for one ALD cycle for the deposition of metal oxides. Adapted with permission from Ref. ¹⁴¹, © Creative Commons Attribution License. (b) Schematic illustrating the steps involved in the ALD deposition of a metal oxide on a vertically aligned CNT forest. Adapted with permission from Ref. ¹⁵⁰, © Creative Commons Attribution License.

1.1.5 Defect engineering for photocatalysis

Another direction which has been also intensively investigated is the defect engineering in semiconductor photocatalytic materials where different types of defects are tailored to achieve high photocatalytic activity. For long time, defects were considered as factors always reducing the photocatalytic activity of semiconductor photocatalysts by acting as recombination centers

or as scattering centers preventing photo-induced charge carriers to reach the surface easily.¹⁵¹ With time possible positive influence of certain defects on the photocatalytic activity and selectivity were discovered. Early studies about the influence of defects on the photocatalytic activity were performed by Yanagida et al. where it was shown that surface sulfur vacancies in CdS were found to increase the photocatalytic activity towards the conversion of CO₂ to CO.¹⁵² Similar results were also obtained for the photocatalytic activity of defective ZnS nanocrystallites.¹⁵³ With the introduction of defects the band structure of wide band gap semiconductors could be tuned for visible light absorption enabling further use of the solar spectrum. Here, extensive research has been conducted especially after the discovery of black TiO₂ by Chen et al.^{63,154} Furthermore, defects on the surface could also act as catalytic sites for specific reactions.^{155,156}

Defects are any irregularities which can occur in a perfect crystal structure and can be classified into point defects (zero-dimensional) which include vacancies and heteroatom doping, line defects (one-dimensional) which include screw dislocation and edge dislocation, planar defects (two-dimensional) including grain boundaries and twin boundaries and finally volume defects (three-dimensional) which include voids or disorders as shown in the schematic in **Figure 14a**.^{151,157} Especially the zero-dimensional point defects have been extensively investigated and applied for increasing the photocatalytic activity of semiconductor photocatalysts. For example, anion vacancies like oxygen vacancies V_O were introduced into metal oxides like TiO₂ resulting in the formation of mid-gap states resulting in visible light absorption together with an enhanced electron-hole separation efficiency and enhanced dissociative adsorption.¹⁵⁸⁻¹⁶⁰ Cation vacancies where the metal is missing are less common in literature as they do not greatly contribute to a visible light response as determined for TiO₂ but still they are expected to suppress charge carrier combination and thus increase the photocatalytic activity.^{161,162} Vacancies are also accompanied by a change in the oxidation state of the surrounding ions in order to maintain charge neutrality.¹⁵⁸ Thus, an oxygen vacancy V_O in TiO₂ for example is accompanied by the presence of two self-doped Ti³⁺ sites and a titanium vacancy V_{Ti} is surrounded by four self-doped O⁻ sites as shown in **Figure 14b**.^{151,163} Through vacancy formation and self-doping nonstoichiometric compounds can be produced without the insertion of heteroatoms with a resultant change in the band structure and thus a possible increase in the photocatalytic activity.¹⁵¹ Besides vacancies there can be also an insertion of anions or cations into the crystal lattice which is represented in **Figure 14b** by the example of TiO₂ where oxygen

interstitials O_{int} or titanium interstitials Ti_{int} are present at interstitial positions of the lattice.^{151,163} Taking titanium dioxide as example, titanium interstitials result in a formula of $Ti_{1+x}O_2$, titanium vacancies in a formula of $Ti_{1-x}O_2$ and the same for oxygen interstitials and vacancies would result in the formula TiO_{2+x} and TiO_{2-x} , respectively. In practice, TiO_2 is generally oxygen-deficient with the general formula TiO_{2-x} resulting in a n-type semiconductor¹⁶⁴ but recent studies have also shown that oxidation at elevated temperatures can result in a metal deficient TiO_2 with the general formula $Ti_{1-x}O_2$ with p-type semiconductor characteristics due to the titanium vacancies.^{163,165,166}

Also, heteroatom doping which includes metal and non-metal doping^{32,56,167,168} was successfully used as for example the well-known nitrogen doping of TiO_2 where nitrogen replaces some oxygen atoms or occupies some interstitial positions in the lattice with a resultant effective increase in the photocatalytic activity.^{31,49,169,170} Simultaneous co-doping with two anions, two cations or even one anion and one cation has been also performed.¹⁷¹⁻¹⁷³

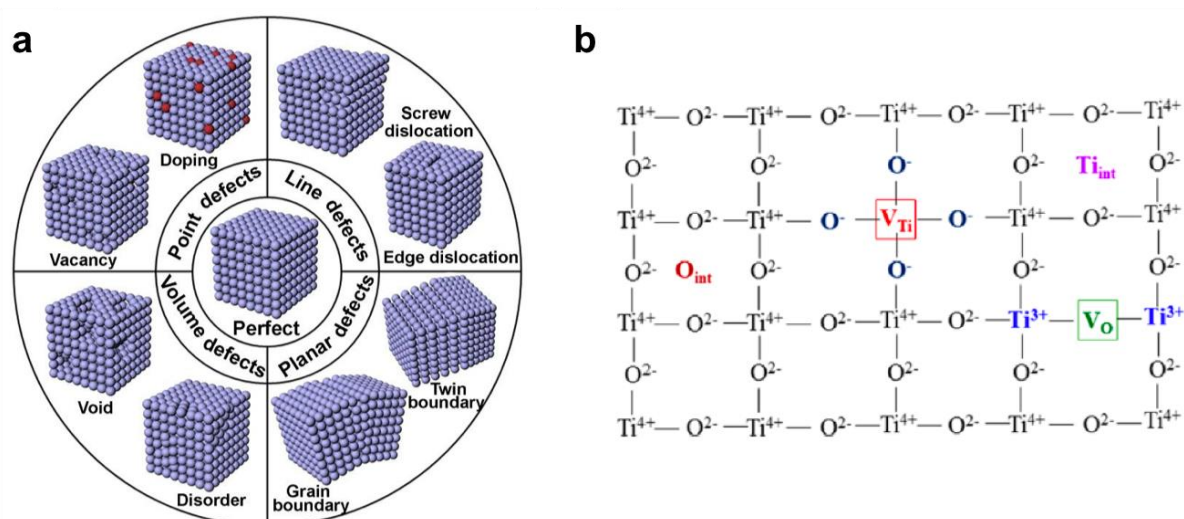


Figure 14 (a) Schematic showing the different types of defects which can occur in an inorganic crystal. Adapted with permission from Ref. ¹⁵¹, © 2018 Elsevier. (b) Schematic showing possible defects occurring in undoped TiO_2 . Adapted with permission from Ref. ¹⁶³, © 2015 American Chemical Society.

It is also important to consider the location of the defect. According to the defect location, defects can be classified into bulk and surface defects.^{155,156,174} Kong et al. found that TiO_2 crystals where the ratio of bulk defects to surface defects is small have an improved charge separation efficiency which greatly enhances the photocatalytic activity.¹⁵⁵ Yan et al. also determined the importance of surface defects for increasing the photocatalytic activity and explained their findings by the role of surface defects in trapping photo-induced charge carriers

at the surface of the photocatalyst making it available for subsequent redox reactions with species from the surrounding medium while bulk defects trap the photo-induced charge carriers preventing them to reach the surface and facilitates their recombination.¹⁵⁶ This shows that the type as well as the location of the defect has to be considered to evaluate its role in increasing or decreasing the photocatalytic activity of the investigated photocatalyst.

1.1.6 Photocatalysis with two-dimensional materials

Two-dimensional materials are another category of materials which awakened large interest for diverse applications including photocatalysis. It is known that two-dimensional materials can provide increased photocatalytic activity as the diffusion pathway of photo-induced charge carriers to the surface is reduced enabling them to reach the surface before any bulk recombination occurs.^{175–178} Furthermore, due to the two-dimensional structure they possess a large surface area and increased catalytic adsorption sites compared to their bulk counterparts. The two-dimensional arrangement of atoms also presumably permits quicker and more efficient charge transfer at the interface. And for a lot of two-dimensional materials it is known that the band gap changes with the number of layers and thus can be carefully tuned.¹⁷⁹ Even extensive work has been done in order to design and synthesize two-dimensional TiO₂ due to the advantage of the two-dimensional morphology for photocatalysis.²⁹ Other two-dimensional materials as graphitic carbon nitride (g-C₃N₄)¹⁸⁰ and different two-dimensional transition metal oxides and chalcogenides¹⁷⁹ were tested for photocatalytic applications and showed good activities. Defect engineering has been also combined with the design of two-dimensional photocatalysts which greatly increased the potential of efficient photocatalyst design.¹⁸¹

Transition metal chalcogenides are a class of materials with an intrinsic layered structure due to their layered crystal structure. Their general structure is a laminar structure where a layer is composed of a metal plane sandwiched between two chalcogen planes as chalcogen-metal-chalcogen (X-M-X). These layers are held together by weak van der Waals interactions. Thus, exfoliation can produce atomically thin two-dimensional materials resembling graphene.^{182–186} The layered crystal structure of transition metal chalcogenides is shown in **Figure 15** taking titanium disulfide TiS₂ and titanium trisulfide TiS₃ as example. Titanium disulfide TiS₂ has a hexagonal CdI₂-type structure where the titanium plane is sandwiched between two chalcogen atom planes forming one layer which is attracted to the adjacent layer by van der Waals interactions (**Figure 15a**).¹⁸² Titanium trisulfide TiS₃ has a monoclinic ZrSe₃-type structure where also the X-M-X structure forms one layer but here also two of the three sulfur atoms per

unit formula are bound forming a S-S bond resulting in disulfide anion species S_2^{2-} (**Figure 15b**) and therefore the formula of TiS_3 can also be expressed as $Ti^{4+}S_2^{2-}(S_2^{2-})$.^{187–189}

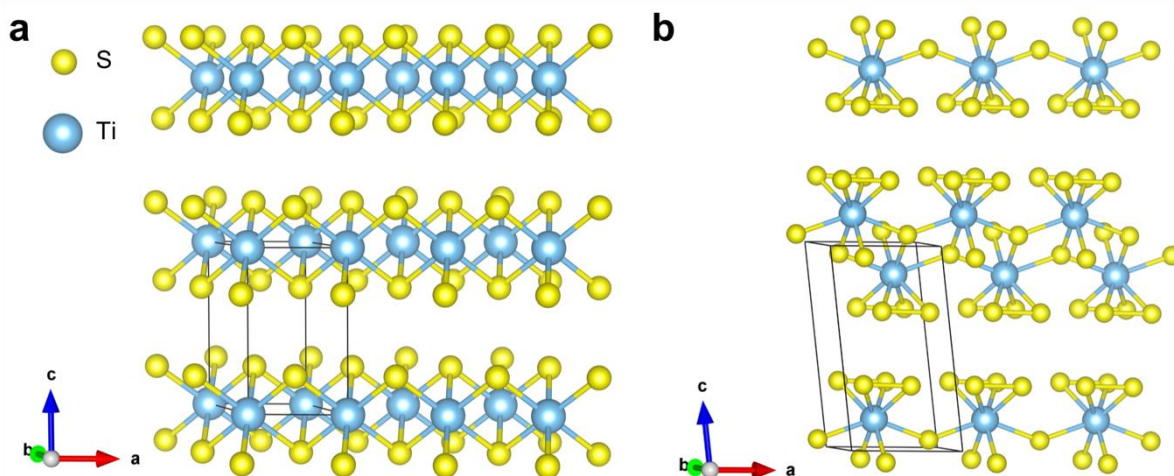


Figure 15 Crystal structure of (a) TiS_2 and (b) TiS_3 showing the layered structure of both compounds. The unit cell is marked in each crystal structure by black solid lines. Adapted with permission from Ref. ¹⁹⁰, © 2020 Royal Society of Chemistry.

Titanium-based di- and trichalcogenides other than oxides such as TiS_2 , $TiSe_2$, $TiTl_2$ and TiS_3 have an interesting lamellar structure and possess narrow band gaps ($E_g < 2$ eV)^{191–194} even in the bulk which makes them interesting candidates for efficient photocatalysis. But still they have not been extensively tested for their photocatalytic activity although some recent studies show the high potential of some two-dimensional titanium chalcogenides in photocatalysis.^{195,196} Barawi et al. prepared TiS_3 nanoribbons and used them for effective hydrogen photogeneration under visible light in a photoelectrochemical cell.¹⁹⁵ Similar results were also obtained by Flores et al. where besides TiS_3 also the layered metal trichalcogenides ZrS_3 and HfS_3 have been tested for the photoelectrochemical production of hydrogen.¹⁹⁶ Titanium disulfide has not been used for photocatalysis due to its semi-metallic behavior which does not enable an effective charge separation as the synthesis of TiS_2 easily results in non-ideal stoichiometry. But still literature shows that there is a debate about the semiconductor or semi-metallic behavior of titanium disulfide as different synthesis conditions result in different defects and thus a different electric behavior.^{186,197} Phase diagrams of titanium sulfides show the variety and complex nature of phases which can be obtained where a small change in the conditions can result in an entirely different phase as shown in **Figure 16**.¹⁹⁸ In titanium sulfides the deviation from stoichiometry can be generally either due to sulfur vacancies (TiS_{2-x} and TiS_{3-x}) or due to insertion of titanium into the interstitials between the layers i.e. in the van der Waals gaps ($Ti_{1+x}S_2$ and $Ti_{1+x}S_3$)

where deviations in stoichiometry due to titanium insertion are more common and have been proved by X-ray measurements of different titanium sulfide crystals.¹⁹⁹

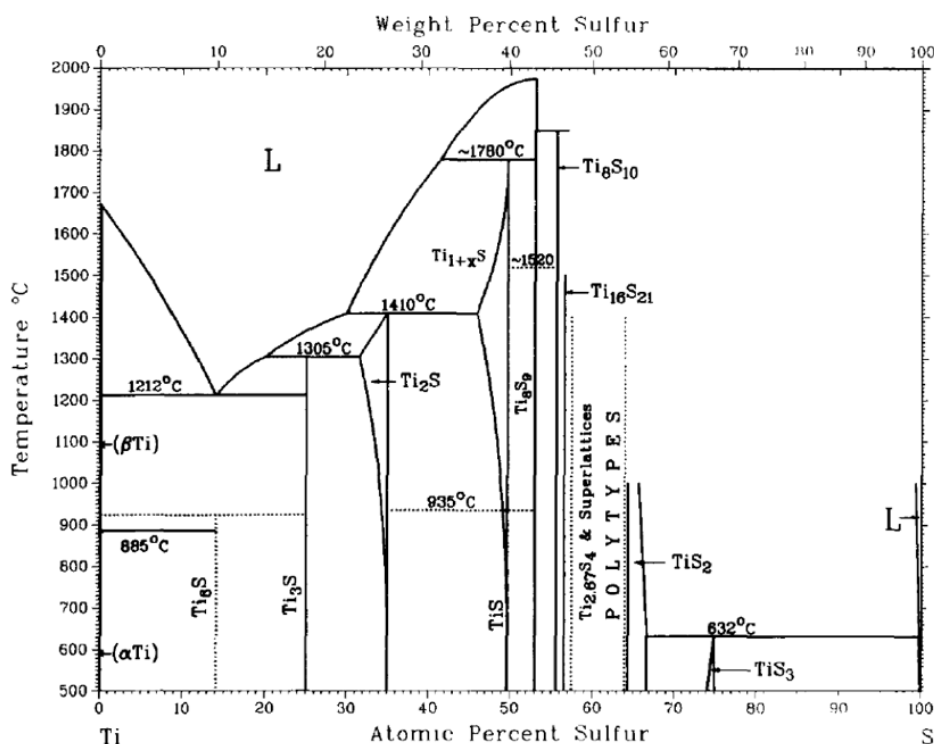


Figure 16 Phase diagram for the Ti-S system showing the various existing phases and polytypes where some phases like TiS₂ and TiS₃ have only a narrow window. Adapted with permission from Ref. ¹⁹⁸, © 1986 Springer Nature.

From the previous discussion it is obvious that titanium chalcogenides have several interesting characteristics which are suitable for efficient photocatalysts. At the same time there is plenty room for trying a wide range of phases and compositions in titanium chalcogenides in the long way of search for highly effective next generation photocatalysts.

1.2 Plasmonic nanomaterials for optical analyte detection using surface-enhanced Raman Spectroscopy (SERS)

1.2.1 Motivation and aim of this work

Surface-enhanced Raman scattering (SERS) is an interesting method for the qualitative and quantitative analysis of different analytes at low concentrations which is interesting for various fields including environmental analysis. Therefore, it is important to develop efficient SERS substrates which enable sensitive detection of various analytes. Furthermore, it is of high importance that the preparation method of SERS substrates is easy, cheap and reliable to enable technological relevant applications.

As the preparation of anodic aluminum oxide (AAO) is well established in our group it was interesting to test their performance when incorporated in SERS substrates as AAO provides several advantages including the formation of structured surface in case of porous anodic aluminum oxide (PAOX) which can be efficiently used for the self-organization of hot spots upon coating with a noble metal. Furthermore, the use of dielectrics beneath the noble metal alter the dielectric environment around the noble metal depending on the dielectric function of the dielectric resulting in a change of the local electric field enhancement which could be interesting for efficient SERS substrates. In case of anodized aluminum, the aluminum serves as support for the SERS substrate and also serves as a reflecting surface for the incident radiation so that for the Al/AAO/noble metal-based SERS substrate the SERS signal can be further enhanced through interference which makes this system very attractive for further investigations.

Another approach for the facile preparation of SERS substrates could be offered through plasma treatment of deposited noble metal films. Plasma treatment for the modification and cleaning of metal surfaces has been always used in industry especially in microelectronics and it would be very interesting to use plasma treatment for the modification of silver thin films in order to investigate the influence of plasma treatment on the resulting SERS activity of the thin silver films. As plasma treatment is widely distributed in industry this approach could present an attractive alternative for the commercial production of efficient SERS substrates.

In the following the basic theory of SERS together with the fabrication methods of SERS substrates found in literature is presented with special focus on the use of plasma treatment for the preparation of SERS substrates and the preparation of SERS substrates based on anodic aluminum oxide.

1.2.2 Understanding the Raman scattering phenomena

When light passes through a sample it can interact with the sample in different ways. Part of the incident light is absorbed causing either an electronic transition (in case of ultraviolet and visible light) or molecular vibrations (in case of infrared light), a part is transmitted and very small portion is scattered (**Figure 17**).²⁰⁰ In some samples fluorescence can also occur where some molecules are transferred to an excited electronic state and emit photons upon their return to the ground state.²⁰¹

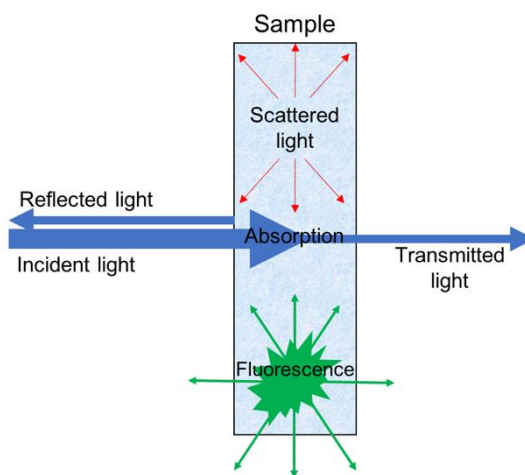


Figure 17 Different phenomena occurring when light interacts with a sample.

In the scattering process the molecule is imagined to be excited to a virtual energy state depending on the energy of the incident light. This state is very unstable and relaxes instantly re-emitting a photon.²⁰⁰

There are three possibilities for the scattering to take place as shown in **Figure 18**:

1. **Elastic scattering** where no energy is lost which is known as **Rayleigh scattering**.
2. **Inelastic scattering** where the incident photons lose some of their energy to the molecule resulting in scattered photons with less energy. The transferred energy increases the vibrational energy of the molecule. This is known as **Stokes scattering**.
3. **Inelastic scattering** where the incident photons gain some energy from a molecule present initially in a higher vibrational state. Thus, the scattered photon has more energy and the molecule falls to a lower vibrational energy state. This is known as **Anti-Stokes scattering**.

The probability of elastic scattering is the highest (about 1 in a 1000), followed by Stokes scattering and finally Anti-Stokes scattering which is the rarest. To get a feeling for the weakness

of the Raman scattering, approximately 1 in 1000 of the scattered photons are scattered inelastically.²⁰² This is the reason why the Raman effect is very weak. At the same time, the Anti-Stokes Raman scattering is much weaker than the Stokes Raman scattering as the population of molecules present initially in a higher vibrational energy state is much lower than the population of molecules present in the ground vibrational state.²⁰⁰

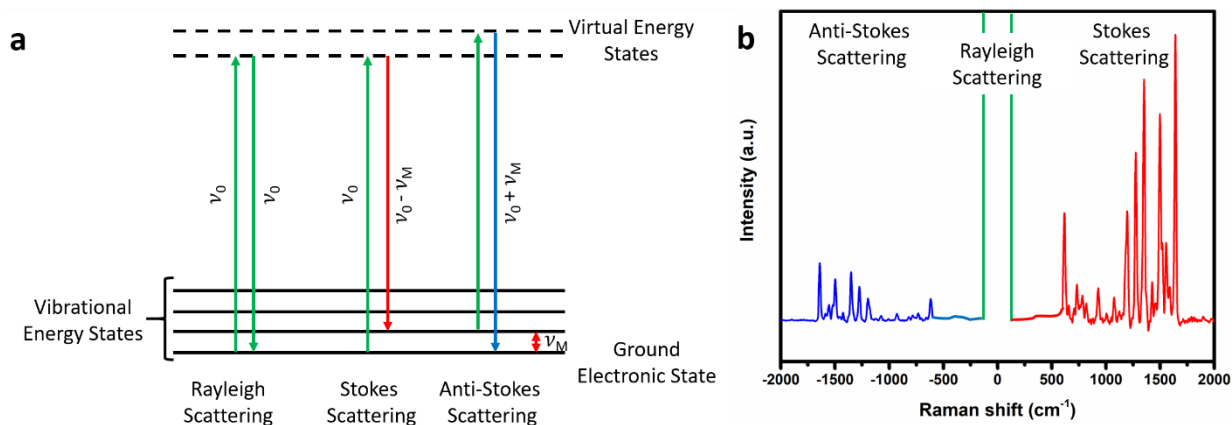


Figure 18 (a) Energy diagram showing the different types of scattering where the incident radiation lifts the molecule to a virtual energy state which upon return to the ground state releases a photon of the same frequency (Rayleigh scattering), a photon having a lower frequency (Stokes Raman scattering) or a photon of a higher frequency (Anti-Stokes Raman scattering) with a frequency difference of ν_M corresponding to the energy difference between the different vibrational energy states and (b) a spectrum showing the Stokes Raman scattering, Anti-Stokes Raman scattering and Rayleigh scattering.

The reason for the inelastic scattering of the photons could be explained as follows: The incident photons with a specific energy or frequency interact with the electrons present in the different bonds of the material resulting in a “movement” of the electron cloud resulting in an induced dipole.²⁰³ The ability of the photons to move the electron cloud depends on the environment of the electron which is determined by the surrounding atoms. The property which determines the ability of electron cloud to be “moved” by the incident photons is the polarizability.²⁰⁴ The polarizability is defined as the ability of an electron cloud to be deformed by an external electric field.²⁰³ The resulting Raman signals depend on the chemical and structural properties of the analyzed material and therefore presents a fingerprint for each molecule which is the reason for using Raman spectroscopy for the identification and determination of structural information of the material.²⁰⁴

1.2.3 Raman spectroscopy

Raman spectroscopy is therefore a vibrational spectroscopic technique where the Raman scattering of the analyte or material under investigation is measured and is complementary to infrared spectroscopy where the signals are obtained through direct absorption of the infrared radiation leading to excitation of the molecules to higher vibrational energy states. The Raman signal is obtained when the molecular vibrations result in a change in the molecular polarizability in contrast to the infrared spectroscopy where the change in the dipole moment results in a signal. The intensity of the Raman signal I_R can be expressed as shown in equation 2.1:

$$I_R \propto \frac{1}{\lambda^4} I_0 N \left(\frac{\partial \alpha}{\partial Q} \right)^2 \quad \text{Equation 2.1}$$

where λ is the wavelength of incident radiation, I_0 is the intensity of the incident radiation, N is the number of scattering molecules, α is the molecular polarizability and Q is the amplitude of the corresponding vibration.²⁰³ This equation shows that the intensity of the Raman signal decreases with the fourth power of increasing wavelength. Therefore, the intensity of the Raman signal is highly sensitive to the wavelength of the laser used for excitation. Furthermore, the intensity of the Raman signal increases with increasing power of the laser used. Therefore, the great advancement in the design of highly powerful monochromatic lasers led to a big jump in Raman spectroscopy where the measurement of the weak Raman scattering was made possible even for small amounts of sample.^{200,201} As the intensity of the Raman signal is proportional to the number of scattering molecules, Raman spectroscopy is suitable for quantitative determinations as with increasing concentration the number of scattering molecules increases. The term $\left(\frac{\partial \alpha}{\partial Q} \right)$ indicates that only vibrations resulting in a change in the polarizability result in a Raman signal as only in this case the term is not zero. Molecular vibrations which cause greater changes in the polarizability with respect to the amplitude of the vibration result in higher Raman signals.²⁰³

As the Raman effect is very weak but can be detected nowadays easily thanks to the advanced lasers and sensitive charge-coupled device (CCD) detectors,²⁰⁵ it still has no access to low concentrations of analyte or thin films of inorganic materials.

1.2.4 Emergence of Surface-enhanced Raman scattering (SERS)

Accidental discovery of the SERS effect was achieved by Fleischmann et al.²⁰⁶ in 1974 during their work on a method for in situ measurement of electrochemical processes occurring at the

electrode surface where pyridine was showing an extraordinary strong Raman spectrum on roughened silver electrodes. In a first attempt to explain the unusual phenomenon, this enhancement was first dedicated to the increased surface area of the electrodes which permitted the adsorption of an increased number of molecules.²⁰⁶ This explanation quickly turned out to be insufficient as the increase in the number of adsorbed molecules was still not sufficient to result in an increase of the observed Raman intensity of 10^5 - 10^6 times which lead Jeanmaire and Van Duyne²⁰⁷ as well as Albrecht and Creighton²⁰⁸ to the explanation that surface plasmons which enhance the incident electromagnetic field result in an increased excitation of the adsorbed molecules.

SERS thus is a method where the analyte is adsorbed on the surface of a noble metal like gold or silver with nanoscale roughness leading to an immense increase in the resulting Raman spectrum by factors up to 10^{10} which gives access to very low analyte concentrations and even permits single molecule detection.^{209,210} In addition, the advantage of Raman spectroscopy in providing fingerprint spectra enabling identification of the analyzed compound resulted in SERS being a widely applied technique in different areas as material science²¹¹, biochemistry²¹², biosensing²¹³, medical diagnostics^{214,215} and environmental analysis.^{216,217}

1.2.5 Explanation of the properties of metals and surface plasmons

To understand why especially in the proximity of metal surfaces the Raman spectra are enhanced and why some metals are more suitable for SERS applications than others, the optical properties of metals have to be discussed further. Metals are conductors where the electrons are present as an electron cloud around the positively charged metal ions which is the classical model called electron sea model for metals as shown in **Figure 19a**. This is the basis of the so-called Drude model. This model was first developed by Paul Drude in 1900 in order to explain the conduction properties of materials.²¹⁸ In this model the metal is regarded to be consisting of fixed positive metal ions (the vibrational movement of these ions in the solid is not taken into consideration for simplification) around which there is a sea of free moving electrons. This sea of free moving electrons which also accounts for the conductivity of the metals can be regarded as solid-state plasma. In this model the interaction between electrons and metal ions as well as the interaction between the free moving electrons are neglected while still giving some good insight in the material behavior.²¹⁹

This simple model can be used as basis for the investigation of the behavior of the free conducting electrons in metals upon interaction with light.²¹⁹ When light interacts with a metal

the oscillation of the electric field in the electromagnetic waves of the light results in an oscillation of the electron cloud at the metal surface which is termed surface plasmon.^{209,220} The collective oscillations of the electrons at the metal surface is produced by an electromagnetic field which extends to the outside the metal (i.e. the outside which represents a dielectric such as air, water ...etc.) as well as to the inside of the metal propagating at the metal-dielectric interface. The interaction of photons from the exciting electromagnetic wave with the electron surface oscillations which presents a bound state is called surface plasmon polariton.²¹⁹ The propagation of the surface plasmons occurs parallel to the metal-dielectric interface and decays exponentially away from the interface in the direction of the dielectric as well as in the metal where the decay inside the metal is more prominent as shown in **Figure 19b**.²²¹

In case of particles with dimensions much smaller than the wavelength of the incident electromagnetic radiation the surface plasmons are even confined as they cannot propagate due to spatial limitations leading to a so-called localized surface plasmon resonance (LSPR) (**Figure 19c**).^{219,221} The wavelength resulting in the localized resonance condition in metallic particles strongly depends on their size and geometry which enables a fine tuning of the LSPR.^{220,222,223}

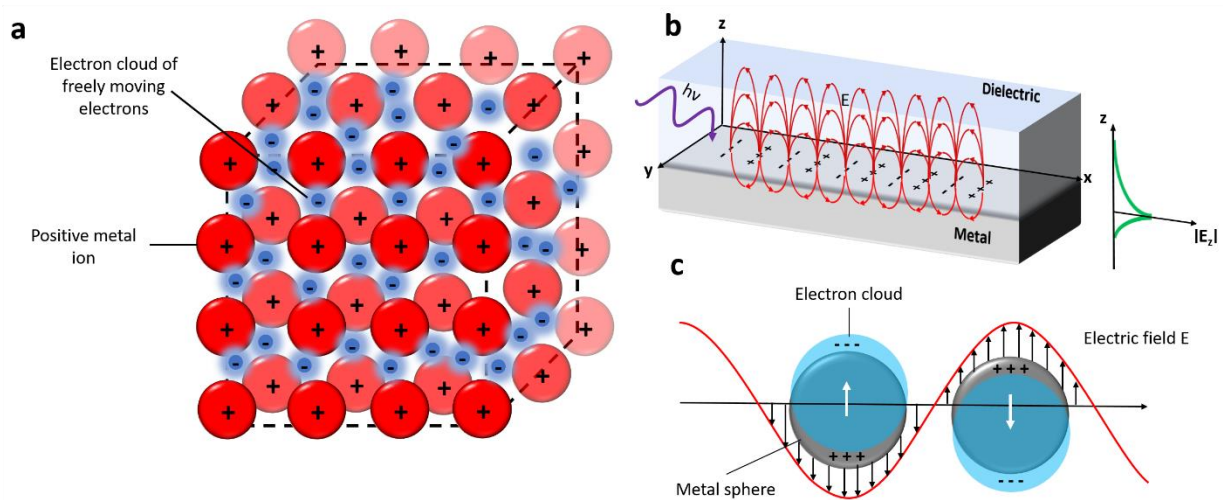


Figure 19 (a) Atomic model demonstrating the classical electron sea model for metals where the positive metal ions are surrounded by a freely moving electron cloud. (b) Schematic showing the propagation of surface plasmon polariton (SPP) at the metal-dielectric interface where the evanescent wave decays exponentially when moving away from the interface with a more prominent decay in the metal than in the dielectric. (c) Schematic demonstrating the localized surface plasmon resonance (LSPR) in a metallic sphere.

But still not all metals have the same ability to produce surface plasmons upon excitation. The property which explains why metals are unique compared to standard dielectrics and which

determines whether a metal can provide surface plasmons efficiently and at which wavelength these surface plasmons are excited depends on the complex dielectric constant of the metal.^{219,224,225} The complex dielectric constant of any material is frequency-dependent i.e. dependent on the frequency of the incident electromagnetic radiation interacting with it. According to the Drude model the complex dielectric function can be expressed according to equation 2.2

$$\varepsilon(\omega) = 1 - \frac{\omega_p^2}{\omega^2 + i\gamma\omega} \quad \text{Equation 2.2}$$

where $\varepsilon(\omega)$ represents the dielectric function depending on the frequency, γ is the damping factor which is reciprocal to the relaxation time τ which represents the mean free time between electron collisions, ω the frequency of the electromagnetic waves and ω_p is the plasma frequency.^{219,225,226} The complex dielectric function can be subdivided in the real part expressed as equation 2.3 and the imaginary part expressed as equation 2.4:

$$\text{Re}(\varepsilon(\omega)) = 1 - \frac{\omega_p^2}{\omega^2 - \gamma^2} \quad \text{Equation 2.3}$$

$$\text{Im}(\varepsilon(\omega)) = \frac{\omega_p^2\gamma}{\omega(\omega^2 - \gamma^2)} \quad \text{Equation 2.4}$$

In the complex dielectric constant, the real part accounts for the polarization of the material and the imaginary part accounts for absorption.^{227,228} The plasma frequency is defined according to equation 2.5 and represents the eigenfrequency of the electron gas in the material:

$$\omega_p = \sqrt{\frac{ne^2}{m\varepsilon_0}} \quad \text{Equation 2.5}$$

where n is the density of free electrons, e the elementary charge, m the effective mass of the electron and ε_0 is the permittivity of vacuum. It can be also expressed in terms of wavelength, known as critical wavelength λ_p , which can be calculated according to equation 2.6

$$\lambda_p = \frac{2\pi c}{\omega_p} \quad \text{Equation 2.6}$$

with c being the speed of light ($c=2.99792 \times 10^8 \text{ ms}^{-1}$).²²⁴

For metals where n is large as shown in **Table 1** the plasma frequency is also large resulting in a plasma frequency in the ultraviolet to visible or at least infrared region in contrast to dielectrics where the plasma frequency is small which is the reason why most dielectrics are transparent in the visible region.^{219,228,229} For most dielectrics or semiconductors the free carrier density is low compared to metals and strongly depends on the doping resulting in a low plasma frequency which is mainly within the infrared to terahertz range of the electromagnetic spectrum.²³⁰

Table 1 Parameters defining the optical properties of some metals.

Material	Carrier density (cm ⁻³)	Plasma frequency ω_p (s ⁻¹)	Critical plasma wavelength λ_p (nm)	Damping factor γ (s ⁻¹)	Reference
Ag	5.90 x 10 ²²	14.0 x 10 ¹⁵	134.5	0.032 x 10 ¹⁵	231
Au	5.73 x 10 ²²	13.8 x 10 ¹⁵	136.5	0.11 x 10 ¹⁵	231
Cu	5.41 x 10 ²²	13.4 x 10 ¹⁵	140.6	0.14 x 10 ¹⁵	231
Al	15.8 x 10 ²²	22.9 x 10 ¹⁵	82.3	0.92 x 10 ¹⁵	231
Na	2.43 x 10 ²²	8.99 x 10 ¹⁵	209.5	0.58 x 10 ¹⁵	232
Li	2,88 x 10 ²²	9.78 x 10 ¹⁵	192.6	0.20 x 10 ¹⁵	232
Pd	2.07 x 10 ²²	8.29 x 10 ¹⁵	227.3	0.023 x 10 ¹⁵	233
Pt	1.84 x 10 ²²	7.82 x 10 ¹⁵	241.0	0.11 x 10 ¹⁵	233
Ti	0.44 x 10 ²²	3.82 x 10 ¹⁵	492.6	0.072 x 10 ¹⁵	233

In the high frequency region which corresponds to ultraviolet and visible light the damping is usually relatively small compared to the applied frequency ($\omega \gg \gamma$).^{227,228} Thus, equation 2.3 and 2.4 can be further simplified to equation 2.7 and 2.8

$$Re(\varepsilon(\omega)) = 1 - \frac{\omega_p^2}{\omega^2} \quad \text{Equation 2.7}$$

$$Im(\varepsilon(\omega)) = \frac{\omega_p^2 \gamma}{\omega^3} \quad \text{Equation 2.8}$$

According to equation 2.7, it can be inferred that for $\omega < \omega_p$ (i.e. above λ_p) then ω_p/ω will be greater than one resulting in a negative dielectric constant (permittivity). In this case, the material is not transparent to the electromagnetic radiation and it is completely reflected in the ideal case. For $\omega > \omega_p$ (i.e. below λ_p) the ratio ω_p/ω will be less than one resulting in a positive dielectric constant (permittivity) making the material transparent to the electromagnetic radiation (**Figure 20**).²²⁸

For metals the interesting property lies in the fact that for optical frequencies metals possess a negative real part and a very small imaginary part of the dielectric function.²²⁰ The negative real part of the complex dielectric constant results in highly reflective surfaces as known for metals as the electromagnetic wave is not able to penetrate the material and this gives the metal the ability to produce surface plasmons while a small positive imaginary part of the dielectric constant results in low absorption.^{219,224}

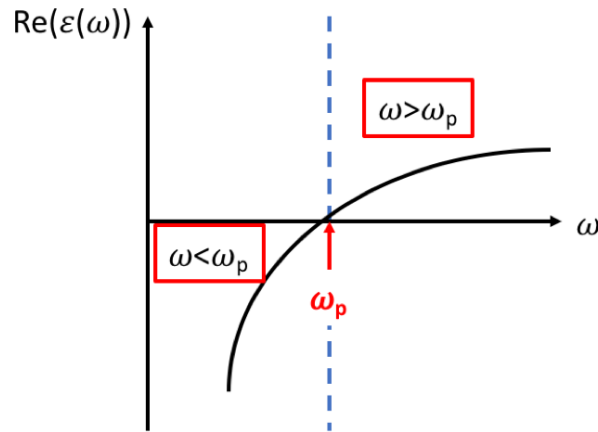


Figure 20 A general plot of the real part of the dielectric function versus the frequency showing the regions of negative and positive permittivity relative to the plasma frequency.

According to equation 2.8 the imaginary part of dielectric function will approach zero with increasing frequency resulting in a very low imaginary permittivity for optical frequencies. But unfortunately, this is not the case for most of the metals as can be clearly seen in the comparison of the real and imaginary part of the dielectric function of silver and gold in the ultraviolet and visible range of the electromagnetic spectrum shown in **Figure 21**.

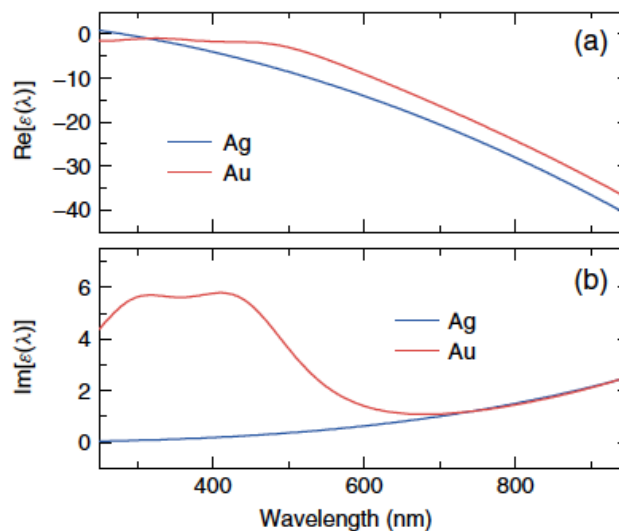


Figure 21 Comparison of the (a) real and (b) imaginary parts of the dielectric function of silver and gold in the ultraviolet to visible spectrum. Adapted with permission from Ref. ²²⁴, © 2011 Wiley-VCH.

For gold there are interband electronic transitions (i.e. transitions of bound electrons through optical excitation to a higher band) which account for the increased imaginary part of the dielectric function of gold below 600 nm. This results in the absorption of light in that

wavelength region of the visible light which leads to the well-known golden yellow color of gold.^{224,226} Thus, silver is a superior plasmonic material compared to gold in that range of the visible light spectrum. For longer wavelengths above 650 nm to the near-infrared (NIR) region the losses observed for silver and gold are very similar as the imaginary part of the permittivity are very close, thus making gold in that region preferable due to its higher chemical stability.^{219,224}

From the previous discussion it can be seen that most of the metals possess similar real dielectric functions at optical frequencies due to similar free charge carrier densities resulting in a negative real permittivity in the optical region. But for the imaginary part the situation is different due to the appearance of different interband transitions in different regions of the electromagnetic spectrum for each metal which account for high losses in the surface plasmon resonance and thus let the metal be not effective for plasmonic applications in that region of the electromagnetic spectrum. A comparison of the real and imaginary part of the dielectric function for various metals in the ultraviolet to NIR region can be found in **Figure 22** showing that the metals Ag, Au, Na, K and Al possess a negative real permittivity. But upon looking on the imaginary part of their dielectric function it can be found that only silver and the alkali metals (Na and K) show low losses in the visible region. While alkali metals theoretically are efficient plasmonic substrates their problem lies in their high reactivity towards air and water which limits their use as plasmonic substrates. When looking at aluminum one can find that despite having large negative real permittivity which would make it suitable for plasmonic applications, its imaginary part is also very large (several orders of magnitude larger than gold and silver) in the whole visible and NIR range resulting in a poor performance of aluminum as plasmonic substrate in that region. The imaginary part of the permittivity of aluminum is only comparable to silver in the ultraviolet range making it a suitable plasmonic material in that range only.²³⁴

In general, for a good plasmonic material there are two important guidelines:

1. **Negative $\text{Re}(\epsilon(\omega))$:** Having a negative real permittivity in the wavelength range of interest. As a rule of thumb a real permittivity between -1 and -20 is recommended.
2. **Small $\text{Im}(\epsilon(\omega))$:** A small imaginary part of the dielectric function in the region of interest is of high importance as a high $\text{Im}(\epsilon(\omega))$ results in damping of the surface plasmon resonance.²¹⁹

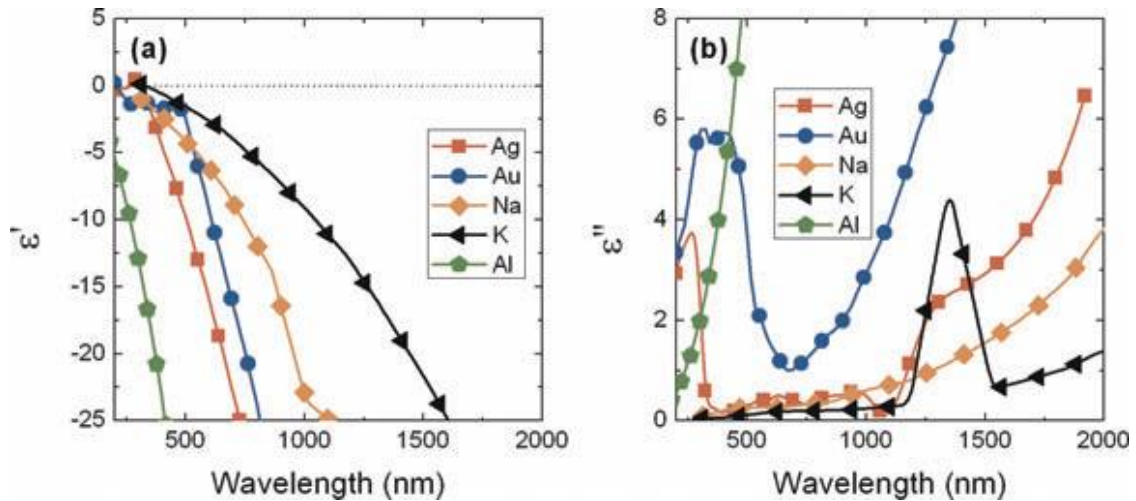


Figure 22 (a) Real and (b) imaginary part of the dielectric function of the metals silver, gold, sodium, potassium and aluminum in the UV, visible and NIR range of the electromagnetic spectrum. Adapted with permission from Ref. ²³⁴, © 2010 Wiley-VCH.

In order to get a better overview on the quality of a plasmonic material and its suitability for plasmonic applications the so-called quality factor Q has been introduced and it shows in general how much a material can amplify the incident electric field. In the quality factor both the real part and the imaginary part of the dielectric function are included as can be found in equation 2.9

$$Q = \frac{\omega \left(\frac{d\varepsilon'}{d\omega} \right)}{2(\varepsilon''(\omega))^2} \quad \text{Equation 2.9}$$

where ε' and ε'' represent the real and imaginary part of the dielectric function, respectively.²¹⁹ This equation shows that a smaller imaginary part of the dielectric function results in a greater quality factor and hence in a greater enhancement in the region of interest. **Figure 23** shows a plot of the quality factor of different metals versus the wavelength from the UV to the NIR region where the shaded area corresponds to the quality factors suitable for plasmonic applications where enhancement factors up to 10^5 can be reached.²³⁵ Usually for a good plasmonic material the quality factor should at least exceed 2 and be preferably above 10.²¹⁹ Thus, it can be seen on the first spot that silver is the best material in terms of performance in the visible and NIR region. Then, the metals gold and copper follow which are especially suitable for the NIR region. Aluminum is only suitable for the UV region and SERS on aluminum surfaces with high enhancement factors up to 10^6 have been achieved in the deep UV region.²³⁶ Other metals like platinum and palladium show very low quality factors in the UV to NIR region and are therefore not suitable plasmonic materials in this region.

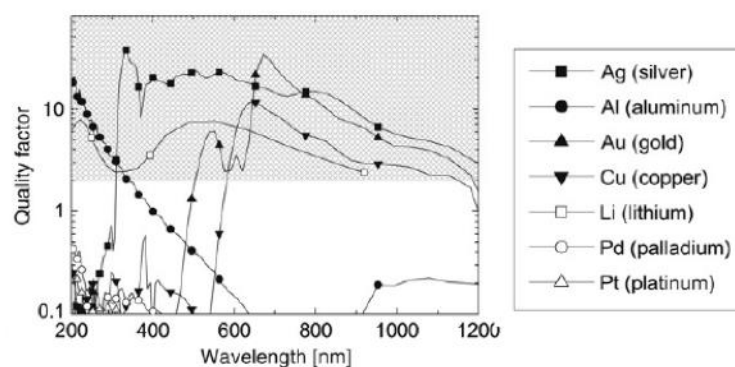


Figure 23 Quality factors of different metals depending on the wavelength where the shaded region represents the appropriate quality factors for plasmonic applications. Adapted with permission from Ref. ²¹⁹, © 2009 Elsevier B.V.

1.2.6 Effect of surface roughness, hot spots and geometry

The importance of the surface roughness in metals comes in the sense that surface roughness of the metal enables the excitation of surface plasmon polaritons through coupling of the photons of the incident electromagnetic wave by breaking the conservation of momentum restriction which restricts the coupling of the photons to SPP in flat metal surfaces.^{219,237} That is the reason why a greater random surface roughness of the metal on nanometer scale will increase the observed SERS effect. Thus, producing rough metallic surfaces for SERS applications has been performed through various ways as electrochemical roughening,^{206,238–241} plasma treatment of silver films^{242–244} and deposition of metallic films on rough or nanostructured substrates^{245–250} in order to achieve high enhancement factors.

Surface roughness has been also related to the formation of hot spots at the intersection angles of the neighboring grains which increases the enhancement further.²⁵¹ Hot spots are defined as spacings where the distance between plasmonic structures are in sub-10 nm regime thus resulting in an coupling of the produced localized surface plasmons resulting in an immense increase in the local electric field which increases the enhancement factors several orders of magnitude achieving single molecule detection in some cases.^{252–255} The hot spots are thus considered to highly concentrate the incident electromagnetic field resulting in enhancement factors up to $\sim 10^{11}$.^{253,256} **Figure 24** shows a simulation of the electric field in a hot spot formed between two spherical gold nanoparticles at 2 nm distance and the corresponding wavelength dependency of the enhancement factor in this gap. There it can be seen that the electric field achieves its maximal enhancement in the point where the spheres are closest to each other

which represents the hot spot. Even in places near to that point the enhancement will be still large showing the spatial expansion of the electric field enhancement.

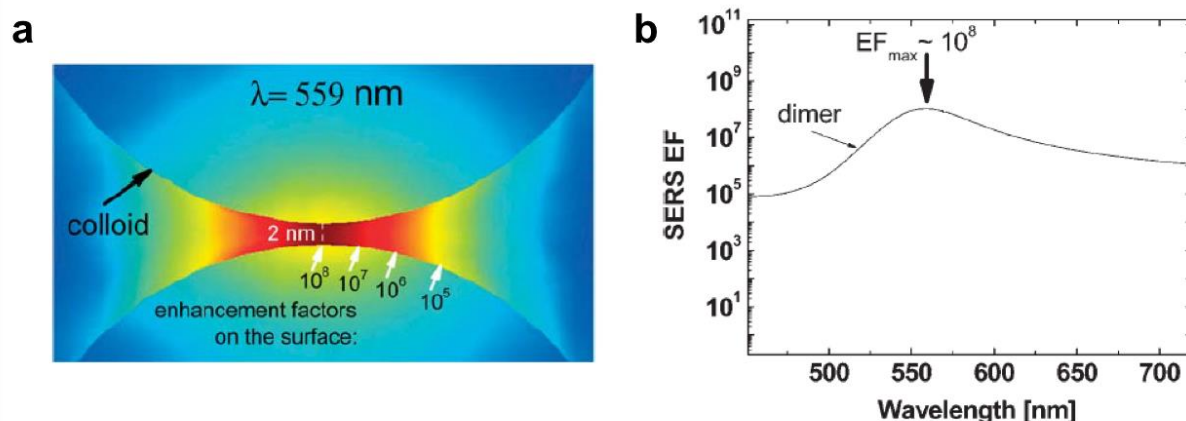


Figure 24 (a) Simulation showing the intensity of the electric field and the corresponding enhancement factors formed in a 2 nm gap between two gold spheres of 60 nm diameter and excited with light having a wavelength $\lambda = 559 \text{ nm}$ where red represents the highest intensity and blue represents the lowest intensity. (b) The enhancement factor in the 2 nm gap at different wavelengths showing the wavelength dependency of the enhancement factor. Adapted with permission from Ref. ²⁵⁴, © 2008 Royal Society of Chemistry.

Due to the effectiveness of hot spots in SERS enhancement which can even enable single molecule detection several approaches have been used to achieve the formation of hot spots where nanoparticle aggregation presents the simplest method of hot spot generation but lacking the control over the hot spots.^{257–261} The nanoparticle assembly can be also further controlled through chemical functionalization of the nanoparticle surface with special moieties like short chain single-stranded DNA oligonucleotides resulting in a programmable particle aggregation through hybridization.^{262,263} This even offers the advantage of reversibility which enables the recyclability for analyte detection.²⁶³

Other methods providing more control on the number and density of hot spots involve methods like metal film over nanospheres (MFONs) where a metal film like silver is evaporated on a periodic array of self-assembled polystyrene sphere monolayer (**Figure 25a**).^{264,265} The self-assembled polystyrene sphere monolayer can be also used as a mask which is then removed after metal evaporation leaving a triangular nanoparticle array behind (**Figure 25b**) which is known as nanosphere lithography (NSL).^{266,267} More expensive lithographic techniques like electron beam lithography (EBL) enable the production of nanoparticle arrays with different shapes and with tunable interparticle distance but having the problem of scalability.^{256,268,269} Templated synthesis of nanostructures like electrochemical deposition in porous anodic

aluminum oxide (PAOX) templates producing metallic nanowire arrays with small interwire distances has been also performed to produce a large number of hot spots.²⁷⁰ Direct deposition of gold or silver on the surface of PAOX has been also performed to achieve a large area of equally spaced hot spots by making use of the hexagonal cell self-ordering in PAOX.^{250,271} The idea of hot spot was also combined with the high spatial resolution of the atomic force microscopy or scanning tunneling microscopy resulting in the emergence of the tip-enhanced Raman spectroscopy (TERS) where a tip covered with a noble metal, usually gold, is used to investigate molecules adsorbed on a substrate which is usually also a noble metal.²⁷² Here, the distance can be fine-tuned creating a hot spot with high enhancement factors enabling single molecule detection achieving an enhancement factor up to 10^{13} .^{273,274} **Figure 25c** shows a schematic of TERS where the tip covered with gold is in a distance of 2 nm from a gold surface showing the enhancement factors experienced on the gold surface.

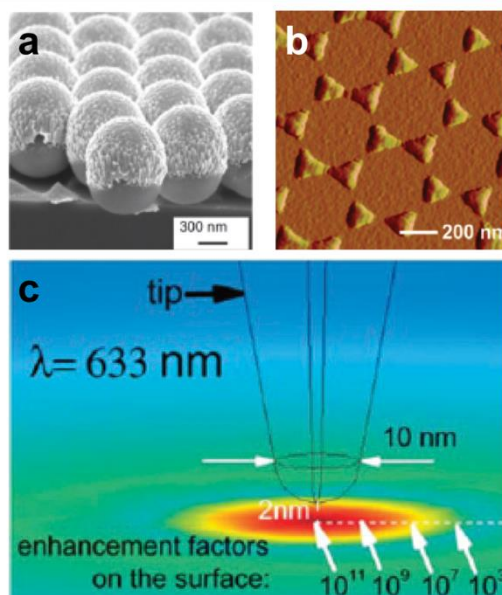


Figure 25 (a) SEM image of a metal film over nanosphere (MFON) substrate where silver is thermally evaporated over closely packed nanospheres. Adapted with permission from Ref. ²⁵⁶, © 2013 Royal Society of Chemistry. (b) AFM of a silver triangular nanoparticle array produced through nanosphere lithography. Adapted with permission from Ref. ²⁶⁷, © 2008 American Chemical Society. (c) Schematic diagram showing the enhancement factor distribution in and around the gap of a gold tip used in TERS at 2 nm distance from a gold surface at 633 nm excitation. Adapted with permission from Ref. ²⁵⁴, © 2008 Royal Society of Chemistry.

The geometry, size and shape in case of metallic nanoparticles is also an important factor to consider for the enhancement and determining the resonant wavelength of the LSPR.²²⁸ In case of spherical nanoparticles, the polarizability which also determines the enhancement of the incident electric field can be expressed as shown in equation 2.10:

$$\alpha = a^3 \frac{\varepsilon(\omega) - \varepsilon_M}{\varepsilon(\omega) + 2\varepsilon_M} \quad \text{Equation 2.10}$$

where α is the polarizability of the metal sphere, a is the radius of the sphere, $\varepsilon(\omega)$ the dielectric function of the metal and ε_M the permittivity of the medium.^{228,275} The polarizability is used to calculate the absorption and scattering cross-sections (σ_{abs} and σ_{sca}) of the particle according to equation 2.11 and 2.12:^{228,275}

$$\sigma_{abs} = \frac{8\pi^2 \sqrt{\varepsilon_M}}{\lambda} \text{Im}(\alpha) \quad \text{Equation 2.11}$$

$$\sigma_{sca} = \frac{128 \pi^5 \varepsilon_M^2}{3\lambda^4} \alpha^2 \quad \text{Equation 2.12}$$

The absorption cross-section can be defined as the effective area resulting in absorption and analogously the scattering cross-section corresponds to the effective area responsible for scattering which usually differs from the geometric cross-section of the particle.^{219,228}

In equation 2.10 the denominator is of special interest as for a given frequency at which the real permittivity of the metal $\text{Re}(\varepsilon(\omega))$ equals $-2\varepsilon_M$, then the denominator will reach a minimum as the imaginary part of the dielectric constant is left resulting in a resonance condition where the polarizability is maximized which in turn maximizes the scattering cross-section. Furthermore, a very low imaginary permittivity will thus increase the polarizability at the resonance condition according to equation 2.10 and decrease the absorption cross-section according to 2.11, thus resulting in an efficient scattering as the scattering cross-section will be maximized.²²⁴ From these equations it is also obvious that the resonant wavelength is also affected by the surrounding dielectric where an change in the dielectric permittivity will result in shift in the wavelength resulting in the LSPR.²²⁸

1.2.7 Mechanisms involved in SERS enhancement

The SERS enhancement can be due to two different mechanisms, namely electromagnetic enhancement mechanism (EM) and chemical enhancement mechanism (CM) where the former is the more common mechanism contributing to the SERS enhancement.^{209,276,277} In the following the origin of the EM and CM will be shortly discussed:

1. Electromagnetic enhancement mechanism (EM)

The EM enhancement occurs due to the generation of surface plasmons on metallic surfaces through resonance with the frequency of the incident radiation leading to an increase in the local electric field experienced by the adsorbed analyte resulting in an enhancement of the intensity of the Raman signal by E^4 (known as E^4 rule). The E^4 enhancement is divided into an E^2 enhancement resulting from the enhancement of the

electromagnetic field due to the generated surface plasmons and another E^2 enhancement arising from the electric field of the induced dipole of the surface adsorbed analyte molecule.²⁷⁶ First, the electric field of the incident electromagnetic radiation used for excitation couples with the localized surface plasmon (LSP) of the roughened metal surface resulting in an increased local electric field at the surface. The adsorbed analyte molecule thus experiences a local electric field stronger than the incident electromagnetic field. Secondly, the polarization of the adsorbed molecule results in the irradiation of scattered photons for a particular vibrational mode which in turn further excite a LSPR of the underlying plasmonic substrate (**Figure 26a**).²³⁵ This can be expressed by the following equation 2.13:

$$I_{SERS} = I_{inc}(\omega_{inc}) \times I(\omega_s) = |E_{inc}(\omega_{inc})|^2 |E(\omega_s)|^2 \quad \text{Equation 2.13}$$

where I_{SERS} is the SERS intensity observed for a particular vibrational mode, $I_{inc}(\omega_{inc})$ and $E_{inc}(\omega_{inc})$ are the field intensity and the magnitude of the electric field, respectively produced from the incoming electromagnetic radiation with the frequency ω_{inc} , $I(\omega_s)$ and $E(\omega_s)$ are the field intensity and the magnitude of the electric field, respectively produced from the scattered radiation with a frequency ω_s which is red shifted to ω_{inc} in case of Stokes Raman scattering.²³⁵

2. Chemical enhancement mechanism (CM)

In case of chemical enhancement usually a charge transfer between the metal and the analyte molecule takes place (charge transfer complex) altering the electronic distribution of the analyte molecule and thus increasing its polarizability which results in a Raman enhancement (**Figure 26b**).²⁷⁸ The chemical enhancement therefore depends on the type of analyte and its affinity to the substrate as it requires some sort of chemisorption to occur to result in an enhancement.^{228,235,279} Thus, chemical enhancement is not observed in a wide range of cases and is rather limited.²⁷⁹ The chemical enhancement can be also viewed as a type of resonance Raman effect where the electronic nature of the analyte is altered by the interaction with the substrate so that its absorbance maximum is shifted towards the laser excitation wavelength.²²⁸ The chemical enhancement is generally weaker than the electromagnetic enhancement resulting in enhancement factors of about 10 to 100 and it does not require any surface roughness or localized surface plasmons to occur. In SERS substrates chemical

enhancement, if present, occurs together with the electromagnetic enhancement which makes it hard to distinguish their contributions in the resultant enhancement factor.²³⁵

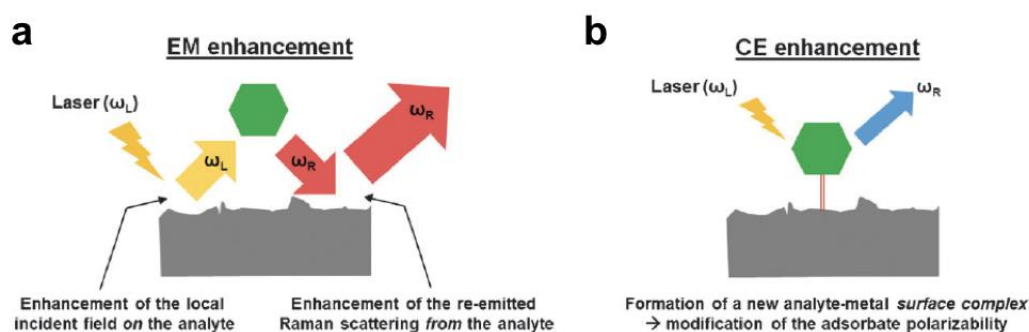


Figure 26 Schematic illustrating the mechanisms involved in (a) electromagnetic enhancement and (b) chemical enhancement in SERS. Adapted with permission from Ref. ²⁷⁸, © 2012 Royal Society of Chemistry.

1.2.8 Calculation of SERS enhancement factor

The enhancement factor represents a tool to evaluate the relative performance of different substrates concerning their SERS enhancement ability.²³⁵ The main definition of the SERS enhancement factor is the ratio of the intensity of the strongest band observed for the analyte from the SERS spectrum to the conventional non-enhanced Raman intensity each normalized to the number of molecules taking part at the scattering process under identical measurement conditions as shown in equation 2.14

$$EF = \frac{I_{SERS}/N_{SERS}}{I_{RS}/N_{RS}} \quad \text{Equation 2.14}$$

where EF is the enhancement factor, I_{SERS} and I_{RS} are the intensities obtained for the strongest band of the analyte in SERS and conventional Raman, respectively and N_{SERS} and N_{RS} are the number of molecules contributing to the scattering process in SERS and conventional Raman, respectively.²³⁵ Here, the problem of estimating the number of molecules taking part at the scattering process arises. For SERS it is usually assumed that complete monolayer adsorption takes place as especially the molecules which are in direct contact with the noble metal contribute to the obtained SERS spectrum but which is not always the case. The number of scattering molecules depends highly on the sample preparation technique (for example spin coating, dipping or drying) and has to be carefully estimated.²¹⁹

Another easier approach for the estimation of the enhancement factor is the analytical enhancement factor (AEF) where instead the number of scattering molecules N the concentration of the analyte measured in each case is considered based on the assumption that

the number of scattering molecules is proportional to the analyte concentration used as shown in equation 2.15

$$AEF = \frac{I_{SERS}/c_{SERS}}{I_{RS}/c_{RS}} \quad \text{Equation 2.15}$$

where c_{SERS} and c_{RS} are the analyte concentrations used for the measurement of SERS spectrum and normal Raman spectrum, respectively. The AEF can thus give an estimation on the average performance of the used substrate and is suitable for analytical applications.^{219,235}

Generally, it is not completely satisfactory to compare SERS substrates only by the obtained enhancement factor as there are different factors which can strongly influence the magnitude of the resulting enhancement factor. First, it is very important to check for the metal used in the fabrication of the SERS substrate. From the previous discussion about the properties of metals it is obvious that the resulting enhancement depends on the intrinsic properties of the used metal. Silver is generally known to result in higher enhancement factors than gold in the visible region. Second, the enhancement factor largely depends on the type of analyte used. Analytes with a large Raman cross-section such as dyes usually result in greater enhancement factors. Furthermore, any interaction between the analyte and the SERS substrate resulting in a chemical enhancement will further increase the obtained enhancement factor when not identified as such. Third, the excitation laser used also has a big influence on the observed enhancement. If the wavelength of the used excitation laser meets the absorbance maximum of the analyte then this further enhances the SERS effect due to resonance conditions which is known as surface-enhanced resonant Raman scattering (SERRS). Therefore, it is always important to carefully compare the SERS enhancement factors for different substrates taking into consideration how and under which conditions these enhancement factors were calculated as an overestimation of the SERS enhancement factor can easily be the result. A more detailed and complete discussion about possible problems and misconceptions for the calculation of the enhancement factors can be found elsewhere.²⁸⁰

1.2.9 SERS substrates

There is a big variety of SERS substrates present which depends on a wide range of different fabrication techniques. The characteristics of a good SERS substrate are²⁸¹:

1. A good SERS substrate should provide high enhancement factors for different analytes so that it is capable to analyze different analytes with high sensitivity. This can be achieved by tuning the particle size and hence the LSPR so that it matches the laser

excitation wavelength. Furthermore, a good control over the particle or nanostructure spacing resulting in sub-10 nm gaps results in the formation of hot spots which provide high enhancement factors.

2. The fabrication of the substrate should be easy and inexpensive.
3. The SERS substrate should provide uniform enhancement over the whole substrate so that the deviation in the obtained SERS spectra from different spots on the substrate is less than 20%. This is also of high importance for analytical applications where quantification is desired.
4. The difference between the SERS enhancement obtained from different batches prepared by the same method should be also as small as possible and should not exceed 20%.
5. The stability of the SERS substrate is also an important issue as SERS substrates are usually not directly used after their fabrication. A long shelf-life without considerable deterioration of the SERS performance is desirable. Although silver as a noble metal gives high enhancement factors in the visible light region due to its intrinsic properties it suffers from the problem of chemical stability as its surface easily becomes oxidized and binding of adventitious carbon can take place under ambient atmosphere resulting in a rapid decay of its SERS performance.²⁸² On the contrary, gold offers higher chemical stability enabling long-term use of SERS substrates. Some approaches have been developed to increase the stability of silver-based SERS substrates like coating with a very thin layer of ALD-deposited Al₂O₃.²⁸³
6. The used SERS substrate should have a clean surface so that different analytes including analytes which do not strongly adsorb to the surface can be reliably analyzed.
7. Re-use of SERS substrates is also highly desirable which would enable to effectively lower the cost of SERS measurements compared to single-use substrates. Therefore, SERS substrates with a self-cleaning ability through photocatalysis have been developed through the synthesis of composite materials composed of a semiconductor material in contact to the sensing noble metal.^{284–288}

Various techniques and preparation methods were developed for fabrication of SERS substrates such as nanolithographic techniques and nanoimprinting,^{289–297} nanosphere lithography,^{264,298–304} electrochemical roughening of silver electrodes,^{206,238–241} the synthesis of nanoparticles of various size and shape for use in solution or assembling them on a solid substrate,^{272,278,305–308} oblique angle deposition technique for the fabrication of three-dimensional nanorod

arrays^{276,309–311} and metal deposition on structured substrates as carbon nanotubes,^{312–316} graphene foam,³¹⁷ biological scaffolds,^{246,318} black silicon,^{247,319} plasma-treated plastic²⁴⁹ and anodic aluminum oxide.^{250,320–322} Also, attempts for quick large scale production of SERS substrates through inkjet printing and simple techniques as pen-on-paper have been used.^{323,324} With time the control over the size, shape and spacing between the noble metal particles or structures significantly increased since the first discovery of the SERS effect but still it is hard to find a SERS substrate which meets all the above mentioned characteristics for an ideal SERS substrate. Depending on the area of application some points gain more weight in the design of the suitable SERS substrate than others. For example, for analytical applications where quantification is of interest the substrate uniformity is of great importance while for single molecule detection the maximized enhancement factor most important.²⁸¹ In the following, I will concentrate on especially two interesting and not widely distributed techniques or methods for SERS substrate fabrication, namely plasma-assisted fabrication and the use of anodized aluminum or anodic aluminum oxide for SERS substrate fabrication.

1.2.9.1 Plasma-assisted surface roughening

Plasma which is known as the fourth state of matter is nothing else than a partially ionized gas containing a mixture of neutral atoms or molecules, ions and free electrons.^{325–327} The neutral atoms or molecules present in the plasma are also continuously excited and relaxing again to the ground state emitting photons giving plasmas a characteristic colors. Overall, the plasma is electrically neutral but contains a sea of free electrons and ions which are free charge carriers making the plasma gas conductive in nature.³²⁶ Plasma treatment is known for decades and has been widely used in industry especially in microelectronics for etching, cleaning and for surface modifications.^{327,328} Different configurations and setups exist for the production of plasma and they differ in the excitation source, the device geometry and operating pressure.^{326,328} Plasma can be classified into hot or thermal plasma and cold or non-thermal plasma where especially the cold plasma is used for industrial applications in microelectronics and surface modifications of different materials like polymers and textiles.³²⁷ Cold plasma can be generated at low pressure through the direct application of an electric field between two parallel electrodes known as capacitively coupled plasma or through the formation of an electric field by inducing an radio frequency current in a coil which is known as inductively coupled plasma.^{326,329}

Radio frequency (rf) capacitively coupled plasma enables the formation of plasma at room temperature through the application of an alternating electric field with a standard frequency

of 13.56 MHz between two parallel electrodes as shown in **Figure 27**. The gas to be ionized then flows between these two plate electrodes where highly energetic electrons accelerated by the applied electric field collide with the atoms or molecules of the feed gas. The collisions may be elastic or inelastic. Elastic collisions only result in a change of the velocity and direction of the colliding particles. An inelastic collision of electrons with the atoms or molecules of the feed gas either result in their ionization by knocking out secondary electrons or result in the excitation of the gas molecules or atoms depending on their kinetic energy.^{325,329}

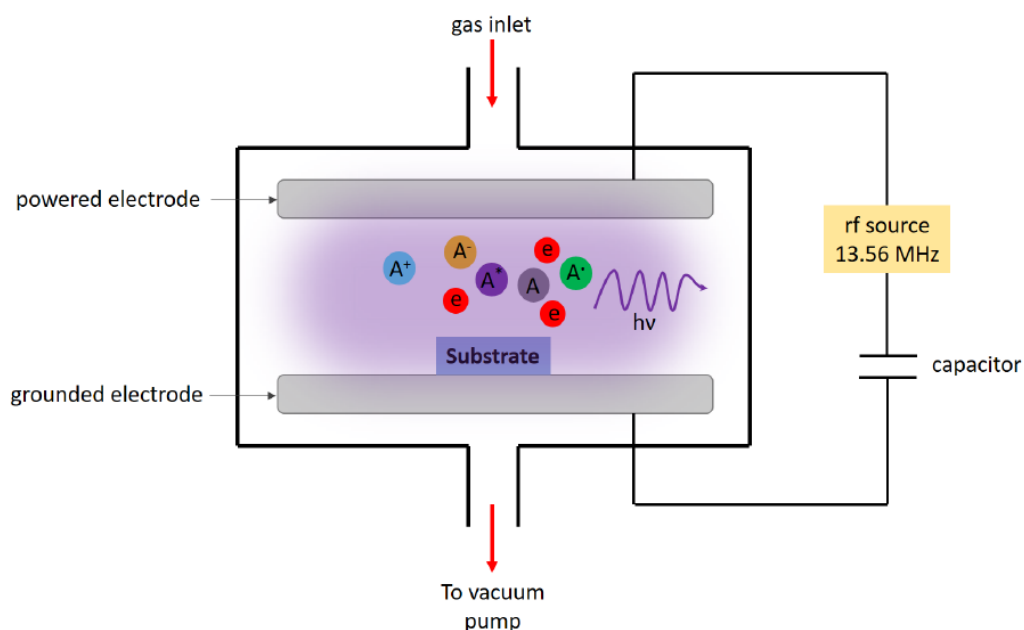


Figure 27 Schematic representation of the parallel plate radio frequency capacitively coupled plasma showing the different species formed in the produced plasma together with emitted light from the relaxing excited species. Adapted with permission from Ref. ²⁴⁴, © Creative Commons Attribution License.

The different processes which occur in a plasma resulting in the formation of different ions, electrons, radicals and excited species are shown in equations 2.16-2.20.^{325,329}



Equation 2.16 shows the electron impact ionization. Here, the impact of the electron on an atom or molecule of the feeding gas results in knocking out an electron leading to the formation of a positively ionized species accompanied by an increase in the number of free electrons in the

plasma. Sometimes electrons do not knock out other electrons upon collision with the neutrals but instead they combine as shown in equation 2.17 and this electron attachment results in the formation of negatively ionized species. The inelastic collision of an electron with an atom or molecule can also result in its excitation as shown in equation 2.18 which is then followed by the relaxation of the excited species emitting photons of specific wavelength as shown in equation 2.19. Finally, the collision of an highly energetic electron with a molecule can also lead to breaking bonds and thus resulting in radical formation as demonstrated in equation 2.20.^{325,329}

Plasma treatment has been used in different areas to achieve quick chemical modifications under gas phase at room temperature without the need for any toxic chemicals or solvents.^{327,330,331} Plasma treatment has been also applied for cleaning and modification of the surface of metals.³³²⁻³³⁵ Tiller et al. investigated the effect of plasma treatment on the surface roughness of vapor-deposited metal films where different plasma gases as argon, hydrogen and oxygen were tested on the metals gold, tin and nickel. This study found out that there is a general increase of the surface roughness of the plasma treated metals together with surface cleaning.³³² Kim et al. investigated the influence of nitrogen, argon and oxygen plasma on the removal of surface carbon contamination from various metal surfaces and found out that especially oxygen plasma and high density argon plasma are effective in the removal of surface carbon contamination.³³³ Another study investigated the effect of O₂, CF₄ and SF₆ plasma on a spin-coated silver nanoparticle layer. It was found out that a change was observed in the silver nanoparticle layer after plasma treatment where it was explained that the impact of ions and electrons from the plasma result in physical damaging and modification of the silver nanoparticle film. Furthermore, reactions between the silver nanoparticles and the plasma gas could change the chemical nature of the silver nanoparticle film where etching, surface oxidation in case of oxygen plasma, re-deposition of sputtered particles as well as deposition of carbon in case of the CF₄ plasma treatment were observed.³³⁴ Shanmugan et al. investigated the effect of different oxygen plasma parameters as power, flow rate and time on the surface of sputtered zinc thin films where a noticeable change in morphology and an increase in surface roughness was observed.³³⁵ Although the effect of plasma on metal surfaces has been investigated especially for electronic applications, plasma has not been used much for the preparation of SERS substrates till date. According to the previous discussed studies it should be possible to easily modify the surface of silver films with plasma treatment and increase the surface roughness which is highly beneficial for the fabrication of efficient SERS substrates.

Furthermore, the gas phase modification eliminates the need for any chemicals or liquid solvents which makes the process more environmentally friendly. Kinnan et al. used air plasma for the reduction of several silver salts which were previously melted on a quartz substrate for the application as SERS substrates.²⁴² Ma et al. used oxygen plasma for the oxidation of a thermally evaporated silver films followed by a wet reduction with citrate to obtain highly porous silver films for efficient SERS substrates with high enhancement factors.²⁴³

1.2.9.2 Anodized aluminum oxide as platform for SERS applications

While SERS is a surface effect mainly depending on the surface of the used noble metal it was found that an underlying dielectric also can influence the enhancement factor. The dielectric underlying the noble metal determines the dielectric constant and thus the refractive index of the medium surrounding the metal resulting in a change of the electromagnetic enhancement. Hunter et al. investigated the influence of the complex refractive index of different dielectrics on the local-field enhancement achieved by silver nanoparticles lying on that dielectric and they found that dielectrics with a high real part n and a high imaginary part k of the refractive index result in high enhancements. It was also found that an increasing k of the complex refractive index has a more profound effect on the electric field enhancement than the real part of the refractive index (**Figure 28**).³³⁶ Wang et al. also performed a comparison on the local field enhancement and thus SERS enhancement obtained by two different systems, namely silver/germanium (Ag/Ge) and silver/silicon (Ag/Si) substrates. They came to the result that Ag/Ge substrates were more efficient SERS substrates which was attributed to the higher imaginary part of the dielectric constant of the underlying germanium dielectric.³³⁷ This shows the influence of the dielectric underlying the noble metal in the electric field enhancement and the resulting SERS enhancement. The study of different dielectrics forming a layer beneath the actual noble metal could therefore offer more efficient SERS substrates.

A possible dielectric which can be studied beneath the noble metal is aluminum oxide. Especially electrochemical preparation of aluminum oxide through anodization of aluminum is interesting as it easily forms an aluminum oxide layer whose thickness can be controlled directly on an aluminum substrate. It offers also the possibility to obtain nanostructured aluminum oxide as in case of porous anodic aluminum oxide (PAOX) which will be discussed in the following.

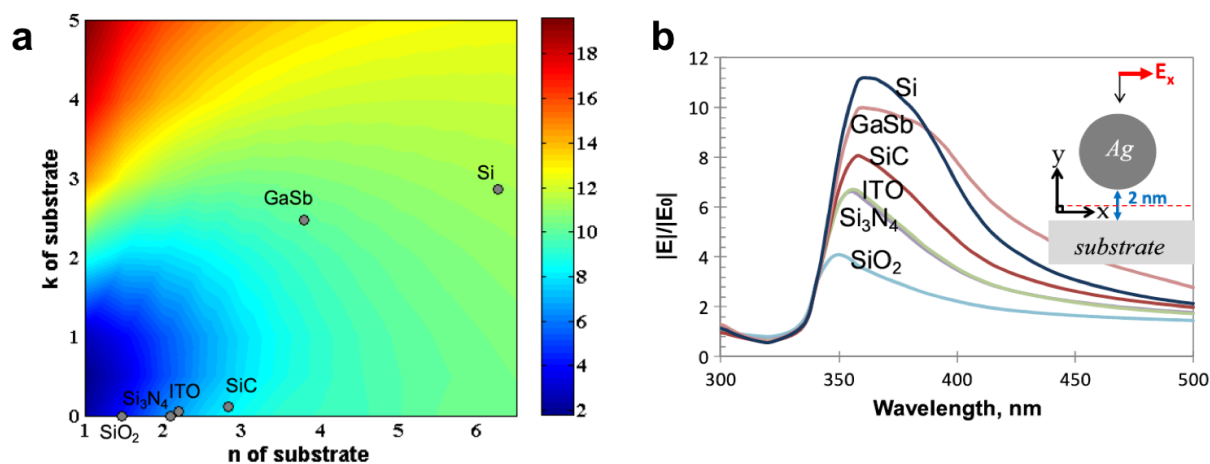


Figure 28 (a) Plot showing the maximum enhancement of the electric field of different dielectrics in relation with the real n and imaginary k part of the refractive index. (b) Electric field enhancement $|E|/|E_0|$ of different dielectrics in relation to the excitation wavelength. These data were calculated according to the model of a silver nanoparticle with 25 nm radius with a distance of 2 nm to the studied dielectric. Adapted with permission from Ref. ³³⁶, © 2013 IOP Publishing.

Anodization of aluminum has become an interesting approach for the passivation of the aluminum surface electrochemically through the formation of a thick aluminum oxide layer which is thicker than the 2-3 nm native oxide film thus enabling excellent corrosion resistance for the underlying aluminum.³³⁸ Since the discovery of the self-organized nanopore formation by Masuda et al. the interest in the use of these porous anodic aluminum oxide (PAOX) membranes in different areas has dramatically increased.^{339,340} PAOX membranes have been used for different applications such as filtration^{341,342} and they have been employed as a template for the preparation of different nanostructured materials.³³⁸

Anodization of aluminum can result either in a closely packed alumina film known as barrier-type anodic aluminum oxide or a porous alumina membrane known as porous anodic aluminum oxide (**Figure 29a**).^{338,343} The growth type depends on several factors, mainly the type of electrolyte used. The barrier-type is formed when electrolytes which are not capable of dissolving the formed aluminum oxide are used i.e. the formed oxide is completely insoluble in these electrolytes as neutral boric acid solution, ammonium borate and some organic electrolytes as citric and malic acid. Here, it is important that the pH of the used electrolyte is between 5-7 in order to obtain barrier-type aluminum oxide.³⁴³ The growth rate of the barrier-type anodic aluminum oxide decreases exponentially with time which results in the limitation of the maximum obtainable film thickness and the film thickness is mainly dependent on the applied voltage rather than the anodization time.^{338,343} On the other hand, PAOX is formed in

acidic electrolytes as sulfuric acid, phosphoric acid, chromic acid and oxalic acid as the formed oxide is partially soluble in these electrolytes. PAOX consists of a thin barrier-layer at the interface with the aluminum metal and a porous layer on top as shown in **Figure 29b**. The porous layer is formed of parallel cylindrical nanopores where each nanopore is surrounded by a hexagonal cell forming a honeycomb-like structure. The kinetics of PAOX formation differ from the barrier-type in the sense that the thickness of the porous layer is proportional to the amount of charge involved in the electrochemical reaction and thus the thickness of the formed PAOX can be controlled through the period of time used for anodization.³³⁸

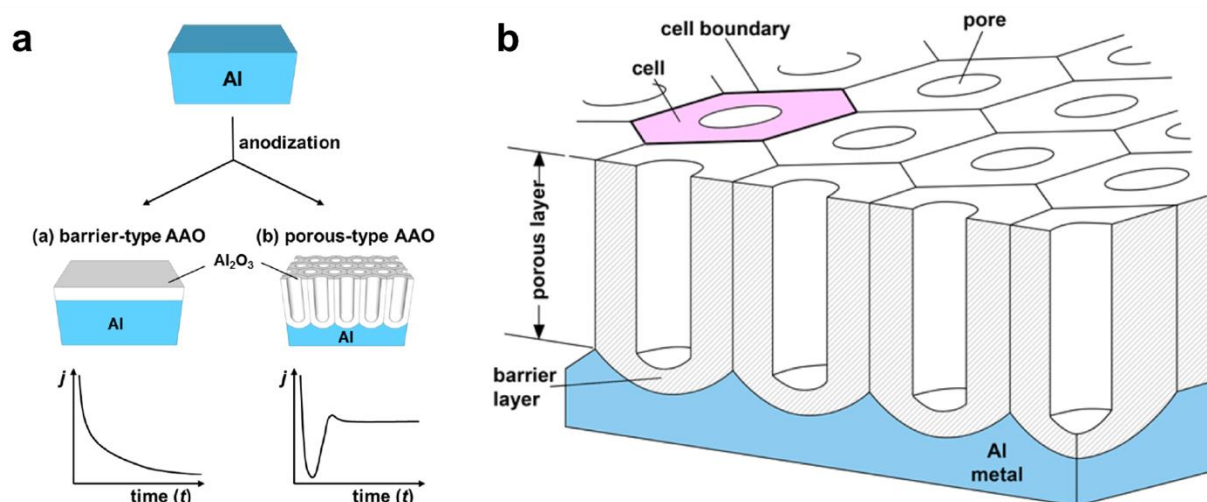


Figure 29 (a) Schematic showing the types of anodic aluminum oxide which can be formed upon anodization with the corresponding current density-time profiles at potentiostatic conditions. (b) Schematic representation of the structure of porous anodic aluminum oxide on aluminum substrate. Adapted with permission from Ref. ³³⁸, © 2014 American Chemical Society.

The use of aluminum/anodic aluminum oxide as a substrate for the preparation of SERS substrates can be very interesting as it offers a pre-designed structure and a platform for interference-enhanced Raman scattering (IERS) where the interference of the light reflected from the aluminum/aluminum oxide interface and the light reflected from a silver layer deposited on top could result in an enhancement of the Raman signal depending on the anodic aluminum oxide thickness. Thus, a combined SERS and IERS co-enhancement could be achieved in such a system.³⁴⁴⁻³⁴⁶ Shan et al. prepared aluminum supported PAOX and coated it with silver through electron-beam evaporation and showed that when the excitation laser wavelength is coincident an reflection minimum of the substrate then the SERS enhancement achieved was higher than in substrates where this condition was not met. This difference in enhancement was explained by an interference and SERS co-enhancement (**Figure 30a**).³⁴⁶

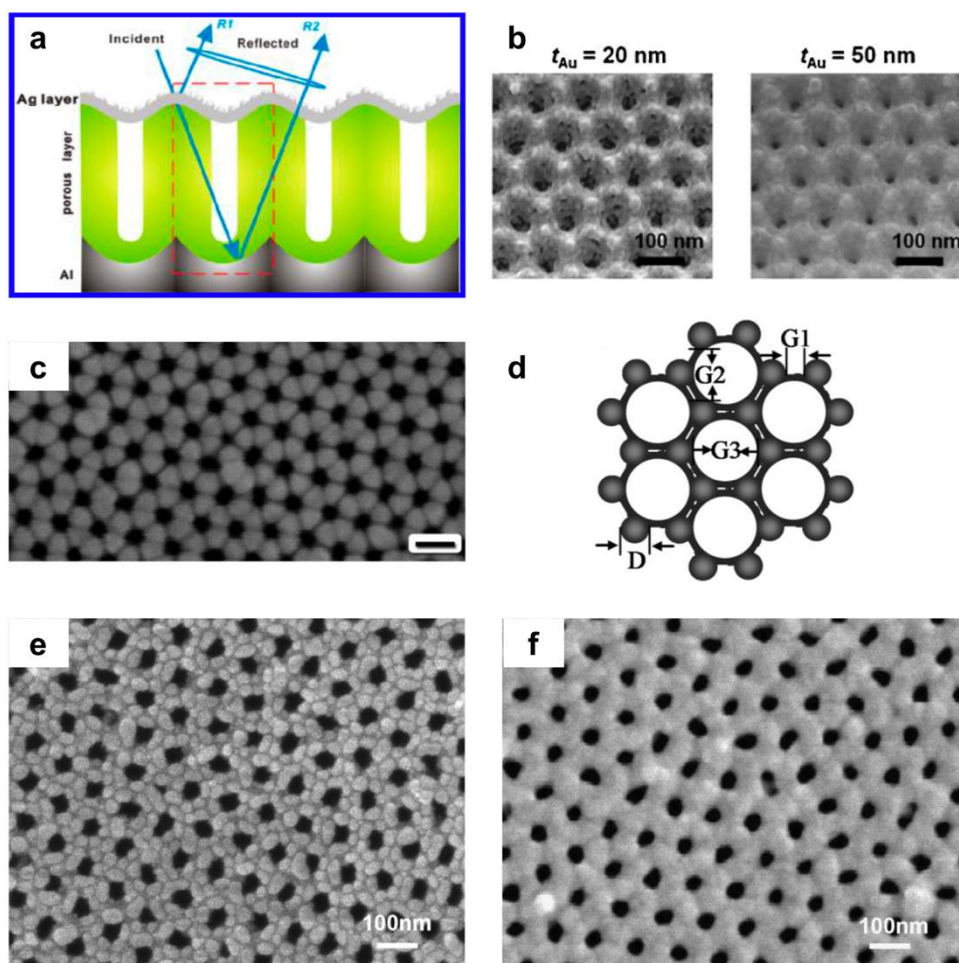


Figure 30 (a) Schematic showing the SERS substrate system composed of Al/PAOX/Ag showing the interference taking place through the reflected radiation from the Al/PAOX interface and the reflected radiation from the silver on top. Adapted with permission from Ref. ³⁴⁶, © 2014 American Chemical Society. (b) SEM image of PAOX coated with two different thicknesses of gold (20 nm and 50 nm) by electron-beam evaporation showing the narrowing of the pore diameter with increasing gold thickness. Adapted with permission from Ref. ²⁵⁰, © 2010 Wiley-VCH Verlag GmbH. (c) SEM image of PAOX formed in 0.5 M oxalic acid at 40 V and coated with silver through direct-current magnetron-sputtering forming sub-10 nm gaps between the pores. The scale bar represents 100 nm. (d) Schematic presentation of the arrangement of the silver nanoparticles on PAOX observed in (c) with the distances controlled in the process. Adapted with permission from Ref. ²⁷¹, © 2009 Wiley-VCH Verlag GmbH. (e) SEM image of complex patterned silver nanoparticle array obtained through electron-beam evaporation of silver on PAOX at 473 K and (f) SEM image of hexagonal nanopore array obtained through electron-beam evaporation of silver on PAOX at 295 K. Adapted with permission from Ref. ³⁴⁷, © 2012 Elsevier.

Other work concentrated mainly on the large area structuring obtained easily through the deposition of noble metals like silver and gold on PAOX for the generation of equally distributed hot spots between and at the PAOX nanopores.^{250,271,322,347,348} Choi et al. deposited gold through electron-beam evaporation on PAOX prepared in 0.3 M oxalic acid and studied the influence of

deposited gold thickness and PAOX thickness on the SERS enhancement obtained. It was found that with increasing gold thickness the SERS enhancement increased reaching a maximum and then decreased again with increasing thickness which also depends on the used excitation laser wavelength. As can be seen in **Figure 30b** an increasing thickness of deposited gold results in the narrowing of the nanopores resulting in the formation of hot spots. With increasing thickness of the underlying PAOX it was also shown that the SERS intensity decreased which was attributed to the changing dielectric environment which can be used to tune the SERS effect.²⁵⁰ Qi et al. reported the fabrication of so-called “silver nanocap arrays” which were templated by the underlying PAOX formed in 0.5 M oxalic acid at different anodization voltages. The silver was deposited by direct-current magnetron-sputtering for a constant time of 10 min where depending on the underlying PAOX template the gap distances could be tuned (**Figure 30c** and **30d**).²⁷¹ Wang et al. showed that by changing the deposition temperature of silver on PAOX through electron-beam evaporation different substrates could be obtained. High temperature deposition of silver resulted in a complex patterned nanoparticle array (**Figure 30e**) while low temperature deposition resulted in a hexagonal nanopore array (**Figure 30f**).³⁴⁷ This shows the different systems and the tuning which can be achieved via PAOX templates used for the fabrication of SERS substrates.

2 Organisation of the cumulative part of this dissertation

The following chapters of the thesis are arranged in two major categories. The first category consists of the development of new nanomaterials for effective photocatalysis for water remediation. In this part two different systems of photocatalysts are investigated in depth: nanoparticle@CNT (ZnO@CNT, ZnS/ZnO@CNT and ZnS@CNT) nanocomposites prepared through a gas phase approach and two-dimensional titanium chalcogenides.

In the second category different approaches for the preparation of efficient SERS substrates are investigated. The first approach demonstrates the plasma-assisted fabrication of efficient SERS substrates with tunable SERS enhancement factors while the second approach depends on the production of different aluminum/anodic aluminum oxide/silver (Al/AAO/Ag) systems to be used as efficient SERS substrates.

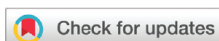
2.1 ZnS/ZnO@CNT and ZnS@CNT nanocomposites by gas phase conversion of ZnO@CNT.

A systematic study of their photocatalytic properties

Zinc sulfide ZnS is an interesting wide band gap photocatalyst due to its ability of the rapid generation of electron-hole pairs which is highly beneficial for photocatalysis. But unfortunately, being a wide band gap semiconductor with a band gap of 3.72 eV for sphalerite and 3.77 eV for the wurtzite crystal form, it is unable to make use of most of the sunlight as only UV light is absorbed. Through the formation of nanocomposite heterostructures of ZnS with carbon nanotubes (CNTs), the photocatalytic properties can be boosted achieving several advantages at the same time. Combining ZnS with CNTs enable use of most of the solar spectrum as the light absorption will be extended not only to the visible but also to the near infrared region. Furthermore, the formed heterojunction with the conducting CNTs offers a good possibility for spatial charge separation, thus increasing the recombination time of the photo-induced charge carriers and making them available for the photocatalytic reactions. Finally, the high adsorptive capacity of CNTs also enables efficient removal of any organic residues besides photocatalysis.

Here, a new approach for the synthesis of such ZnS@CNT nanocomposites is demonstrated which enables a direct contact of the ZnS nanoparticles with the CNT for optimal charge transfer during photocatalysis. Through atomic layer deposition (ALD) ZnO nanoparticles are deposited on an array of vertically aligned CNTs (VACNTs) forming a ZnO@CNT nanocomposite where the particle size of the deposited ZnO nanoparticles can be nicely tuned by the number of ALD cycles. Gas phase conversion of the resulting ZnO@CNT nanocomposite to ZnS@CNT by hydrogen sulfide formed from the decomposition of thioacetamide as precursor enables the formation of a wide range of nanocomposites as ZnS/ZnO@CNT, sphalerite ZnS@CNT and wurtzite ZnS@CNT including varying mixture of both depending on the conversion temperature and time used. Thus, a systematic study and direct comparison of these different nanocomposites is possible.

Photocatalytic degradation experiments using methyl orange as model pollutant for this investigation revealed a high photocatalytic activity of the different nanocomposites using simulated sunlight as radiation source. Especially the ZnS@CNT nanocomposites formed at high temperatures (750°C) and thus composed mainly of wurtzite ZnS showed the highest photocatalytic activity in the degradation of methyl orange. Higher temperatures for longer time can also induce some defects in the ZnS resulting in a further increase of the photocatalytic activity of the ZnS@CNT nanocomposite. Thus, the photocatalytic activity can be carefully tuned.



Cite this: *Dalton Trans.*, 2017, **46**, 5189

ZnS/ZnO@CNT and ZnS@CNT nanocomposites by gas phase conversion of ZnO@CNT. A systematic study of their photocatalytic properties†

Sherif Okeil, Jan Krausmann, Inga Dönges, Sandra Pflieger, Jörg Engstler and Jörg J. Schneider *

ZnS nanoparticles have been synthesized on vertically aligned carbon nanotubes by gas-phase conversion of ZnO nanoparticles which have been tethered on vertically aligned carbon nanotubes using atomic layer deposition (ALD). The resulting ZnO@CNT nanocomposite has been converted to ZnS@CNT by reacting it with hydrogen sulfide using thioacetamide as a precursor. The composition of the resulting nanocomposite could be tuned from a mixed ternary ZnS/ZnO@CNT nanocomposite to a pure ZnS@CNT nanocomposite. At the same time, the amount of wurtzite and sphalerite phases varies in the ZnS@CNT nanocomposite. The resulting nanocomposites were characterized by X-ray diffraction (XRD), scanning electron microscopy (SEM), energy dispersive X-ray spectroscopy (EDX), transmission electron microscopy (TEM), selected area electron diffraction (SAED), ultraviolet-visible diffuse reflectance spectroscopy (UV-VIS DRS) and photoluminescence spectroscopy (PL). Finally, the different nanocomposites were tested for their photocatalytic activity by the photocatalytic decomposition under visible light using methyl orange (MO). Herein a systematic study of the photocatalytic activity of different compositions of ZnS in the ZnS@CNT nanocomposite was performed for the first time.

Received 2nd February 2017,
Accepted 17th March 2017

DOI: 10.1039/c7dt00407a

rsc.li/dalton

1. Introduction

Photocatalytic degradation of organic materials in water represents a green way to eliminate organic hazardous materials from aquatic systems.^{1–4} Therefore, it is important to explore new ways to produce efficient photocatalysts which are able to make full use of sunlight in the photocatalytic degradation process. ZnS is a semiconductor which has been extensively investigated for its use in photocatalysis due to its ability for rapid generation of electron–hole pairs.⁵ It has a direct band gap of 3.72 electron volts in its cubic form sphalerite⁶ and 3.77 electron volts in its hexagonal form wurtzite.⁷ However, in both modifications, due to its wide band gap, its effectiveness as a photocatalyst is decreased as UV-light forms only about 3% of the total sun radiation.⁸ Composite formation with carbon nanotubes (CNTs) has several advantages. First, it can extend the absorption towards the visible light region and thus may increase the photocatalytic efficiency of the semiconductor under sunlight.⁹ Second, the direct contact between

CNTs and the ZnS semiconductor material enables better electron–hole separation and retards the carrier recombination which is reflected in a higher photocatalytic activity.¹⁰ Therefore, electrons which are excited by the photons can easily be channeled to the CNT structure leaving holes in the semiconductor. The oxygen adsorbed on the CNT reacts with the electrons forming superoxide radicals and the holes on the semiconductor oxidize water molecules forming hydroxyl radicals. These highly reactive species then attack the organic pollutant leading to its decomposition.¹¹ Finally, CNTs are known to be efficient adsorbers for organic compounds, which leads to more efficient removal of the organic pollutants from the aquatic environment.¹² There are several reports in which ZnS@CNT nanocomposites have been described. Usually, CNTs were modified by linking groups in order to be able to attach the ZnS nanoparticles onto their outer surface.¹³ In this case, the problem for photocatalytic applications is that these organic linker molecules decrease the efficient electron transfer between the ZnS semiconductor and the CNT which in turn leads to decreased photocatalytic activity. Thus, other methods which enable direct contact between ZnS and CNT have been developed.¹⁴ ZnS nanoparticles have been produced by microwave irradiation,^{15,16} by thermal treatment⁵ or by photochemical synthesis¹⁷ directly on the surface of previously oxidized CNTs. In these cases, the oxidation of the CNT results in a

Fachbereich Chemie, Eduard-Zintl-Institut für Anorganische und Physikalische Chemie, Alarich-Weiss-Strasse 12, Technische Universität Darmstadt, 64287 Darmstadt, Germany. E-mail: joerg.schneider@ac.chemie.tu-darmstadt.de

† Electronic supplementary information (ESI) available. See DOI: 10.1039/c7dt00407a

change in the electronic structure of the CNT which affects the electron transfer between the semiconductor and the CNT.¹⁸ Thus, all of the developed methods depend on solution-based procedures and most of them start with a modification of the CNT surface.

Herein we report on a new route for the synthesis of ZnS@CNT nanocomposites based entirely on a gas-phase process. The ZnS@CNT nanocomposite was obtained by employing vertically aligned CNTs grown *via* chemical vapor deposition (CVD) subsequently followed by an atomic layer deposition (ALD) step on the ZnS@CNT nanocomposite. This tethers nanoscale ZnO particles directly and without the need of any further surface modification to the surface of the CNTs. The resulting ZnO@CNT nanocomposite was then treated with hydrogen sulfide gas converting it to a ZnS@CNT nanocomposite with retention of its morphology. By variation of the reaction temperature, it is possible to tune the rate of conversion resulting in the controlled formation of ZnS/ZnO@CNT composites to pure ZnS@CNT nanocomposites showing different ratios of wurtzite and sphalerite modifications. This chemical and structural tunability enabled a systematic study of the photocatalytic activity of the resulting nanocomposites.

2. Experimental

2.1. Synthesis of vertically aligned CNTs

Vertically aligned CNTs were synthesized employing a water-assisted chemical vapor deposition (CVD) process.¹⁹ In a typical synthesis run, 10–13 nm Al were thermally deposited on a 1 cm × 1 cm Si/SiO₂ wafer to form an Al₂O₃ buffer layer, and then 1.2 nm Fe catalyst were sputter deposited on top of this layer. The vertically aligned CNTs were allowed to grow at a temperature of 850 °C for 15 min using ethylene as a carbon precursor together with a controlled amount of water. The CNTs are double walled with a small amount of multiwalled CNTs (between 3–5). Further details about the synthesis of the vertically aligned CNTs can be found elsewhere.²⁰

2.2. Synthesis of a ZnO@CNT nanocomposite through atomic layer deposition (ALD)

The vertically aligned CNTs were inserted into the ALD chamber (Savannah G2, Ultratech/CNT, Cambridge Nanotech, USA) for deposition of a predefined thickness of ZnO using diethylzinc (99.9%) and water (HPLC grade) as precursors at 200 °C. The precursors were vaporized at room temperature and 20 sccm argon was used as a carrier gas. The exposure times for both diethylzinc and water were 0.015 s and the flushing between the precursor pulses was done with argon for 10 s. Dynamic mode was used for all depositions.

2.3. Gas-phase conversion of a ZnO@CNT nanocomposite to a ZnS@CNT nanocomposite

The obtained ZnO@CNT nanocomposite was placed in a quartz tube in the middle of a tube furnace (Horst GmbH tube furnace, 500 mm length and 50 mm inner diameter with a

NiCr–Ni temperature sensor and a HT MC1 microprocessor temperature regulator). One end of the quartz tube was inserted into a smaller tube furnace to be used as a preheating zone for decomposing the H₂S source. A ceramic boat loaded with 0.1 g thioacetamide was placed in the middle of the small tube furnace. The large tube furnace containing the sample was first heated to the desired temperature. Then the small home-made tube furnace was heated to 200 °C to decompose the thioacetamide, releasing hydrogen sulfide gas, which was transported by an argon stream of 600 sccm to the ZnO@CNT sample and reacted for the desired reaction time (see Fig. S1† for the experimental set up).

2.4. Synthesis of ZnS nanoparticles

ZnS nanoparticles were synthesized through a route similar to the synthesis of the ZnS nanoparticles on the CNT. ZnO nanopowder was first synthesized as follows: 1 g zinc chloride was dissolved in 100 mL distilled water followed by dropwise addition of 25 mL of 1 M sodium hydroxide under vigorous stirring. The obtained suspension was stirred for further 30 min. The formed precipitate was collected by filtration and was dried overnight at 100 °C. The dried powder was then heated in a tube furnace at 800 °C for 1 h under an air atmosphere to obtain pure ZnO nanopowder. The obtained ZnO nanopowder was then converted to ZnS through gas-phase conversion using thioacetamide as a hydrogen sulfide precursor as mentioned for the formation of the ZnS@CNT nanocomposite. In this case, 0.5 g thioacetamide were used to convert 0.03 g ZnO nanopowder at 750 °C for 1 h using an argon stream of 200 sccm to ensure complete conversion of the ZnO nanopowder to ZnS.

2.5. Characterization of the nanocomposites

Scanning electron microscopy (SEM) measurements were performed on a Philips XL-30 FEG coupled with an energy-dispersive X-ray (EDX) analyzer using an electron beam at 25 kV. Transmission electron microscopy (TEM) images and selected area electron diffraction (SAED) were recorded using a Tecnai G2 F20 microscope operating at 200 kV. The samples were prepared by dispersing a minute amount of the nanocomposite in ethanol by short ultrasonication followed by drop-casting on TEM copper grids. X-ray diffraction (XRD) was performed on a Rigaku Miniflex 600@40 kV 15 mA diffractometer using Cu K_{α1} radiation ($\lambda = 1.541 \text{ \AA}$). Ultraviolet-visible diffuse reflectance spectra (UV-VIS DRS) of the nanocomposites were recorded on a Thermo Scientific UV-VIS spectrophotometer (Evolution 600) with an integrating sphere. Photoluminescence spectra (PL) of the synthesized nanocomposites were recorded on a Varian Cary Eclipse fluorescence spectrophotometer (Agilent Technologies).

2.6. Photocatalytic activity measurement through degradation of methyl orange

Photocatalytic performance studies of the ZnO@CNT, ZnS/ZnO@CNT and ZnS@CNT nanocomposites were performed using methyl orange (MO) dye as a model pollutant. A 2 mg

mL⁻¹ stock solution of MO was prepared in distilled water. The test solution was freshly prepared by adding 1 mL MO stock solution, 1 mL 0.1 M HCl, 1 mL 3.5% (w/w) H₂O₂ and completing it to 100 mL with distilled water. In a typical experiment, 50 mL of the test solution was transferred to a quartz test tube and mixed with 1 mg of the composite material. The test tube was covered by Parafilm®, wrapped with aluminum foil and allowed to stir for 2 hours in the dark to allow adsorption to take place. Then the aluminum foil was removed and a 150 W mercury vapor bulb placed at a distance of 10 cm from the test tube, simulating sunlight, was focused onto the sample. At predefined time intervals, the nanocomposite was allowed to settle and about 2 mL of the test solution were withdrawn and the UV-VIS spectrum was measured on a Thermo Scientific UV-VIS spectrophotometer (Evolution 600) to determine the dye degradation. The change in the absorption maximum of methyl orange solution at 503 nm was monitored and the ratio C/C_0 was plotted against the photocatalysis time, where C/C_0 denotes the ratio of the concentration of methyl orange at the sampling time to the initial concentration of methyl orange when the photocatalysis experiment started.

3. Results and discussion

3.1. Materials synthesis and characterization

Thermogravimetric analysis of thioacetamide revealed a weight loss starting from about 75 °C up to 160 °C (see ESI Fig. S2†). Thioacetamide decomposition under an inert atmosphere occurs with the release of hydrogen sulfide gas and acetonitrile according to the following equation:



Thus, to ensure complete decomposition and the release of all hydrogen sulfide gas from the precursor a final decomposition temperature of 200 °C was used.

The product obtained after ZnO deposition on vertically aligned CNTs employing the ALD technique was characterized using SEM and EDX in order to ensure the presence of ZnO and its homogeneous distribution on the CNT array (Fig. 1 and 2). EDX analysis of the nanocomposite confirms the presence of the elements Zn and O in an appropriate ratio of about 1 : 1 (Fig. 2). Further analysis of the ZnO@CNT nanocomposite by XRD showed reflexes of a wurtzite polymorph of ZnO (Fig. 3). The significant broadening of reflexes nicely indicates the formation of nanocrystalline ZnO deposited on the surface of the CNTs. An approximate crystallite size of 20 nm could be calculated using the Scherrer equation. The TEM image indicates the formation of particulate ZnO on the surface of the CNTs in a dense manner (Fig. 4). Moreover, the vertical arrangement of the CNT array remains nicely intact after ALD deposition (Fig. 1a and b). Most obviously structural defects on the carbon nanotubes serve as nucleation sites for the deposition of the ZnO nanoparticles formed by ALD.²¹ This might be a most efficient process since the molecular layers of

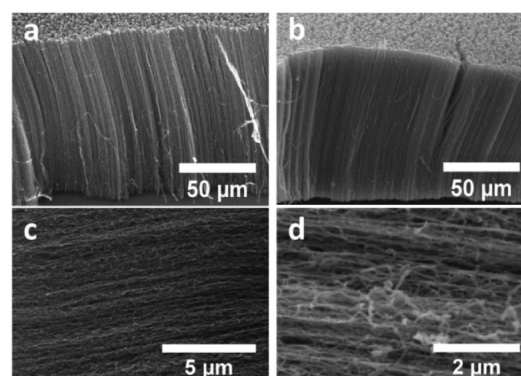


Fig. 1 SEM image of a vertically aligned CNT (a) and (c) before and (b) and (d) after ALD coating with 20 nm ZnO particles.

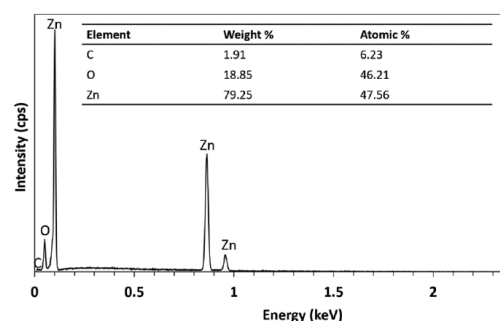


Fig. 2 EDX of the ZnO@CNT nanocomposite obtained from the deposition of 20 nm ZnO by ALD.

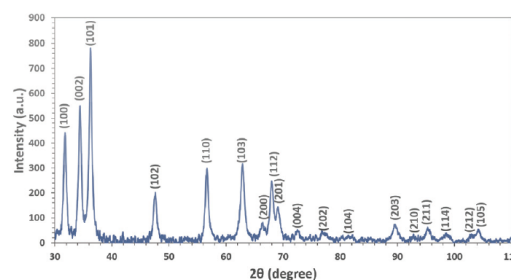


Fig. 3 XRD of the ZnO@CNT nanocomposite showing solely the reflexes of the hexagonal wurtzite structure of ZnO.

the deposited $\text{Zn}(\text{C}_2\text{H}_5)_2$ used as a precursor might nucleate on these defects. The finally formed ZnO particles are evenly distributed on the CNT surface having an average particle size of 20 nm as determined by XRD analysis.

The obtained ZnO@CNT nanocomposite was then further converted by the gas-phase reaction of precursor-derived

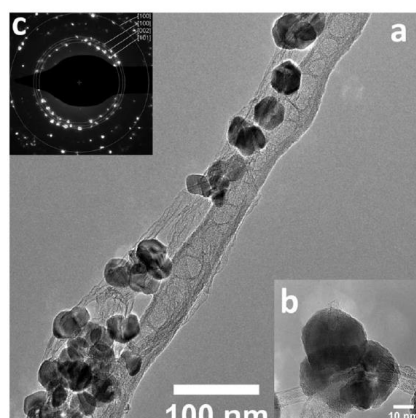


Fig. 4 (a) Characteristic TEM image of the ZnO@CNT nanocomposite showing a narrow size distribution of the particles and the wrapping of the CNTs with ZnO nanoparticles; (b) HRTEM of a ZnO particle attached to a CNT; (c) SAED pattern of the ZnO nanoparticles showing the diffraction pattern for ZnO (wurtzite structure).

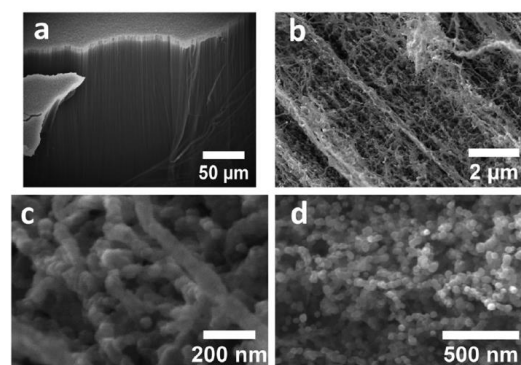
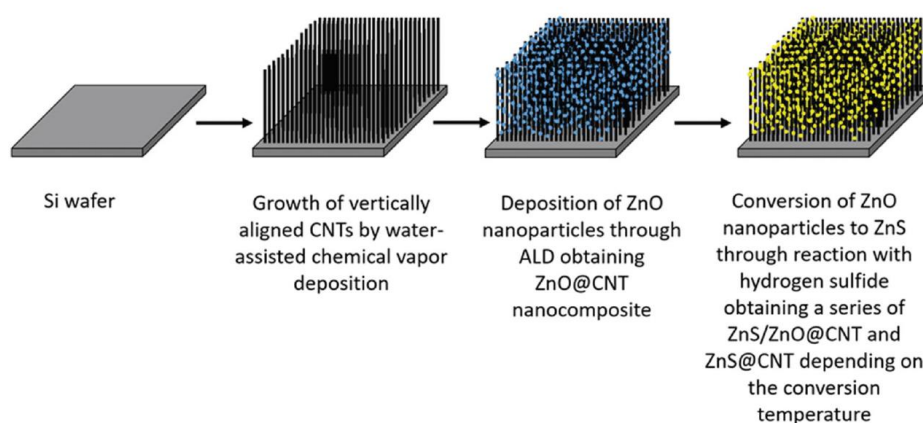


Fig. 5 SEM of the nanocomposites obtained after the reaction of the ZnO@CNT composite with hydrogen sulfide gas at (a) 500 °C, ZnS@CNT nanocomposite; (b) and (c) 650 °C, ZnS@CNT nanocomposite and at (d) 300 °C, ZnS/ZnO@CNT nanocomposite.

hydrogen sulfide gas obtained from the decomposition of thioacetamide at 200 °C. While the decomposition temperature of the precursor was kept constant, different temperature regimes ranging from 200 °C up to 950 °C were studied for the gas-phase conversion of the ZnO@CNT composite to the ZnS@CNT composite using a constant argon transport gas flow rate of 600 sccm and an overall reaction time of 5 min (Scheme 1). The morphology of the obtained nanocomposite did not change significantly after the gas phase conversion of the ZnO@CNT composite with hydrogen sulfide (Fig. 5a–d). EDX analysis of the different nanocomposites obtained at varying reaction temperatures revealed a gradual increase of the ZnS content with increasing reaction temperature in the

formed composite (Fig. 6). At 200 °C, a minor amount of sulfur could be detected which could be attributed to the conversion of only a small amount of zinc oxide to zinc sulfide on the surface of the CNT host. With increasing temperature up to 400 °C, the amount of ZnS increases while ZnO decreases proportionally and at about 400 °C the conversion of ZnO to ZnS is almost complete. The presence of small amounts of oxygen in the EDX analysis at temperatures above 400 °C could be attributed to the native SiO₂ buffer layer of the Si wafer substrate on which the CNTs have been grown.

To assign the phase composition of the formed ZnS an XRD analysis of the obtained composites has been performed (Fig. 7). As confirmed by the EDX analysis ZnO in the wurtzite structure is present in the ZnS/ZnO@CNT nanocomposite obtained at temperatures of 200 °C and 300 °C. At a reaction temperature of 350 °C, the presence of a mixed-phase of ZnS



Scheme 1 Schematic of the overall fabrication process leading to the subsequent formation of 3D oriented arrays of ZnO@CNT, ZnS/ZnO@CNT and ZnS@CNT composites.

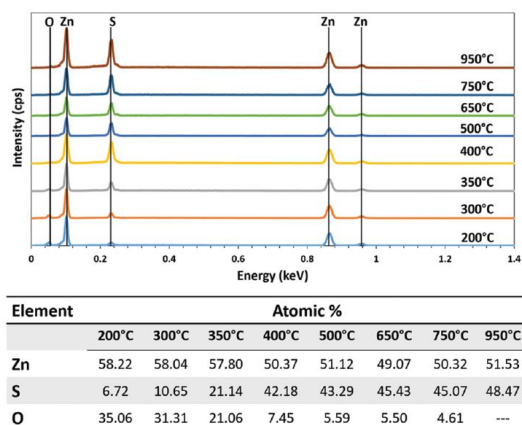


Fig. 6 EDX analysis of the ZnO@CNT nanocomposite after conversion to ZnS/ZnO@CNT and finally ZnS@CNT with hydrogen sulfide at different temperatures for 5 min each.

in its sphalerite structure and ZnO in the wurtzite phase can be detected. In addition, EDX analysis of the ZnS/ZnO@CNT nanocomposite at 350 °C reveals that ZnO and ZnS are present in almost the same ratio. From 400 °C onwards reflexes for ZnO have vanished and only reflexes for ZnS in its sphalerite as well as wurtzite modification are detected. The ratio of ZnS (sphalerite) to ZnS (wurtzite) changes gradually when going from 400 °C to 950 °C where the wurtzite proportion increases until almost all of the ZnS is in its wurtzite structure at 950 °C as detected from the distinctive reflexes at 27.1°, 30.7°, 39.7° and 51.9°. The reflexes for the sphalerite phase are partially overlapped by the reflexes of the wurtzite phase of ZnS making it difficult to determine the actual amount of the sphalerite

phase present in the ZnS@CNT composite. The variation of the relative heights of reflexes at 27.1° and 28.7° indicates an increase in the wurtzite phase and a decrease in the sphalerite phase in the ZnS@CNT composite. The phase transition of sphalerite to wurtzite for bulk ZnS is usually observed at 1020 °C but it was found that this phase transition temperature decreases with decreasing particle size^{22,23} thus explaining the evolution of the wurtzite phase of ZnS starting from about 400 °C. The coexistence of sphalerite and wurtzite phases of ZnS and the increase of the wurtzite phase proportion with increasing temperature has been recently reported and it was found that the presence of sphalerite besides the wurtzite phase enhances the separation of photo-induced charge carriers resulting in a higher photocatalytic activity.²⁴ The particle size of the formed ZnS at 950 °C has significantly increased and the particles have agglomerated significantly due to Ostwald ripening and further sintering indicated by the sharp reflexes in the XRD now observed compared to the samples at lower conversion temperatures. This is also manifested in the SEM of the ZnS@CNT nanocomposite formed at 950 °C depicting this strong aggregation of the ZnS (see ESI Fig. S3†).

Further insights into the morphology of the ZnS/ZnO@CNT and ZnS@CNT nanocomposites are provided by the TEM images at 350 °C and 650 °C (Fig. 8a and d). The zinc chalcogenide particles are distributed on the CNT surface and selected area electron diffraction (SAED) of these particles manifests the presence of a mixed phase of ZnO and ZnS on the CNT surface, the latter in the sphalerite phase, for a synthesis temperature of 350 °C (Fig. 8c) and pure ZnS mainly in the wurtzite phase at 650 °C as the synthesis temperature (Fig. 8f). Interestingly the metal chalcogenide particles in the ZnS/ZnO@CNT composite formed at 350 °C show a hollow core as deduced from the image contrast difference in the

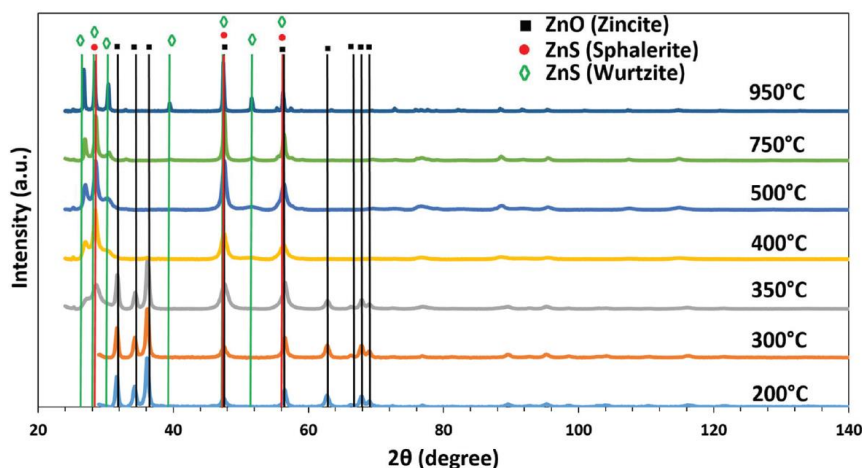


Fig. 7 XRD analysis of the ZnO@CNT nanocomposite after conversion with hydrogen sulfide at different temperatures for 5 min each showing the main reflexes for ZnO (zincite), ZnS (sphalerite) and ZnS (wurtzite).

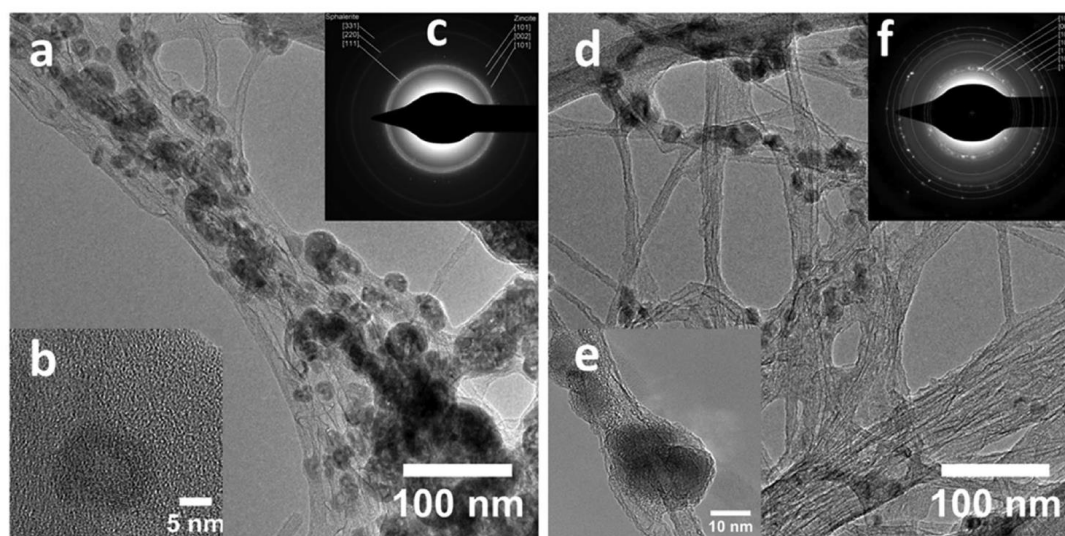
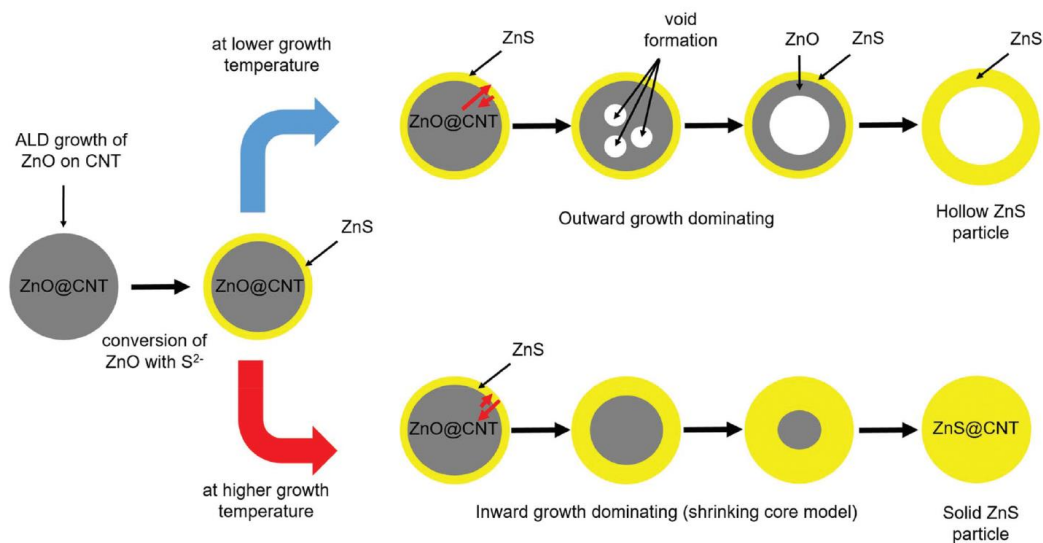


Fig. 8 (a) TEM images of the ZnS/ZnO@CNT nanocomposite synthesized at 350 °C; (b) magnification of a ZnO@ZnS particle tethered onto a CNT showing the void formed in the nanoparticle; (c) SAED pattern of the ZnO@ZnS nanoparticles showing the diffraction pattern for ZnO (wurtzite structure) and ZnS (sphalerite structure); (d) TEM image of the ZnS@CNT nanocomposite synthesized at 650 °C for 30 min. (e) TEM magnification of a ZnS nanoparticle tethered onto the surface of a double-walled CNT; (f) SAED of a ZnS nanoparticle synthesized at 650 °C showing the diffraction pattern for ZnS.

TEM (Fig. 8b). A possible void formation in ZnO/ZnS core-shell nanostructures has been observed for different nanostructures^{25–29} and hollow ZnO/ZnS core-shell particles have been tested for their photocatalytic activity showing improved activity compared to single phase ZnO nanoparticles.³⁰ Void formation might be due to the well-known Kirkendall-effect and it originates from the difference in diffusivity of the Zn^{2+} and O^{2-} ions moving out of the ZnO core and the S^{2-} ions which diffuse inward on the ZnO/ZnS interface.²⁵ At a conversion temperature of 650 °C however, solid ZnS particles are observed (Fig. 8e). This might be due to sintering or an altered and increased inward growth rate of the ZnS shell at higher temperatures outperforming the outward diffusion of the Zn^{2+} and S^{2-} ions, thus preventing significant void formation. Different explanations have been discussed for understanding the conversion of nanoparticles, *e.g.* the shrinking-core model³¹ and reaction regimes depending on different factors involved in the conversion reaction of nanoparticles have also been described.³² Recently, experimental evidence for an outward growth of the ZnS phase in a ZnO sulfidation reaction, leading to void formation has been provided, however only at lower temperatures of about 300 °C.²⁹ The observation of nanoparticle conversion at different temperatures leads to the conclusion that not only one process is involved but rather several temperature dependent processes are involved in the conversion process. Other reported conversion processes show that a temperature increase results in the formation, *e.g.*, of hollow nanoparticles with a thicker CuO shell or even completely solid CuO nanoparticles both formed

from the oxidation of Cu nanoparticles at high temperature.³³ When the probability of the reaction at the solid–solid interface of the core and shell is higher than at the solid–solution interface, solid nanostructures could be obtained even if the diffusivity of the outward diffusing ions is higher than the diffusivity of the inward diffusing ones.³² Thus, a combined inward and outward growth could explain the nanoparticle conversion process. The outward growth is mainly governed by the outward diffusion of the ions in the core particle and the inward growth depends on the reaction rate at the solid–solid interface of the core and shell. At lower temperatures, the outward diffusion dominates due to a low reaction rate leading to the formation of hollow particles, while at higher temperatures the inward growth of the shell dominates due to the increased reaction rate leading to the formation of solid particles (Scheme 2). Altogether these processes offer a reasonable explanation for the observed particle morphology. Further TEM and HRTEM images for ZnS/ZnO@CNT at 350 °C, ZnS@CNT at 500 °C and ZnS@CNT at 750 °C can be found in ESI Fig. S4.† In the HRTEM images the void formation in the ZnO@ZnS particles formed at 350 °C and in the ZnS particles formed at 500 °C can be clearly seen while at 750 °C also solid ZnS particles are obtained.

To gain an insight into the optical properties of the formed nanocomposites the UV-VIS diffuse reflectance spectra as well as the photoluminescence spectra were recorded (Fig. 9). In the UV-VIS diffuse reflectance spectra it can be seen that the nanocomposites benefit from the extended absorption in the visible region due to the attachment of the nanoparticles



Scheme 2 Proposed formation mechanism of ZnO nanoparticles and conversion to ZnS of different morphologies on the surface of the vertically aligned CNTs.

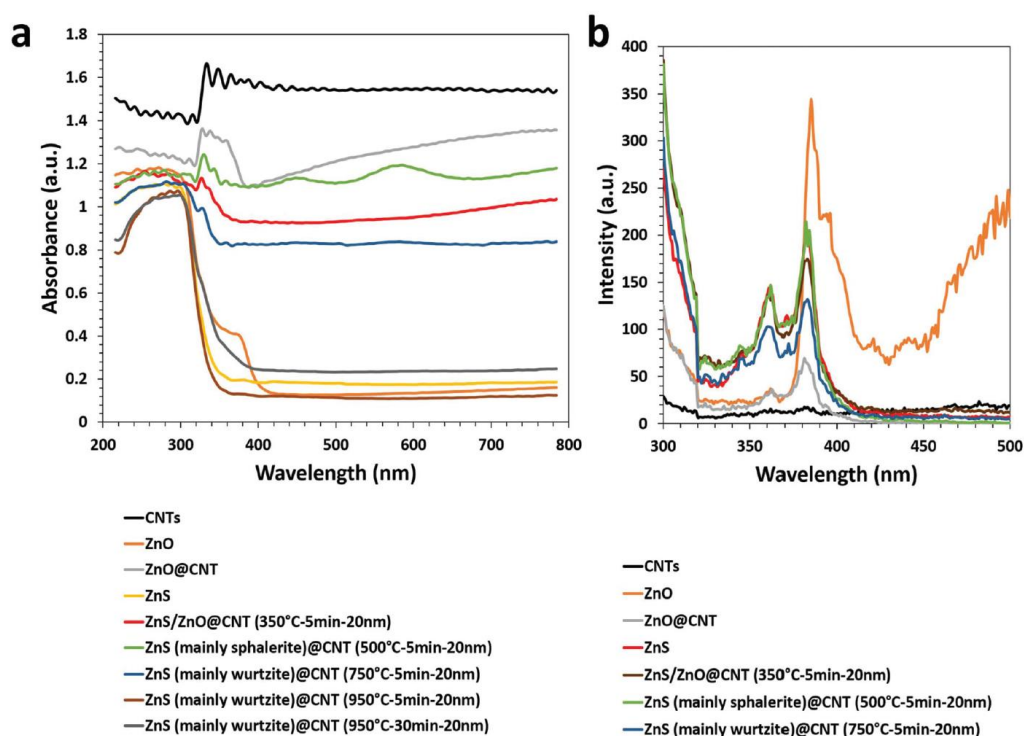


Fig. 9 (a) UV-VIS diffuse reflectance spectra and (b) photoluminescence spectra at an excitation wavelength of 280 nm of the different nano-composites and their comparison with pristine CNTs and bare ZnO and ZnS nanoparticles.

to the CNTs which absorb in the whole UV-VIS region while the nanoparticles alone absorb only in the UV-region (Fig. 9a). In the diffuse reflectance spectra of ZnS@CNT at 950 °C for 5 min and 30 min the extended absorption in the visible region is not clearly visible as the ZnS forms aggregates completely covering the measured surface leading to lower absorbance from the CNTs during measurement. Upon comparison of the diffuse reflectance spectra obtained for the ZnS@CNT nanocomposite at 950 °C for 5 min and 30 min, a slight extended absorption for the nanocomposite synthesized for 30 min is observed which is an indication for the formation of sulfur vacancies upon long heat treatment at high temperatures.³⁴ The photoluminescence spectra were recorded at an excitation wavelength of 280 nm (Fig. 9b). While the photoluminescence spectrum of CNTs is featureless, the photoluminescence spectra of ZnO and ZnS nanoparticles as well as the different nanocomposites show mainly two emission peaks at 362 nm and 381 nm. The presence of these emission peaks for the nanocomposites shows the successful attachment of the nanoparticles to the CNTs but it can also be seen that the emission intensity of the nanocomposites is lower than that of bare nanoparticles which is due to the electron-transfer of the excited electrons to the CNTs leading to a quenching of the fluorescence emission.^{35,36}

Besides the effect of temperature on the formation of the ZnS@CNT nanocomposite, the flow rate of the argon carrier gas as well as the effect of the reaction time was investigated. A comparison of the EDX analysis obtained for nanocomposites synthesized at argon flow rates of 200 sccm and 600 sccm shows no significant difference in the composition (ESI Table S1†). To determine the effect of the reaction time on the composition of the nanocomposite selected reaction time intervals of 1 min, 5 min, and 30 min were chosen. The EDX analysis results of the therefrom obtained different nanocomposites are listed in ESI Table S2.† At a 5 min reaction time the reaction is complete, because for the reaction temperatures of 300 °C and 500 °C no significant difference in the composition is obtained at 5 min and 30 min reaction times. At a temperature of 400 °C and above the reaction rate is sufficient to convert the ZnO@CNT nanocomposite to a ZnS@CNT nanocomposite in about one minute. A further increase of the reaction time at these temperatures does not lead to a significant change in the composition of the nanocomposite. However, starting from a temperature of 650 °C it is interesting to observe that at a 30 min reaction time compared to a five-minute reaction time a significant decrease in the final sulfur content of the ZnS@CNT nanocomposite is observed. At 950 °C and a 30 min reaction time, this becomes even more significant as most sample areas which were studied by EDX analysis show a decreased sulfur content meaning that a non-stoichiometric form of ZnS is present in the nanocomposite. This could be attributed to the partial decomposition of the ZnS nanoparticles at high temperatures and at longer reaction times, a fact which has also been observed for other ZnS nanostructures.^{37,38} This partial decomposition might also be regarded as a pathway leading to

the formation of sulfur vacancies in ZnS. This has indeed been proven beneficial for photocatalysis.³⁴ In order to compare the photocatalytic activity of the ZnS@CNT nanocomposites with bare ZnS, a sample of ZnS nanoparticles was prepared independently. The thus formed ZnO was then converted to ZnS by reaction with hydrogen sulfide at 750 °C as it was the case for the conversion of the ZnO@CNT nanocomposite. The obtained nanoscaled ZnS powder was characterized by SEM, XRD and EDX indicating the formation of the wurtzite phase in the correct stoichiometry (ESI Fig. S5, S6 and S7†).

3.2. Photocatalytic activity

The ability to synthesize ZnS@CNT composites using a gas-phase conversion pathway has led to the possibility to synthesize a series of nanocomposites ranging from composition ZnO@CNT to ZnS/ZnO@CNT to ZnS@CNT the latter having different proportions of sphalerite and wurtzite phases where the proportion of the wurtzite phase increases with increasing conversion temperature. Thus, it was intriguing to compare these different nanocomposites with respect to their photocatalytic activity to obtain a more complete and systematic view of the behavior of such composite materials in photocatalysis especially towards the photocatalytic degradation of MO dye as a test reaction.

For the photocatalytic experiments, one mg of the respective nanocomposite was used. First, this photocatalyst was stirred for 2 h in the dark in a MO solution to enable the adsorption process to take place while reaching its equilibrium state. The different nanocomposites produced at different temperatures for 5 min were tested for their photocatalytic efficiency. The reaction kinetics for the degradation of MO dye was found to follow a pseudo-first-order kinetics as the plot of $\ln(C_0/C)$ against the time fits a linear relationship according to the following equation:

$$\ln(C_0/C) = kt, \quad (2)$$

where C_0/C is the ratio of the initial dye concentration at the beginning of the photocatalysis experiment to the dye concentration at time t , k is the apparent reaction rate constant in min^{-1} and t is the time in min.

Degradation of MO in the presence of different nanocomposites with varying composition ZnO@CNT, ZnS/ZnO@CNT and ZnS@CNT formed at different reaction temperatures was studied (Fig. 10 and ESI Fig. S8†). Interestingly, the pure ZnO@CNT nanocomposite does not show a significant photocatalytic activity under simulated sunlight conditions when compared to pristine CNTs or solely irradiated MO. Comparing the rate constants for the different composites the ZnO@CNT nanocomposite has the lowest photocatalytic activity with an apparent reaction rate constant of $3 \times 10^{-4} \text{ min}^{-1}$ (Fig. 10b). The ZnS/ZnO@CNT nanocomposite obtained at a reaction temperature of 350 °C showed an increase in the photocatalytic activity compared to the ZnO@CNT nanocomposite with a three-time increase in the apparent reaction rate constant ($k = 9 \times 10^{-4} \text{ min}^{-1}$). The ZnS@CNT nano-

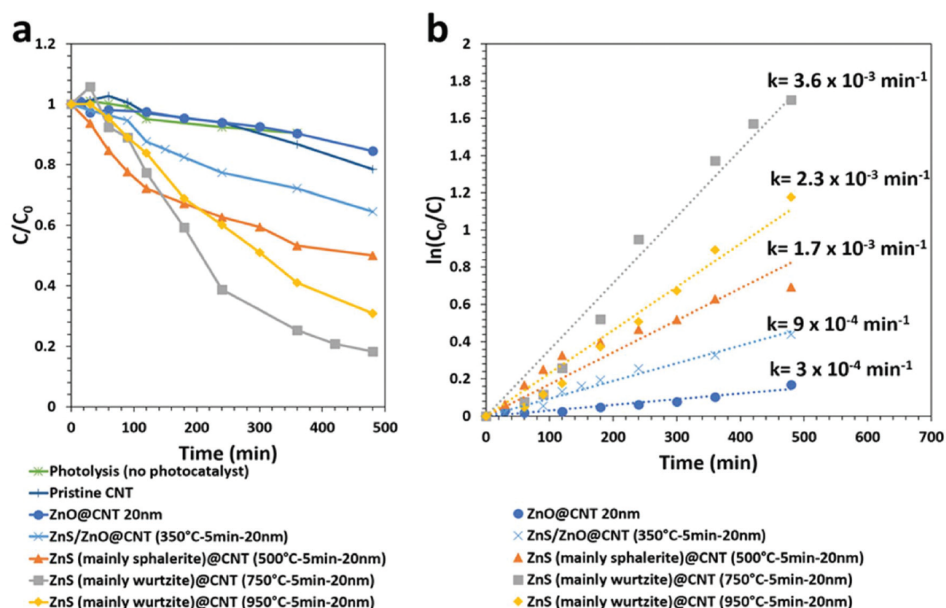


Fig. 10 (a) Photocatalytic degradation profile of MO dye employing different ZnO@CNT and ZnS@CNT photocatalysts formed at different temperatures under visible light irradiation, (b) pseudo-first-order kinetics of the degradation of MO using ZnO@CNT and ZnS@CNT photocatalysts under visible light irradiation for the determination of the apparent reaction rate constant.

composite (sphalerite phase) obtained at 500 °C showed a further increase in the photocatalytic activity with an apparent reaction rate constant of $1.7 \times 10^{-3} \text{ min}^{-1}$. Finally, the ZnS@CNT nanocomposite obtained at a reaction temperature of 750 °C and containing pure ZnS (wurtzite phase) showed a still even higher apparent reaction rate constant of $3.6 \times 10^{-3} \text{ min}^{-1}$ with a further two-fold increase over the latter. Density functional theory calculations carried out by Dong *et al.*³⁹ predicted the higher photocatalytic activity of the wurtzite phase of ZnS which is further substantiated with the present results. The ZnS@CNT nanocomposite finally obtained at 950 °C (5 min reaction time) however showed an unexpected decrease in the apparent reaction rate constant when compared to the sample obtained at 750 °C, whereas a further increase would have been expected. This could be due to severe particle aggregation of ZnS, at such high temperatures, which manifests itself in an increase of the crystallite size observed in XRD (Fig. 7) as well as SEM (see ESI Fig. S3†). At the same time, it was found that a mixture of the sphalerite phase and the wurtzite phase of ZnS would enhance the photocatalytic activity²⁴ which could be the case in the 750 °C sample when compared to the 950 °C sample which consists almost entirely of the wurtzite phase.

In a different set of experiments, different amounts of the 20 nm ZnS@CNT nanocomposite material obtained at 500 °C for 5 min were studied regarding its photocatalytic activity to determine how the increase of the photocatalyst amount would increase the apparent reaction rate constant (Fig. 11). A

five-fold increase in the nanocomposite from 1 mg to 5 mg led to a three-fold increase in the apparent reaction rate constant from $1.7 \times 10^{-3} \text{ min}^{-1}$ to $5.1 \times 10^{-3} \text{ min}^{-1}$. This shows that there is potential for obtaining even higher reaction rates by increasing the nanocomposite amount.

In addition the effect of particle size on the different ZnS@CNT nanocomposites was investigated. Therefore 5 nm ZnO was deposited by ALD onto the VACNT material and finally converted to ZnS at 500 °C and 750 °C in order to obtain the ZnS@CNT composite material and compare its photocatalytic activity with the photocatalytic activity obtained for the same ZnS@CNT nanocomposites, however with 20 nm particle size. From Fig. 12 it can be seen that the degradation rates for MO using the ZnS@CNT nanocomposites produced under the same conditions but with different particle sizes do not differ significantly. Nevertheless, the ZnS@CNT nanocomposites with 5 nm ZnS show a slightly smaller reaction rate constant when compared to the ZnS@CNT composite containing the 20 nm ZnS particles. This could be attributed to the lower loading of ZnS onto the CNT structure compared to the ZnS@CNT material with 20 nm ZnS particle size.

Finally, the ZnS@CNT composite obtained at 950 °C and a 30 min reaction time was studied in order to see whether an increased number of sulfur vacancies in ZnS would further enhance the photocatalytic activity due to the formation of midgap defect states, which would influence the visible light absorption (Fig. 13).^{24,34} Indeed, the apparent reaction rate constant for the ZnS@CNT photocatalyst formed at 950 °C and

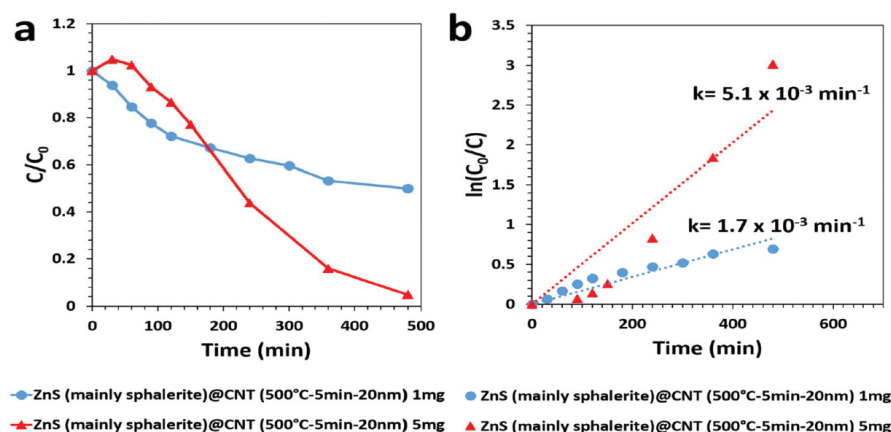


Fig. 11 (a) Degradation profile of MO dye using different amounts of ZnS@CNT photocatalysts formed at 500 °C for 5 min under visible light irradiation, (b) rate constant of the pseudo-first-order kinetics of the degradation of MO under visible light irradiation using different amounts of ZnS@CNT photocatalysts formed at 500 °C for 5 min.

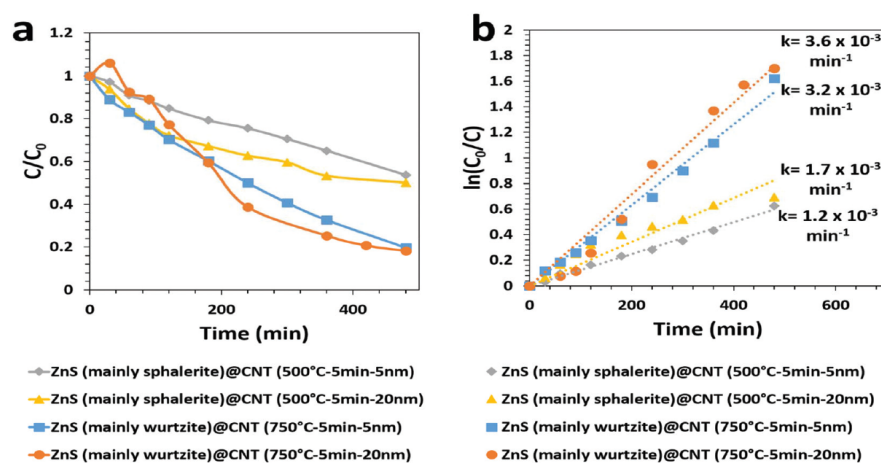


Fig. 12 (a) Degradation profile of MO dye using ZnS@CNT photocatalysts obtained at 500 °C and 750 °C for 5 min having different particle sizes, (b) determination of the reaction rate constants of the pseudo-first-order kinetics of the degradation of MO under visible light irradiation using ZnS@CNT photocatalysts obtained at 500 °C and 750 °C for 5 min having different particle sizes.

30 min is about three times higher than that for the respective ZnS@CNT photocatalyst formed at 950 °C for 5 min. The apparent reaction rate constant of $6.6 \times 10^{-3} \text{ min}^{-1}$ is the highest obtained for all ZnS@CNT photocatalysts. This substantiates the high potential of combining ZnS with a higher degree of sulfur vacancies together with CNTs in such photocatalytic applications.

The recyclability of the photocatalyst is a crucial factor which should be considered for an ideal photocatalyst. To test the recyclability of the synthesized nanocomposites, one mg of the ZnS@CNT nanocomposite synthesized at 500 °C for 5 min was taken as an example for performing three successive

cycles (Fig. 14). As can be seen the photocatalytic activity of the nanocomposite increases from the first to the third cycle which can be attributed to the increased dispersion of the nanocomposite in the dye solution with increasing cycle number. The increased dispersion thus leads to a higher surface area in contact with the dye solution which results in an increased degradation of the dye. The TEM images of the ZnS@CNT nanocomposite synthesized at 750 °C for 5 min before and after one photocatalysis cycle show a slight decrease in the particle loading which could be due to the detachment of some nanoparticles from the CNTs (ESI Fig. S9†).

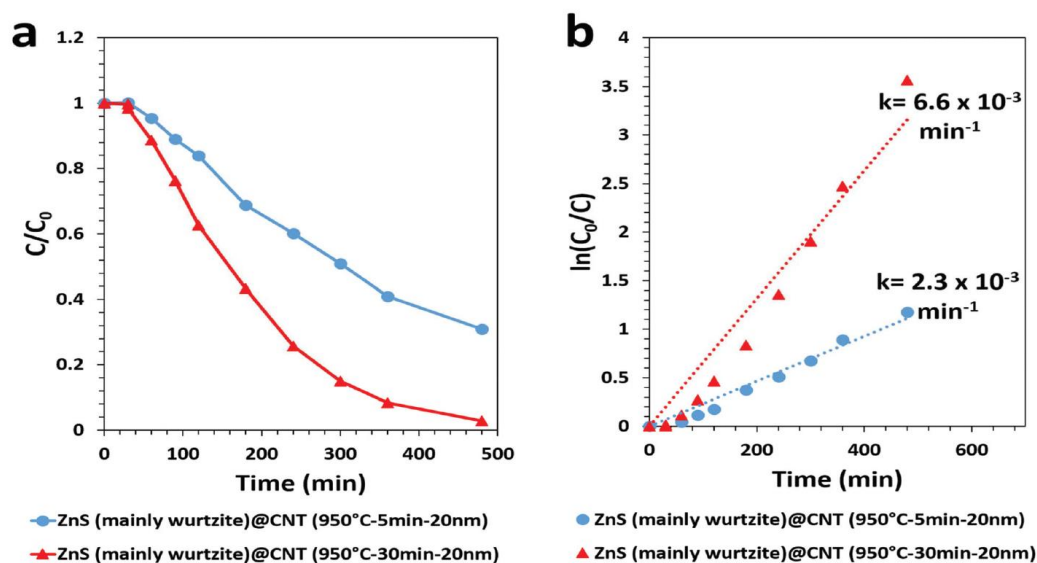


Fig. 13 (a) Degradation profile of MO dye using ZnS@CNT photocatalysts obtained at 950 °C for 5 min and 950 °C for 30 min under visible light irradiation, (b) rate constant determination of the pseudo-first-order kinetics of the degradation of MO under visible light irradiation using ZnS@CNT nanocomposites produced at 950 °C for 5 min and 950 °C for 30 min.

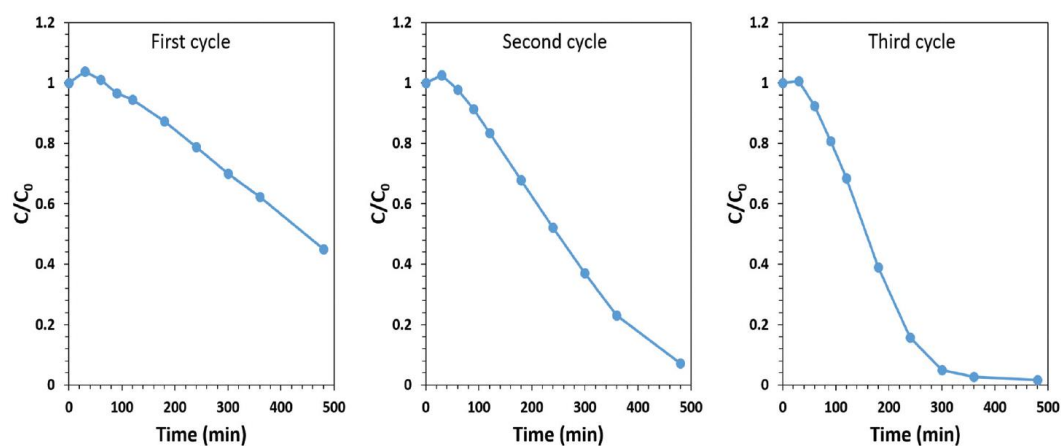


Fig. 14 Three cycles using the ZnS@CNT nanocomposite synthesized at 500 °C for 5 min for the photocatalytic degradation of MO.

As sunlight contains a small fraction of UV-light and a large fraction of visible and infrared light it should be noted that the synthesized nanocomposites make use of all these fractions. The UV-light is mainly absorbed by the nanoparticles as these are wide band-gap semiconductors and their absorption of the UV part results in exciton formation. In order to prevent the quick recombination of the generated electron-hole pair, which is disadvantageous for the photocatalytic performance, the CNT structure is able to act as an electron sink. This results in quick electron transfer from the conduction band of

the semiconductor to the CNT resulting in efficient electron-hole separation and preventing charge carrier recombination. In the case of visible light absorption, it is absorbed by the CNT material in which the electrons are excited and are transferred to the conduction band of the semiconductor nanoparticles. The electron deficiency generated by visible light absorption in the CNT material is neutralized by transfer of an electron from the valence band of the semiconductor nanoparticle to the CNT thus leaving a hole. It is well-known that the electron-hole pair formed participates in reduction and

oxidation reactions leading to the formation of superoxide anions and hydroxyl radicals in aqueous solution, respectively. These radicals may then attack the organic pollutant leading to its degradation.^{40,41} The synthesis pathway using ALD deposition is an additional advantage for the photocatalytic activity of the produced nanocomposite due to the intimate contact between the semiconductor and the CNT surface which needs no further functionalization for attaching ZnO and ZnS to the surface.¹⁴ However, the reason for the very low activity of the ZnO@CNT as well as the mixed ZnS/ZnO@CNT composite in comparison with the ZnS@CNT nanocomposites still needs further investigation.

4. Conclusion

The work presented herein describes a systematic study on the formation of ZnO@CNT, mixed ZnS/ZnO@CNT and ZnS@CNT containing sphalerite and wurtzite modifications in different compositions by a combination of ALD and solid/gas phase conversion and their subsequent photocatalytic efficiency in the degradation of an organic model compound. Employing the ALD approach it was possible to control the nanoparticle size on the CNT host by using a defined number of cycles in the atomic layer deposition process. Furthermore, we have devised a straightforward way to convert a ZnO@CNT nanocomposite into a mixed phase ZnS/ZnO@CNT or a pure ZnS@CNT nanocomposite showing an increasing amount of the ZnS wurtzite phase on the CNT when increasing the conversion temperature in the gas-phase conversion process. At the same time, the different zinc chalcogenide semiconductor CNT composites showed good photocatalytic activity under simulated sunlight conditions. ZnS@CNT with a high amount of the wurtzite phase and ZnS@CNT with ZnS containing sulfur vacancies showed the highest photocatalytic efficiency.

Acknowledgements

TEM studies were performed at the Ernst-Ruska Center (ERC) at Forschungszentrum (FZ) Jülich under the contract ERC-TUD1. We thank Dr R. Hoffmann for TGA-MS analysis as well as D. J. Babu, S. Yadav and S. Heinschke (all Eduard-Zintl-Institut für Anorganische und Physikalische Chemie) for providing the CNT materials for this study and for XRD measurements (SH). SO acknowledges the DAAD for support through the GERLS scholarship program (funding program number 57030312).

References

- 1 L. Li, X. Huang, T. Hu, J. Wang, W. Zhang and J. Zhang, *New J. Chem.*, 2014, **38**, 5293–5302.
- 2 X. Pan, Y. Zhao, S. Liu, C. L. Korzeniewski, S. Wang and Z. Fan, *ACS Appl. Mater. Interfaces*, 2012, **4**, 3944–3950.
- 3 Y. Lin, D. Li, J. Hu, G. Xiao, J. Wang, W. Li and X. Fu, *J. Phys. Chem. C*, 2012, **116**, 5764–5772.
- 4 C. Hariharan, *Appl. Catal., A*, 2006, **304**, 55–61.
- 5 J.-S. Hu, L.-L. Ren, Y.-G. Guo, H.-P. Liang, A.-M. Cao, L.-J. Wan and C.-L. Bai, *Angew. Chem., Int. Ed.*, 2005, **44**, 1269–1273.
- 6 T. K. Tran, W. Park, W. Tong, M. M. Kyi, B. K. Wagner and C. J. Summers, *J. Appl. Phys.*, 1997, **81**, 2803–2809.
- 7 H. C. Ong and R. P. H. Chang, *Appl. Phys. Lett.*, 2001, **79**, 3612–3614.
- 8 C. Belder, R. Bellod, S. J. Stewart, F. G. Requejo and M. Fernández-García, *Appl. Catal., B*, 2006, **65**, 309–314.
- 9 Z.-D. Meng, S. Sarkar, L. Zhu, K. Ullah, S. Ye and W.-C. Oh, *Synth. React. Inorg., Met.-Org., Nano-Met. Chem.*, 2015, **45**, 1373–1379.
- 10 Y. Yu, J. C. Yu, J.-G. Yu, Y.-C. Kwok, Y.-K. Che, J.-C. Zhao, L. Ding, W.-K. Ge and P.-K. Wong, *Appl. Catal., A*, 2005, **289**, 186–196.
- 11 T. A. Saleh, The Role of Carbon Nanotubes in Enhancement of Photocatalysis, in *Syntheses and Applications of Carbon Nanotubes and Their Composites*, ed. S. Suzuki, InTech, 2013, ch. 21, pp. 479–493. Available from: <http://www.intechopen.com/books/syntheses-and-applications-of-carbon-nanotubes-and-their-composites/the-role-of-carbon-nanotubes-in-enhancement-of-photocatalysis>.
- 12 F. Yu, J. Ma and S. Han, *Sci. Rep.*, 2014, **4**, 5326.
- 13 A. Naeimi, A. M. Arabi, M. Shafiee Afarani and A. R. Gardeshzadeh, *J. Mater. Sci.: Mater. Electron.*, 2015, **26**, 1403–1412.
- 14 S.-a. Feng, J.-h. Zhao and Z.-p. Zhu, *New Carbon Mater.*, 2008, **23**, 228–234.
- 15 H. Wu, Q. Wang, Y. Yao, C. Qian, X. Zhang and X. Wei, *J. Phys. Chem. C*, 2008, **112**, 16779–16783.
- 16 G. Wan and G. Wang, *J. Optoelectron. Biomed. Mater.*, 2015, **7**, 85–91.
- 17 Z. Fang, Y. Fan and Y. Liu, *Front. Optoelectron. China*, 2011, **4**, 121–127.
- 18 X. Peng, J. Chen, J. A. Misewich and S. S. Wong, *Chem. Soc. Rev.*, 2009, **38**, 1076–1098.
- 19 M. Rahimi, D. J. Babu, J. K. Singh, Y.-B. Yang, J. J. Schneider and F. Müller-Plathe, *J. Chem. Phys.*, 2015, **143**, 124701.
- 20 R. Joshi, J. Engstler, L. Houben, M. Bar Sadan, A. Weidenkaff, P. Mandaliev, A. Issanin and J. J. Schneider, *ChemCatChem*, 2010, **2**, 1069–1073.
- 21 Y.-S. Min, I. H. Lee, Y. H. Lee and C. S. Hwang, *CrystEngComm*, 2011, **13**, 3451–3454.
- 22 F. Huang and J. F. Banfield, *J. Am. Chem. Soc.*, 2005, **127**, 4523–4529.
- 23 H. Zhang, F. Huang, B. Gilbert and J. F. Banfield, *J. Phys. Chem. B*, 2003, **107**, 13051–13060.
- 24 Z. Fang, S. Weng, X. Ye, W. Feng, Z. Zheng, M. Lu, S. Lin, X. Fu and P. Liu, *ACS Appl. Mater. Interfaces*, 2015, **7**, 13915–13924.

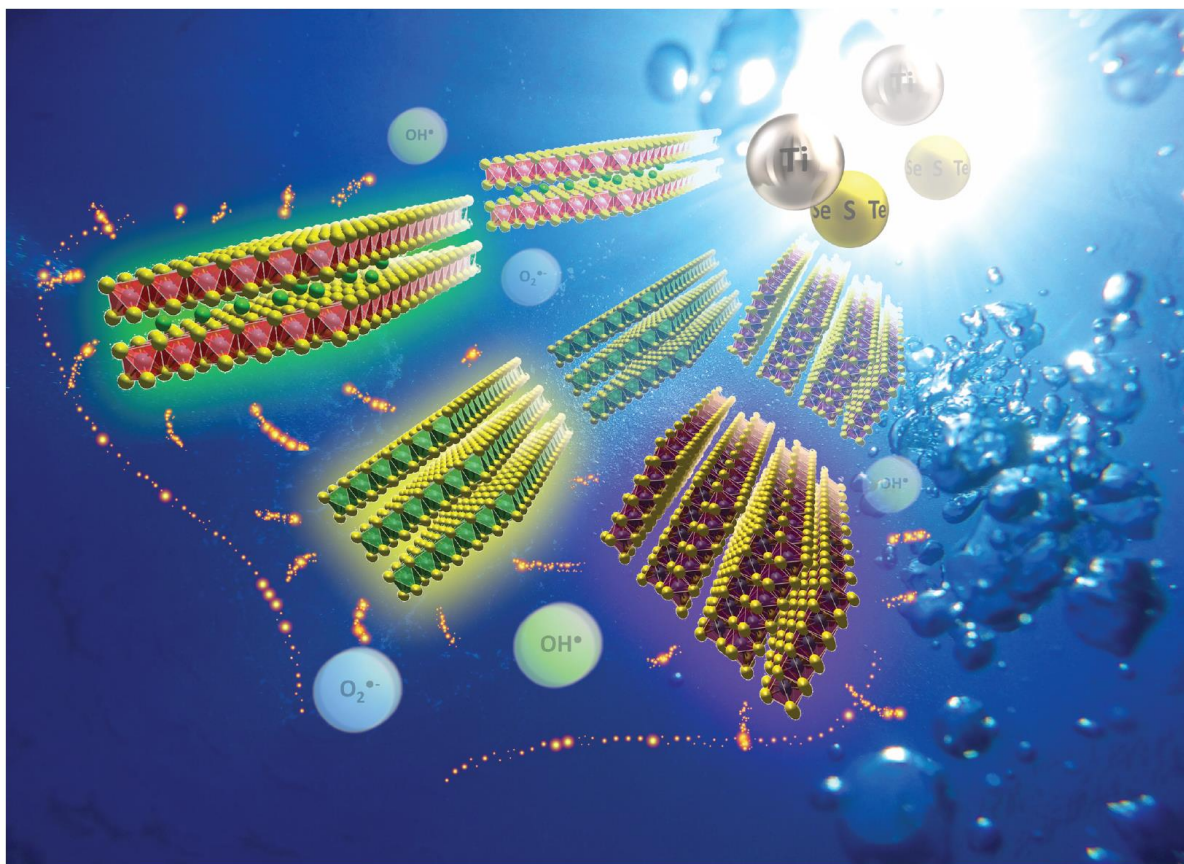
- 25 H. B. Ahn and J. Y. Lee, *CrystEngComm*, 2013, **15**, 6709–6714.
- 26 X. Huang, M. Wang, M.-G. Willinger, L. Shao, D. S. Su and X.-M. Meng, *ACS Nano*, 2012, **6**, 7333–7339.
- 27 W. H. Nam, Y. S. Lim, W.-S. Seo, H. K. Cho and J. Y. Lee, *J. Nanopart. Res.*, 2011, **13**, 5825–5831.
- 28 Y. Wang, Q. Guo, S. Lin, B. Chen and D. Zheng, *J. Phys.: Conf. Ser.*, 2009, **152**, 012018.
- 29 L. Neveux, D. Chiche, D. Bazer-Bachi, L. c. Favergeon and M. l. Pijolat, *Chem. Eng. J.*, 2012, **181–182**, 508–515.
- 30 W. Chen, H. Ruan, Y. Hu, D. Li, Z. Chen, J. Xian, J. Chen, X. Fu, Y. Shao and Y. Zheng, *CrystEngComm*, 2012, **14**, 6295–6305.
- 31 M. Ishida and C. Y. Wen, *Chem. Eng. Sci.*, 1971, **26**, 1031–1041.
- 32 A. Cabot, M. Ibáñez, P. Guardia and A. P. Alivisatos, *J. Am. Chem. Soc.*, 2009, **131**, 11326–11328.
- 33 J. M. Won, J. H. Kim, Y. J. Choi, J. S. Cho and Y. C. Kang, *J. Alloys Compd.*, 2016, **671**, 74–83.
- 34 G. Wang, B. Huang, Z. Li, Z. Lou, Z. Wang, Y. Dai and M.-H. Whangbo, *Sci. Rep.*, 2015, **5**, 8544.
- 35 M. Olek, T. Büsgen, M. Hilgendorff and M. Giersig, *J. Phys. Chem. B*, 2006, **110**, 12901–12904.
- 36 A. Cao, Z. Liu, S. Chu, M. Wu, Z. Ye, Z. Cai, Y. Chang, S. Wang, Q. Gong and Y. Liu, *Adv. Mater.*, 2010, **22**, 103–106.
- 37 K. Ravichandran and D. Nedumaran, *Int. J. Mech. Eng. Mater. Sci.*, 2011, **4**, 25–31.
- 38 S. C. Kim, J. W. Kim, H.-S. Chung, D. H. Kim and K. H. Oh, *J. Korean Phys. Soc.*, 2009, **55**, 978–981.
- 39 M. Dong, J. Zhang and J. Yu, *APL Mater.*, 2015, **3**, 104404.
- 40 M. Samadi, H. A. Shivace, M. Zanetti, A. Pourjavadi and A. Moshfegh, *J. Mol. Catal. A: Chem.*, 2012, **359**, 42–48.
- 41 W. Wang, P. Serp, P. Kalck and J. L. s. Faria, *J. Mol. Catal. A: Chem.*, 2005, **235**, 194–199.

2.2 Photothermal catalytic properties of layered titanium chalcogenide nanomaterials

Layered materials possess interesting properties for photocatalytic applications as they can be easily exfoliated forming two-dimensional materials which offer a large surface area and enable efficient charge separation as the photo-induced charge carriers reach the surface quickly before recombining in the bulk, thus being more available for photocatalytic reactions at the surface. Many transition metal chalcogenides have a layered structure owing to their unique crystal structure which consists of layers hold together by weak van der Waals interactions which can be easily overcome to produce atomically thick two-dimensional materials through exfoliation. In contrast to the wide band gap titanium dioxide, other titanium chalcogenides where the chalcogen is S, Se or Te are known to possess much smaller band gaps and they spontaneously form as two-dimensional materials owing to their unique crystal structure which makes it very interesting to investigate a series of these compounds for photocatalytic applications.

In this work, a series of titanium chalcogenides TiX_n ($X=S$, $n=1-3$; $X=Se$, $n=2$; $X=Te$, $n=1$) have been synthesized through a chemical vapor transport technique from their elements and the resulting materials were investigated for their photocatalytic properties towards the degradation of methyl orange as model pollutant under simulated sunlight. For the synthesis of titanium sulfides different parameters were investigated as the ratio of elements used as starting material, the reaction time and temperature where a range of different titanium sulfides (TiS_3 , TiS_2 , low temperature titanium monosulfide (lt-TiS) and high temperature titanium monosulfide (ht-TiS)) were obtained. In depth characterization of the titanium sulfides revealed that the “titanium monosulfides” were defective titanium disulfides where excess titanium was occupying the interstitials within the van der Waals gaps of the layered structure with a general formula $Ti_{1+x}S_2$. This shows that by tuning the reactants ratio together with other synthesis parameters like temperature and time a whole range of materials with different properties can be prepared.

Photocatalytic testing of these materials showed that especially TiS_3 , lt-TiS and ht-TiS have high photocatalytic activity. Investigations also revealed that these materials possess besides their photocatalytic activity also a thermocatalytic activity where solely heat is sufficient to induce the degradation process of the dye in presence of the catalyst. Thus, a synergistic effect from their photocatalytic and thermocatalytic activity is achieved. These materials also showed excellent recyclability, which was attributed to the surface oxidation of the titanium sulfides forming titanium sulfide/titanium oxide core-shell heterostructures with time which further enables a spatial separation of the formed photo-induced charge carriers thus increasing the photocatalytic activity of the material even more.

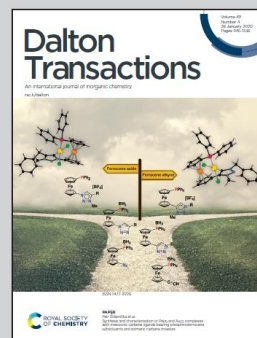


Showcasing materials research from the Schneider lab at the Technische Universität Darmstadt, Germany.

Photothermal catalytic properties of layered titanium chalcogenide nanomaterials

In extension to our research on CNT/metal chalcogenide photocatalysts we have studied titanium chalcogenides as interesting alternatives to traditional titanium dioxide. A systematic investigation of the photothermal catalytic properties of various titanium chalcogenides revealed a high activity especially of non-stoichiometric titanium sulfides as well as titanium trisulfide. This may open a door for the design of highly active titanium chalcogenide based photocatalysts.

As featured in:



See Jörg J. Schneider *et al.*, *Dalton Trans.*, 2020, **49**, 1032.

Cite this: *Dalton Trans.*, 2020, **49**,
1032Photothermal catalytic properties of layered
titanium chalcogenide nanomaterials†‡Sherif Okeil,[§] Sandeep Yadav,[§] Michael Bruns,^b Alexander Zintler,^c
Leopoldo Molina-Luna^c and Jörg J. Schneider^{§*}

The search for novel photocatalysts that make use of almost the entire solar spectrum remains an ongoing task to achieve high efficiency in energy conversion. While titanium chalcogenides offer a variety of phase compositions with different photophysical properties, their photocatalytic performance in pollutant degradation has not been investigated to date. In contrast to the model photocatalyst titanium dioxide, titanium chalcogenides possess small band gaps which make them eligible to absorb light in the visible range up to the near-infrared region, thus making them interesting candidates for photocatalysis. Herein titanium chalcogenide-based photocatalysts are synthesized by the chemical vapor transport (CVT) method and studied for their photocatalytic activity towards pollutant degradation. A series of titanium chalcogenides TiX_n ($X = S, n = 1-3$; $X = Se, n = 2$; $X = Te, n = 1$) have been characterized by a variety of physico-chemical methods. Due to the expected non-stoichiometry of some titanium sulfides, they offer a large number of defect states which make them interesting candidates for photocatalysis. Thus, these titanium-chalcogenides were systematically studied for the photocatalytic degradation of pollutants using methyl orange dye as the test pollutant under simulated sunlight. Particularly TiS and TiS_3 show high photocatalytic and thermocatalytic activity, outperforming the activity of titanium dioxide (pure anatase). By controlling the ratios of titanium and chalcogen elements and the specific reaction conditions, a variety of titanium chalcogenides with different compositions and phases showing a high photocatalytic activity can be accessed. Furthermore, it is found that the formation of a titanium dioxide passivation layer during photocatalysis results in a titanium oxide/titanium sulfide heterostructure. This allows further enhancement of the photocatalytic and thermocatalytic activity compared to the bare Ti-chalcogenides.

Received 25th September 2019,
Accepted 2nd December 2019

DOI: 10.1039/c9dt03798e

rsc.li/dalton

Introduction

The use of solar energy as a clean energy source for water purification and detoxification through photocatalytic removal of organic pollutants has been recognized as an important research area over the last few decades. A lot of effort has gone into the search for potential materials that are able to utilize most of the solar spectrum for an efficient photocatalysis process.¹ Titanium dioxide is a model photocatalyst that has been intensively investigated for its activity due to its stability,

abundance, nontoxicity and cost-effectiveness.^{2,3} The main drawback of titanium oxide is that it is mainly active under ultraviolet light due to its wide band gap (3.2 eV for anatase and 3.0 eV for the rutile phase)³ and thus is not making use of the whole spectrum of sunlight which consists of 4% UV-A radiation (320–400 nm, 3.88–3.09 eV), 53% visible light (400–800 nm, 3.09–1.55 eV) and 43% IR radiation (>800 nm, <1.55 eV).^{4,5} Several approaches have been used in order to modify the band gap of titanium dioxide to make use of visible light, such as metal doping, non-metal doping, modification with metal nanoparticles, modification with visible-light-absorbing dyes, inducing defects and its inclusion in heterostructures.^{1,3,6} Particularly the so-called black titanium dioxide has become a hot topic since its first synthesis by Chen *et al.*⁷ who relied on the fact that the hydrogenation of pure white titanium dioxide results in the formation of a disordered shell on the titanium dioxide particles leading to its black appearance. This led to an efficient reduction of the band gap to 1.54 eV which extended the absorption into the visible and infrared region of the sunlight spectrum resulting in a significant enhancement of the photocatalytic activity.

^aEduard-Zintl-Institut für Anorganische und Physikalische Chemie,
Technische Universität Darmstadt, Alarich-Weiss-Straße 12, 64287 Darmstadt,
Germany. E-mail: joerg.schneider@ac.chemie.tu-darmstadt.de

^bInstitut für Angewandte Materialien (IAM-ESS), Karlsruher Institut für Technologie,
Hermann-von-Helmholtz-Platz 1, B 321, D-76344 Eggenstein-Leopoldshafen, Germany

^cFachbereich Material- und Geowissenschaften, Technische Universität Darmstadt,
64287 Darmstadt, Germany

† Dedicated to Prof. Manfred Scheer on the occasion of his 65th birthday.

‡ Electronic supplementary information (ESI) available. See DOI: 10.1039/
C9DT03798E

§ Both authors contributed equally to this work.

Due to the efficiency of titanium-based materials in photocatalysis and the intense research into their modification to achieve even better photocatalytic behavior, it appears highly interesting to study other non-oxygen containing titanium chalcogenide-based materials and to assess their photocatalytic activity. This could pave the way for finding new and efficient photocatalysts operating under visible light. To the best of our knowledge, the heavier titanium chalcogenides where the chalcogen elements are S, Se and Te have not been reported for their photocatalytic activity in pollutant degradation to date. Theoretical band gap calculations of different titanium chalcogenides determine a narrow band gap, for example, $E_g < 1.2$ eV for TiS_3 ^{8–10} and $E_g < 2$ eV for titanium dichalcogenides (TiS_2 , TiSe_2 and TiTe_2),¹¹ which shows that these materials could have a potential for visible light or even IR-driven photocatalysis.

Moreover, it is known that two-dimensional nanostructures lead to better charge separation resulting in higher photocatalytic activity.¹² Consequently, two dimensional titanium dioxide sheets have been studied for their photocatalytic applications.¹³ The improved charge separation efficiency of two-dimensional materials, compared to the respective bulk material, can be ascribed to a lower bulk diffusion of any photogenerated charge carriers which allow them to reach the surface much faster, thus reducing the risk of exciton bulk recombination.^{14,15} An important characteristic of transition metal chalcogenides is that they often possess a bulk structure that is composed of sandwiched layered components that can be individually exfoliated to form isolated two-dimensional materials.^{2,16}

Belt like titanium trisulfide morphologies have been synthesized and have shown effective performance in energy storage,^{17–19} transistors^{20,21} and photoelectrocatalysis for hydrogen generation.^{22,23} Titanium trisulfide nanobelts have also been used as sacrificial templates for the production of different TiS_{2-x} nanobelt morphologies preserving the overall two-dimensional structure.²⁴ All this makes it interesting to investigate titanium chalcogenides (S, Se, Te) with a lamellar structure for photocatalysis.

In non-stoichiometric materials where vacancies and defects exist, typically the photocatalytic activity is increased as the vacancies can act as effective surface electron trapping sites, thus further enhancing the necessary charge separation for efficient performance.²⁵ Furthermore, vacancies and defects produce intermediate states in the band gap of the material, thus extending its absorption edge to longer wavelengths.²⁶ Particularly for titanium disulfide it is well-known that on the one hand an exact stoichiometry is hard to control, and on the other hand such a non-stoichiometric composition possesses interesting properties.²⁴ Therefore, a study of the photocatalytic behavior of non-stoichiometric titanium sulfides seems justified in order to test the importance of vacancies and defects for the photocatalysis of such titanium-chalcogenide-based photocatalysts that differ chemically and structurally from the well-investigated titanium dioxide. Thus, herein the first in depth investigation of the use of different

titanium chalcogenides for photocatalysis has been undertaken. Our work could be useful to shed light on new potentially active photocatalyst materials based on titanium. These could then even be employed for the design of different heterostructures, which could allow further improvement in their photocatalytic activity as shown in this study in which a partial surface oxidation of titanium sulfides leads to the formation of titanium oxide/titanium sulfide heterostructures, which is accompanied by a further increase in the photocatalytic activity. A previous study by Ranjith *et al.*²⁷ showed that the sulfidation of TiO_2 nanofibers leads to the formation of a thin TiS_3 shell, thus forming a heterostructure that promotes carrier separation and decreases the exciton recombination rate resulting in an enhanced photocatalytic activity. Whereas the sulfidation process of titanium dioxide is difficult due to the oxophilic nature of titanium, the surface oxidation of titanium chalcogenides would provide a simple approach to obtain titanium oxide/titanium chalcogenide heterostructures for improved photocatalysis. As shown in the following study, such heterostructures could be readily formed during their use in subsequent photocatalytic cycles, which results in an improvement in the photocatalytic performance.

Materials and methods

Synthesis of titanium chalcogenides

Titanium powder (abcr 99.5%, ~325 mesh), sulfur powder (Sigma-Aldrich 99.998%), selenium granules (EVOCHEM 99.999%, 1–5 mm) and tellurium powder (abcr 99.99%, ~325 mesh) were used as received. Different titanium chalcogenides were synthesized according to general procedures using chemical vapor transport (CVT) following previously published methods;^{22,28–30} titanium and the respective chalcogen powder with the required ratio were mixed and ground together in a mortar. The well mixed powder was then used to produce a pellet using a manual hydraulic press under 10 tons load for 10 min. The resulting pellet containing titanium and the respective chalcogen was then inserted in one end of a quartz ampule together with about 5 mg of iodine which was used as the transport medium and the ampule was sealed under a vacuum of 10^{-3} mbar. This ampule was placed in an oven and heated slowly to the desired temperature which was held for a certain period of time and then allowed to cool slowly to room temperature. After cooling to room temperature, the titanium chalcogenide either formed on the other end of the ampule or at the same position of the initial pellet. For the preparation of different titanium sulfides, different molar ratios of the element powder were used: for titanium trisulfide a molar ratio of Ti : S of 1 : 3, for titanium disulfide a molar ratio of 1 : 2 and for titanium monosulfide a molar ratio of 1 : 1.

For the preparation of titanium trisulfide 0.33 g of titanium were mixed with 0.67 g of sulfur powder to form the pellet. The ampule was heated up to 550 °C within 5 h and held at that temperature for 48 h before cooling down. In the case of

titanium disulfide 0.43 g of titanium was mixed with 0.57 g of sulfur to produce the pellet. The ampule was then heated up to 750 °C within 7 h and held at that temperature for 48 h before cooling. For titanium monosulfide a molar ratio of 1 : 1 was used corresponding to 0.60 g of titanium and 0.40 g of sulfur which were mixed for the preparation of the pellet. For low temperature titanium monosulfide (lt-TiS) the ampule was heated up to 450 °C within 4 h and this temperature was held for 48 h before cooling down. For high temperature titanium monosulfide (ht-TiS) a temperature of 900 °C was achieved in 9 h and maintained for 6 h only before cooling down to room temperature.

For the preparation of titanium selenide and titanium telluride 0.23 g of titanium were mixed with 0.77 g of selenium powder and 0.16 g of titanium were mixed with 0.84 g of tellurium to form the pellet, respectively. The ampules containing the titanium–selenium and titanium–tellurium mixtures were heated to 800 °C over a 8 h period and 750 °C over a 7 h period and maintained for 72 h, respectively.

Post-treatment of titanium trisulfide to introduce sulfur vacancies

Titanium trisulfide was used as a starting material to obtain several non-stoichiometric titanium sulfides through the removal of sulfur under argon atmosphere at 450 °C for different time intervals. Titanium trisulfide powder was placed in a quartz boat inside a quartz tube and heated in a tube furnace (Horst GmbH tube furnace, 500 mm length and 50 mm inner diameter with a NiCr–Ni temperature sensor and HT MC1 microprocessor temperature regulator) to 450 °C under a flow of 250 sccm argon. The temperature was held for 20 min, 40 min and 60 min to produce three different samples TiS_{3-x}/20 min, TiS_{3-x}/40 min and TiS_{3-x}/60 min with different sulfur contents. The removed sulfur could be clearly observed as yellow deposition at the cold end of the quartz tube which gave evidence of the efficient removal of sulfur from titanium trisulfide in these short time periods.

Characterization

Scanning electron microscopy of the synthesized titanium chalcogenides was performed on a Philips XL-30 FEG coupled with an energy-dispersive X-ray (EDX) analyzer for element analysis using an electron beam at 20 kV as accelerating voltage. Thermogravimetric analysis (TGA) measurements of the different titanium sulfides for the determination of their bulk composition were performed using a TG209F1-Iris (Netzsch) thermal analyzer, employing aluminum crucibles. The samples were heated at a rate of 10 K min⁻¹ till 800 °C under oxygen atmosphere and this temperature was held for one hour to ensure complete conversion to stoichiometric titanium dioxide.

XPS characterization of the titanium chalcogenide powder samples was performed using a K-Alpha XPS spectrometer (ThermoFischer Scientific, East Grinstead, UK) equipped with a microfocused, monochromated Al K_α X-ray source (400 μm spot size). Data acquisition and processing was done using the Thermo Advantage software. The K-Alpha charge compensation

system was employed during analysis, using electrons of 8 eV energy and low-energy argon ions to prevent any localized charge build-up. The charge shift correction was employed using a C 1s electron binding energy of 285.0 eV.

The synthesized titanium chalcogenides were characterized using X-ray diffraction (XRD) which was performed on a Rigaku Miniflex 600@40 kV 15 mA diffractometer using Cu K_{α1} radiation ($\lambda = 1.541 \text{ \AA}$). Transmission electron microscopy (TEM) was performed using JEOL ARM-200F operated at 200 kV. TEM samples were prepared from the powdered samples obtained through grinding followed by ultrasonically dispersing about 20 mg of the powder in about 10 mL ethanol for 15 hours. The obtained dispersion was then drop cast on a holey carbon grid. Images and selected area electron diffraction (SAED) patterns were recorded on a Gatan US1000. Energy dispersive X-ray spectra (TEM-EDX) were recorded on a JEOL JED-2300 60 mm² detector.

Raman spectra of the different titanium chalcogenides were recorded on a Horiba Jobin-Yvon LabRAM HR800 micro-Raman spectrometer using a 632.8 nm HeNe laser with a 50× LWD objective (NA = 0.5) and 20 s acquisition time.

UV-VIS-NIR diffuse reflectance spectroscopy (UV-VIS-NIR DRS) of the synthesized titanium chalcogenides was performed with an integrating sphere on a PerkinElmer Lambda 900 UV-VIS-NIR spectrophotometer using the Kubelka–Munk function to obtain the corresponding absorption spectra.

Photocatalytic activity measurement

The photocatalytic activity of the different titanium chalcogenides was tested using methyl orange (MO) (ACS, Reag. Ph Eur, Merck) as a model pollutant. The details of the performed experiments can be found elsewhere.³¹ In short, the prepared test solution consisted of 0.02 mg mL⁻¹ MO, 0.001 M HCl and 0.035% (w/w) hydrogen peroxide. The test solution was mixed together with 1 mg of the photocatalyst to be tested in a quartz test tube and was left for 2 hours in the dark to reach adsorption equilibrium. After that the test solution was illuminated with a lamp simulating sunlight (Exo Terra Solar Glo® mercury vapor bulb, 150 W) at a 10 cm distance. At predefined time intervals samples were drawn from the test solution and analyzed by UV-VIS to determine the amount of the remaining MO. The change in the absorption maximum of the MO solution at 503 nm was monitored and the ratio C/C_0 was plotted against the photocatalysis time, where C/C_0 denotes the ratio of the concentration of MO at the sampling time to the initial concentration of MO when the photocatalysis experiment started. The photocatalytic activity of the different synthesized titanium chalcogenides was compared to commercial anatase TiO₂ (EMPROVE® ESSENTIAL Ph Eur, BP, USP, JP, E 171, Merck).

Results and discussion

Materials synthesis and characterization

Transition-metal dichalcogenides (MX₂) and transition-metal trichalcogenides (MX₃) are known to possess a sheet like

arrangement composed of the layers of chalcogen–metal–chalcogen (X–M–X) which are held together by van der Waals forces. This makes it easy to cleave the crystal along the horizontal axis perpendicular to the crystal symmetry axis to obtain few-layered or even single layered flakes by breaking the van der Waals forces acting between these layers. The titanium-based transition-metal dichalcogenides TiS_2 , TiSe_2 and TiTe_2 have a hexagonal CdI_2 -type structure where one layer is formed of a transition-metal plane sandwiched between two planes of chalcogen atoms (Fig. 1a).^{24,32,33} Titanium trisulfide (TiS_3) which belongs to the layered transition-metal trichalcogenides has a monoclinic ZrSe_3 -type structure having the space group $P2_1/m$ where two of the three sulfur atoms per unit formula contain a S–S bond, resulting in disulfide anion species (S_2^{2-}) forming a triangular base parallel to the crystal a -axis and pointing towards the interlayer gap where weak van der Waals interactions hold the layers together (Fig. 1b).^{34,35} In the case of titanium trisulfide, trigonal prismatic TiS_6 units are individually connected.^{20,24} This is in contrast to individual TiS_6 octahedra in the case of titanium disulfide. The structure of titanium trisulfide can thus be formulated as $\text{Ti}^{4+}\text{S}^{2-}(\text{S}_2^{2-})$ indicating that the oxidation state of titanium is 4+ as in titanium disulfide, however with one sulfide and one disulfide anion.³⁶ Non-stoichiometry in these titanium chalcogenides is very likely and well-known in the literature.³⁷ The deviation from the stoichiometry in titanium sulfides can be either due to the presence of sulfur vacancies (TiS_{2-x} or TiS_{3-x}) or due to the presence of Ti interstitials formed through the

insertion of titanium atoms into the interlayer gaps ($\text{Ti}_{1+x}\text{S}_2$ or $\text{Ti}_{1+x}\text{S}_3$). In the case of titanium sulfides the non-stoichiometry resulting from the synthesis is mainly due to titanium interstitials which has been proved by X-ray and density measurements on different titanium sulfide crystals indicating the presence of different interphases between stoichiometric TiS_2 (CdI_2 -type structure), Ti_2S_3 (Fig. 1c) and TiS with its non-layered NiAs -type structure (Fig. 1d).³⁸ Phase diagrams of the titanium-sulfur system also reflect the complexity of the Ti/S phase regime with various phases and polytypes which makes it hard to define the exact boundary lines between these phases and polytypes.³⁹

Fig. 2 shows the products obtained from the solid state reaction of titanium and sulfur powder at 550 °C to form TiS_3 nanobelts.^{20–22,40} While the powder material shows the presence of a mixture of different sized TiS_3 nanobelts together with some sheet-like structures and nanobelt fragments (Fig. 2 and Fig. S1a and b†), the TiS_3 belts that are formed at the end of the tube have a width between 3 and 12 μm and are usually several hundreds of μm long with a thickness ranging from 50 nm to 200 nm showing the presence of belt type structures in the range of several nanometers up to micrometers in size (Fig. 2a and b). For the ease of discussion all the TiS_3 belts formed at the end of the ampule will be termed “ TiS_3 nanobelts”. In the region where the powder-like material is formed, a mixture of different long and short nanobelt structures or even nanobelt fragments exists beside some sheet-like structures (Fig. 2c and d). Additional heat treatment of the TiS_3 powder material, after removal from the ampule, at 450 °C under argon flow in a tube furnace allows the removal of some elemental sulfur but does not change the morphology of the TiS_3 nanobelts and fragments found (Fig. S2†). The reaction of titanium and sulfur powder at 750 °C (ratio 1 : 2) yields a shiny

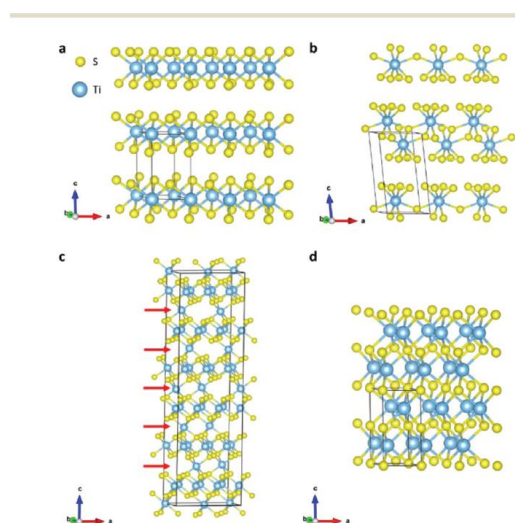


Fig. 1 Representation of the crystal structure and unit cell of (a) hexagonal TiS_2 (CdI_2 -type, space group: $P\bar{3}m1$), (b) monoclinic TiS_3 (space group: $P2_1/m$), (c) monoclinic Ti_2S_3 (space group: Cc), where the red arrows show the positions of interstitial titanium between the “ TiS_2 layers” and (d) hexagonal TiS (space group: $P6_3/mmc$) where the interlayer gaps are filled with titanium resulting in a non-layered NiAs -type structure.

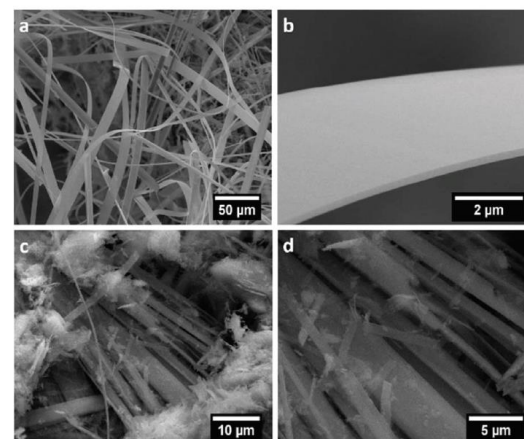


Fig. 2 SEM images at different magnifications of (a and b) TiS_3 crystals attached to the ampule inner wall showing the formation of TiS_3 nanobelts and (c and d) TiS_3 powder showing the presence of TiS_3 nanobelts of different sizes together with sheet-like structures.

dark greenish powder of composition TiS_2 (Fig. S1c and d[†]) which reveals the presence of micrometer-sized prism-shaped crystals that show a lamellar structure upon further magnification (Fig. 3a and b). In the case of TiS two different synthesis temperatures (450 °C and 900 °C) have been investigated while keeping the stoichiometric ratio of the elements Ti and S at 1 : 1. In both cases, a greyish to black powder is obtained (Fig. S1e and f[†] for lt-TiS) where the powder of the lt-TiS is dull while that of ht-TiS is shiny similar to TiS_2 . SEM of both powders reveals the presence of layered prism structures for ht-TiS similar to the crystals of TiS_2 in which the layers are electron transparent (Fig. 3c and d) while for lt-TiS crumpled sheet-like structures with thickness of a few nm are observed (Fig. 3e and f). The other titanium chalcogenides, TiSe_2 and TiTe , synthesized in this work also show layered crystals in the SEM ranging from a few micrometers to several hundred micrometers in size (Fig. S3[†]).

EDX analysis gives a deeper insight into the bulk composition of the synthesized nanomaterials.^{41,42} XPS analysis yields mainly information from the material surface with an information depth of 1 to 5 nm which thus supplements this information nicely.⁴³ For TiS_3 crystal compositions of 74.52% S and 25.48% Ti (S/Ti ratio of 2.92), while for the TiS_3 powder 75.44% S and 24.56% Ti (S/Ti ratio of 3.07) were obtained by EDX analysis (Fig. S4a and b[†]) indicating the formation of

stoichiometric TiS_3 . For TiS_2 64.84% S and 35.16% Ti (S/Ti ratio of 1.84) were obtained (Fig. S4c[†]) which are close to the values for the stoichiometric TiS_2 and agree well with reports that indicate that TiS_2 usually does not form with an ideal stoichiometry of 2 : 1 (S/Ti).^{24,37} For the non-stoichiometric titanium sulfides 56.81% S and 43.19% Ti (S/Ti ratio of 1.32) for lt-TiS and 61.64% S and 38.36% Ti (S/Ti ratio of 1.61) for ht-TiS were obtained (Fig. S4d and e[†]). Thermogravimetric (TG) analysis leads to similar results, thus confirming the obtained stoichiometries, independently. For the crystalline TiS_3 a S/Ti ratio of 2.85, while for the TiS_3 powder a ratio of 3.29 were obtained, indicating the presence of some excess sulfur in the case of the TiS_3 powder. For TiS_2 a S/Ti of 1.94 was found while for the non-stoichiometric titanium monosulfides (lt-TiS and ht-TiS), the ratios of 1.23 and 1.57 were obtained, respectively. The EDX for the selenium-based titanium chalcogenide TiSe_2 , 67.06% Se and 32.94% Ti is in accord with the 1 : 2 stoichiometry. However, for the tellurium-based titanium chalcogenide, the EDX determined atomic percentages of 47.58% Te and 52.42% Ti, thus suggesting the formation of TiTe in 1 : 1 stoichiometry (Fig. S5a and b[†]). EDX analysis of the obtained TiS_3 powder thermally treated for different time periods at 450 °C under argon ($\text{TiS}_{3-x}/20$ min, $\text{TiS}_{3-x}/40$ min and $\text{TiS}_{3-x}/60$ min) indicates a stepwise removal of sulfur with increasing treatment time. The S/Ti ratio is 3.07 for the TiS_3 powder and decreases to 2.16 for $\text{TiS}_{3-x}/20$ min, then to 1.59 for $\text{TiS}_{3-x}/40$ min and finally reaches 1.23 for $\text{TiS}_{3-x}/60$ min (Fig. S6[†]). EDX spectra do indicate the presence of trace amounts of oxygen. A potential oxygen source could come from the sample handling process. A reliable quantification of oxygen is not possible due to the severe overlap of the O K peak with the Ti L excitation line.

Photoelectron spectroscopic characterization

Titanium trisulfide TiS_3 . XPS analysis for the different titanium sulfides could give more detailed information about their surface structure and composition which is extremely important to understand their photocatalytic activity. The Ti 2p high-resolution core level spectra of the freshly prepared TiS_3 nanobelts display two main peaks at 455.9 eV and 461.9 eV which can be assigned to Ti^{4+} Ti 2p_{3/2} and Ti 2p_{1/2}, respectively, with a spin-orbit doublet splitting of 6 eV which represents Ti associated with S.⁴⁴ Upon deconvolution two further small peaks at 458.8 eV and 464.6 eV could be fitted corresponding to the Ti 2p_{3/2} and Ti 2p_{1/2} of TiO_x , respectively⁴⁵ indicating the presence of additional surface oxidation as the crystals were kept under ambient atmosphere before the XPS measurements (Fig. 4a). Long term stability experiments (two years) under ambient atmosphere before the initial XPS measurements reveal, besides the Ti 2p_{3/2} and Ti 2p_{1/2} peaks indicating Ti^{4+} of Ti-S at 456.5 eV and 462.5 eV, two further prominent peaks at 459.5 eV and 465.4 eV corresponding to the Ti 2p_{3/2} and Ti 2p_{1/2} of TiO_x , respectively (Fig. 4a). This reveals that even at longer periods of time, surface oxidation proceeds at a rather slow rate, indicating good stability of the synthesized TiS_3 . In contrast to this observation, XPS analysis

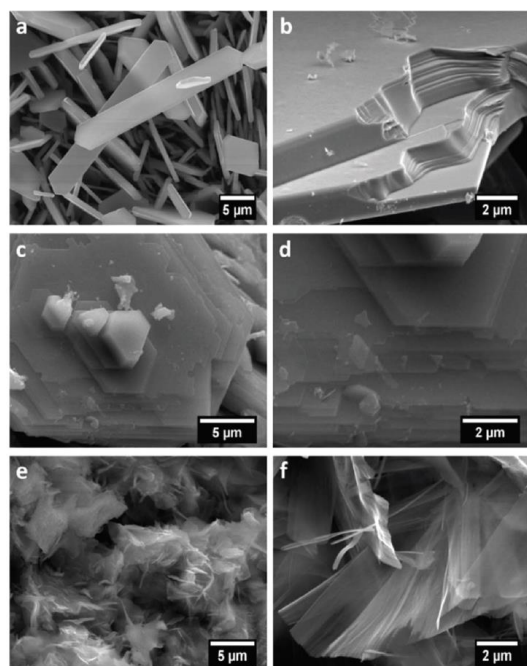


Fig. 3 SEM image of (a and b) TiS_2 crystals, (c and d) ht-TiS and (e and f) lt-TiS at different magnifications showing the different morphologies and the layered composition of these nanomaterials.

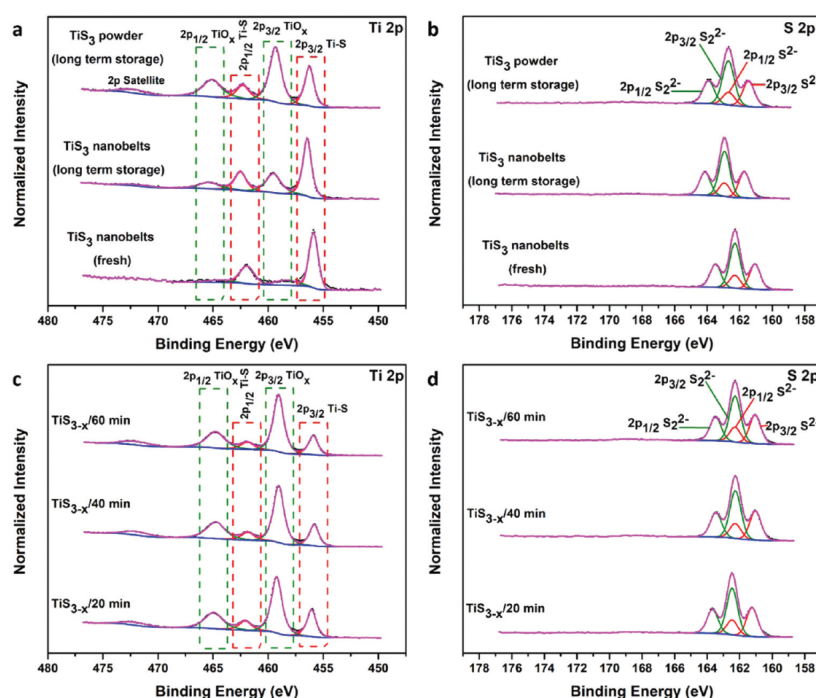


Fig. 4 High-resolution XPS showing Ti 2p and S 2p core level signals of (a and b) TiS_3 powder and TiS_3 nanobelts (freshly prepared and after two years of storage under ambient conditions) and (c and d) TiS_3 powder treated at 450°C under argon for 20 min, 40 min and 60 min.

of the Ti 2p core level spectrum for the TiS_3 powder formed during the same synthesis and which is also stored for two years under ambient atmosphere, however shows intense surface oxidation compared to the sample composed of large crystals. This is due to the higher surface area exposed in the powder (Fig. 4a). The presence of oxygen related to TiO_x can also be found in the O 1s high-resolution core level deconvoluted spectra at 530.6 eV together with oxygen related to the surface-bound O=C-O species at 532.3 eV as well as signals corresponding to aliphatic alcohol and ether species at 533.5 eV stemming from adventitious carbon formed due to sample exposure to ambient atmosphere (Fig. S7a, ESI†).^{45,46} The amount of surface oxidation can be clearly seen from the deconvoluted O 1s spectra through the ratio of the peaks related to TiO_x and the adventitious carbon related O=C-O species thus showing that the freshly prepared crystals have the lowest degree of surface oxidation followed by the two-year-old nanobelt crystals and finally the two-year-old TiS_3 powder. A comparison of the S 2p spectra of these TiS_3 samples shows no difference where the S 2p can be deconvoluted to two pairs of peaks at 161.5 eV and 162.7 eV corresponding to the S $2p_{3/2}$ and S $2p_{1/2}$ of sulfide S^{2-} and 162.7 eV and 163.9 eV representing the S $2p_{3/2}$ and S $2p_{1/2}$ of disulfide anion S_2^{2-} (Fig. 4b). The ratio of $\text{S}_2^{2-}/\text{S}^{2-}$ is close to 2 : 1 which is typical of titanium trisulfide which consists of one S_2^{2-} unit and one S^{2-} unit.⁴⁷

XPS analysis of the TiS_3 powder heated under argon at 450°C for 20 min, 40 min and 60 min (Fig. 4c and d) shows the presence of disulfide and sulfide anions which can be attributed to the high-resolution S 2p core level spectra which upon deconvolution show the corresponding characteristic doublets, thus indicating that after heat treatment TiS_3 is still present (Fig. 4d). In a study by Hawkins *et al.*²⁴ heat treatment of TiS_3 in a vacuum sealed vial using elemental titanium powder as a sink for the released sulfur at 450°C for 24–144 h resulted in a transformation of TiS_3 into non-stoichiometric TiS_{3-x} . Calculation of the $\text{S}_2^{2-}/\text{S}^{2-}$ ratio in these spectra shows a decrease in the $\text{S}_2^{2-}/\text{S}^{2-}$ ratio to about 1.6 in comparison with 1.8 in the untreated powder indicating the formation of sulfur vacancies. This might be a first indication that qualifies that material for further photocatalytic studies. This finding is also supported by an overall decrease in the S/Ti ratio deduced from the S 2p and Ti 2p peaks of the corresponding XPS survey spectra ranging from 2.5 for the untreated TiS_3 powder to 1.8 for $\text{TiS}_{3-x}/20$ min, to 1.5 for $\text{TiS}_{3-x}/40$ min and to 1.35 for $\text{TiS}_{3-x}/60$ min (Fig. S8,† XPS survey spectra). This trend is in line with the EDX analysis (see above) for the heat treated TiS_3 powders. Comparing the high-resolution Ti 2p core level spectra of these heat treated TiS_3 samples, they all show the doublets corresponding to the Ti^{4+} characteristic for the Ti-S bond ($\text{Ti}^{4+}(\text{S})$) and TiO_x indicating the presence of different

degrees of surface oxidation dependent on the heat treatment time (Fig. 4c). By determination of the ratio of $\text{TiO}_x/\text{Ti}^{4+}(\text{S})$ as 1.80, 2.35, 2.85 and 3.27 for the untreated TiS_3 powder and for the heat treated TiS_3 samples $\text{TiS}_{3-x}/20$ min, $\text{TiS}_{3-x}/40$ min and $\text{TiS}_{3-x}/60$ min, respectively, a systematic increase in surface oxidation is observed. The same trend can be observed in the deconvoluted high-resolution O 1s core level spectra (Fig. S7b, ESI†).

Titanium disulfide, TiS_2 . Titanium disulfide, TiS_2 , shows a high-resolution Ti 2p core level spectrum similar to that of TiS_3 (Fig. 5a), in which two doublets are also observed. One doublet is at 456.3 eV and 462.4 eV with a doublet splitting of 6.1 eV, thus corresponding to the Ti $2p_{3/2}$ and Ti $2p_{1/2}$ of Ti^{4+} associated with the Ti-S bond, respectively and the other doublet is at 459.0 eV and 464.7 eV with a doublet splitting of 5.7 eV corresponding to the Ti $2p_{3/2}$ and Ti $2p_{1/2}$ of TiO_x , respectively, the latter due to surface oxidation during sample storage (see also O 1s core level spectrum in Fig. S7c†).

The S 2p core level spectrum of TiS_2 (Fig. 5b) differs significantly from that of TiS_3 . No doublet signal corresponding to the disulfide anions S_2^{2-} is observed, but instead another high binding energy doublet at 163.8 eV and 165.0 eV corresponding to S $2p_{3/2}$ and S $2p_{1/2}$ with a doublet splitting of 1.2 eV can be found besides the characteristic S 2p doublet of sulfide S^{2-} found at 160.9 eV and 162.2 eV for S $2p_{3/2}$ and S $2p_{1/2}$, respectively. In accord with the literature, the high

binding energy doublet could not be assigned to a specific sulfur species.^{44,48} It can be speculated that it could correspond to some surface-bound thiol species.⁴⁹

Titanium monosulfide TiS . Titanium monosulfides, lt-TiS and ht-TiS, reveal, similar to the TiS_2 and TiS_3 samples, two doublets in the Ti core level spectra, one at 456.2 eV and 462.2 eV with a splitting of 6 eV assigned to Ti $2p_{3/2}$ and the Ti $2p_{1/2}$ of Ti^{4+} and associated with the Ti-S bond, and the other at 458.9 eV and 464.7 eV with a splitting of 5.8 eV corresponding to the Ti $2p_{3/2}$ and Ti $2p_{1/2}$ peaks of TiO_x (Fig. 5c). ht-TiS synthesized at 900 °C shows a diminished degree of surface oxidation with a $\text{TiO}_x/\text{Ti}^{4+}(\text{S})$ ratio of 0.47 compared to lt-TiS synthesized at 450 °C with a $\text{TiO}_x/\text{Ti}^{4+}(\text{S})$ ratio of 1.98. The two-year-old lt-TiS shows complete surface oxidation as no $\text{Ti}^{4+}(\text{S})$ can be found anymore. The same can be seen in the corresponding high-resolution O 1s core level spectra (Fig. S7d, ESI†) where the O 1s (TiO_x)/O 1s (O=C-O) ratio is 1.91, 3.58 and 5.09 for ht-TiS, lt-TiS and the two-year-old lt-TiS, respectively, indicating the increasing degree of surface oxidation as well. The high-resolution S 2p core level spectra of TiS (Fig. 5d) show a similar pattern to that observed for TiS_2 with a deconvolution into two doublets, one at 161.2 eV and 162.4 eV corresponding to the S $2p_{3/2}$ and S $2p_{1/2}$ peaks of sulfide S^{2-} . The second doublet at 163.5 eV and 164.7 eV corresponds to the S $2p_{3/2}$ and S $2p_{1/2}$ peaks of the yet unidentified sulfur species. Thus, the XPS data reveal that the titanium monosul-

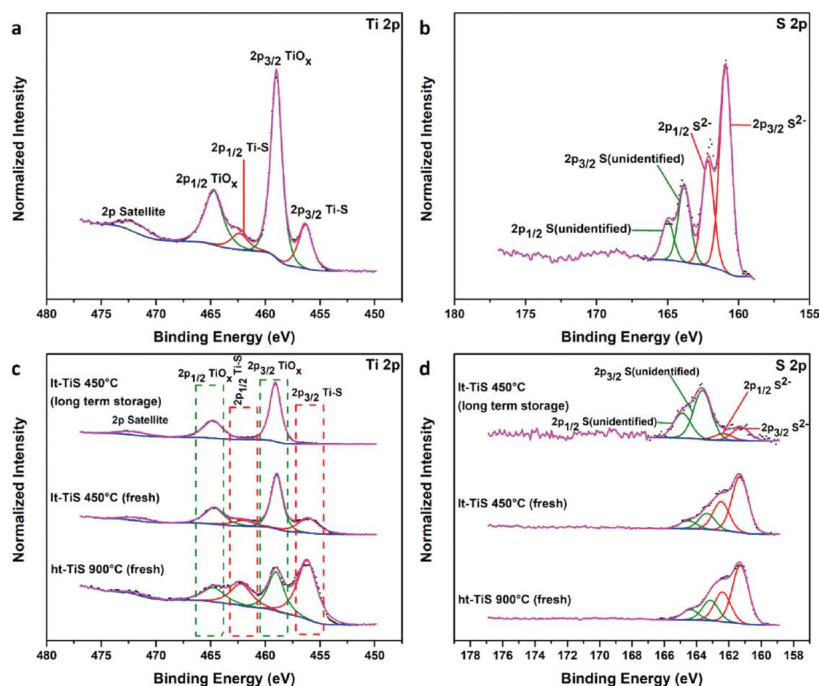


Fig. 5 High-resolution XPS showing the Ti 2p and S 2p core level spectra of (a and b) TiS_2 and (c and d) low temperature TiS (freshly prepared and after two years of aging) and high temperature TiS.

vide TiS represents a non-stoichiometric material, most probably due to a large number of defect sites.

X-ray characterization

For TiS₃ nanobelts the XRD shows main reflexes for the (001), (002), (003), (004), (005) and (006) planes. Additional reflexes are missing due to the preferential orientation of the TiS₃ nanobelts along their *c*-axis (Fig. 6a). For TiS₃ powder the XRD however shows different crystal orientations (Fig. 6b) indicating that different nanostructures exist in the powder besides the nanobelt morphology which has a preferential growth direction. Additional reflexes are due to traces of elemental sulfur present (S₈ ICDD PDF no. 85-0799). The XRD of TiS₂ (Fig. 6c) matches well with the powder diffraction file ICDD PDF no. 88-2479 for titanium disulfide where the difference observed in the measured intensities is also due to the preferential orientation of the hexagonal crystals. In the case of the phases obtained for lt-TiS and ht-TiS, an unambiguous assignment is difficult due to the presence of a huge number of different polytypes for different titanium sulfides. An assignment to the non-stoichiometric titanium sulfides Ti_{2.45}S₄ (ICDD PDF no. 72-0820) and Ti_{1.083}S₂ (ICDD PDF no. 84-0372) for lt-TiS and ht-TiS, respectively represents the best fit (Fig. 6d and e).

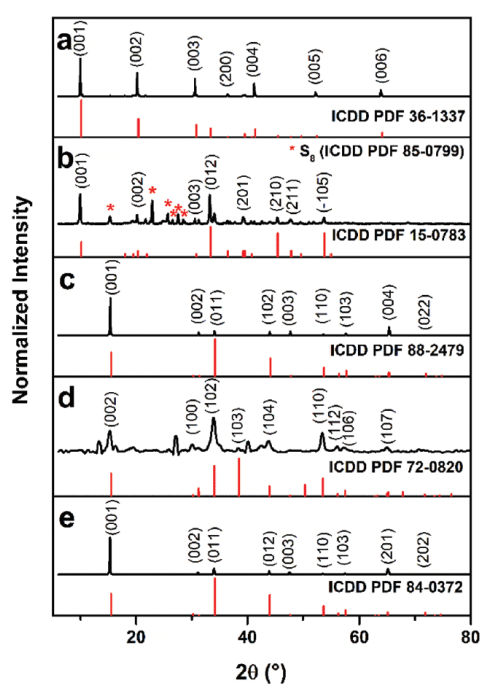


Fig. 6 XRD of (a) TiS₃ nanobelts, (b) TiS₃ powder (reflexes with asterisk correspond to elemental sulfur), (c) TiS₂, (d) lt-TiS and (e) ht-TiS. The lt-TiS phase is best fitted with Ti_{2.45}S₄ (ICDD PDF no. 72-0820) and ht-TiS matches Ti_{1.083}S₂ (PDF no. 84-0372).

XRD analysis of the TiS₃ powder heated at 450 °C under argon for different time intervals shows some changes. However, the main reflexes for TiS₃ remain unchanged while the reflexes for elemental sulfur (S₈) observed in the as-prepared TiS₃ powder disappear and a new broad peak at 25.15° appears and is assigned to anatase TiO₂ (Fig. 7). Relating these data to the observations obtained from the EDX (Fig. S6†) and the XPS (Fig. 4c and d) confirms that some sulfur vacancies are formed, parallel to a certain degree of surface passivation due to oxide formation. The significant broadening of the (001) peak at 25.15° of the formed anatase also indicates the formation of TiO₂ nanocrystallites which agrees with the idea of filling of surface sulfur vacancies with oxygen from the atmosphere to which the material is exposed after the annealing process resulting in the formation of such isolated nanocrystallites on the surface.

Transmission electron microscopic characterization

The bright-field TEM images (Fig. 8a₁–e₁) show that after extensive sonication exfoliation of the different titanium sulfides takes place resulting in very thin and mostly electron-transparent specimens underlining their layered two-dimensional structure. The lattice fringes in the HRTEM (Fig. 8a₂–e₂) and the corresponding SAED patterns with well-defined spots (Fig. 8a₃–e₃) reveal the monocrystalline nature of the different titanium sulfide samples. The spacings of the lattice fringes obtained for the TiS₃ nanobelts are 3.3 Å, 2.4 Å and 1.7 Å corresponding to the (010), (200) and (020) planes of TiS₃, respectively (Fig. 8a₂) and show a preferential growth direction along their *b*-axis [010]. For the TiS₃ powder also nanobelts are observed (Fig. 8b₁) which in the HRTEM show lattice spacings of 4.7 Å and 3.3 Å corresponding to the (100) and (010) planes of TiS₃, respectively.

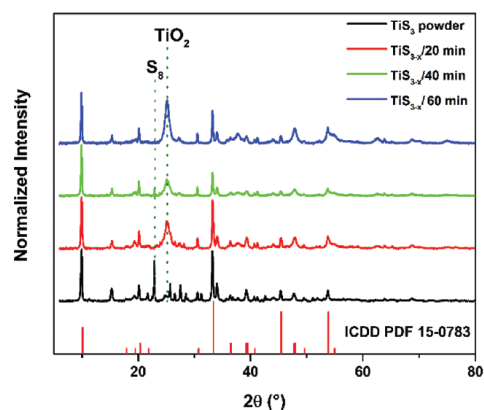


Fig. 7 XRD of the as-prepared TiS₃ powder, TiS_{3-x}/20 min, TiS_{3-x}/40 min and TiS_{3-x}/60 min obtained by heating of the as-prepared TiS₃ powder at 450 °C under argon resulting in the disappearance of elemental sulfur and the appearance of some anatase TiO₂ (ICDD PDF no. 15-0783 of TiS₃ is given for comparison).

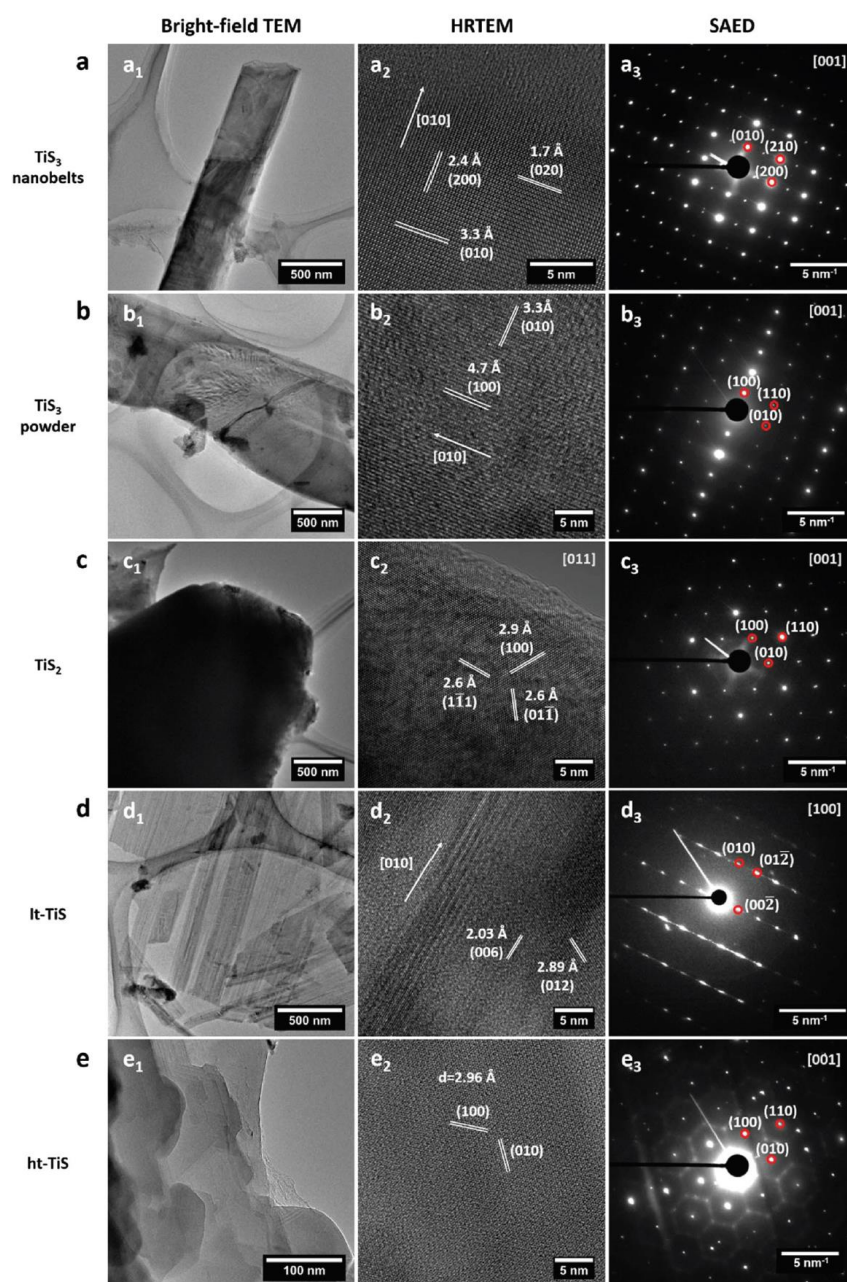


Fig. 8 Bright-field TEM (a₁–e₁) are overview images. HRTEM with the corresponding *d*-spacing of the lattice fringes is shown in (a₂–e₂) and the indexed SAED is given in (a₃–e₃) where (a–e) denote: (a) TiS₃ nanobelts with SAED along the [001] zone axis, (b) TiS₃ powder with SAED along the [001] zone axis, (c) TiS₂ with HRTEM along the [011] and SAED along the [001] zone axis showing a hexagonal structure, (d) lt-TiS with SAED along the [100] zone axis and (e) ht-TiS with SAED along the [001] zone axis.

In the case of TiS_2 , the hexagonal crystal structure is formed according to the crystal form, the observed lattice angles and on the basis of the SAED (Fig. 8c₁₋₃). Lattice spacing of the TiS_2 crystals as determined from the HRTEM (Fig. 8c₂) revealed a spacing of 2.9 Å, 2.6 Å and 2.6 Å corresponding to the (100), (011) and (111) planes, respectively.

For the titanium monosulfides (lt- and ht-TiS) the SAED (Fig. 8d₃ and e₃) also shows a hexagonal pattern indicating the similarity to the TiS_2 unit cell. Streaking is indicated in the SAED, which relies on crystallographic stacking faults in lt-TiS (Fig. 8d₂ and d₃) or short-range ordering, the latter being observed in the HRTEM and SAED of ht-TiS (Fig. 8e₂ and e₃). This might most probably refer to the insertion of Ti in the van der Waals gap interstitials forming partially filled metal layers.^{37,50,51} Interestingly, ht-TiS shows hexagonal symmetry in the bright-field TEM (Fig. 8e₁) while lt-TiS (Fig. 8d₁) shows more elongated structures indicating a preferential growth direction along the crystallographic *b*-axis [010] (Fig. 8d₂). Lattice spacing as determined from the HRTEM of lt-TiS (Fig. 8d₂) shows distances of 2.03 Å and 2.89 Å which are in accord with the (006) and (012) planes of $\text{Ti}_{2.45}\text{S}_4$, respectively, while for ht-TiS (Fig. 8e₂) a distance of 2.96 Å is obtained which correlates with the (100) and (010) planes of $\text{Ti}_{1.083}\text{S}_2$.

TEM-EDX analyses of the TiS_3 samples (both nanobelts and powder) show an ideal stoichiometry with 25% Ti and 75% S in the case of the nanobelts and 24% Ti and 76% S in the case of the powder. For TiS_2 a near ideal stoichiometry with 37% Ti

and 63% S was obtained. For lt-TiS a ratio close to 1:1 was obtained where Ti is 53% and S is 47%. However, for the ht-TiS sample, the TEM-EDX unravels a difference in composition between the center and edge position of the hexagonal crystals. The crystal center shows an almost ideal TiS_2 stoichiometry (38% Ti and 62% S) while the edge is highly sulfur deficient with 70% Ti and 30% S.

Raman studies

Raman measurements of the different titanium sulfides further confirmed the identities of the synthesized materials. For the TiS_3 nanobelts and for the TiS_3 powder a similar Raman spectrum was obtained, showing the four A_{1g} modes characteristic of TiS_3 at 175, 298, 368, and 557 cm^{-1} (Fig. 9).⁵² In the case of TiS_2 , the two Raman active modes E_g (in-plane vibrational mode) and A_{1g} (out-of plane vibrational mode) characteristic of TiS_2 are observed at 222 and 331 cm^{-1} , respectively which indicate that the measured position of the bulk TiS_2 sample, as detected by micro-Raman measurement, contains about two individual layers of TiS_2 as the position of these modes is sensitive and characteristic to the number of layers.⁵³ Furthermore, a shoulder at about 387 cm^{-1} is

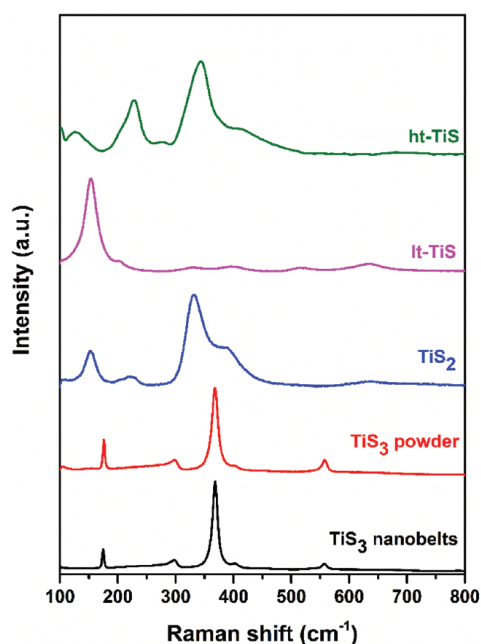


Fig. 9 Raman spectra of TiS_3 nanobelts, TiS_3 powder, TiS_2 , lt-TiS and ht-TiS.

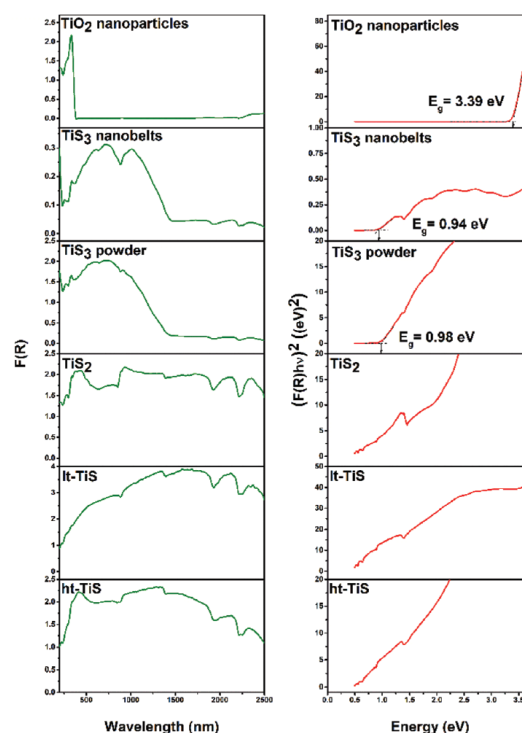


Fig. 10 UV-VIS-NIR DRS spectra (Kubelka–Munk function) and the corresponding Tauc plot for the determination of the direct band gap of TiO_2 nanoparticles (EMPROVE® ESSENTIAL, Merck), TiS_3 nanobelts, TiS_3 powder, TiS_2 , lt-TiS and ht-TiS.

observed and is most probably due to the defects in TiS_2 .⁵³ Two further peaks are observed at 152 and 635 cm^{-1} and correspond to TiO_2 ⁵⁴ which is formed due to some surface oxidation of the sample when it is in contact with the atmosphere. The Raman spectra of the non-stoichiometric titanium sulfides (lt- and ht-TiS) show features that are similar to the Raman spectrum of TiS_2 but typically with some peak shift. For lt-TiS mainly two peaks at 329 and 395 cm^{-1} are observed which are analogous to the A_{1g} mode of TiS_2 and correspond to the vibrations of sulfur atoms perpendicular to the sulfur layer. An additional shoulder that is observed in TiS_2 is due to the defects obtained by the interlayer insertion of titanium atoms thus resulting in phonon mode stiffening.^{53,55} The peaks found at 153, 512 and 635 cm^{-1} correspond to anatase TiO_2 ⁵⁴ which is also formed due to surface oxidation due to contact with the atmosphere. For ht-TiS the similarity to the TiS_2 Raman spectrum is even more obvious, where the peaks obtained at 228 and 343 cm^{-1} are analogous to the E_g and A_{1g} vibrational modes of TiS_2 and even a shoulder similar to the shoulder found in the TiS_2 spectrum is observed at about 407 cm^{-1} . Interestingly, there is an increase in the E_g

vibrational mode relative to the A_{1g} mode when compared to the Raman spectrum of TiS_2 which is in accord with non-stoichiometric titanium sulfides.⁵⁵

UV-VIS-NIR studies

UV-VIS-NIR diffuse reflectance spectra (Fig. 10) give direct information about the spectral absorptivity especially in the visible region important for photocatalysis. The diffuse reflectance spectra were recorded using the Kubelka–Munk function $F(R)$ which enables to determine the optical absorbance of the solid material from its reflectance R according to:⁵⁶

$$F(R) = \frac{(1 - R)^2}{2R}$$

Besides, the Tauc plot was obtained in order to determine the direct band gap of the different titanium sulfides. The Tauc plot for the determination of the direct band gap was calculated from the Kubelka–Munk function according to the following formula:⁵⁶

$$[F(R)h\nu]^2 = A(h\nu - E_g)$$

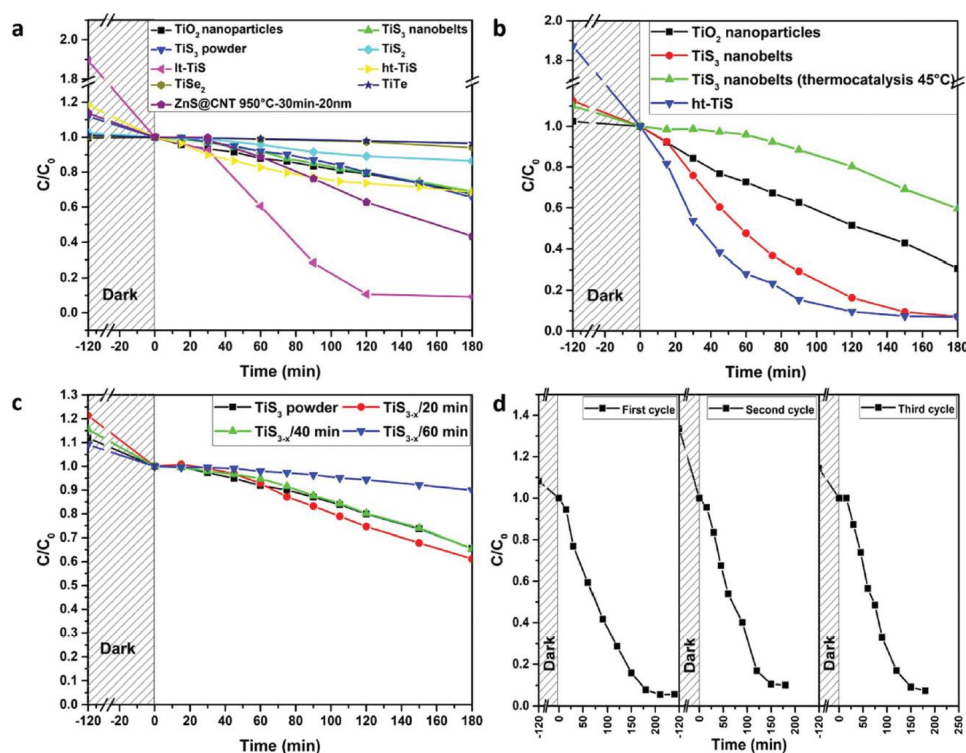


Fig. 11 (a) Comparison of the degradation profile of methyl orange using one mg of TiO_2 nanoparticles, different titanium chalcogenides and a ZnS@CNT nanocomposite³¹ photocatalyst under irradiation of simulated sunlight, (b) comparison of the degradation profile of methyl orange using 5 mg of each of TiO_2 nanoparticles, TiS_3 nanobelts and ht-TiS, (c) comparison of the degradation profile of methyl orange using one mg of TiS_3 powder treated at 450 °C under argon for different time intervals and (d) recyclability of 5 mg TiS_3 nanobelts over three cycles.

where A is a constant, h is the Planck constant, ν is the frequency and E_g is the band gap of the material. The diffuse reflectance spectrum of TiO_2 nanoparticles that were used in this study for a comparison of the photocatalytic activity shows only light absorption in the ultraviolet range of the spectrum resulting in a wide band gap of 3.39 eV as obtained from the corresponding Tauc plot (Fig. 10). TiS_3 nanobelts and the TiS_3 powder showed similar absorption spectra where the absorption extends to the near infrared region of about 1500 nm which is reflected in the low band gaps of 0.94 eV and 0.98 eV obtained from the corresponding Tauc plots of TiS_3 nanobelts and TiS_3 powder. In the case of TiS_2 and the non-stoichiometric titanium sulfides (lt- TiS and ht- TiS) their absorption extends over the whole measured UV-VIS-NIR region and so no band gap determination using the Tauc plot method was possible (Fig. 10). This however indicates that these sulfides can make full use of the whole sunlight spectrum.

Photocatalytic activity of titanium chalcogenides

The studied low band gap materials are suggested to be able to utilize most of the sunlight where the IR radiation of the sunlight could activate the low band gap materials through two possible pathways. One pathway could be indirect as IR radiation is able to activate molecular vibrations and rotations of the water molecules typically resulting in a rise in the temperature of the aqueous medium containing the photocatalyst. Due to the small band gap the resulting thermal energy produced by molecular vibrations and rotations is sufficient to induce further electron-hole separations leading to an increase in the photocatalytic efficiency itself. On the other hand, direct infrared excitation should be possible as IR radiation in the range of 700–3000 nm which has an energy between 1.77 and 0.41 eV is still sufficient to induce charge separation in these low band gap materials.

IR radiation accounts for 43% of the total solar radiation⁴ and would be very beneficial if it is efficiently used for photocatalysis. The design of materials that make use of IR radiation in photocatalysis *e.g.* for water decontamination could show an efficient way to use solar radiation in photocatalysis and eventually result in more efficient photocatalysts compared to TiO_2 . Testing the different synthesized titanium chalcogenides for their photocatalytic performance under simulated sunlight indeed revealed the high activity of TiS_3 (nanobelts and powder) and also titanium monosulfides (lt- and ht- TiS) where lt- TiS showed the highest photocatalytic activity (Fig. 11a). On the other hand, other titanium chalcogenides (stoichiometric TiS_2 , TiSe_2 and TiTe) synthesized in this work show almost no activity (Fig. 11a).

It is known that TiS_2 and TiSe_2 show semimetallic behavior^{24,32,57} which results in no effective charge separation thus explaining the absence or low photocatalytic activity of these materials. On the other hand, TiS_3 is found to be a semiconductor with a small band gap of about 1.2 eV⁸ which enables good charge separation even at longer wavelengths extending towards the IR-region (till about 1033 nm). While

Table 1 Comparison of the photocatalytic activity of the photocatalytically active titanium chalcogenides presented in this work with different photocatalysts presented in the literature for the degradation of MO

Photocatalyst	MO amount	Catalyst amount	Degradation time	Light source	Decolorization efficiency %	Ratio of catalyst/MO (w/w)	Decolorization rate per 1 mg of catalyst (mg h^{-1})	Ref.
CoWO_4 nanoparticles	0.5 mg L^{-1} , 50 mL (0.025 mg MO)	100 mg	70 min	UV light	70%	4000:1	1.5×10^{-4}	59
Graphene-ZnO nanocomposite	$5 \times 10^{-5} \text{ M}$, 50 mL (0.8 mg MO)	50 mg	120 min	Sunlight	97%	62.5:1	7.76×10^{-3}	60
TiO_2 @PMMA nanoparticles	10 mg L^{-1} , 100 mL (1 mg MO)	100 mg	50 min	UV light	90.9%	100:1	0.011	61
VS_2 /carbon Powder nanocomposite	10 mg L^{-1} , 50 mL (0.5 mg MO)	50 mg	30 min	Sunlight	70.1%	100:1	0.014	62
Ag-AgI/ $\text{Bi}_2\text{O}_3\text{Cl}$	20 mg L^{-1} , 50 mL (1 mg MO)	10 mg	180 min	Visible light	61%	10:1	0.020	63
ZrO_2 nanoparticles	10 mg L^{-1} , 100 mL (1 mg MO)	100 mg	110 min	UV light	99%	100:1	5.4×10^{-3}	64
$\text{g-C}_3\text{N}_4$ /graphene oxide aerogel	20 mg L^{-1} , 30 mL (0.6 mg MO)	30 mg	240 min	Visible light	92%	50:1	4.6×10^{-3}	65
Graphene oxide/ TiO_2 composites	12 mg L^{-1} , 50 mL (0.6 mg MO)	50 mg	180 min	Visible light	36%	83.3:1	1.44×10^{-3}	66
ZnS @CNT nanocomposite (950 °C–30 min–20 nm)	20 mg L^{-1} , 50 mL (1 mg MO)	1 mg	480 min	Sunlight	96%	1:1	0.12	31
lt- TiS	20 mg L^{-1} , 50 mL (1 mg MO)	1 mg	120 min	Sunlight	90%	1:1	0.45	This work
ht- TiS	20 mg L^{-1} , 50 mL (1 mg MO)	1 mg	180 min	Sunlight	32%	1:1	0.11	This work
TiS_3 powder	20 mg L^{-1} , 50 mL (1 mg MO)	1 mg	180 min	Sunlight	34%	1:1	0.11	This work

one mg of the tested TiO_2 nanoparticles, TiS_3 (nanobelts and powder) and ht-TiS showed similar profiles for the degradation of methyl orange, increasing the photocatalyst amount gave

further differentiation, showing that ht-TiS and TiS_3 have higher photocatalytic activities than TiO_2 (Fig. 11b). The different active titanium sulfides also show different degra-

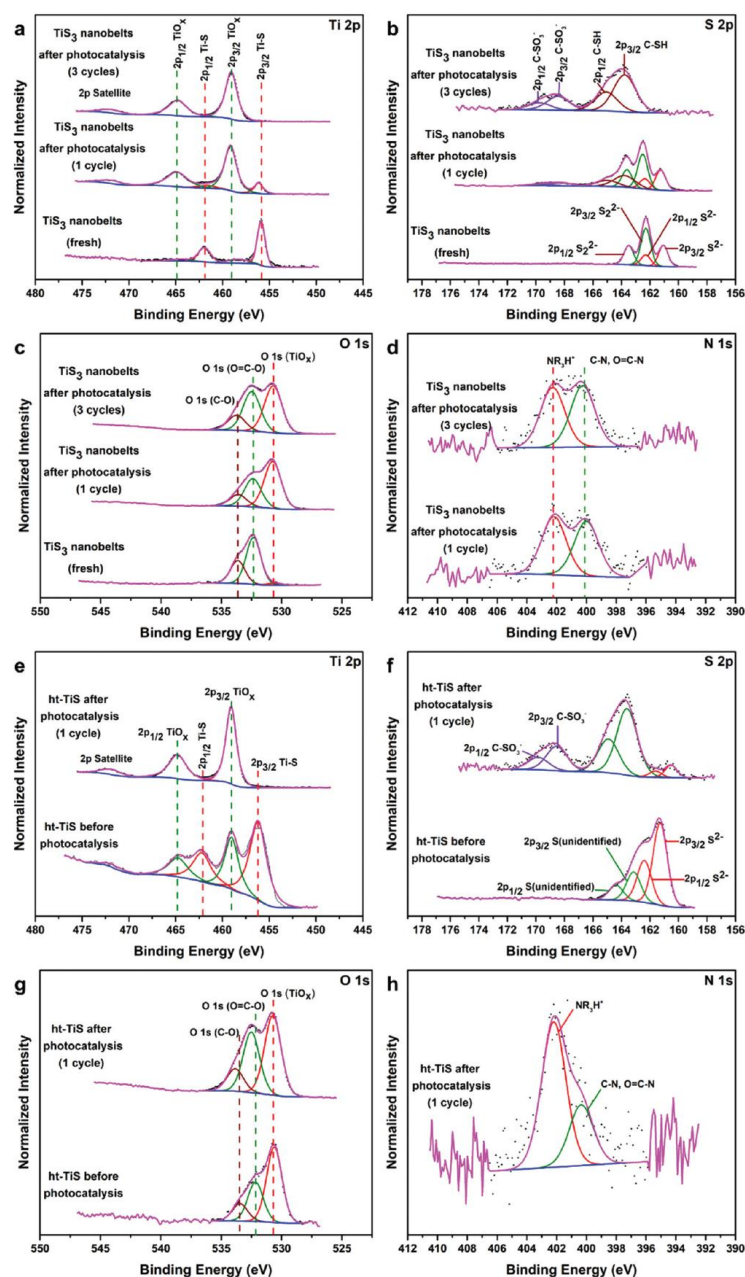


Fig. 12 High-resolution XPS spectra showing (a) Ti 2p, (b) S 2p, (c) O 1s and (d) N 1s core level spectra of TiS_3 nanobelts (fresh before photocatalysis), TiS_3 nanobelts after one photocatalytic cycle and TiS_3 nanobelts after three photocatalytic cycles. Spectra showing (e) Ti 2p, (f) S 2p, (g) O 1s and (h) N 1s core level spectra of ht-TiS before and after one photocatalytic cycle.

dation kinetics when compared to TiO_2 where the titanium sulfides reveal a zero order reaction behavior while TiO_2 shows a first order reaction behavior (Fig. S9[†]). Interestingly, it was observed for the active photocatalysts that they also lead to significant degradation of the dye in the dark before the actual photocatalytic experiment under simulated sunlight started when compared to the TiO_2 nanoparticles (Fig. 11a and b). Even when the catalysts TiS_3 and non-stoichiometric titanium sulfides (lt- and ht-TiS) were kept at room temperature in the dark for longer times in contact with the dye solution, considerable activity towards dye degradation could be observed (Fig. S10,[†] adsorption effects can be ruled out here). Thus, heat is sufficient to result in the desired charge separation resulting in a catalytic activity in the dark which is known as thermocatalysis. This concept was also tested by external heating while keeping the mixture in the dark. This results in a significant degradation of the dye as shown for TiS_3 nanobelts at 45 °C in Fig. 11b. This suggests that the use of IR radiation by the catalyst can be through two ways: either through direct absorption of IR radiation by the photocatalyst which results in charge separation or through indirect heat transfer to the catalyst wherein heat is generated through the absorption of IR radiation by water molecules. This should also result in charge separation and thus catalytic activity. Therefore, these materials represent a photocatalyst and thermocatalyst at the same time resulting in a photo-thermocatalytic synergistic effect. Recently, some composite materials have been prepared to combine the photocatalytic and thermocatalytic properties of two different materials to achieve this synergistic effect.⁵⁸

Table 1 gives a comparison of the activity of the active titanium chalcogenides of this study with other photocatalysts reported in the literature^{31,59–66} in the degradation of MO. Interestingly the herein presented titanium-based catalysts show a superior activity of all catalysts where only one mg is sufficient to degrade MO almost completely within 120 min in the case of the lt-TiS material. Based on the used ratios the new titanium sulfide photocatalysts outperform the thus far reported materials.

Having seen the high activity of the titanium sulfide catalysts it was interesting to check whether it is possible to increase the catalytic efficiency of TiS_3 through the production of sulfur vacancies even further. Sulfur vacancies result in the formation of mid-gap states⁶⁷ which could be beneficial for the photocatalytic process. Sulfur vacancies were introduced into TiS_3 through heating at 450 °C under argon. The resulting material $\text{TiS}_{3-x}/20$ min showed some increase in the photocatalytic activity followed by a decrease for longer treatment times where the $\text{TiS}_{3-x}/40$ min sample has the same activity as the as-prepared TiS_3 powder and $\text{TiS}_{3-x}/60$ min has a lower activity than the as-prepared powder (Fig. 11c). Thus, there are two possible centers which result in the increased catalytic activity of the titanium sulfides. On the one hand the presence of Ti^{3+} centers in non-stoichiometric titanium sulfides and on the other hand the presence of sulfur vacancies could lead to a high catalytic activity in titanium sulfides. At the same time,

TiS_3 nanobelts proved to be highly efficient photocatalysts, even exceeding the photocatalytic activity of TiO_2 .

The reusability of the active titanium sulfides was tested and it shows a behavior where with an increasing number of cycles an increase in the degradation activity was observed (Fig. 11d and S11[†]). EDX of the materials after photocatalysis (Fig. S12[†]) shows an increase in the carbon and oxygen content due to the presence of organic decomposition products on the surface while the stoichiometry of the investigated titanium sulfides is preserved. XPS of the materials after photocatalysis (Fig. 12) mainly shows the presence of an oxidized surface even after one photocatalytic cycle which is not surprising due to the presence of dissolved oxygen and hydrogen peroxide which was added in small amounts to the dye solution to serve as an additional oxygen source. However, this does not degrade the performance of the photocatalyst but could be even beneficial with the increasing number of cycles due to the formation of a titanium oxide/titanium sulfide heterostructure, thus enabling better charge separation by decreasing the electron-hole recombination rate. This speculation is strongly supported by the fact that there is an increase in the photocatalytic activity when the catalyst is re-used in successive photocatalytic cycles as seen in Fig. 11d and S11.[†] Heterostructures are well known to increase photocatalytic activity due to their ability in the spatial separation of the electrons and holes formed, thus preventing their recombination, which leads to the design and specific synthesis of different heterostructures to be used in photocatalysis.^{27,31,68,69} In the present case, the titanium oxide/titanium sulfide heterostructure is even formed spontaneously during its use in wastewater treatment. Further causes for the increasing activity with re-use could be the increase of surface area of the used material due to exfoliation with time while stirring it in the dye solution. Furthermore, organic degradation products can be detected by XPS on the catalyst surface^{49,70–72} (Fig. 12b–d and f–h) most probably stemming from the degradation of the used methyl orange dye.

Conclusions

Titanium chalcogenides based on S, Se and Te show interesting properties due to their narrow band gaps which could be beneficial for the design of new and different photo-thermocatalysts. In this work the binary titanium chalcogenides TiS_3 , TiS_2 , TiS , TiSe_2 and TiTe were synthesized through chemical vapor transport reaction by employing different ratios of the powdered elements as starting materials at different synthesis temperatures. While the titanium dichalcogenides (TiS_2 , TiSe_2) and TiTe show semimetallic behavior which makes them poor candidates for direct use in photocatalysis, they could be still beneficial for the design of heterostructures. On the other hand, the non-stoichiometric TiS and TiS_3 show a high photocatalytic activity especially in the presence of small amounts of hydrogen peroxide. It was shown that Ti^{3+} present in non-stoichiometric titanium sulfides and a certain extent of sulfur

vacancies lead to an increase in the photocatalytic activity. The small band gap of these materials also results in an additional thermocatalytic activity and the ability to make use of the whole sunlight spectrum. Thus, this work shows that the non-stoichiometric titanium sulfides (It-TiS and ht-TiS) along with titanium trisulfide are very interesting candidates for efficient photocatalysis and can easily outperform the activity of titanium dioxide. A great advantage of these materials is the spontaneous formation of an oxide layer on the surface of active titanium sulfides leading to a titanium oxide/titanium sulfide heterostructure. It is formed in successive photocatalytic cycles and obviously allows better charge separation leading to a highly enhanced photocatalytic activity. The tuning of the reactant ratios and the reaction temperatures employed enable the creation of a wide range of non-stoichiometric titanium sulfides with varying morphologies and good photocatalytic activities. Next, further investigations should help to elucidate the detailed mechanism and allow a fine tuning of the photocatalytic performance of titanium sulfides as novel photocatalyst materials.

Conflicts of interest

There are no conflicts to declare.

Acknowledgements

The authors thank S. Heinschke and T. Bies (both at Eduard-Zintl-Institut für Anorganische und Physikalische Chemie, TU Darmstadt) for XRD measurements and thermogravimetric analysis (TGA), respectively. XPS measurements were carried out at the Karlsruhe Nano Micro Facility at KIT under the KNMF program.

References

- 1 *Visible-Light-Active Photocatalysis: Nanostructured Catalyst Design, Mechanisms, and Applications*, ed. S. Ghosh, Wiley-VCH, 2018.
- 2 B. Luo, G. Liu and L. Wang, *Nanoscale*, 2016, **8**, 6904–6920.
- 3 R. Asahi, T. Morikawa, H. Irie and T. Ohwaki, *Chem. Rev.*, 2014, **114**, 9824–9852.
- 4 N. Alonso-Vante, *Chalcogenide Materials for Solar Energy Conversion*, Springer, 2018.
- 5 J. Moan, in *Radiation at home, outdoors and in the workplace*, ed. D. Brune, R. Hellborg, B. Persson and R. Pääkkönen, Scandinavian Science Publisher, Oslo, 2001, pp. 69–85.
- 6 G. Liu, L. Wang, H. G. Yang, H. M. Cheng and G. Q. Lu, *J. Mater. Chem.*, 2010, **20**, 831–843.
- 7 X. Chen, L. Liu, P. Y. Yu and S. S. Mao, *Science*, 2011, **331**, 746–750.
- 8 A. J. Molina-Mendoza, M. Barawi, R. Biele, E. Flores, J. R. Ares, C. Sánchez, G. Rubio-Bollinger, N. Agraït, R. D'Agosta, I. J. Ferrer and A. Castellanos-Gomez, *Adv. Electron. Mater.*, 2015, **1**, 1500126.
- 9 J. Kang, H. Sahin, H. D. Ozyaydin, R. T. Senger and F. M. Peeters, *Phys. Rev. B: Condens. Matter Mater. Phys.*, 2015, **92**, 075413.
- 10 J. Kang and L. W. Wang, *Phys. Chem. Chem. Phys.*, 2016, **18**, 14805–14809.
- 11 F. A. Rasmussen and K. S. Thygesen, *J. Phys. Chem. C*, 2015, **119**, 13169–13183.
- 12 *Materials Nanoarchitectonics*, ed. K. Ariga and M. Ebara, Wiley-VCH, 2018.
- 13 L. Wang and T. Sasaki, *Chem. Rev.*, 2014, **114**, 9455–9486.
- 14 *Photocatalysis and Water Purification: From Fundamentals to Recent Applications*, ed. P. Pichat, Wiley-VCH, 2013.
- 15 Y. Li, Y. L. Li, B. Sa and R. Ahuja, *Catal. Sci. Technol.*, 2017, **7**, 545–559.
- 16 H. Zhang, *ACS Nano*, 2015, **9**, 9451–9469.
- 17 M. Arsentev, A. Missyul, A. V. Petrov and M. Hammouri, *J. Phys. Chem. C*, 2017, **121**, 15509–15515.
- 18 N. Tanibata, T. Matsuyama, A. Hayashi and M. Tatsumisago, *J. Power Sources*, 2015, **275**, 284–287.
- 19 J. Wu, D. Wang, H. Liu, W.-M. Lau and L.-M. Liu, *RSC Adv.*, 2015, **5**, 21455–21463.
- 20 A. Lipatov, P. M. Wilson, M. Shekhirev, J. D. Teeter, R. Netusil and A. Sinitskii, *Nanoscale*, 2015, **7**, 12291–12296.
- 21 J. O. Island, M. Barawi, R. Biele, A. Almazán, J. M. Clamagirand, J. R. Ares, C. Sánchez, H. S. J. Van Der Zant, J. V. Álvarez, R. D'Agosta, I. J. Ferrer and A. Castellanos-Gomez, *Adv. Mater.*, 2015, **27**, 2595–2601.
- 22 M. Barawi, E. Flores, I. J. Ferrer, J. R. Ares and C. Sánchez, *J. Mater. Chem. A*, 2015, **3**, 7959–7965.
- 23 E. Flores, J. R. Ares, I. J. Ferrer and C. Sánchez, *Phys. Status Solidi RRL*, 2016, **10**, 802–806.
- 24 C. Hawkins and L. Whittaker-Brooks, *ACS Appl. Nano Mater.*, 2018, **1**, 851–859.
- 25 A. Zaleska-Medynska, *Metal Oxide-Based Photocatalysis: Fundamentals and Prospects for Application*, Elsevier, 2018.
- 26 M. Long and L. Zheng, *Chin. J. Catal.*, 2017, **38**, 617–624.
- 27 K. S. Ranjith and T. Uyar, *J. Mater. Chem. A*, 2017, **5**, 14206–14219.
- 28 R. M. A. Lieth and J. C. J. M. Terhell, in *Preparation and Crystal Growth of Materials with Layered Structures*, ed. R. M. A. Lieth, Springer Science+Business Media, B.V., 1977, pp. 141–223.
- 29 H. P. B. Rimmington, A. A. Balchin and B. K. Tanner, *J. Cryst. Growth*, 1972, **15**, 51–56.
- 30 J. O. Island, A. J. Molina-Mendoza, M. Barawi, R. Biele, E. Flores, J. M. Clamagirand, J. R. Ares, C. Sánchez, H. S. J. Van Der Zant, R. D'Agosta, I. J. Ferrer and A. Castellanos-Gomez, *2D Mater.*, 2017, **4**, 022003.
- 31 S. Okeil, J. Krausmann, I. Dönges, S. Pflieger, J. Engstler and J. J. Schneider, *Dalton Trans.*, 2017, **46**, 5189–5201.
- 32 M. Chhowalla, H. S. Shin, G. Eda, L. J. Li, K. P. Loh and H. Zhang, *Nat. Chem.*, 2013, **5**, 263–275.

- 33 A. V. Kolobov and J. Tominaga, *Springer Series in Materials Science, Vol. 239: Two-dimensional Transition-metal Dichalcogenides*, Springer International Publishing, Switzerland, 2016.
- 34 J. Dai, M. Li and X. C. Zeng, *Wiley Interdiscip. Rev.: Comput. Mol. Sci.*, 2016, **6**, 211–222.
- 35 S. K. Srivastava and B. N. Avasthi, *J. Mater. Sci.*, 1992, **27**, 3693–3705.
- 36 R. R. Chianelli and M. B. Dines, *Inorg. Chem.*, 1975, **14**, 2417–2421.
- 37 *Crystallography and crystal chemistry of materials with layered structures*, ed. F. Lévy, D. Reidel Publishing Company, Dordrecht, Holland, 1976.
- 38 J. Benard and Y. Jeannin, *Nonstoichiometric Compounds*, American Chemical Society, 1963, pp. 191–203.
- 39 J. L. Murray, *Bull. Alloy Phase Diagrams*, 1986, **7**, 156–163.
- 40 A. S. Pawbake, J. O. Island, E. Flores, J. R. Ares, C. Sanchez, I. J. Ferrer, S. R. Jadhkar, H. S. J. Van Der Zant, A. Castellanos-Gomez and D. J. Late, *ACS Appl. Mater. Interfaces*, 2015, **7**, 24185–24190.
- 41 J. I. Goldstein, D. E. Newbury, P. Echlin, D. C. Joy, C. E. Lyman, E. Lifshin, L. Sawyer and J. R. Michael, *Scanning Electron Microscopy and X-ray Microanalysis*, Springer, Boston, MA, 2003.
- 42 H. S. Wong and N. R. Buenfeld, *Cem. Concr. Res.*, 2006, **36**, 1076–1082.
- 43 H. Hantsche, *Scanning*, 1989, **11**, 257–280.
- 44 D. Gonbeau, C. Guimon, G. Pfister-Guillouzo, A. Levasseur, G. Meunier and R. Dormoy, *Surf. Sci.*, 1991, **254**, 81–89.
- 45 F. Fedorov, M. Vasilkov, A. Lashkov, A. Varezchnikov, D. Fuchs, C. Kübel, M. Bruns, M. Sommer and V. Sysoev, *Sci. Rep.*, 2017, **7**, 9732.
- 46 N. Zydziak, C. Hübner, M. Bruns and C. Barner-Kowollik, *Macromolecules*, 2011, **44**, 3374–3380.
- 47 M. E. Fleet, S. L. Harmer, X. Liu and H. W. Nesbitt, *Surf. Sci.*, 2005, **584**, 133–145.
- 48 A. J. Huckaba, S. Gharibzadeh, M. Ralaiarisoa, C. Roldán-Carmona, N. Mohammadian, G. Grancini, Y. Lee, P. Amsalem, E. J. Plichta, N. Koch, A. Moshaii and M. K. Nazeeruddin, *Small Methods*, 2017, **1**, 1700250.
- 49 C. Kleber, M. Bruns, K. Lienkamp, J. Rühle and M. Asplund, *Acta Biomater.*, 2017, **58**, 365–375.
- 50 R. Moret, M. Huber and R. Comès, *Phys. Status Solidi A*, 1976, **38**, 695–700.
- 51 A. I. Gusev, *Phys.-Usp.*, 2006, **49**, 693–718.
- 52 P. Gard, F. Cruege, C. Sourisseau and O. Gorochov, *J. Raman Spectrosc.*, 1986, **17**, 283–288.
- 53 P. C. Sherrell, K. Sharda, C. Grotta, J. Ranalli, M. S. Sokolikova, F. M. Pesci, P. Palczynski, V. L. Bemmer and C. Mattevi, *ACS Omega*, 2018, **3**, 8655–8662.
- 54 T. Ohsaka, F. Izumi and Y. Fujiki, *J. Raman Spectrosc.*, 1978, **7**, 321–324.
- 55 M. Ishii, M. Saeki and I. Kawada, *Phys. Status Solidi A*, 1984, **124**, K109–K112.
- 56 M. T. Uddin, Y. Nicolas, C. Olivier, W. Jaegermann, N. Rockstroh, H. Junge and T. Toupance, *Phys. Chem. Chem. Phys.*, 2017, **19**, 19279–19288.
- 57 C. Tan and H. Zhang, *Chem. Soc. Rev.*, 2015, **44**, 2713–2731.
- 58 J. Zhang, S. Meng, X. Ye, C. Ling, S. Zhang, X. Fu and S. Chen, *Appl. Catal., B*, 2017, **218**, 420–429.
- 59 F. Ahmadi, M. Rahimi-Nasrabadi, A. Fosooni and M. Daneshmand, *J. Mater. Sci.: Mater. Electron.*, 2016, **27**, 9514–9519.
- 60 V. R. Posa, V. Annavaram, J. R. Koduru, V. R. Ammireddy and A. R. Somala, *Korean J. Chem. Eng.*, 2016, **33**, 456–464.
- 61 Y. Li, H. Zhao and M. Yang, *J. Colloid Interface Sci.*, 2017, **508**, 500–507.
- 62 R. Cai, B. Zhang, J. Shi, M. Li and Z. He, *ACS Sustainable Chem. Eng.*, 2017, **5**, 7690–7699.
- 63 B. Xu, Y. Li, Y. Gao, S. Liu, D. Lv, S. Zhao, H. Gao, G. Yang, N. Li and L. Ge, *Appl. Catal., B*, 2019, **246**, 140–148.
- 64 S. N. Basahel, T. T. Ali, M. Mokhtar and K. Narasimharao, *Nanoscale Res. Lett.*, 2015, **10**, 73.
- 65 Z. Tong, D. Yang, J. Shi, Y. Nan, Y. Sun and Z. Jiang, *ACS Appl. Mater. Interfaces*, 2015, **7**, 25693–25701.
- 66 C. Chen, W. Cai, M. Long, B. Zhou, Y. Wu, D. Wu and Y. Feng, *ACS Nano*, 2010, **4**, 6425–6432.
- 67 Z. Hu, Z. Wu, C. Han, J. He, Z. Ni and W. Chen, *Chem. Soc. Rev.*, 2018, **47**, 3100–3128.
- 68 Y. Wang, Q. Wang, X. Zhan, F. Wang, M. Safdar and J. He, *Nanoscale*, 2013, **5**, 8326–8339.
- 69 J. Fu, J. Yu, C. Jiang and B. Cheng, *Adv. Energy Mater.*, 2018, **8**, 1701503.
- 70 F. Obstals, M. Vorobii, T. Riedel, A. de los Santos Pereira, M. Bruns, S. Singh and C. Rodriguez-Emmenegger, *Macromol. Biosci.*, 2018, **18**, 1700359.
- 71 M. Bruns, C. Barth, P. Brünner, S. Engin, T. Grehl, C. Howell, P. Koelsch, P. Mack, P. Nagel, V. Trouillet, D. Wedlich and R. G. White, *Surf. Interface Anal.*, 2012, **44**, 909–913.
- 72 E. Blasco, M. Piñol, L. Oriol, B. V. K. J. Schmidt, A. Welle, V. Trouillet, M. Bruns and C. Barner-Kowollik, *Adv. Funct. Mater.*, 2013, **23**, 4011–4019.

2.3 Controlling surface morphology and sensitivity of granular and porous silver films for surface-enhanced Raman scattering, SERS

The development of efficient surface-enhanced Raman scattering (SERS) substrates is crucial to exploit the great potential of SERS in trace analysis of different analytes which requires the development of methods enabling the ease fabrication of efficient SERS substrates at low cost. Plasma technology has advanced in the previous decades and has been widely used in industry for different applications where different surface modifications for a wide range of materials can be achieved in a short time at ambient temperatures without the need for toxic or polluting chemicals and solvents. Although plasma technology has been widely used for the treatment of metal surfaces in microelectronics such as cleaning and etching purposes, it has been not widely investigated for the production of SERS substrates till date.

In this work, silver films of different thicknesses (10 nm and 200 nm) have been sputtered on glass substrates and have been subjected to different plasma treatments in order to investigate the effect of different plasma gases together with different parameters such as the plasma power, gas flow rate and treatment time on the morphology and surface roughness of the treated silver films. The use of hydrogen, nitrogen and argon plasma treatment of sputtered silver films results in an increase of the surface roughness due to the ion bombardment of the silver films during plasma treatment, thus increasing the SERS performance of these SERS substrates. Combining different plasma treatments could even result in complex structures starting from a smooth silver film which enables the fabrication of highly efficient SERS substrates. Treating silver films with oxygen or air plasma resulting in the oxidation of silver followed by a reductive treatment with hydrogen, nitrogen or argon plasma results in highly porous silver films. These oxidation-reduction cycles resemble the electrochemical surface roughening of silver but do not require the preparation of electrolyte solutions and the structures obtained can be simply tuned by the treatment conditions, thus being able to fabricate substrates with different enhancement factors.

Thin silver films of about 10 nm thickness offer the advantage of being transparent enabling the fabrication of transparent SERS substrates while thicker silver films of about 200 nm enable the formation of complex three-dimensional silver structures upon subsequent oxidative-reductive plasma treatment. Plasma treatment also offers a surface cleaning opportunity for SERS substrates where mild argon plasma treatment was shown to restore the SERS substrate after initial use or long-term storage by removing the measured analyte or the formed surface oxidation without serious surface modifications enabling re-use of the same silver substrate for several times.



Controlling surface morphology and sensitivity of granular and porous silver films for surface-enhanced Raman scattering, SERS

Sherif Okeil and Jörg J. Schneider*

Full Research Paper

Open Access

Address:
Eduard-Zintl-Institut für Anorganische und Physikalische Chemie,
Technische Universität Darmstadt, Alarich-Weiss-Straße 12, 64287
Darmstadt, Germany

Email:
Jörg J. Schneider* - joerg.schneider@ac.chemie.tu-darmstadt.de

* Corresponding author

Keywords:
plasma treatment; silver; sputtering; surface-enhanced Raman
spectroscopy (SERS); surface roughening

Beilstein J. Nanotechnol. 2018, 9, 2813–2831.
doi:10.3762/bjnano.9.263

Received: 22 May 2018
Accepted: 30 September 2018
Published: 07 November 2018

Associate Editor: C. Jagadish

© 2018 Okeil and Schneider; licensee Beilstein-Institut.
License and terms: see end of document.

Abstract

The design of efficient substrates for surface-enhanced Raman spectroscopy (SERS) for large-scale fabrication at low cost is an important issue in further enhancing the use of SERS for routine chemical analysis. Here, we systematically investigate the effect of different radio frequency (rf) plasmas (argon, hydrogen, nitrogen, air and oxygen plasma) as well as combinations of these plasmas on the surface morphology of thin silver films. It was found that different surface structures and different degrees of surface roughness could be obtained by a systematic variation of the plasma type and condition as well as plasma power and treatment time. The differently roughened silver surfaces act as efficient SERS substrates showing greater enhancement factors compared to as prepared, sputtered, but untreated silver films when using rhodamine B as Raman probe molecule. The obtained roughened silver films were fully characterized by scanning electron microscopy (SEM), atomic force microscopy (AFM), X-ray diffraction (XRD), transmission electron microscopy (TEM), X-ray photoelectron (XPS and Auger) and ultraviolet–visible spectroscopy (UV–vis) as well as contact angle measurements. It was found that different morphologies of the roughened Ag films could be obtained under controlled conditions. These silver films show a broad range of tunable SERS enhancement factors ranging from 1.93×10^2 to 2.35×10^5 using rhodamine B as probe molecule. The main factors that control the enhancement are the plasma gas used and the plasma conditions, i.e., pressure, power and treatment time. Altogether this work shows for the first time the effectiveness of a plasma treatment for surface roughening of silver thin films and its profound influence on the interface-controlled SERS enhancement effect. The method can be used for low-cost, large-scale production of SERS substrates.

Introduction

The great enhancement of Raman signals obtained from molecules when they are in close vicinity to a rough noble-metal surface (e.g., gold, silver and copper) has attracted a great deal of interest in the last decades [1]. This phenomenon, called surface-enhanced Raman scattering [2,3], depends on the fact that incident light leads to the excitation of surface plasmon reso-

nances, which in turn lead to a concentration of the incident electromagnetic field thus enhancing the Raman scattering effect. This effect is even further enhanced by the presence of so called hot spots, which are sub-10 nm gaps where the electromagnetic field is further magnified due to constructive interference of the plasmon resonances [4]. Electromagnetic enhancement is the main reason for the observed Raman enhancement and depends on the local electromagnetic field at the metal surface while the chemical enhancement depends on the analyte itself and results from an effective charge transfer between the noble metal and the adsorbed probe molecule [5,6].

While the Raman effect is intrinsically weak and typically does not permit the analysis of low concentrations, the SERS signal dramatically enhances the sensitivity typically by orders of magnitude and allows for the analysis of low analyte concentrations [5,7]. The fabrication of SERS substrates began with electrochemical oxidation/reduction cycles especially of silver electrodes. This is the most widely studied synthesis and is still subject to further investigation and optimization to obtain more efficient SERS substrates [2,8-11]. One modification of the electrochemical fabrication of SERS substrates involves the electrochemical etching of silver to obtain porous silver nanostructures [12]. Other routes include the use of gold or silver nanoparticles of different shapes in solution and their assembly on a solid substrate [6,13-17], nanosphere lithography [18-25] as well as nanolithography and nanoimprinting [26-34]. Additional methods appeared in which nanoparticles or metal films are deposited on structured substrates as carbon nanotubes [35-39], graphene foam [40], nanorod or nanopillar arrays [41,42], biological scaffolds [43,44], black silicon [45,46], anisotropically etched single-crystal silicon [47], plasma-treated plastic [48] and anodic aluminum oxide films [49-52]. Some methods aim at the fabrication of three-dimensional silver or gold structures, such as oblique-angle vapor deposition used for the fabrication of silver nanorod arrays [53-56], and nanotransfer printing, which was used to build stacks of gold nanorods or nanowires [4]. The production of nanoporous metal films or particles through a dealloying process also emerged as an effective tool for the facile formation of a large number of SERS-active hot spots [57-60]. Recently, other methods emerged with the aim of producing SERS substrates at low cost, enabling their large-scale production. These methods include inkjet-printing and pen-on-paper approaches [61,62].

Plasma treatment has been widely used for the last decades for microelectronics and surface modification in industry [63,64]. A large variety of plasmas exist depending on the excitation source, the operating pressure and the device geometry [63,65]. Advantages of the use of a radio frequency (rf) plasma for chemical modification is that no hazardous chemicals and sol-

vents are involved. Moreover, it enables a quick chemical modification under ambient conditions in the gas phase [64,66-71]. Thus, plasma treatment could present a straightforward and affordable alternative to the electrochemical roughening of silver and can be even used as a technological reliable alternative for the production of SERS substrates. Interestingly, up to date the use of plasma treatment for SERS applications is still limited [72,73] despite its high potential in modifying metal surfaces. Especially a systematic study is lacking.

Herein we report on our studies towards a systematic investigation of the effect of different rf plasmas on sputtered silver surfaces to determine the potential of plasma treatment in a controlled increase of the surface roughness of silver as well as the formation of hot spots on the silver surface for the use in SERS. To the best of our knowledge this is the first systematic investigation in that direction.

Experimental

Preparation of sputtered silver films

Thin films of silver were sputtered on glass substrates cleaned with acetone. Different thicknesses of silver were sputtered using a benchtop Cressington 208HR sputter coater in which the thickness of the sputtered silver layer was monitored by a MTM-20 high-resolution thickness controller. The sputtered silver films are named according to the thickness indicated by the thickness controller. A silver target (99.99%) from Evochem with 57 mm diameter and 0.2 mm thickness was used as sputter target. The deposition rate used was about 0.4 nm/s at a chamber pressure of about 0.05 mbar.

Plasma treatment of the prepared silver films

The sputtered silver films of different thicknesses were treated with different plasma gases using a capacitively coupled rf plasma apparatus operated at 13.56 MHz (Diener electronic, model Femto, Germany) with a maximum power of 200 W. After introduction of the sample into the plasma chamber, where the sample was placed on the lower electrode, the chamber was evacuated to a pressure below 0.2 mbar. Then the gas to be used for plasma treatment was introduced at a specified flow rate, controlled by a mass flow controller. When the pressure in the plasma chamber achieved its equilibrium the radio frequency controller was switched on at a specified power and left for a defined period of time to obtain the desired plasma treatment for the silver films. The operating temperature was set at 25 °C but heating occurred during the plasma treatment depending on the plasma treatment time. The gases used for plasma treatment were argon at a pressure of 1.5 mbar for a flow rate of 16.7 sccm, nitrogen at a pressure of 0.8 mbar for a flow rate of 12 sccm, hydrogen at a pressure of 0.22 mbar for a flow rate of 6 sccm and 0.38 mbar for a flow rate of 12 sccm,

oxygen at a pressure of 0.4 mbar for a flow rate of 6 sccm and 0.8 mbar for a flow rate of 12 sccm, and finally air at a pressure of 0.8 mbar for a flow rate of 12 sccm. When describing the experiments, the used gases get a notation according to the gas flow and power used for the plasma treatment, i.e., a plasma gas with the notation g12-p200 indicates a gas flow of 12 sccm and a power of 200 W, which was used for almost all samples unless otherwise indicated. For simplicity, any sample without notation for gas flow and power has been synthesized using 12 sccm gas flow and a power of 200 W except for argon plasma where the standard gas flow used is 16.7 sccm. Samples obtained under other conditions will get a notation stating the gas flow and power used.

Characterization of the as-prepared silver films

The prepared silver films were characterized using atomic force microscopy (AFM) in contact mode on a CP-II AFM (Bruker-Veeco) with SiC cantilevers to determine the topography and surface roughness (root mean square roughness, R_q). Scanning electron microscopy (SEM) of the silver films was performed on a Philips XL-30 FEG using an electron beam at 25 kV. Cross-sectional transmission electron microscopy (TEM) images of the silver films were recorded using a Tecnai G2 F20 microscope operating at 200 kV after the use of focused-ion beam (FIB) for sample preparation [74]. X-ray diffraction (XRD) was performed on a Rigaku Miniflex 600@40 kV 15 mA diffractometer using Cu $K\alpha_1$ radiation ($\lambda = 1.541 \text{ \AA}$). XPS measurements were performed using a K-Alpha XPS spectrometer (ThermoFischer Scientific, East Grinstead, UK). Data acquisition and processing was done using the Thermo Avantage software. All samples were analyzed using a microfocused, monochromated Al $K\alpha$ X-ray source (30–400 μm spot size). The K-Alpha charge compensation system was employed during analysis, using electrons of 8 eV energy and low-energy argon ions to prevent any localized charge build-up. Auger spectroscopy was performed using a PHI 680 (Physical Electronics) scanning Auger nanoprobe operated at an acceleration voltage of 20 keV and a current of 10 nA. Sputtering was carried out under ultra-high vacuum (5×10^{-9} Torr), with an argon gun operated at 250 eV and 500 nA. The UV–vis spectra of the silver films on glass substrate were recorded by a Thermo Scientific UV–vis spectrophotometer (Evolution 600). The water contact angle was measured using a Krüss DSA 30 model drop-shape analysis system. The water contact angle was measured by placing 5 μL water droplets on the silver surface.

Atomic layer deposition (ALD) of Al_2O_3

Silver films on glass substrates were inserted into the ALD chamber (Savannah G2, Ultratech/CNT, Cambridge Nanotech) for deposition of a 1 nm thick layer of Al_2O_3 using trimethyl-

aluminium (98+%, Strem Chemicals, Inc.) and water (HPLC grade, Sigma Aldrich) as precursors at 200 °C. The precursors were vaporized at room temperature and 20 sccm argon was used as carrier gas. The exposure time for both, trimethylaluminium and water, were 0.015 s and the flushing between the precursor pulses was done with argon for 5 s. For deposition of 1 nm Al_2O_3 ten cycles were carried out.

SERS measurements on the prepared silver films

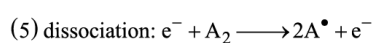
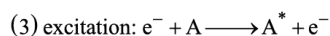
Rhodamine B (RhB) was used as Raman probe to compare the performance of the different silver films. A 10^{-6} M solution of RhB was prepared in deionized water. A sufficient amount of this solution was dropped on the surface of the silver SERS substrates to cover the surface completely. The SERS substrate was left for 30 min in the aqueous RhB solution to enable the adsorption of the RhB on the silver surface. After that the SERS substrate was rinsed with deionized water to remove any excess of the RhB. The performance of the different SERS substrates was then evaluated through the measurement of the SERS spectra of RhB using a Horiba Jobin-Yvon LabRAM HR800 micro-Raman spectrometer employing a 514.5 nm Ar laser and a $10\times$ objective ($\text{NA} = 0.25$), and a measurement time of 30 s with a laser power of 1.0 mW. Alternatively, a 632.8 nm HeNe laser using a $50\times$ LWD objective ($\text{NA} = 0.5$) and a measurement time of 30 s with a laser power of 2.0 mW was used. For Raman mapping as well as single scans another Raman setup (Alpha300 R micro-Raman, WITec, Germany) with a Nd:YAG 532 nm laser was used. The samples were exposed to the laser with a power of 1.0 mW through a $50\times$ microscope objective ($\text{NA} = 0.80$) resulting in a spot size of about 0.8 μm . SERS spectra were collected using 1 s as integration time for single scans. For Raman mapping a $30 \mu\text{m} \times 30 \mu\text{m}$ area was scanned, collecting 900 points (30 lines with 30 points each). The same parameters as for single scans were used. A commercial SERS substrate provided from Abacus (Analytical Systems GmbH) consisting of silver nanoparticles on a paper substrate was used for comparison.

Results and Discussion

Processing and characterization of sputtered and plasma-treated silver films

Radio frequency plasma is generated through exposing the feed gas to an external radio frequency field using a frequency of 13.56 MHz. The setup consists simply of two parallel plates about 10 cm apart where the substrate is placed on the bottom electrode. These electrodes are connected to radio frequency generator generating the alternating electric field at 13.56 MHz frequency (Scheme S1, Supporting Information File 1). At this frequency, electrons quickly respond to any minor changes in the electric field thus gaining a significant amount of energy.

When these highly energetic electrons collide with the feed gas atoms or molecules this results into a series of successive complex processes, namely ionization (1 and 2), excitation (3) and relaxation (4) as well as dissociation in case of diatomic species (5) [75]:



Thus controlled rf plasma treatment is a very interesting technique for the modification of surfaces as a number of different chemical species can be generated at low temperature in the gas phase, which can strongly interact with the exposed surface leading to distinct physical and chemical changes [63,76]. Therefore, it is interesting to investigate the influence of different kinds of rf plasmas on the surface of thin silver films, which are important substrates for SERS applications due to their great SERS enhancement factors. The question is whether plasma treatment can beneficially modify the thin silver films leading to an enhancement of their SERS activity or vice versa. Scheme 1 gives an overview of the steps performed in fabrication of the SERS substrates and their subsequent studies.

As-sputtered silver films

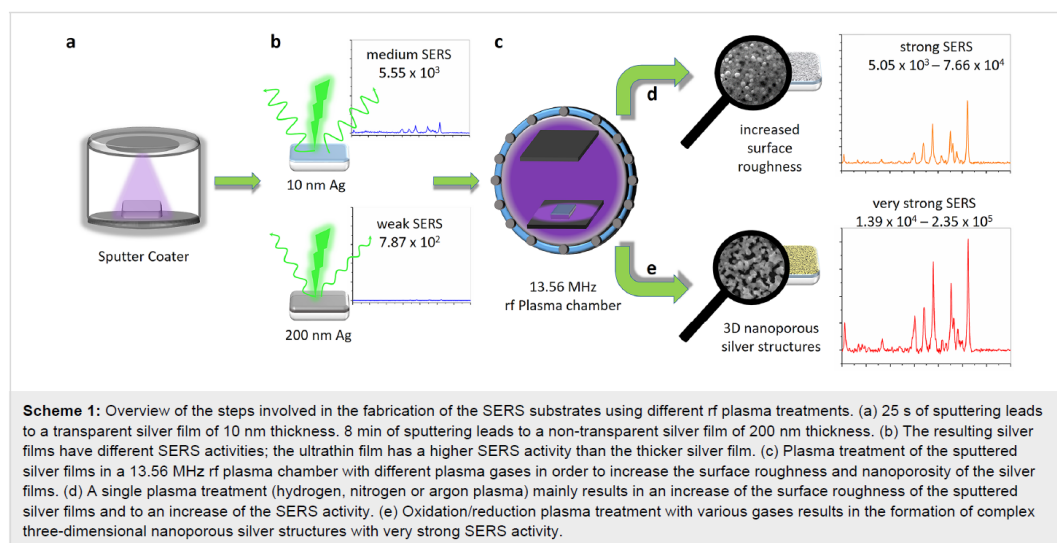
Different thicknesses of silver have been sputtered on cleaned glass substrates. At very low thicknesses up to about 20 nm a

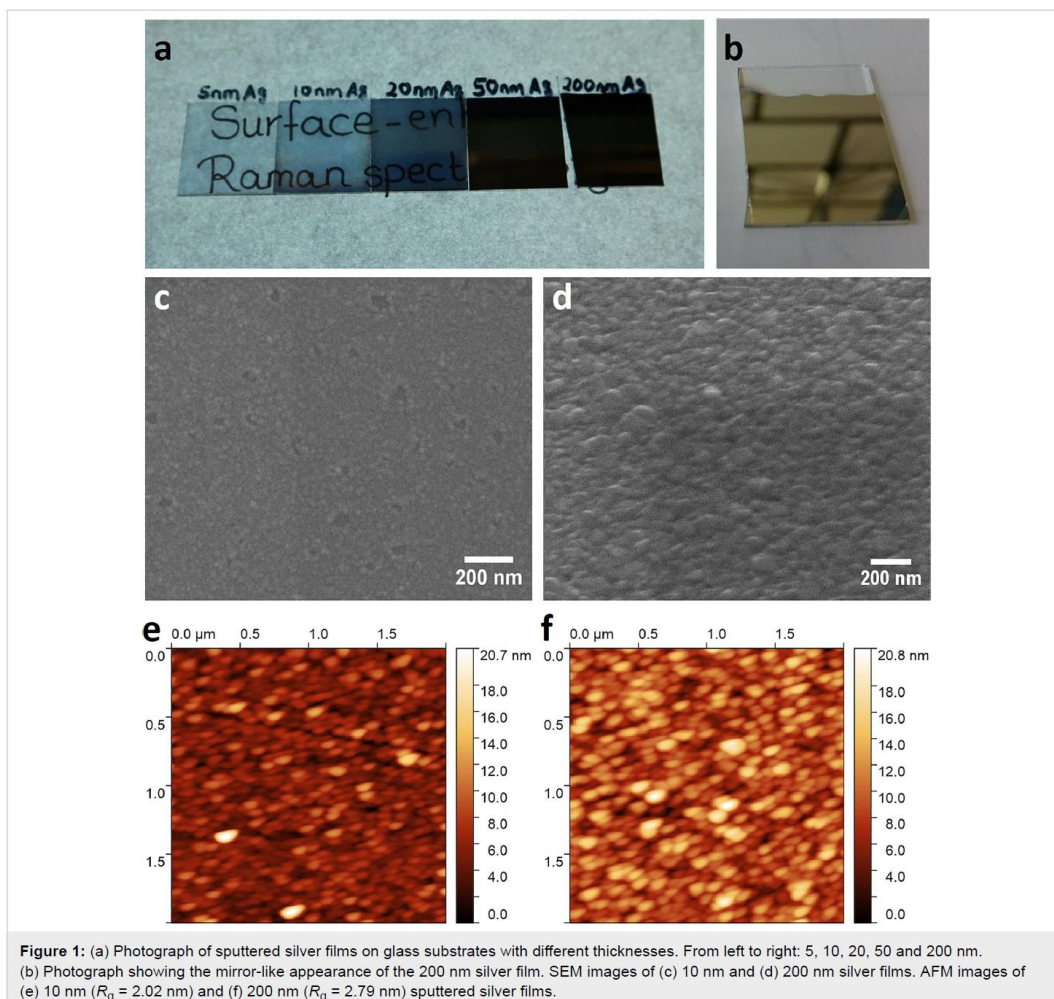
transparent silver film could be observed, which became increasingly reflective and finally non-transparent with increasing thickness (Figure 1a,b).

Low-magnification SEM images of freshly sputtered silver films (10 and 200 nm) show no significant structural features, which confirms the uniformity of the sputtered silver films. In the 10 nm thick silver film small grains adjacent to each other together with some voids are observed due island formation during sputtering (Figure 1c,d) [77]. The granular morphology could be advantageous for the formation of hot spots resulting in an efficient SERS activity of the silver film. For the 200 nm thick silver film the coalescence of the adjacent silver clusters formed in the early stages of the sputtering deposition is visible, leading to a continuous silver film having a visible surface roughness. The sputter deposition yields silver films with a certain surface roughness (Figure 1e,f), which appears to be useful for SERS applications. However, in order to increase this initial surface roughness even more and to create further potential hot spots for increased SERS performance, systematic rf plasma treatments under different conditions were investigated.

Formation of hydrogen plasma treated silver films

Employing hydrogen plasma treatment (200 W) using a gas flow rate of 12 sccm results in a chamber pressure of 0.38 mbar. The maximum treatment time was set to 2 min for the ultrathin 10 nm silver films. For the 200 nm silver hydrogen plasma treatment was performed for 5, 15, 30 and 45 min. The SEM images in Figure 2 and Figure S1 (Supporting Information File 1) reveal black spots on the silver surface that become





darker and increase in size with increasing hydrogen plasma treatment time. These areas show the formation of holes in the silver film which deepen and increase in size with increasing hydrogen plasma treatment time. Using AFM (Figure S2, Supporting Information File 1) it shows that surface roughness increases from 2.02 nm for an untreated silver film to 5.03 nm for 5 min, 6.29 nm for 15 min and 6.85 nm for 45 min hydrogen plasma treatment time. The relatively small increase in surface roughness when going from 15 to 45 min can be explained by the fact that with increasing hydrogen plasma treatment time the etched holes become deeper but at the same time silver is etched away from the surface leading to a decrease in the overall film thickness. Thus, the overall peak-to-valley distance will not change much. A cross-sectional SEM of the silver films before and after hydrogen plasma treatment (Figure 2d) clearly reveals

the presence of holes as well as a decrease in the silver film thickness from about 152 nm to about 71 nm supporting the claim that the silver is effectively etched away by hydrogen plasma with an average etch rate of 2.7 nm/min. Etching of silver films by means of hydrogen plasma in an inductively coupled plasma system has also been previously observed and the reasons for this etching could be ion bombardment leading to physical sputtering together with chemical etching for which the formation of a silver dihydride anion (AgH_2^-) as etching product has been suggested as it is more stable than silver hydride [78]. As can be seen in the top SEM images (Figure 2a–c) and in the cross-sectional SEM images (Figure 2d) holes are formed in the silver film, which increase in size and depth with increasing hydrogen plasma treatment time. The formation of the holes can be mainly attributed to

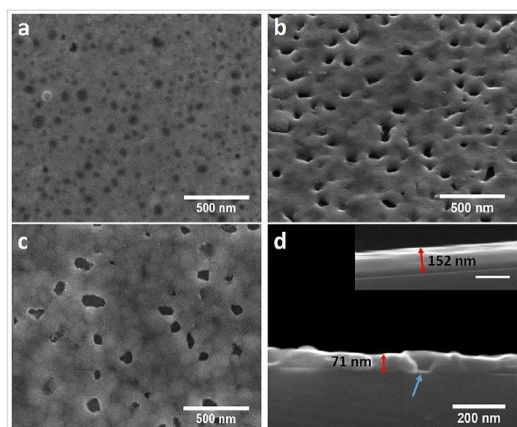


Figure 2: SEM image of a 200 nm sputtered silver film treated with hydrogen plasma (g12-p200) for (a) 5 min, (b) 30 min (taken at 45° tilt) and (c) 45 min at 100000× magnification showing the formation of etched holes and increasing grain structure of the silver film. (d) Cross-sectional SEM image of a 200 nm sputtered silver film after 30 min of hydrogen plasma treatment (g12-p200) depicting the actual lowered thickness of the hydrogen plasma-treated silver films compared to the as-sputtered silver film seen in the inset (scale bar: 200 nm). The blue arrow indicates a hole in the hydrogen plasma treated silver film.

physical sputtering of silver due to ion bombardment. But at the same time there is a homogenous decrease in the thickness of the silver film, which would point to a chemical etching process that takes place over the whole area exposed to the plasma. Other samples treated with hydrogen plasma using different plasma gas flow conditions and plasma power show the ability of this process for tuning the surface morphology and roughness further (Figure S3, Supporting Information File 1).

Formation of nitrogen plasma treated silver films

Treatment of the 200 nm thick silver films with a nitrogen rf plasma does create a groove-like morphology, which transforms over time (10–60 min) into deeper voids (Figure 3 and Figure S4, Supporting Information File 1). This comes along with an increasing particle formation with increasing treatment time (from 10 to 30 min). Furthermore, a faceting of the silver film underlying the formed nanoparticles is visible, which becomes more prominent with increasing nitrogen plasma treatment time from 10 to 60 min (Figure 3a–c). For the ultrathin 10 nm film as well as for the 50 nm film, this granular and faceted surface can be also observed depending on the nitrogen plasma treatment time (Figure S5, Supporting Information File 1). AFM analysis (Figure S6, Supporting Information File 1) revealed a significant increase in the surface roughness of the 200 nm silver films treated with nitrogen plasma, depending on the treatment time. After 10 min of nitrogen plasma treatment, the surface roughness R_q was 5.12 nm and

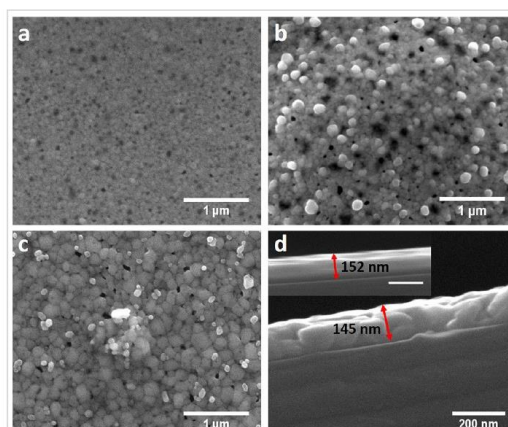


Figure 3: SEM image of a 200 nm sputtered silver film treated with nitrogen plasma (g12-p200) for (a) 10 min, (b) 30 min and (c) 60 min at 50000× magnification. (d) Cross-sectional SEM image of 200 nm sputtered silver film treated with nitrogen plasma (g12-p200) for 30 min showing the actual thickness of the prepared silver film after nitrogen plasma treatment compared to the as-sputtered silver film seen in the inset (scale bar is 200 nm).

reached 23.1 nm after 60 min of treatment. The formation of grooves, which is also observed after hydrogen plasma treatment, is a result of the physical sputtering effect of the silver surface. However, the formation of a particulate morphology and the faceting of the silver surface is best explained by an anisotropic etching or a restructuring process of the silver surface by reactive nitrogen plasma species such as N_2^+ , N_2^* (excited nitrogen), N^{++} and N^* (nitrogen radicals) [79]. The faceting of the silver surface depends on the plasma treatment time when using varying nitrogen plasma treatment parameters and leads to different structural characteristics with respect to the surface roughness (Figure S7 and Figure S8, Supporting Information File 1).

A cross-sectional SEM image of a nitrogen plasma treated silver film (Figure 3d) shows a slight decrease in film thickness compared to untreated silver films, which indicates minor etching by the nitrogen plasma mainly due to ion bombardment. A reasonable explanation for the restructuring of the silver surface, which leads to particle formation and surface faceting could be the in situ formation of silver nitride, which directly decomposes to metallic silver and nitrogen gas [80]. This dynamic process of incorporation of nitrogen followed by its extrusion could lead to a granular structure of the silver surface.

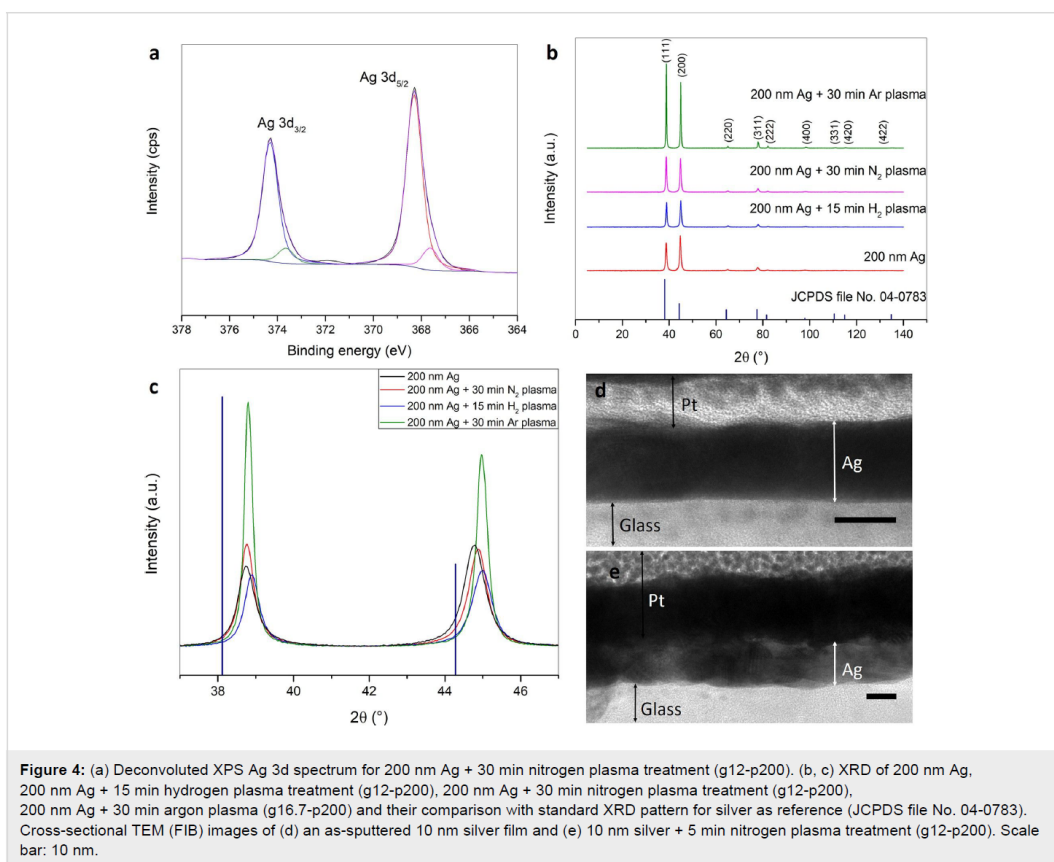
Materials characterization of hydrogen and nitrogen plasma treated silver films

Neither XPS analysis nor Auger spectroscopy could detect the presence of nitrogen in the nitrogen plasma treated samples

(Figure 4a and Figures S9–S11 and Table S1 and Table S2, Supporting Information File 1). Even depth profiling using Auger spectroscopy did not reveal any traces of nitrogen (Figure S12, Supporting Information File 1). For further insight, the XPS spectra of untreated sputtered silver, hydrogen plasma treated silver and nitrogen plasma treated silver was compared. The comparison of the Ag 3d peaks obtained for the three samples shows that there is a slight broadening in the direction of lower binding energies for nitrogen plasma treated silver (Figure 4a and Figure S9a, Supporting Information File 1). Only for the nitrogen plasma treated silver film, a second small peak at 367.63 eV can be fitted besides the main peak at 368.30 eV in the silver 3d peaks (Figure 4a and Figure S9b,c, Supporting Information File 1). Auger spectroscopy of the nitrogen plasma treated silver film shows a typical spectrum in which only the elements silver, carbon, oxygen, and no nitrogen, can be found (Figure S9d, Supporting Information File 1). The reference position of the different elements [81] was inserted and there is a small shift of the silver peak relative to the reference value. The presence of carbon and oxygen,

which were also detected by XPS, is due to adventitious carbon and chemisorbed oxygen as the sample was in contact with the atmosphere before the measurement. Although XPS and Auger measurements could not detect nitrogen functionalization on the metal surface, these techniques do reveal that nitrogen plasma treated silver films differ slightly from the as-sputtered films and from the hydrogen plasma treated films. This indicates, together with the different surface structure, a dedicated influence of the nitrogen plasma in addition to the impact of nitrogen ions on the silver surface.

XRD analysis of the 200 nm as-sputtered silver film as well as hydrogen, nitrogen and argon plasma treated silver films of this thickness show a dependence of the significant and most prominent reflexes on the film texture (Figure 4b). As can be seen from Figure 4b and Figure 4c the preferential orientation of the crystallites is different from that of bulk silver (JCPDS file No. 04-0783). In case of the as-sputtered silver film the crystallites show a preferential (200) orientation. After plasma treatment a gradual change of the preferential orientation can be observed.



After argon plasma treatment the preferential orientation completely changes to (111). At the same time the peak width and the positions of the (111) and (200) reflexes after different plasma treatments slightly change when compared to those of as-sputtered silver (Figure 4c). This indicates changes in the lattice parameters and thus a change in the macro- and microstrains present in the silver film. All these changes can be explained by the energy transferred to the silver atoms through the impact of high energy ions and electrons on the silver surface during plasma treatment. This leads to an increased mobility of the silver atoms, which either rearrange on the surface by displacement or are completely removed through sputtering.

A comparison of the cross-sectional TEM (FIB) images of an as-sputtered 10 nm silver film with a 10 nm silver film treated with nitrogen plasma (g12-p200) for 5 min shows a decrease in the silver film density indicated by a contrast change through which the boundaries of the different crystallites become visible (Figure 4d,e). At the same time, a morphological change of the interface of silver to the substrate is observed. It shows an increased roughness indicating that the plasma treatment affects the complete thickness of the silver film down to the substrate interface.

Argon plasma treated silver films

Compared to the nitrogen plasma treated silver films, argon plasma treatment of the sputtered silver films resulted in the distinct formation of voids similar to those in the silver films treated with hydrogen plasma. But in contrast to the hydrogen plasma treated films no depth etching effect was observed in the cross-sectional SEM (Figure 5).

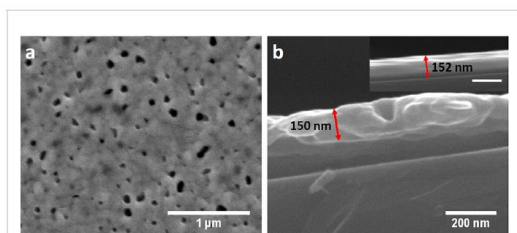


Figure 5: (a) SEM image of 200 nm sputtered silver film treated with argon plasma (g16.7-p200) for 30 min. (b) Cross-sectional SEM image of 200 nm sputtered silver film treated with argon plasma (g16.7-p200) for 30 min showing the actual thickness after argon plasma treatment compared to the as-sputtered silver film shown in the inset (scale bar: 200 nm).

Plasma treated silver films under oxidation/reduction conditions

Oxygen rf plasmas are well known to efficiently oxidize metallic silver films resulting in granular and nanoporous silver

oxide films [73]. For any application in SERS a subsequent reduction to metallic silver is necessary. However, the advantage of this oxidation process is its capability to completely change the morphology of the silver surface converting the originally flat silver surface into a three-dimensional nanoporous surface. The use of hydrogen, nitrogen or even argon plasma as a dry reducing agent would provide an attractive alternative to the often used wet chemical process [75] for obtaining efficient SERS substrates from previously oxidized silver films.

A 200 nm sputtered silver film was treated with oxygen plasma at a power of 200 W and a chamber pressure of 0.8 mbar for 15 min. The reduction of the oxidized silver film was performed with a hydrogen plasma at a power of 200 W and a chamber pressure of 0.38 mbar for 20 min in order to ensure complete reduction of the silver oxide film. Oxidation of sputtered silver films with oxygen plasma yields a polycrystalline silver oxide film with distinct grain boundaries (Figure 6a). After reduction of the silver oxide film to silver a highly porous structure is formed (Figure 6b). At the same time the drastic increase in film thickness compared to the as-sputtered silver film is observed (Figure 6c). The measured film thickness from the cross-sectional SEM for the oxidized silver film is about 407 nm, which is about 2.7 times the film thickness measured for the sputtered silver film. This large increase in film thickness is obviously due to the formation of silver oxide during the oxygen plasma treatment as a mixture of Ag_2O and AgO [82].

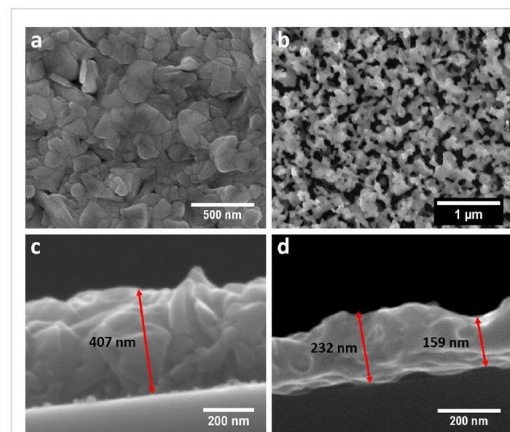


Figure 6: SEM images of a 200 nm sputtered silver film treated with (a) oxygen plasma (g12-p200) for 15 min and (b) after reducing the oxidized silver film with hydrogen plasma (g12-p200) for 20 min. Cross-sectional SEM image of 200 nm sputtered silver film treated with (c) oxygen plasma (g12-p200) for 15 min and (d) after reducing the oxidized silver film with hydrogen plasma (g12-p200) for 20 min showing the actual thickness of the prepared silver film after plasma treatment.

The incorporation of oxygen into the silver lattice leads to a volume expansion and a change in film morphology. The subsequent reduction of this silver oxide film with the hydrogen plasma results in a subsequent film shrinkage back to nearly half of its former value (159–232 nm; Figure 6d) [83,84]. Due to the volume shrinkage the film porosity increases significantly.

Changing plasma treatment time, chamber pressure and plasma power of the oxygen and hydrogen plasmas allows for a further tuning of the morphology of the nanoporous silver films (Figure S13, Supporting Information File 1). Longer treatment with hydrogen plasma can lead to further etching of the pores and the surface after completion of the reduction, while a longer oxygen plasma treatment leads to smaller pores.

An AFM study of the 200 nm oxidized/reduced silver films proves the drastic increase in surface roughness with increasing oxygen and hydrogen plasma treatment times and plasma power (Figure S14, Supporting Information File 1). A surface roughness R_q of 38.4 nm was obtained for a 200 nm sputtered silver film treated for 20 min with oxygen plasma (g12-p200) followed by another 20 min of hydrogen plasma (g12-p200) treatment.

If however, the as-sputtered silver film is heated before plasma treatment to 400 °C for 15 min, dewetting of the continuous silver film into isolated silver particles occurs [85]. Oxidation of these particles by oxygen plasma followed by reduction by hydrogen plasma results in nanoporous particles with a spongy morphology (“silver nanosponges”, Figure 7).

In addition, argon plasma was tested as an alternative to hydrogen plasma for the reduction of the silver oxide films obtained after oxygen plasma treatment. In this case the reduction process mainly depends on the electron density of the used plasma. The reduction of silver oxide is facilitated by plasma treatment due to the presence of high-energy UV photons that can easily break the silver–oxygen bond [78,86].

Again a 200 nm silver film was first oxidized using an oxygen rf plasma for 15 min at a power of 200 W and 12 sccm oxygen flow rate (chamber pressure of 0.8 mbar). After that, the oxidized silver film was reduced using an argon plasma at a power of 200 W and an argon flow rate of 16.7 sccm (chamber pressure 1.5 mbar). The morphology of the nanoporous silver film is very similar to the one obtained from the reduction using hydrogen as reducing plasma (Figure S15, Supporting Information File 1). Further changes to the oxidation/reduction protocol were made in order to determine whether varying plasma conditions could lead to different 3D silver morphologies. Subse-

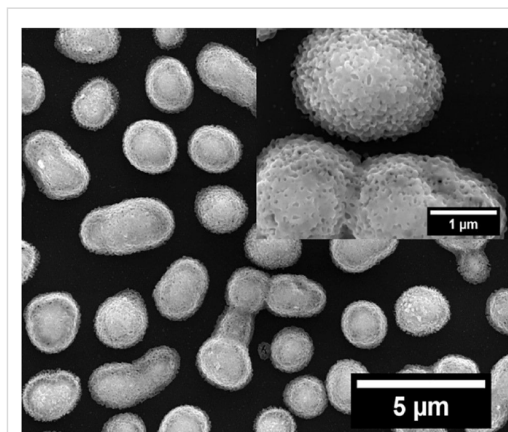
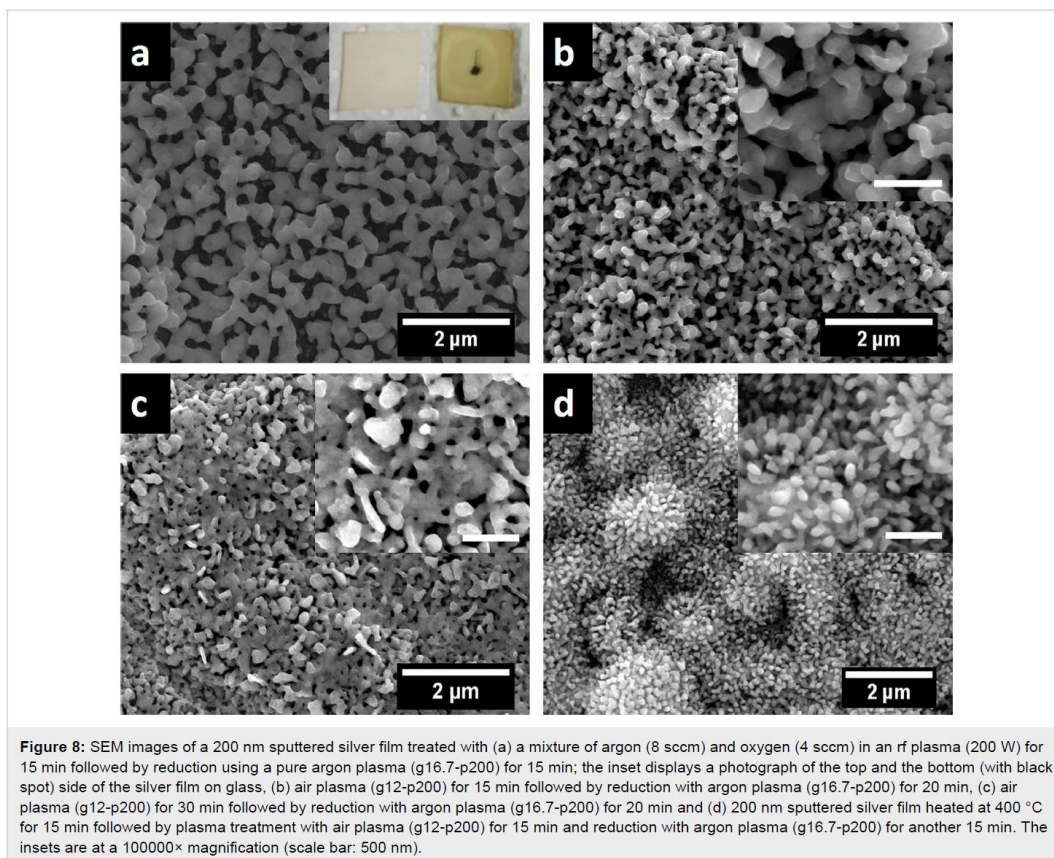


Figure 7: SEM image (10000× magnification) of a 200 nm sputtered silver film heated at 400 °C for 15 min followed by plasma treatment with oxygen plasma (g12-p200) for 10 min and reduction with hydrogen plasma (g12-p200) for another 10 min. The inset shows particles at 50000× magnification.

quently, a 200 nm sputtered silver film was treated with an rf plasma containing a mixture of argon and oxygen gas (8 sccm argon, 4 sccm oxygen gas flow at a power of 200 W for 15 min). Treatment of the so obtained oxidized silver film with pure argon rf plasma (argon flow rate 16.7 sccm, power 200 W, 15 min) results in a complex network of interconnected silver particles with large pore size (Figure 8a). This difference in morphology is already observed in the silver film oxidized by the argon/oxygen mixture when compared to the silver film oxidized by oxygen plasma alone (Figure S16a,d, Supporting Information File 1). The difference in the obtained morphologies can eventually be explained by a competing process of oxidation and reduction taking place during the plasma treatment with a mixture of argon and oxygen. Silver might be oxidized, followed by partial reduction both in a dynamic process. To proof this idea further, an rf plasma using air (78.08% N₂, 20.95% O₂ and 0.97% other gases) was used for the initial oxidation step (flow rate 12 sccm, 200 W for 15 min) followed by a reduction using argon plasma for 20 min (g16.7-p200). SEM reveals again a similar complex network of interconnected silver particles resembling a coral reef as found before when using the argon/oxygen mixture as oxidizing plasma (Figure 8b). Even the silver film oxidized by air plasma for 15 min and 30 min as well as the silver film oxidized by the argon/oxygen plasma mixture show different surface structures compared to the silver films oxidized by pure oxygen plasma (Figure S16, Supporting Information File 1). This indicates that the competing oxidation/reduction reactions might play an important role for the in situ structuring of the silver surface. Increasing the plasma treatment time when using an air plasma up



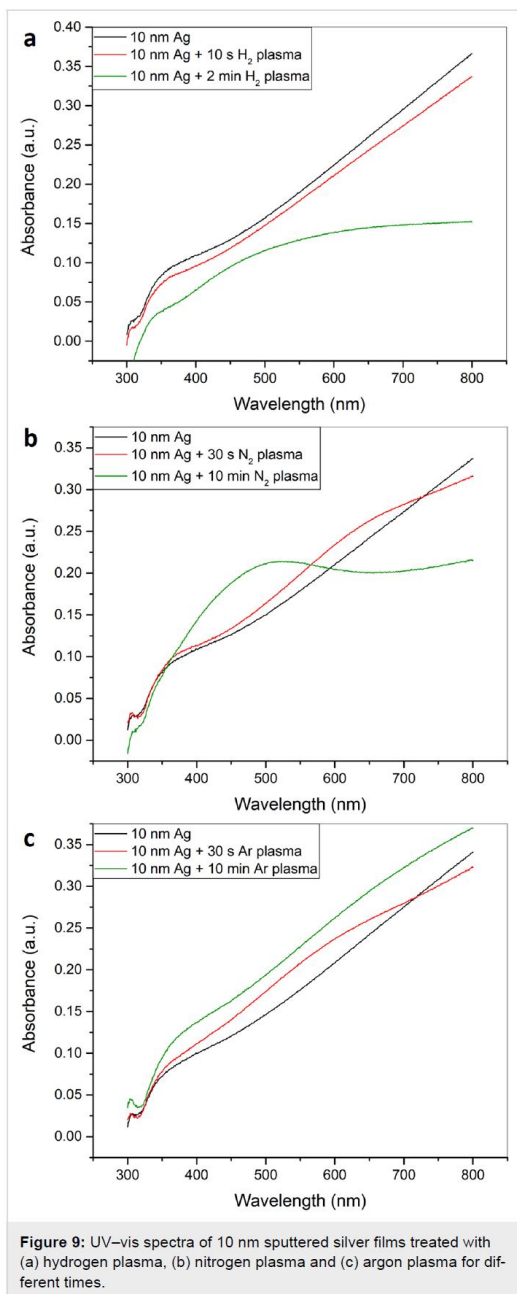
to 30 min results in an intact porous silver film however with a dense arrangement of short protrusions on the silver particle surfaces (Figure 8c). This unique silver morphology might represent the preliminary stage for the coral reef structure obtained with longer argon plasma treatment relative to the plasma oxidation time. Heating an as-prepared silver film for 15 min at 400 °C followed by oxidation with air plasma (g12-p200) for 15 min and reduction with argon plasma (g16.7-p200) for another 15 min results in silver particles having short rod-like protrusions (Figure 8d). Finally, a reduction with nitrogen plasma was also performed on silver surfaces oxidized by oxygen and air plasma treatment and yielded similar results as those obtained with hydrogen or argon as reducing gases (Figure S17, Supporting Information File 1).

XRD analysis of the silver films after oxidation/reduction proves that the reduction to metallic silver is complete in all cases revealing only the reflexes of elemental silver without any traces of silver oxide (Figure S18, Supporting Information File 1). Comparison of the XRD of the silver nanostructures re-

sulting from oxidation/reduction of silver films with as-sputtered silver films shows a variation of the preferential orientation of the silver crystallites in the films. With the systematic combination of oxidizing and reducing rf plasmas and a variation of the different plasma parameters, complex 3D silver nanostructures with tunable surface roughness and nanoporosity can be obtained.

Optical behavior and surface wetting of differently plasma treated silver films

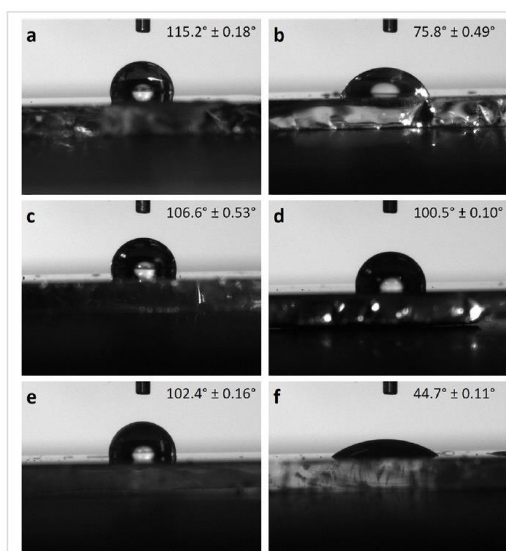
Figure 9a shows the UV–vis absorption spectra obtained after two different hydrogen rf plasma treatment times in comparison to the silver film before plasma treatment. With increasing hydrogen plasma treatment time, the absorption decreases over the entire spectrum while the decrease is more prominent for longer wavelengths as can be seen for the 2 min hydrogen plasma treatment. This decrease in absorption in the hydrogen plasma treated films might be due to the etching of the silver film. For nitrogen plasma treatment the absorption spectra do not show an overall decrease in absorbance (Figure 9b). While



the absorbance decreases for longer wavelengths it increases for shorter wavelengths resulting in the formation of an absorption shoulder due to surface plasmons. While this effect is hardly visible for 30 s nitrogen plasma treatment time at about 650 nm, it becomes much more prominent for 10 min nitrogen plasma

treatment at about 500 nm. This indicates a restructuring of the film surface leading to the formation of particulate structures on the surface as has been proven by SEM. This restructuring might result in the emergence of localized surface plasmon resonances as they are well-known for silver nanoparticles. In case of argon plasma treatment (Figure 9c) increasing plasma treatment time results in an increase of absorption of the silver film over the whole UV-vis spectrum indicating some sort of densification of the silver film [87].

The wetting behavior was analyzed by contact angle measurements of the plasma treated silver films (Figure 10). A change in surface wettability was obtained after the different plasma treatments. Obviously all rf plasma treatments lead to better wettabilities (water contact angles between $44.7^\circ \pm 0.11^\circ$ and $106.6^\circ \pm 0.53^\circ$) when compared to the as-sputtered silver films (contact angle of $115.2^\circ \pm 0.18^\circ$). This enables a better contact between the analyte in aqueous solution and the SERS substrate. In all cases plasma treatment generates a more hydrophilic silver surface as compared to the as-sputtered silver films manifested by a decrease in the water contact angle. Especially after subsequent oxidation/reduction plasma treatments where nanoporous silver films are obtained, the silver films quickly absorb the droplets through capillary effects thus enabling the analyte to get in good contact with the silver surface.



Evaluation of the SERS performance of rf-plasma treated silver films

The SERS effect for the different plasma treated silver films was evaluated in order to determine the influence of the different silver film morphologies obtained by plasma treatment on the SERS performance.

Effect of silver film thickness on SERS performance

First, the effect of thickness of the as-sputtered silver film on the SERS intensity was evaluated. 5 nm, 10 nm, 20 nm and 50 nm silver films obtained by sputtering were incubated for 30 min with a 10^{-6} M solution of RhB. SERS performance is increasing from 5 nm to 10 nm silver films and then decreases again with increasing thickness of the films (Figure 11). This can be attributed to the fact that during the initial stages of sputtering silver islands are formed on the substrate. The distance between these islands decreases with increasing sputtering time until the islands coalesce to form one continuous silver film [77]. Thus for the thinner sputtered silver film (10 nm) an optimal distance is generated between the silver islands leading to the presence of hot spots and an effective SERS enhancement. With increasing thickness of the films these hot spots disappear leading to a marked decrease in the SERS performance. The 10 nm sputtered film and 200 nm sputtered film exhibit similar roughness values (AFM, insets of Figure 2c and Figure 2d) despite the huge difference in SERS performance.

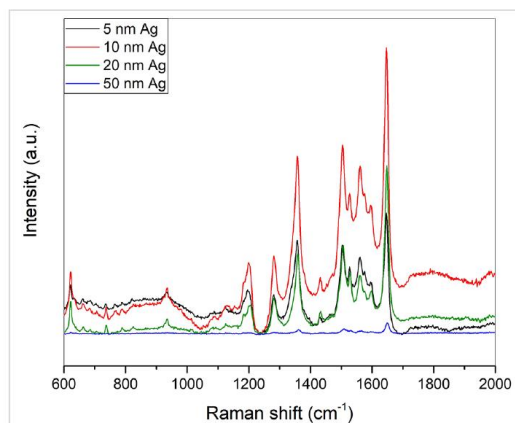


Figure 11: SERS spectra of 10^{-6} M RhB on sputtered silver films of different thicknesses.

This underlines the importance of the generation of hot spots for the evolution of high-intensity SERS spectra.

Effect of single plasma treatment on SERS performance

Hydrogen plasma treatment (g12-p200) on 10 nm silver films shows an increase in the SERS intensity with increasing treatment time until 60 s (Figure 12a,b). After longer hydrogen

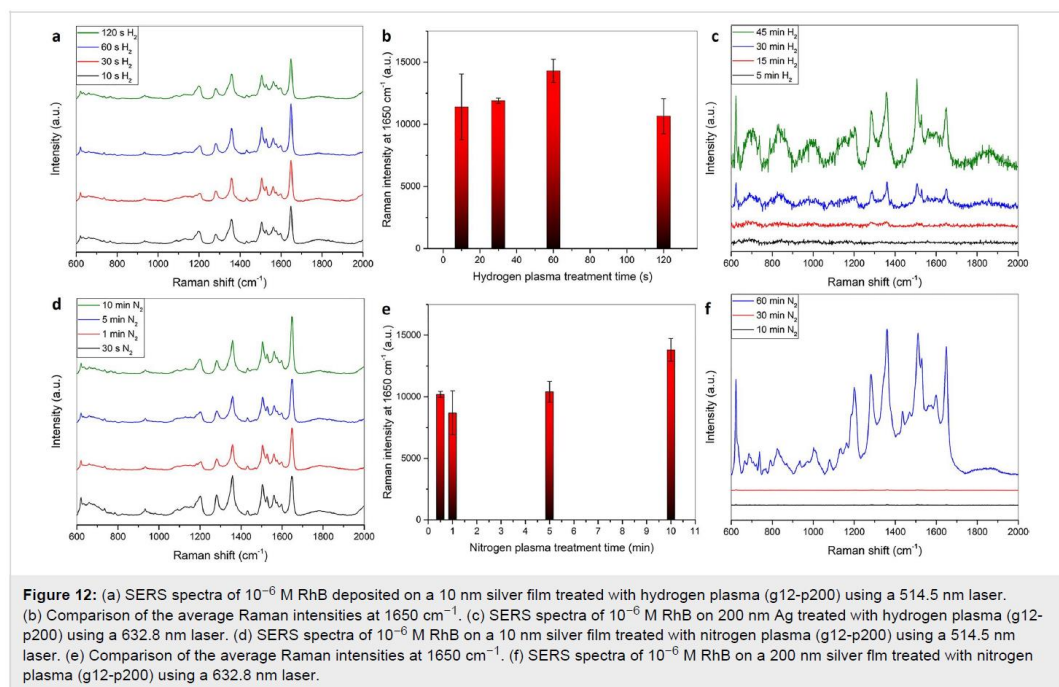
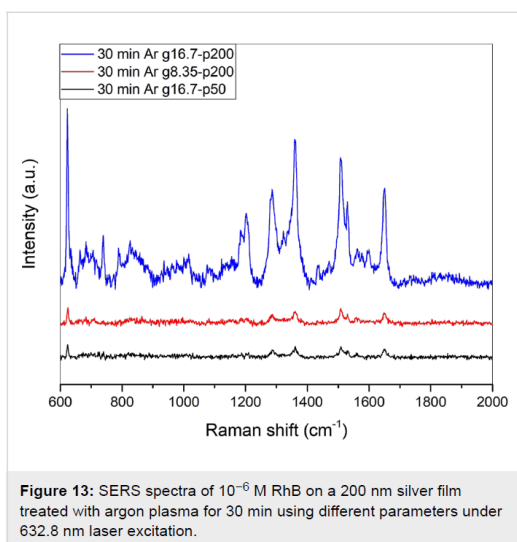


Figure 12: (a) SERS spectra of 10^{-6} M RhB deposited on a 10 nm silver film treated with hydrogen plasma (g12-p200) using a 514.5 nm laser. (b) Comparison of the average Raman intensities at 1650 cm^{-1} . (c) SERS spectra of 10^{-6} M RhB on 200 nm Ag treated with hydrogen plasma (g12-p200) using a 632.8 nm laser. (d) SERS spectra of 10^{-6} M RhB on a 10 nm silver film treated with nitrogen plasma (g12-p200) using a 514.5 nm laser. (e) Comparison of the average Raman intensities at 1650 cm^{-1} . (f) SERS spectra of 10^{-6} M RhB on a 200 nm silver film treated with nitrogen plasma (g12-p200) using a 632.8 nm laser.

plasma treatment times the SERS intensity decreases, and after about five minutes of hydrogen plasma treatment the silver film has vanished from the glass substrate. This also explains why the SERS intensity decreases with increasing hydrogen plasma treatment time. As earlier corroborated by AFM and SEM (Figure 2 and Figures S1–S3, Supporting Information File 1), the hydrogen plasma increases the surface roughness but at the same time etches the silver layer. Therefore, the SERS intensity increases with very short hydrogen plasma treatment and then rapidly decreases for treatment times over 60 s for the ultrathin 10 nm silver film. With 200 nm silver films the same behavior could be observed (Figure 12c). With increasing hydrogen plasma treatment time, the SERS intensity increases, which is attributed to the increase in surface roughness (see AFM, Figure S2, Supporting Information File 1).

Nitrogen plasma treatment of the silver films (g12-p200) also shows an increase of the SERS intensity (Figure 12d–f). Interestingly, there is a sharp increase in the SERS intensity from 30 to 60 min nitrogen plasma treatment of the 200 nm silver film, which cannot be explained just by the increase in surface roughness. However, it could be due to a combined effect of increased surface roughness and a matching of the localized surface plasmon resonance with the employed excitation wavelength.

Argon plasma treatment also leads to an increase in the surface roughness and an increase in SERS intensity. Changing the conditions of the plasma treatment leads to the ability to adjust the surface roughness and thus a change in SERS spectra while keeping the treatment time constant (Figure 13).



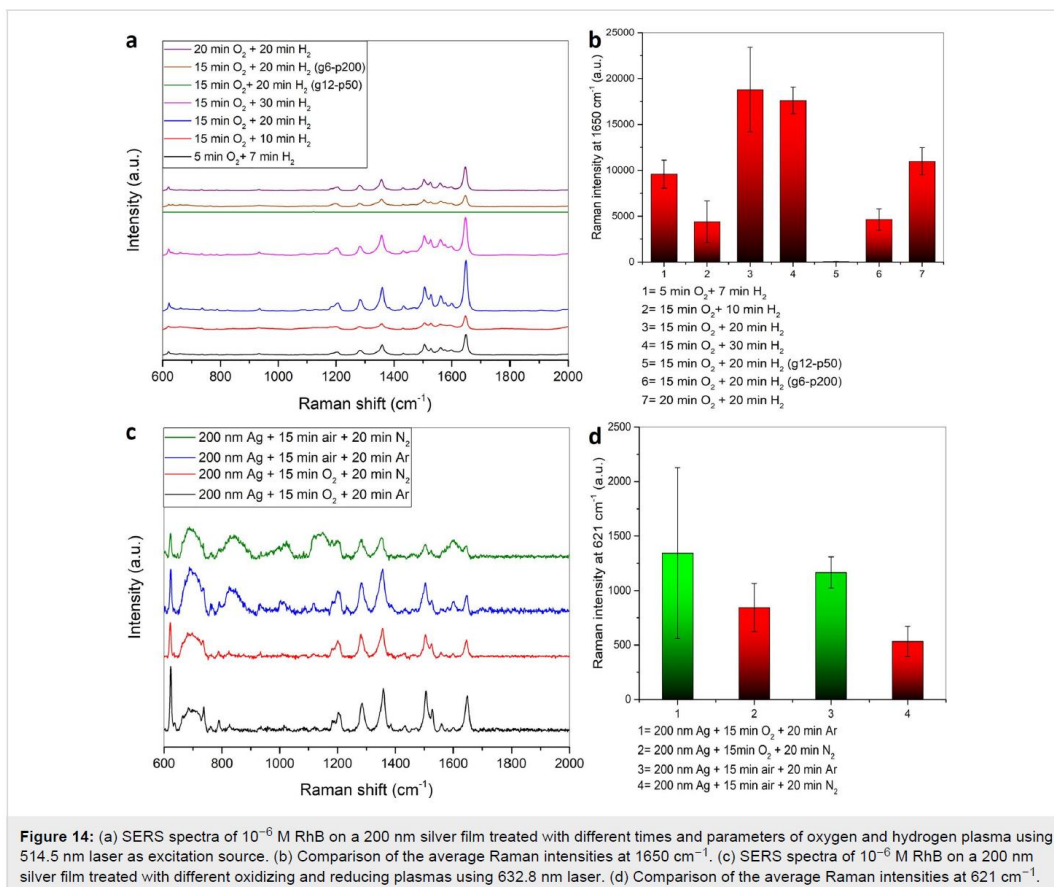
Effect of oxidation/reduction plasma treatment on SERS performance

To obtain more complex silver surface morphologies, oxidation followed by reduction of the as-deposited silver films was performed and studied for their SERS activity. As shown in Figure 14a and Figure 14b, different plasma treatment times for oxygen and hydrogen plasma as well as different plasma conditions were tested. As standard conditions a gas flow of 12 sccm was used for both oxygen and hydrogen together with a plasma power of 200 W. It can be noted that increasing the hydrogen plasma treatment time is important for increasing the SERS intensity. Using a hydrogen plasma time smaller than the oxygen plasma treatment time leads to incomplete reduction of the oxidized silver film and a lower SERS intensity. The use of equal treatment times using oxygen and hydrogen plasma (20 min O_2 plasma and 20 min H_2 plasma) increases the SERS intensity further. Using a hydrogen plasma treatment time is higher than that used for oxygen plasma results in a higher SERS enhancement, as it is observed for 15 min oxygen plasma and 20 min hydrogen plasma treatment due to the more complete reduction of the oxidized silver films. Increasing the hydrogen plasma reduction treatment time to 30 min does not lead to a further increase in the SERS enhancement. Instead there is a slight decrease in the SERS enhancement as excess hydrogen plasma treatment beyond the reduction process results in etching of the silver film: This widens the pores of the formed nanoporous silver network and decreases the SERS enhancement. A decrease in the used gas flow for oxygen and hydrogen as well as the decrease of the used plasma power will result in a decrease in the SERS enhancement with the latter having a more pronounced effect on the SERS enhancement. At low plasma power the surface is modified to a much lower extent leading to a much less nanoporous network (Figure S13, Supporting Information File 1), which is the reason for the low SERS intensities obtained.

To understand if the plasma gas itself used for the reduction process has an effect on the SERS performance, reduction with (i) argon and (ii) nitrogen was studied using oxygen as well as air as oxidizing plasma (Figure 14c,d). The obtained SERS intensities for 10^{-6} M RhB at 621 cm^{-1} (excitation wavelength 632.8 nm) reveal that argon plasma is more efficient irrespective of the oxidizing plasma used. This can be attributed to the lower reduction efficiency of nitrogen plasma [86].

Comparison of the enhancement performance of different SERS substrates

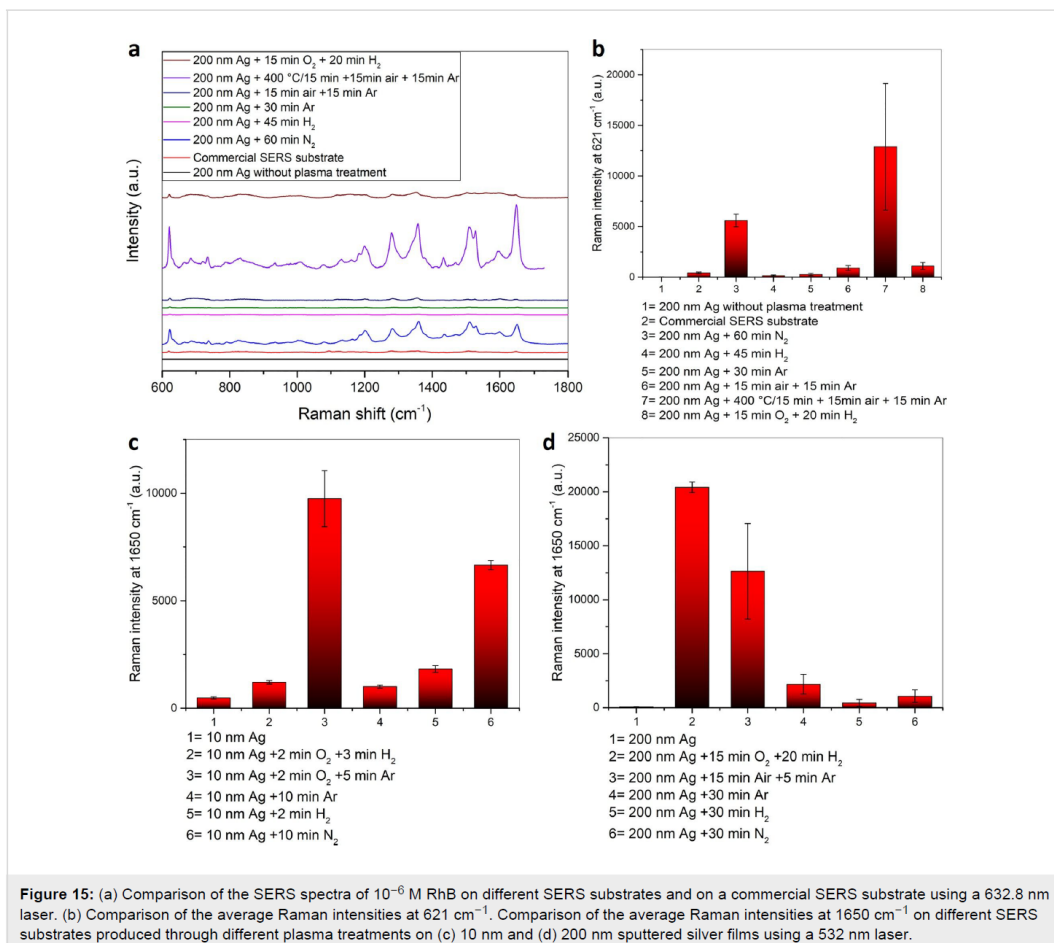
A comparison of different SERS substrates a) a 200 nm sputtered silver film modified by different plasma treatments, b) an as-sputtered 200 nm silver film and c) a commercial SERS substrate (SEM, Figure S19, Supporting Information File 1)



consisting of silver nanoparticles on a paper substrate using 10^{-6} M RhB as probe at an excitation wavelength of 632.8 nm is given in Figure 15a,b and Table S3 (Supporting Information File 1). As expected the commercial SERS substrate displays a higher SERS activity than the as-sputtered 200 nm silver film. However, the SERS enhancement of the as-sputtered 200 nm silver film can be greatly enhanced by an appropriate plasma treatment leading to a 30-fold enhancement compared to a commercial SERS substrate and to an about 1200-fold enhancement when compared with an untreated 200 nm sputtered silver film.

A further comparison of the SERS substrates was done at an excitation wavelength of 532 nm (Figure 15c,d and Table S3, Supporting Information File 1). A comparison of the group of the plasma treated ultrathin 10 nm silver films and the plasma treated 200 nm silver films shows that the SERS intensity obtained with the untreated 10 nm silver film is higher than with the untreated 200 nm film (Figure 15c,d and Table S3). For

both thicknesses a plasma treatment results in an increase in the SERS intensity. However, in case of 10 nm silver films, a short plasma treatment of up to 10 min is already sufficient to yield a significant increase in the SERS intensity of the analyte compared to the untreated silver films considering the single plasma treatments (argon, nitrogen or hydrogen). For these single plasma treatments, the ultrathin transparent silver films are superior compared to their thicker, non-transparent analogues. In case of the oxidation/reduction plasma treatment, the 200 nm silver films result in better SERS enhancements as they provide more volume for the formation of a continuous and deep nanoporous silver network. In the ultrathin 10 nm silver film the oxidation/reduction plasma treatment results in the formation of a number of isolated islands (Figure S20, Supporting Information File 1) compared to the continuous silver network as in case of the thicker 200 nm silver film. Therefore, in the 200 nm silver films more adsorption sites for the analyte are created and an increased SERS effect is observed for a particular concentration of RhB. Thus, for the 10 nm silver films hydrogen and



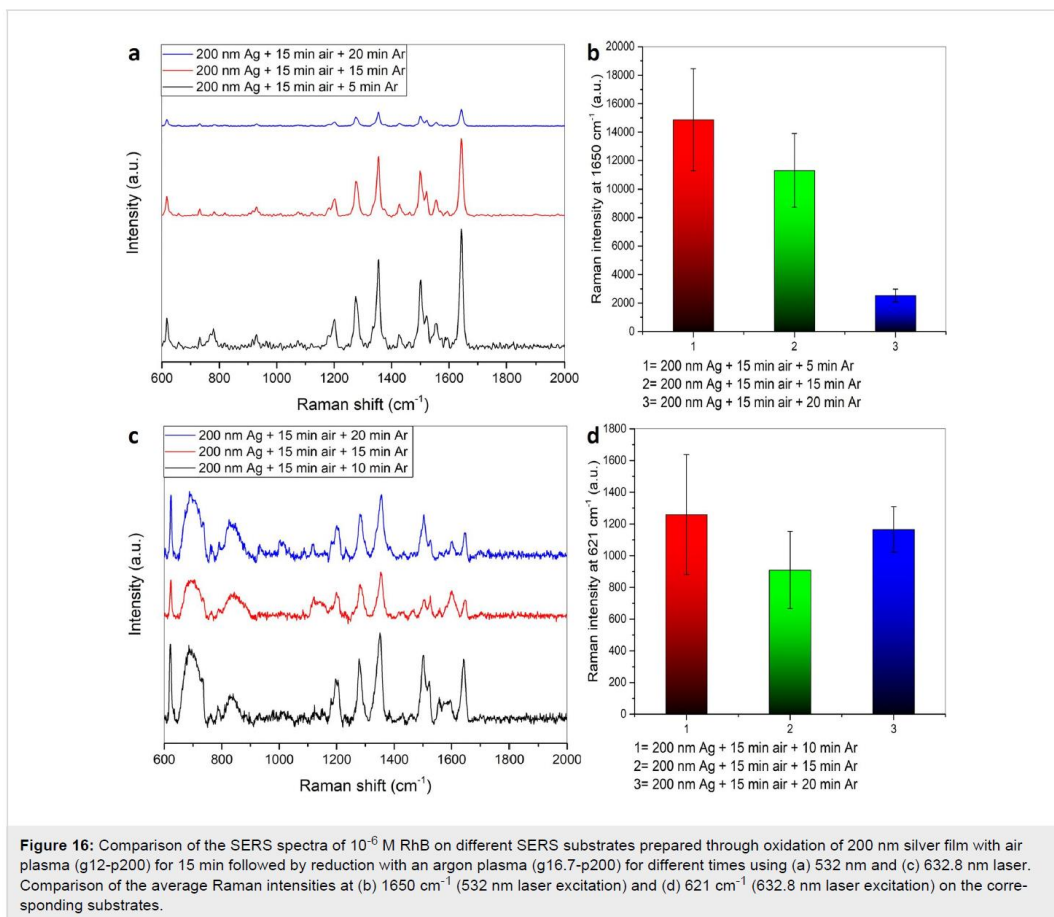
argon were tested as reducing plasma. It was found that using argon plasma as the reducing plasma yielded SERS substrates with higher SERS enhancement probably due to the fact that hydrogen plasma treatment partially results in etching of the silver islands in addition to the reduction. For the 200 nm silver films the oxidation/reduction plasma treatment is more efficient than a single plasma treatment in the formation of efficient SERS substrates.

In order to scrutinize the wavelength-dependence of different SERS substrates a comparison of SERS substrates produced by oxidation through air plasma and reduction through argon plasma with different reduction times was undertaken (Figure 16). The SERS performance of these substrates subjected to lower argon plasma reduction time at 532 nm excitation is much higher and the performance decreases rapidly with increasing argon plasma reduction time. This trend cannot be seen

when using 632.8 nm as excitation wavelength where the SERS performance does not change much with increasing argon plasma reduction time.

Raman mapping of the strongest vibration mode of RhB at $\nu = 1650 \text{ cm}^{-1}$ ($-\text{COOH}$) on different Ag substrates (different thicknesses and plasma treatment conditions) reveals the overall uniformity of this characteristic absorption. Moreover, the different SERS substrates show good enhancement factors and uniformity as obtained from the Raman maps of 10^{-6} M concentration of RhB on these substrates (Figure S21, Supporting Information File 1).

It is known that the SERS activity can deteriorate due to surface oxidation of the silver surface [88]. For increasing the long-term stability of SERS active silver films we have studied a thin layer of dielectric Al_2O_3 as protective coating [89]. A



1 nm thick Al_2O_3 film was deposited on top of the nanoporous silver film by ALD before adding the probe molecule RhB. The influence in SERS activity was compared immediately after deposition and after two weeks. Not unexpectedly, the Al_2O_3 layer reduces the SERS signal significantly as the analyte molecules are not in direct contact with the silver surface anymore (Figure S22, Supporting Information File 1). However, characteristic signals of RhB are still detectable and allow for a secure identification of RhB. Even after two weeks of storage the SERS substrate without Al_2O_3 exhibits great SERS performance superior to that of the Al_2O_3 -coated SERS substrate.

The idea of using plasma treatment for cleaning the used SERS substrates without greatly modifying their response was also tested. This would enable an inexpensive re-use of the SERS substrates. First, the SERS spectrum of 10^{-6} M RhB on a 200 nm sputtered silver film was obtained. An argon

plasma with a gas flow of 16.7 sccm at 50 W for 5 min was sufficient to remove the analyte completely (Figure S23a, Supporting Information File 1). Re-application of RhB to the cleaned SERS substrate gave an SERS spectrum equivalent to that before cleaning which proves that the surface has not been altered extensively by the mild plasma cleaning procedure. A second attempt to clean the SERS substrate under the same conditions also completely removes the analyte providing a clean baseline. The same procedure has been also tested on an older SERS substrate (200 nm Ag + 15 min O_2 + 20 min H_2) that was fabricated six months prior to its use (Figure S23b, Supporting Information File 1). Before the first use it was cleaned using the mentioned short cleaning procedure with argon plasma. Then the same substrate was re-used four times with the short cleaning procedure with argon in-between. No decrease of the performance of the SERS substrate was observed. This shows that mild and short plasma treatment can be used effectively for cleaning of the SERS substrates, whereas

more aggressive and longer plasma treatment can be used to increase the silver surface roughness and complexity yielding more effective SERS substrates from simple silver films.

Conclusion

This systematic study proves the possibility of increasing the surface roughness of sputtered silver films through application of different rf plasma treatments as an alternative to the widely employed method of electrochemical surface roughening of silver films. Different reactive plasma gas compositions as well as different plasma parameters used in the particular plasma treatments result in a variety of different SERS silver substrates with tunable morphology and attractive enhancement factors. A combination of an oxidizing plasma together with a reducing plasma results in the formation of complex three-dimensional silver morphologies showing a huge enhancement factor due to the formation of SERS hot spots. The SERS enhancement of the as-sputtered 200 nm silver film is greatly enhanced by an appropriate plasma treatment reaching about 30-fold enhancement compared to a commercial SERS substrate and about 1200-fold compared to the untreated silver film. At the same time it was also found that ultrathin transparent silver films can be used as efficient SERS substrates. Heating of the silver film under a subsequent oxidative/reductive rf plasma treatment enables the formation of a silver-nanosponge morphology directly on the glass substrate. The morphologies fabricated by various plasma treatment processes are stable over the course of several weeks and can even be recovered and re-used after initial analytical use through employing a mild argon plasma treatment.

To summarize, rf plasma treatment offers flexibility in obtaining a wide variety of silver morphologies on a substrate starting from a thin sputter deposited silver film. We believe that this technique offers an attractive and efficient way for a straightforward fabrication of SERS substrates even based on other host metals.

Supporting Information

Supporting Information File 1

Additional experimental data.

[<https://www.beilstein-journals.org/bjnano/content/supplementary/2190-4286-9-263-S1.pdf>]

Acknowledgements

The authors thank S. Heinschke and Dr. J. Engstler (both at TU Darmstadt) for XRD measurements and TEM analyses, respectively. TEM studies were performed at the Ernst-Ruska Center (ERC) at the Forschungszentrum (FZ) Jülich under contract ERC-TUD1. XPS and Auger measurements were

carried out at the Karlsruhe Nano Micro Facility at KIT under the KNMF program. SO acknowledges the Egyptian Ministry of Higher Education (MoHE) and the German Academic Exchange Service (DAAD) for support through the German-Egyptian Research Scholarship (GERLS) program (funding program number 57030312).

ORCID® iDs

Jörg J. Schneider - <https://orcid.org/0000-0002-8153-9491>

References

- Sharma, B.; Frontiera, R. R.; Henry, A.-I.; Ringe, E.; Van Duyne, R. P. *Mater. Today* **2012**, *15*, 16–25. doi:10.1016/s1369-7021(12)70017-2
- Fleischmann, M.; Hendra, P. J.; McQuillan, A. J. *Chem. Phys. Lett.* **1974**, *26*, 163–166. doi:10.1016/0009-2614(74)85388-1
- Albrecht, M. G.; Creighton, J. A. *J. Am. Chem. Soc.* **1977**, *99*, 5215–5217. doi:10.1021/ja00457a071
- Jeong, J. W.; Arnob, M. M. P.; Baek, K.-M.; Lee, S. Y.; Shih, W.-C.; Jung, Y. S. *Adv. Mater.* **2016**, *28*, 8695–8704. doi:10.1002/adma.201602603
- Kneipp, K. *Phys. Today* **2007**, *60*, 40–46. doi:10.1063/1.2812122
- Guerrini, L.; Graham, D. *Chem. Soc. Rev.* **2012**, *41*, 7085. doi:10.1039/c2cs35118h
- Mosier-Boss, P. *Nanomaterials* **2017**, *7*, 142. doi:10.3390/nano7060142
- Liu, Y.-C.; Yu, C.-C.; Sheu, S.-F. *J. Mater. Chem.* **2006**, *16*, 3546. doi:10.1039/b609417a
- Yang, K.-H.; Liu, Y.-C.; Yu, C.-C. *J. Mater. Chem.* **2008**, *18*, 4849–4855. doi:10.1039/b808516a
- Cao, P.; Gu, R.; Tian, Z. *J. Phys. Chem. B* **2003**, *107*, 769–777. doi:10.1021/jp026747o
- Yang, K.-H.; Liu, Y.-C.; Yu, C.-C. *Langmuir* **2010**, *26*, 11512–11517. doi:10.1021/la100235x
- Fang, C.; Ellis, A. V.; Voelcker, N. H. *J. Electroanal. Chem.* **2011**, *659*, 151–160. doi:10.1016/j.jelechem.2011.05.016
- Zhou, X.; Zhou, F.; Liu, H.; Yang, L.; Liu, J. *Analyst* **2013**, *138*, 5832. doi:10.1039/c3an00914a
- Liang, H.; Li, Z.; Wang, W.; Wu, Y.; Xu, H. *Adv. Mater.* **2009**, *21*, 4614–4618. doi:10.1002/adma.200901139
- Farcau, C.; Potara, M.; Leordean, C.; Boca, S.; Astilean, S. *Analyst* **2013**, *138*, 546–552. doi:10.1039/c2an36440a
- Sharma, B.; Fernanda Cardinal, M.; Kleinman, S. L.; Greeneltch, N. G.; Frontiera, R. R.; Blaber, M. G.; Schatz, G. C.; Van Duyne, R. P. *MRS Bull.* **2013**, *38*, 615–624. doi:10.1557/mrs.2013.161
- Tastekova, E. A.; Polyakov, A. Y.; Goldt, A. E.; Sidorov, A. V.; Oshmyanskaya, A. A.; Sukhorukova, I. V.; Shtansky, D. V.; Grünert, W.; Grigorieva, A. V. *Beilstein J. Nanotechnol.* **2018**, *9*, 880–889. doi:10.3762/bjnano.9.82
- Jensen, T. R.; Malinsky, M. D.; Haynes, C. L.; Van Duyne, R. P. *J. Phys. Chem. B* **2000**, *104*, 10549–10556. doi:10.1021/jp002435e
- Haynes, C. L.; Van Duyne, R. P. *J. Phys. Chem. B* **2001**, *105*, 5599–5611. doi:10.1021/jp010657m
- Dick, L. A.; McFarland, A. D.; Haynes, C. L.; Van Duyne, R. P. *J. Phys. Chem. B* **2002**, *106*, 853–860. doi:10.1021/jp013638i
- Haynes, C. L.; Van Duyne, R. P. *J. Phys. Chem. B* **2003**, *107*, 7426–7433. doi:10.1021/jp027749b

22. Zhang, X.; Yonzon, C. R.; Young, M. A.; Stuart, D. A.; Van Duyne, R. P. *IEE Proc.: Nanobiotechnol.* **2005**, *152*, 195–206. doi:10.1049/ip-nbt:20050009
23. Lin, W.-C.; Liao, L.-S.; Chen, Y.-H.; Chang, H.-C.; Tsai, D. P.; Chiang, H.-P. *Plasmonics* **2011**, *6*, 201–206. doi:10.1007/s11468-010-9188-x
24. Yan, W.-G.; Qi, J.-W.; Li, Z.-B.; Tian, J.-G. *Plasmonics* **2014**, *9*, 565–571. doi:10.1007/s11468-013-9665-0
25. Zhu, Z.; Li, Q.; Bai, B.; Fan, S. *Nanoscale Res. Lett.* **2014**, *9*, 25. doi:10.1186/1556-276x-9-25
26. Huebner, U.; Boucher, R.; Schneidewind, H.; Cialla, D.; Popp, J. *Microelectron. Eng.* **2008**, *85*, 1792–1794. doi:10.1016/j.mee.2008.05.005
27. Yan, B.; Thubagere, A.; Premasiri, W. R.; Ziegler, L. D.; Dal Negro, L.; Reinhard, B. M. *ACS Nano* **2009**, *3*, 1190–1202. doi:10.1021/nn800836f
28. Deng, X.; Braun, G. B.; Liu, S.; Sciortino, P. F., Jr.; Koefer, B.; Tombler, T.; Moskovits, M. *Nano Lett.* **2010**, *10*, 1780–1786. doi:10.1021/nl1003587
29. Im, H.; Bantz, K. C.; Lindquist, N. C.; Haynes, C. L.; Oh, S.-H. *Nano Lett.* **2010**, *10*, 2231–2236. doi:10.1021/nl1012085
30. Dinish, U. S.; Yaw, F. C.; Agarwal, A.; Olivo, M. *Biosens. Bioelectron.* **2011**, *26*, 1987–1992. doi:10.1016/j.bios.2010.08.069
31. Ahn, H.-J.; Thiyagarajan, P.; Jia, L.; Kim, S.-I.; Yoon, J.-C.; Thomas, E. L.; Jang, J.-H. *Nanoscale* **2013**, *5*, 1836. doi:10.1039/c3nr33498h
32. Gillibert, R.; Sarkar, M.; Bryce, J.-F.; Yasukuni, R.; Moreau, J.; Besbes, M.; Barbillon, G.; Bartenlian, B.; Canva, M.; de la Chapelle, M. L. *Nanotechnology* **2016**, *27*, 115202. doi:10.1088/0957-4484/27/11/115202
33. Alvarez-Puebla, R.; Cui, B.; Bravo-Vasquez, J.-P.; Veres, T.; Fenniri, H. *J. Phys. Chem. C* **2007**, *111*, 6720–6723. doi:10.1021/jp070906s
34. Krishnamoorthy, S.; Krishnan, S.; Thoniyot, P.; Low, H. Y. *ACS Appl. Mater. Interfaces* **2011**, *3*, 1033–1040. doi:10.1021/am1011518
35. Chen, Y.-C.; Young, R. J.; Macpherson, J. V.; Wilson, N. R. *J. Phys. Chem. C* **2007**, *111*, 16167–16173. doi:10.1021/jp073771z
36. Altun, A. O.; Bond, T. C.; Park, H. G. *Proc. SPIE* **2014**, *9168*, 916809. doi:10.1117/12.2061539
37. Zhang, J.; Zhang, X.; Lai, C.; Zhou, H.; Zhu, Y. *Opt. Express* **2014**, *22*, 21157–21166. doi:10.1364/oe.22.021157
38. Zhang, K.; Ji, J.; Fang, X.; Yan, L.; Liu, B. *Analyst* **2015**, *140*, 134–139. doi:10.1039/c4an01473a
39. Jin, Y.; Wang, Y.; Chen, M.; Xiao, X.; Zhang, T.; Wang, J.; Jiang, K.; Fan, S.; Li, Q. *ACS Appl. Mater. Interfaces* **2017**, *9*, 32369–32376. doi:10.1021/acsami.7b08807
40. Srichan, C.; Ekpanyapong, M.; Horprathum, M.; Eiamchai, P.; Nuntawong, N.; Phokharatkul, D.; Danvirutai, P.; Bohez, E.; Wisitsoraat, A.; Tuantranont, A. *Sci. Rep.* **2016**, *6*, 23733. doi:10.1038/srep23733
41. Fang, H.; Zhang, C. X.; Liu, L.; Zhao, Y. M.; Xu, H. J. *Biosens. Bioelectron.* **2015**, *64*, 434–441. doi:10.1016/j.bios.2014.09.053
42. Barbillon, G.; Sandana, V. E.; Humbert, C.; Béliier, B.; Rogers, D. J.; Teherani, F. H.; Bove, P.; McClintock, R.; Razezghi, M. *J. Mater. Chem. C* **2017**, *5*, 3528–3535. doi:10.1039/c7tc00098g
43. Shao, F.; Lu, Z.; Liu, C.; Han, H.; Chen, K.; Li, W.; He, Q.; Peng, H.; Chen, J. *ACS Appl. Mater. Interfaces* **2014**, *6*, 6281–6289. doi:10.1021/am4045212
44. Chen, J.; Qin, G.; Chen, Q.; Yu, J.; Li, S.; Cao, F.; Yang, B.; Ren, Y. *J. Mater. Chem. C* **2015**, *3*, 4933–4944. doi:10.1039/c5tc00717h
45. Asiala, S. M.; Marr, J. M.; Gervinskas, G.; Juodkazis, S.; Schultz, Z. D. *Phys. Chem. Chem. Phys.* **2015**, *17*, 30461–30467. doi:10.1039/c5cp04506a
46. Seniutinas, G.; Gervinskas, G.; Verma, R.; Gupta, B. D.; Lapiere, F.; Stoddart, P. R.; Clark, F.; McArthur, S. L.; Juodkazis, S. *Opt. Express* **2015**, *23*, 6763. doi:10.1364/oe.23.06763
47. Zhang, C.; Jiang, S. Z.; Yang, C.; Li, C. H.; Huo, Y. Y.; Liu, X. Y.; Liu, A. H.; Wei, Q.; Gao, S. S.; Gao, X. G.; Man, B. Y. *Sci. Rep.* **2016**, *6*, 25243. doi:10.1038/srep25243
48. Zuo, Z.; Zhu, K.; Gu, C.; Wen, Y.; Cui, G.; Qu, J. *Appl. Surf. Sci.* **2016**, *379*, 66–72. doi:10.1016/j.apsusc.2016.04.022
49. Schierhorn, M.; Lee, S. J.; Boettcher, S. W.; Stucky, G. D.; Moskovits, M. *Adv. Mater.* **2006**, *18*, 2829–2832. doi:10.1002/adma.200601254
50. Wang, H.-H.; Liu, C.-Y.; Wu, S.-B.; Liu, N.-W.; Peng, C.-Y.; Chan, T.-H.; Hsu, C.-F.; Wang, J.-K.; Wang, Y.-L. *Adv. Mater.* **2006**, *18*, 491–495. doi:10.1002/adma.200501875
51. Choi, D.; Choi, Y.; Hong, S.; Kang, T.; Lee, L. P. *Small* **2010**, *6*, 1741–1744. doi:10.1002/smll.200901937
52. Das, G.; Patra, N.; Gopalakrishnan, A.; Zaccaria, R. P.; Toma, A.; Thorat, S.; Di Fabrizio, E.; Diaspro, A.; Salerno, M. *Analyst* **2012**, *137*, 1785–1792. doi:10.1039/c2an16022f
53. Chaney, S. B.; Shanmukh, S.; Dluhy, R. A.; Zhao, Y.-P. *Appl. Phys. Lett.* **2005**, *87*, 031908. doi:10.1063/1.1988980
54. Shanmukh, S.; Jones, L.; Driskell, J.; Zhao, Y.; Dluhy, R.; Tripp, R. A. *Nano Lett.* **2006**, *6*, 2630–2636. doi:10.1021/nl061666f
55. Negri, P.; Dluhy, R. A. *J. Biophotonics* **2013**, *6*, 20–35. doi:10.1002/jbio.201200133
56. He, Y.; Fu, J.; Zhao, Y. *Front. Phys.* **2014**, *9*, 47–59. doi:10.1007/s11467-013-0357-1
57. Jiao, Y.; Ryckman, J. D.; Ciesielski, P. N.; Escobar, C. A.; Jennings, G. K.; Weiss, S. M. *Nanotechnology* **2011**, *22*, 295302. doi:10.1088/0957-4484/22/29/295302
58. Qi, J.; Motwani, P.; Gheewala, M.; Brennan, C.; Wolfe, J. C.; Shih, W.-C. *Nanoscale* **2013**, *5*, 4105–4109. doi:10.1039/c2nr33242f
59. Li, R.; Liu, X. J.; Wang, H.; Wu, Y.; Chu, X. M.; Lu, Z. P. *Corros. Sci.* **2014**, *84*, 159–164. doi:10.1016/j.corsci.2014.03.023
60. Liu, K.; Bai, Y.; Zhang, L.; Yang, Z.; Fan, Q.; Zheng, H.; Yin, Y.; Gao, C. *Nano Lett.* **2016**, *16*, 3675–3681. doi:10.1021/acs.nanolett.6b00868
61. Hoppmann, E. P.; Yu, W. W.; White, I. M. *Methods* **2013**, *63*, 219–224. doi:10.1016/j.ymeth.2013.07.010
62. Polavarapu, L.; Porta, A. L.; Novikov, S. M.; Coronado-Puchau, M.; Liz-Marzán, L. M. *Small* **2014**, *10*, 3065–3071. doi:10.1002/smll.201400438
63. Liston, E. M. *J. Adhes.* **1989**, *30*, 199–218. doi:10.1080/00218468908048206
64. Jellil, R. A. *J. Mater. Sci.* **2015**, *50*, 5913–5943. doi:10.1007/s10853-015-9152-4
65. Tendero, C.; Tixier, C.; Tristant, P.; Desmaison, J.; Leprince, P. *Spectrochim. Acta, Part B* **2006**, *61*, 2–30. doi:10.1016/j.sab.2005.10.003
66. Fraser, D. B.; Westwood, D. W. In *Handbook of plasma processing technology: fundamentals, etching, deposition, and surface interactions*; Rossnagel, S.; Cuomo, J.; Westwood, W., Eds.; Noyes Publications: New Jersey, NJ, U.S.A., 1990; pp 2–12.

67. Pettin, D. G.; Tverdokhlebov, S. I.; Anissimov, Y. G. *J. Controlled Release* **2017**, *266*, 57–74. doi:10.1016/j.jconrel.2017.09.023
68. Tiller, H.-J.; Demme, U.; Lenke, D.; Bühner, P.; Meyer, K. *Krist. Tech.* **1975**, *10*, K103–K108. doi:10.1002/crat.19750101018
69. Kim, S. Y.; Hong, K.; Kim, K.; Yu, H. K.; Kim, W.-K.; Lee, J.-L. *J. Appl. Phys.* **2008**, *103*, 076101. doi:10.1063/1.2874495
70. Kim, H.; Shin, K.-Y.; Kang, H.-S.; Lee, S.-H.; Kim, J.-M. *Microsyst. Technol.* **2016**, *22*, 1135–1142. doi:10.1007/s00542-015-2595-3
71. Shanmugan, S.; Mutharasu, D.; Kamarulazizi, I. *Eur. Phys. J.: Appl. Phys.* **2012**, *58*, 10802. doi:10.1051/epjap/2012110466
72. Kinnan, M. K.; Kumbhar, A.; Chumanov, G. *Appl. Spectrosc.* **2008**, *62*, 721–726. doi:10.1366/000370208784909463
73. Ma, C.; Trujillo, M. J.; Camden, J. P. *ACS Appl. Mater. Interfaces* **2016**, *8*, 23978–23984. doi:10.1021/acsami.6b08191
74. Kruth, M.; Meertens, D.; Tillmann, K. J. *Large-Scale Res. Facil.* **2016**, *2*, A59. doi:10.17815/jlsrf-2-105
75. Chen, F. F.; Chang, J. P. *Lecture Notes on Principles of Plasma Processing*; Springer US: Boston, MA, U.S.A., 2003. doi:10.1007/978-1-4615-0181-7
76. Liston, E. M.; Martin, L.; Wertheimer, M. R. *J. Adhes. Sci. Technol.* **1993**, *7*, 1091–1127. doi:10.1163/156856193x00600
77. Santoro, G.; Yu, S.; Schwartzkopf, M.; Zhang, P.; Koyiloth Vayalil, S.; Risch, J. F. H.; Rübhausen, M. A.; Hernández, M.; Domingo, C.; Roth, S. V. *Appl. Phys. Lett.* **2014**, *104*, 243107. doi:10.1063/1.4884423
78. Choi, T.-S.; Levitin, G.; Hess, D. W. *ECS J. Solid State Sci. Technol.* **2013**, *2*, P275–P281. doi:10.1149/2.012306jss
79. Wagner, A. J.; Fairbrother, D. H.; Reniers, F. *Plasmas Polym.* **2003**, *8*, 119–134. doi:10.1023/a:1023942211714
80. Depla, D.; De Gryse, R. *Vacuum* **2003**, *69*, 529–536. doi:10.1016/s0042-207x(02)00602-4
81. McGuire, G. E. *Auger Electron Spectroscopy Reference Manual*; Plenum Press: New York, NY, U.S.A., 1979. doi:10.1007/978-1-4757-1702-0
82. El Mel, A.-A.; Stephant, N.; Hamon, J.; Thiry, D.; Chauvin, A.; Chettab, M.; Gautron, E.; Konstantinidis, S.; Granier, A.; Tessier, P.-Y. *Nanoscale* **2016**, *8*, 141–148. doi:10.1039/c5nr07145c
83. Biemann, M.; Ruffieux, P.; Schwaller, P.; Sudan, P.; Schlapbach, L.; Gröning, P. *J. Electron. Mater.* **2002**, *31*, 1316–1320. doi:10.1007/s11664-002-0114-7
84. Jelić, D.; Penavin-Škundić, J.; Majstorović, D.; Mentus, S. *Thermochim. Acta* **2011**, *526*, 252–256. doi:10.1016/j.tca.2011.10.001
85. Jacquet, P.; Podor, R.; Ravaux, J.; Teisseire, J.; Gozhyk, I.; Jupille, J.; Lazzari, R. *Scr. Mater.* **2016**, *115*, 128–132. doi:10.1016/j.scriptamat.2016.01.005
86. Ovchinnikov, V. Reduction of Silver Oxide Film in Inert Gas Plasma. In *The Tenth International Conference on Quantum, Nano/Bio, and Micro Technologies*, 2016; pp 6–11.
87. Reinhold, I.; Hendriks, C. E.; Eckardt, R.; Kranenburg, J. M.; Perelaer, J.; Baumann, R. R.; Schubert, U. S. *J. Mater. Chem.* **2009**, *19*, 3384–3388. doi:10.1039/b823329b
88. Han, Y.; Lupitsky, R.; Chou, T.-M.; Stafford, C. M.; Du, H.; Sukhishvili, S. *Anal. Chem.* **2011**, *83*, 5873–5880. doi:10.1021/ac2005839
89. Yüksel, S.; Ziegler, M.; Goerke, S.; Hübner, U.; Pollok, K.; Langenhorst, F.; Weber, K.; Cialla-May, D.; Popp, J. *J. Phys. Chem. C* **2015**, *119*, 13791–13798. doi:10.1021/acs.jpcc.5b01389

License and Terms

This is an Open Access article under the terms of the Creative Commons Attribution License (<http://creativecommons.org/licenses/by/4.0>). Please note that the reuse, redistribution and reproduction in particular requires that the authors and source are credited.

The license is subject to the *Beilstein Journal of Nanotechnology* terms and conditions: (<https://www.beilstein-journals.org/bjnano>)

The definitive version of this article is the electronic one which can be found at: <doi:10.3762/bjnano.9.263>

2.4 SERS enhancement of silver functionalized dense anodic aluminum oxide derived from iodine-based oxoacid electrolytes. Evidence for a combined physical and chemical enhancement effect.

SERS substrates based on anodic aluminum oxide (AAO) have been used in literature for the large area fabrication of nanostructured SERS substrates with an even distribution of hot spots which are easily formed upon the deposition of silver on the top of porous anodic aluminum oxide (PAOX). Furthermore, it is known that the dielectric beneath the noble metal influences the local electric field enhancement which could increase the observed SERS enhancement factor of the substrate. With the deposition of a noble metal like silver on the top of anodized aluminum leads to the formation of an Al/AAO/Ag substrate which has the ability not only to enhance the Raman signal of the analyte through SERS but also through interference-enhanced Raman scattering (IERS) if the thickness of the anodic aluminum oxide is optimized which can result in a SERS-IERS co-enhancement. All these advantages make such a system interesting for further investigation and for the preparation of efficient SERS substrates.

Anodization of aluminum can result in the formation of barrier-type or porous anodic aluminum oxide depending on the electrolyte used. Although several investigations used PAOX for the preparation of SERS substrates, barrier-type AAO has never been tested for Al/AAO/Ag SERS platforms. Here, barrier-type AAO prepared in iodine-based oxoacid electrolytes (periodic and iodic acid) have been sputtered with silver to be tested as SERS substrates where an initial investigation revealed that they outperform SERS substrates prepared similarly with PAOX. Comparison with SERS substrates prepared from other barrier-type AAO obtained from citrate buffer and ALD-deposited alumina showed that SERS substrates containing barrier-type AAO from iodine oxoacids result in a much higher SERS activity even if the thickness of the AAO is not optimized for optimal IERS co-enhancement. In depth investigation of the underlying reason for the high SERS activity of these substrates leads to the assumption that the presence of iodine species in these AAO films could result in a chemical enhancement together with the conventional electromagnetic enhancement mechanism resulting in a synergistic effect as no differences in the physical properties of the different barrier-type AAO was observed. This investigation opens the door for the preparation of more efficient SERS substrates based on aluminum supported anodic aluminum oxide.

**Silver sputtered barrier-type anodic aluminum oxide derived from
iodine-based oxoacid electrolytes as efficient SERS substrates.
Evidence for a combined physical and chemical enhancement effect.**

Sherif Okeil^{a,‡}, Mikhail Pashchanka^{a,‡}, Silvio Heinschke^a, Michael Bruns^b and Jörg J.

Schneider^{a}*

^a Eduard-Zintl-Institut für Anorganische und Physikalische Chemie, Technische Universität Darmstadt, Alarich-Weiss-Straße 12, 64287 Darmstadt, Germany

^b Institut für Angewandte Materialien (IAM-ESS), Karlsruher Institut für Technologie, Hermann-von-Helmholtz-Platz 1, B 321, D-76344 Eggenstein-Leopoldshafen, Germany

*Corresponding Author

E-mail: joerg.schneider@ac.chemie.tu-darmstadt.de

‡ Both authors contributed equally to this work.

Abstract

Surface-enhanced Raman spectroscopy (SERS) presents an important spectroscopic technique with applications in many fields due to its ability to determine structural information of the analyte with high sensitivity which requires the design of SERS substrates with high enhancement factors. Silver sputtered porous anodic aluminum oxide (PAOX) membranes arose as efficient and easy-to access SERS substrates with high enhancement factors. Related barrier-type anodic aluminum oxide (AAO) has not been investigated for SERS applications so far, due to an absence of porosity and the anticipation of low SERS sensitivity. We found that dense barrier-type AAO obtained through electrolysis using periodic and iodic acid sputtered with silver exhibits comparable or even higher SERS enhancements than just silver sputtered porous alumina (PAOX) where the enhancement factor of the best SERS substrate based on barrier-type AAO from periodic acid shows a 2.6-fold increase compared to the prepared PAOX-based SERS substrate. On the other hand, SERS substrates based on barrier-type AAO obtained from citrate buffer or atomic layer deposited alumina used as comparison do not show such enhancements. In depth physical and chemical characterization and comparison of barrier-type AAO obtained from iodine oxoacids (periodic acid and iodic acid) with barrier-type AAO obtained from citrate buffer shows similar physical and optical properties except for the presence of iodine species (periodate, iodate, iodine and pentaiodide) in the AAO films from iodine oxoacids which point towards a chemical enhancement mechanism enhancing the SERS spectra.

1. Introduction

There is an ongoing search for the design of low-cost, reproducible and effective SERS substrates as well as a continuous research on the factors affecting the SERS enhancement of different substrates in order to improve the design of currently available SERS substrates.¹ Effective SERS substrates open the door for the identification and quantification of very low concentrations of analytes due to their higher sensitivity compared to conventional Raman spectroscopy.² Thus, SERS has already found a wide range of applications in areas like material sciences³, bioanalysis⁴⁻⁶, analysis of food^{7,8} and environmental contaminants^{9,10}, forensic science¹¹ and in situ analysis of electrochemical processes in electrochemistry.^{12,13} SERS is based on the enhancement of the Raman signal of an analyte molecule adsorbed on a rough surface of an electron rich metal, usually

a noble metal like silver and gold, through the excitation of surface plasmons in the metal leading to an enhancement of the local electromagnetic fields.^{14,15} There are two possible mechanisms responsible for the observed SERS enhancement of a molecule, namely electromagnetic (EM) and chemical (CM) enhancement where EM enhancement is more common.^{16–18} While the EM enhancement depends on the excitation of surface plasmons which result in the enhancement of the incident electric field, the CM enhancement depends on charge transfer to the analyte molecule resulting in a change of the electronic environment of the adsorbed molecule enhancing its polarizability.^{19,20} Different techniques and procedures have been developed for the design of SERS substrates such as nanolithography^{21–27}, oblique angle vapor deposition for the production of metal nanorod array^{17,28,29}, electrochemical surface roughening of silver electrodes^{30,31}, plasma treatment of metallic surfaces^{32–34} and wet-chemical synthesis of nanoparticles which could be followed by their aggregation for the production of hot spots^{35–39} to name a few. Thus, the methods for designing SERS substrates range from methods requiring sophisticated instrumentation resulting in expensive SERS substrates to simple and cheaper methods which however usually result in less uniform and less reproducible SERS substrates.

Anodization of aluminum represents a method of low cost which permits the passivation of aluminum towards corrosion and is widely used in industry.^{40,41} Since the demonstration of the ability to produce controlled and self-ordered nanoporous structures through the two-step anodization process of aluminum by Masuda et al.^{42,43} the interest in this system has grown enormously and porous anodic aluminum oxide (PAOX) membranes have been used for different applications such as filtration^{44,45} and as templates for preparation of a variety of nanostructures.⁴¹ Recently, PAOX has also been used as a template or platform for the preparation of various SERS substrates due to the ability to control the homogeneity and structure of the SERS substrate over a large area with high reproducibility at low cost.^{46,47} PAOX was e.g. used as template for the preparation of various SERS active nanorod arrays of silver or gold.^{48–51} Furthermore, PAOX has been introduced as a support for the deposition of metal nanoparticles inside its pores to obtain three-dimensional SERS substrates^{52–54} or the noble metal was sputtered or evaporated on PAOX to achieve the production of equally distributed and closely packed hot spots on the basis of the underlying PAOX where the hot spots are formed between the nanopores and also in the nanopores due to their reduced diameter after metal deposition.^{46,47,55–62} On the other hand, barrier-type AAO has not been used to the best of our knowledge as SERS substrate possibly due to the absence of

any surface nanostructuring. However, it is still known that SERS is sensitive to the dielectric material which is present beneath in the close vicinity of the SERS active metal layer^{63,64}. Therefore, it is plausible to study the barrier-type AAO as underlying dielectric for a possible SERS enhancement. It has even been shown that a combination containing a dielectric/noble metal as SERS substrate also have a self-cleaning ability in removing the analyte after a SERS experiment by photocatalysis. This enables its reuse, making such composites further interesting.^{65–69}

The use of anodized aluminum (i.e. aluminum substrate with aluminum oxide on top) sputtered with a noble metal as a platform and substrate for SERS is also interesting in the sense that it could combine SERS with interference-enhanced Raman scattering (IERS) depending on the thickness of the anodic aluminum oxide.⁶⁰ IERS which was introduced by Nemanich et al.^{70,71} relies on systems where a dielectric film of appropriate thickness is present on a metallic reflector where the interference resulting from this configuration cancels out the reflected incident radiation but enhances the emitted Raman scattering. Anodized aluminum where the resulting thickness of the dielectric layer can be controlled in a direct manner experimentally by the anodization time thus represents a system suitable for IERS. Indeed, aluminum/aluminum oxide substrates have been also employed as IERS substrates for the detection of biomolecules⁷² which makes this system very attractive for further investigations. Furthermore, interference effects resulting from barrier-type AAO are expected to have a positive effect compared to PAOX due to the absence of air in the dielectric film whereas the dielectric-air interface in PAOX would result in further light reflection and refraction giving rise to additional light scattering and consequently results in partial loss of the incident light which should be available for excitation and interference.

The aim of this work is to shed light on the interesting properties of such alumina SERS systems based on silver sputtered barrier-type AAO films formed in periodic or iodic acid electrolytes and to understand the found higher enhancement factors. For that, different Al/Alumina/Ag substrates with PAOX, barrier-type AAO from citrate buffer as well as with ALD-deposited alumina were compared to the performance of substrates containing barrier-type AAO from iodine oxoacids showing the superiority of the latter. Thus, in depth physical and chemical characterization of the different barrier-type AAO was performed in this study in order to determine the underlying cause for the high enhancement factors observed with SERS substrates based on AAO obtained from

unusual iodine oxoacids as electrolytes for the first time. We have elucidated the underlying reasons for the great SERS enhancement observed for silver sputtered barrier-type AAO films obtained from periodic and iodic acid and found that a chemical enhancement due to the incorporation of iodine species into the barrier-type AAO films is the possible reason for the observed unusual SERS enhancement.

2. Experimental

2.1. General procedure for electrochemical anodization

Sheeted aluminum metal of 1 mm thickness (PURALUX®, 99.93 % purity) was used as-received for the preparation of the AAO films. Rectangular electrodes having the dimensions 1.5 cm x 8 cm were cut from the aluminum sheets to form the anode and cathode of the electrochemical cell. Before electrochemical anodization the aluminum sheets were sonicated for 10 min in acetone to remove any organic residues from the surface and washed with deionized water. The cleaned electrodes were attached to the potentiostat (Sorensen XEL 250 DC power supply ($\Delta U_{\max} = 250$ V, $I_{\max} = 0.37$ A)) and immersed in the electrolyte solution which was continuously stirred during the anodization experiments. In all cases a two-step anodization technique was used. After the pre-anodization step for a specified period of time at a specified voltage the formed AAO was removed through wet etching in an aqueous mixture solution containing 0.16 M $K_2Cr_2O_7$ and 1.5 M H_3PO_4 at 60°C for about 3 h. This was followed by the main anodization step for a specified time at the same voltage used for the pre-anodization step. In all cases, the formed anodic aluminum oxide film was kept on the aluminum substrate and the Al/AAO was used for further processing in the preparation of the SERS substrates.

2.2. Preparation of barrier-type AAO on aluminum substrate

For the fabrication of barrier-type AAO different electrolytes were used. The first type of barrier-type AAO was produced using 0.3 M and 1 M concentrated aqueous solutions of periodic acid (Honeywell, reagent grade, ≥ 99.0 %) as an electrolyte where the temperature of the electrolyte solution is controlled between 0-1°C using a thermostat (Lauda RM6 T). The film “0.3 M periodic acid 80 V” was prepared using 0.3 M periodic acid as an electrolyte at 80 V voltage, where the pre-anodization step was performed for 2 h, followed by the wet etching in the aqueous $K_2Cr_2O_7/H_3PO_4$ mixture and finally the main anodization at 80 V for 3 h. Similarly, the samples

“1 M periodic acid 100 V” and “1 M periodic acid 200 V” were prepared in a 1 M periodic acid solution as electrolyte using 100 V and 200 V for 2.5 h, respectively for the main anodization step.

The second type of barrier-type AAO was prepared in 0.3 M iodic acid (ACROS Organics™, 99.6 %, ACS reagent) at 150 V where the pre-anodization was done for 2 h and the main anodization was done for 3 h at a temperature of 0-1 °C resulting in the sample “0.3 M iodic acid 150 V”.

For comparison, barrier-type AAO from a non-iodine containing electrolyte was also prepared. For that, barrier-type AAO produced from a citrate buffer was prepared as described in the literature⁷³ with some modifications. In short, a buffer composed of citric acid and sodium citrate (pH = 5.8) as electrolyte was prepared through mixing of 320 mL of 0.1 M citric acid monohydrate (VWR, AnalaR NORMAPUR®) with 1680 mL of 0.1 M trisodium citrate dihydrate (ACROS Organics™, 99 %) which were prepared in distilled water. The two-step anodization was performed at room temperature without temperature control where the measured temperature of the electrolyte bath was 23 °C. The pre-anodization step of 2 h was followed by a wet etching step in the K₂Cr₂O₇/H₃PO₄ aqueous mixture solution and finally, the main anodization was performed for 10 min at a voltage of 50 V and 100 V to obtain different AAO thicknesses.

2.3. Preparation of PAOX on aluminum substrate

PAOX was prepared using 0.3 M sulfuric acid as electrolyte with an anodization voltage of 27 V at a thermostatically controlled temperature of 0 °C. The pre-anodization step was performed for 20 h followed by wet etching of the formed oxide layer in the K₂Cr₂O₇/H₃PO₄ aqueous mixture solution and finally, a main anodization step for 5 min was performed.

2.4. Atomic layer deposition (ALD) of thin alumina layers for comparison with barrier-type AAO

Aluminum oxide was deposited using ALD either on a bare aluminum substrate or on anodized aluminum with barrier-type AAO. For the deposition the substrates were inserted into the ALD chamber (Savannah G2, Ultratech/CNT, Cambridge Nanotech) using trimethylaluminium (98+%, Strem Chemicals, Inc.) and water (HPLC grade, Sigma Aldrich) as precursors. The precursors were vaporized at room temperature using 20 sccm argon as carrier gas. The exposure time for both, trimethylaluminium and water, were 0.015 s and the flushing between the precursor pulses was done with argon for 5 s and the deposition was done at 200 °C. Deposition of 1 nm Al₂O₃ is

equivalent to ten ALD cycles³⁴ which was used to calculate the number of cycles required for a specified thickness.

2.5. *Preparation of different Al/Alumina/Ag based SERS substrates*

The fabricated AAO (barrier-type or porous) was kept on the aluminum substrate and silver of specified thickness was sputtered on top of the AAO using a benchtop Cressington 208HR sputter coater where the sputtered thickness was monitored by a MTM-20 high-resolution thickness controller. The silver sputter target from Evochem (57 mm diameter and 0.2 mm thickness) was used for sputtering using a deposition rate of about 0.4 nm/s at a chamber pressure of about 0.05 mbar.³⁴ Silver was also sputtered on ALD-deposited Al₂O₃ on aluminum to be used as SERS substrate for comparison with other SERS substrates containing barrier-type AAO. The different samples were named according to the source of the formed alumina on the aluminum substrate followed by the thickness of the sputtered silver where SA, PIA, IA, CB and ALD were used as abbreviations for sulfuric acid, periodic acid, iodic acid, citrate buffer and ALD-deposited alumina, respectively. Thus, a sample named PIA80/15Ag represents the SERS substrate consisting of an aluminum substrate with an AAO formed in periodic acid at 80 V and sputtered with 15 nm Ag.

2.6. *Characterization of the barrier-type AAO-based SERS substrates*

Scanning electron microscopy (SEM) was performed on a Philips XL-30 FEG using an electron beam at 25 kV as accelerating voltage to observe any surface structures which could be formed after silver sputtering. Atomic force microscopy (AFM) to determine the surface roughness (root mean square roughness, R_q) of the prepared SERS substrates was carried out on a CP-II AFM (Bruker-Veeco) with SiC cantilevers in contact mode and the resulting topography images were processed using Gwyddion software (Version 2.54). Spectroscopic ellipsometry was performed with a Woolham M-2000 V spectrometer (spectral range 370–1690 cm⁻¹) at 45°–85° using the completeEASE software (version 6.29). Focused ion beam (FIB)⁷⁴ was used to prepare cross-sections of the Al/AAO/Ag SERS substrates which were investigated by a Tecnai G2 F20 transmission electron microscope (TEM) operating at 200 kV. UV-VIS diffuse reflectance spectra (UV-VIS DRS) of the different SERS substrates were recorded by a Thermo Scientific UV-VIS spectrophotometer (Evolution 600) with the help of an integrating sphere accessory. X-ray photoelectron spectroscopy (XPS) was performed on a K-Alpha XPS spectrometer (ThermoFischer Scientific, East Grinstead, UK) using a microfocused, monochromated Al K_α X-

ray source (30–400 μm spot size). Data acquisition and processing was done using the Thermo Avantage software. The K-Alpha charge compensation system was employed during analysis, using electrons of 8 eV energy and low-energy argon ions to prevent any localized charge build-up. A charge shift correction was done for the recorded XPS spectra using a C 1s electron binding energy of 285.0 eV.

2.7. SERS measurements on different Al/Alumina/Ag substrates

Raman measurements were performed on a micro-Raman (Alpha300 R micro-Raman, WITec, Germany) using a Nd:YAG 532 nm laser where Rhodamine B (RhB) has been used as model analyte for investigating the SERS performance. For that, few drops of a 1 μM RhB aqueous solution are added on the SERS substrate and left for about 30 min to allow adsorption to occur. Then the excess solution is drained from the substrate and the substrate is rinsed three times with distilled water to ensure the removal of excess analyte and the SERS substrate is allowed to dry with compressed air. The samples were exposed through a 50x microscope objective (NA = 0.80) to the laser with a power of 1.0 mW resulting in a spot size of about 0.8 μm using 1 s integration time for the collection of the SERS spectra. For the determination of the enhancement factor a drop of 1 mM aqueous solution of RhB is allowed to dry on a glass slide and was measured under the same conditions.

3. Results and Discussion

Barrier-type AAO is expected to result in a lower SERS enhancement compared to PAOX based substrates due to the formation of equally distributed hot spots in case of PAOX upon coating with a noble metal as gold or silver.^{46,56,58} We have now studied a barrier-type AAO film synthesized from periodic acid and found that it outperforms the enhancement observed for PAOX membranes (Figure 1). The PAOX membrane structure used for comparison was sputtered with 5 nm Ag which represents the optimized thickness of sputtered silver for the PAOX obtained from our synthesis resulting in the highest SERS enhancement.

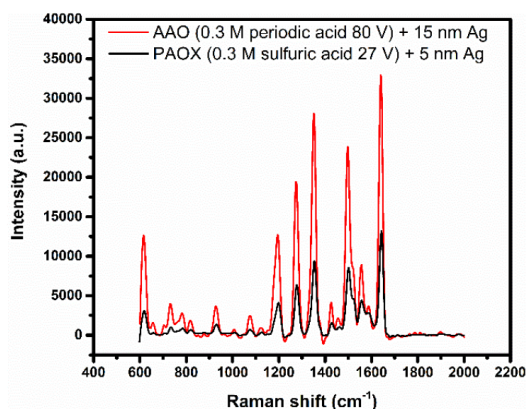


Figure 1. Comparison of the SERS spectra of 1 μM RhB on AAO prepared in 0.3 M periodic acid at 80 V sputtered with 15 nm Ag and PAOX prepared in 0.3 M sulfuric acid at 27 V sputtered with 5 nm Ag.

3.1. Material Characterization of the different SERS substrates

3.1.1. Scanning electron microscopy (SEM) and Atomic Force Microscopy (AFM)

To elucidate the possible reasons for the observed enhancement of the SERS substrates based on barrier-type AAO from periodic acid, first SEM was performed to investigate the presence of a specific surface structuring which could lead to the formation of hot spots or an increased surface roughness. Figure 2 shows a comparison of the SEM of different barrier-type AAO obtained from periodic acid with barrier-type AAO obtained from citrate buffer electrolyte. Each substrate is sputtered with a layer of 15 nm Ag under identical conditions. In all cases no pores can be observed which proves the formation of a dense barrier-type AAO material. For the silver sputtered AAO films obtained from 0.3 M periodic acid at 80 V and 1 M periodic acid at 100 V no specific surface features or specifically increased roughness could be observed when compared to the silver sputtered AAO film obtained from citrate buffer (Figure 2a, b and d) except for the AAO film obtained from 1 M periodic acid at 200 V (Figure 2c), where an increased roughness and dedicated particle formation of metallic silver is observed on the substrate surface.

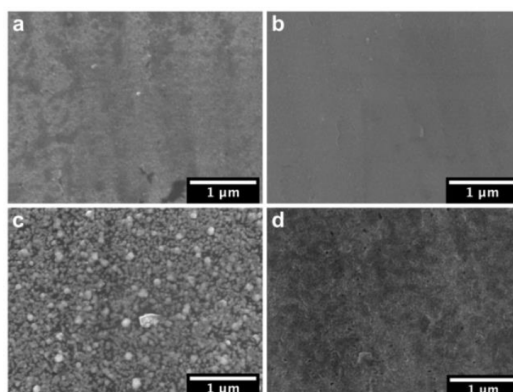


Figure 2. SEM images of AAO films prepared in (a) 0.3 M periodic acid at 80 V, (b) 1 M periodic acid at 100 V, (c) 1 M periodic acid at 200 V and (d) citrate buffer at 100 V. Each sample was sputtered with 15 nm metallic silver.

As the surface roughness of the sputtered silver is a very important factor which would lead to an increased SERS effect^{34,75} the surface roughness of different AAO films from periodic acid before and after sputtering with 15 nm Ag was determined by AFM (Figure 3a-d) and compared to (i) the surface roughness of metallic silver sputtered AAO obtained from citrate buffer (Figure 3e) and (ii) the surface roughness of alumina deposited on aluminum by ALD which was then sputtered with the same layer thickness of metallic silver (Figure 3f). Interestingly, no significant change in the surface roughness could be observed for the AAO films from periodic acid before and after silver sputtering. As can be seen for the AAO film obtained from 0.3 M periodic acid at 80 V without sputtered metallic silver a surface roughness of $R_q = 12.29$ nm was determined (Figure 3a) while after sputtering a 15 nm silver layer on top a slight increase by 0.7 nm in the surface roughness to $R_q = 12.99$ nm was observed (Figure 3b). A still comparable increase in thickness is observed for the initially rougher AAO film obtained from 1 M periodic acid at 200 V where a surface roughness of $R_q = 30.56$ nm without sputtered silver (Figure 3c) is compared to a roughness of $R_q = 31.60$ nm resulting in an increase by 1.04 nm with the sputtering of 15 nm silver (Figure 3d). A comparison of the silver sputtered AAO films which were obtained under aluminum oxidation in 0.3 M periodic acid electrolyte at 80 V (Figure 3b) with the silver sputtered AAO film obtained from the citrate buffer electrolyte (Figure 3e) shows no significant difference ($R_q = 12.99$ nm for PIA80/15Ag versus $R_q = 13.75$ nm for CB100/15Ag). In contrast, a 15 nm silver sputtered

film onto the alumina surface deposited by ALD shows a much lower roughness of $R_q=5.11$ nm (Figure 3f) which is due to the very smooth and uniform alumina layer obtained by ALD deposition. The roughness observed in this case is addressed to be dictated by the underlying aluminum substrate.

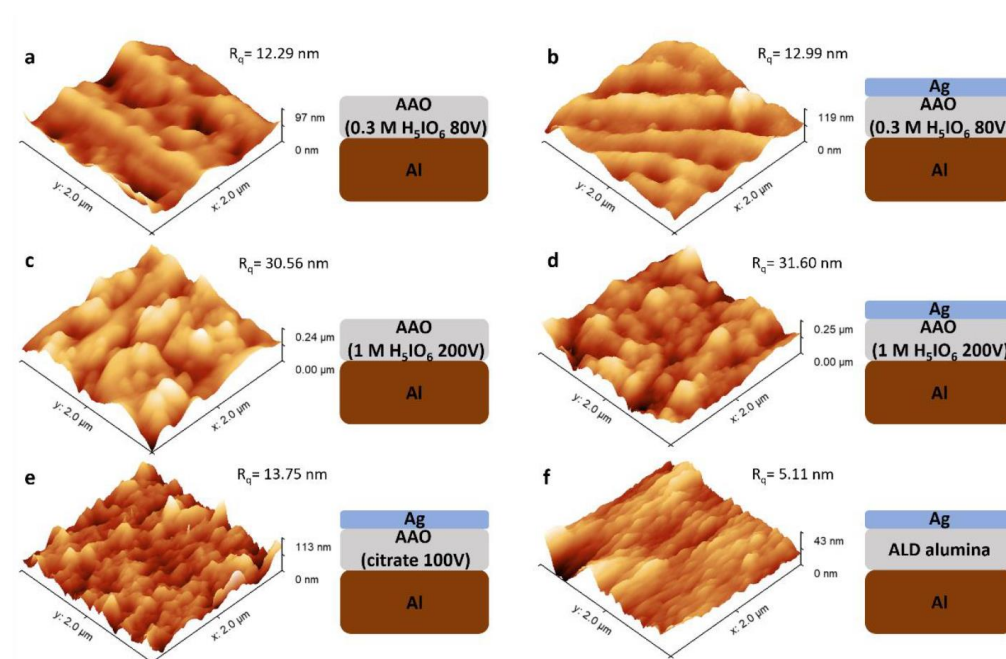


Figure 3. AFM topographic scans with the corresponding scheme showing the substrate composition of an AAO film prepared in 0.3 M periodic acid at 80 V (a) bare film and (b) film sputtered with 15 nm Ag; AAO film prepared in 1 M periodic acid at 200 V (c) bare film and (d) film sputtered with 15 nm Ag; (e) AAO film prepared in citrate buffer at 100 V sputtered with 15 nm Ag and (f) Al substrate with 100 nm of ALD-deposited Al_2O_3 sputtered with 15 nm Ag.

Besides the surface roughness of the SERS substrate another cause for the observed enhancements could be a combined enhancement due to surface-enhanced Raman and interference effects as observed in literature for similar systems.^{60,76} It is known that optimization of the dielectric layer thickness in order to achieve destructive interference results in the enhancement of the Raman scattering which is termed interference-enhanced Raman scattering (IERS).^{70,71} Thus, the SERS signal could be further enhanced by IERS if the thickness of the used AAO matches the required

IERS conditions. This aspect is investigated for the different Al/Alumina/Ag based SERS substrates prepared in this work.

3.1.2. Transmission Electron Microscopy (FIB-TEM)

For the determination of the thickness of the grown barrier-type AAO from periodic acid and citrate buffer as well as the investigation of the silver/AAO and AAO/Al interface (see Figure 3 for the illustrative schemes) cross-sectional TEM was performed (Figure 4). A sample from periodic acid (AAO from 0.3 M periodic acid 80 V + 15 nm sputtered Ag) and citrate buffer (AAO from citrate buffer 100 V + 15 nm sputtered Ag) showed both a compact barrier-type AAO layer of similar thickness with a thickness of 118 nm for AAO obtained from 0.3 M periodic acid at 80 V (Figure 4a) and 136 nm for AAO obtained from citrate buffer at 100 V (Figure 4c). High-resolution TEM (HRTEM) reveals that the barrier-type AAO from periodic acid as well as from the citrate buffer electrolyte are crystalline (presumably γ -alumina) (Figure 4b, d).

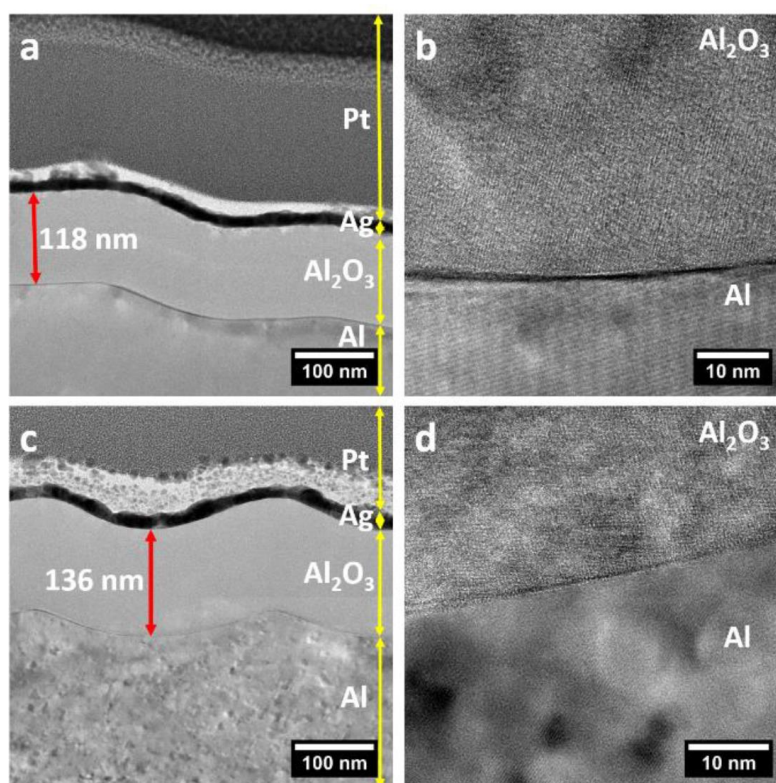


Figure 4. Cross-sectional TEM (FIB-TEM) images of (a, b) barrier-type AAO prepared in 0.3 M periodic acid at 80 V sputtered with 15 nm Ag and (c, d) barrier-type AAO prepared in citrate buffer (pH = 5.8) at 100 V sputtered with 15 nm Ag.

3.1.3. Spectroscopic Ellipsometry Characterization

From the cross-sectional TEM images a model for the Al/AAO system has been developed to be used for the modelling of the spectroscopic ellipsometry data in order to determine the thickness of the AAO as well as other optical properties such as the refractive index. This model includes a pure Al₂O₃ layer followed by a mixed Al/Al₂O₃ layer and finally the Al substrate (Figure S1, Supporting Information). The mixed Al/Al₂O₃ layer can be understood as the interfacial roughness observed between the Al substrate and the AAO as can be also seen in the cross-sectional TEM images (Figure 4a and c).⁷⁷ For AAO (0.3 M periodic acid 80 V) a thickness of 121 nm was obtained for the upper Al₂O₃ layer and 27 nm for the lower Al/Al₂O₃ interface layer where especially the upper layer thickness correlates well with the observed thickness observed in the FIB-TEM. Therefore, the thickness values obtained for the upper pure Al₂O₃ layer are considered to reflect the thickness of the prepared AAO film. For AAO (1M periodic acid 100 V) a thickness of 117 nm, for AAO (0.3 M iodic acid 150 V) a thickness of 190 nm and for ALD-deposited Al₂O₃ a thickness of 104 nm was determined. The prepared PAOX from sulfuric acid is much thicker (378 nm) despite the short anodization time which was applied due to the higher current densities achieved in sulfuric acid electrolytes compared to iodine oxoacid electrolytes. The developed model was also used to determine the complex refractive indices of the pure Al₂O₃ layer of the different barrier-type AAO, PAOX and ALD-deposited Al₂O₃ (Figure S2 and Table S1, Supporting Information). For the real part of the complex refractive index all barrier-type AAO as well as ALD-deposited Al₂O₃ show similar values of about 1.670 at 532 nm. Only PAOX show a lower value of 1.597 at 532 nm which is not surprising due to the porosity of the membrane which includes air leading to the observed decrease of the refractive index. It is known that a higher refractive index (either the real part or the imaginary part or both) results in a higher enhancement of the local electric field and thus a higher SERS enhancement.^{63,64} However, still there is no significant difference in the obtained refractive indices which could explain the great difference in the observed SERS enhancements. Conclusively, from the obtained values of the complex refractive indices it can be deduced that no significant enhancement effects of the electric fields

are generated due to the low n and k values of all dielectric materials used under the sputtered silver films.⁶³

3.1.4. UV-VIS Diffuse Reflectance Spectroscopy (DRS) Characterization

The UV-VIS DRS spectra for the different SERS substrates show a characteristic interference pattern for thin films where several maxima and minima are observed depending on the film thickness on the Al substrate (Figure 5). If an absorption maximum coincides with the wavelength of the exciting laser used for Raman measurement (532 nm) this will result in a combined SERS and IERS enhancement in the resulting Raman spectra. For the SERS substrate based on PAOX obtained from 0.3 M sulfuric acid at 27 V and sputtered with 5 nm Ag there is an absorption maximum at 532 nm making this substrate an ideal candidate for the SERS and IERS co-enhancement. In addition, this substrate offers the advantage of forming nearly equal distributed hot spots upon silver sputtering due to the regular porous structure of the PAOX (see SEM Figure S3, Supporting Information).^{46,56,58}

Comparison of the different SERS substrates based on barrier-type AAO obtained from periodic acid electrolyte reveals an absorption minimum (in case of AAO from 1 M periodic acid at 100 V and 200 V) at 532 nm or being close to the absorption minimum for AAO from 0.3 M periodic acid at 80 V. Thus, in all three cases this is not an ideal condition for the IERS which shows that the enhancement in these substrates can be traced to a significant manner only to the SERS effect itself. In addition, a barrier-type AAO obtained from iodic acid (0.3 M iodic acid 150 V) was prepared to check whether the enhancement effect observed with AAO from periodic acid is also observed in this case. The UV-VIS DRS of the SERS substrate containing the AAO film from iodic acid also shows a minor absorption at 532 nm which is between an absorption maximum and minimum which is again not ideal for observing an additional IERS to take place. Nevertheless, the situation is still in favor over the SERS substrates containing AAO obtained from 1M periodic acid 100 V and 200 V where the absorption at 532 nm represents exactly the minimum.

For further comparison, two additional SERS substrates containing barrier-type AAO from a non-iodine containing electrolyte (citrate buffer) were prepared. In this case, AAO obtained from citrate buffer electrolyte at 100 V was sputter-coated with 15 nm Ag layer. This substrate showed an absorption minimum near 532 nm while AAO from citrate buffer at 50 V and sputtered with 5 nm Ag shows an intense absorption at 532 nm near to its absorption maximum. Another SERS

substrate tested where a better control over the thickness of the Al₂O₃ on the aluminum substrate could be achieved to match an absorption maximum at 532 nm represents the one which contains the ALD-deposited alumina with a thickness 100 nm. This was again sputtered with a 15 nm Ag layer. The SERS substrates containing AAO from citrate buffer at 50 V (with a thickness of about 105 nm, see SEM Figure S4, Supporting Information) and the ALD-deposited alumina both now match the ideal conditions for IERS which should suggest that these substrates should result in higher SERS enhancement factors compared to the SERS substrates containing AAO from periodic or iodic acid.

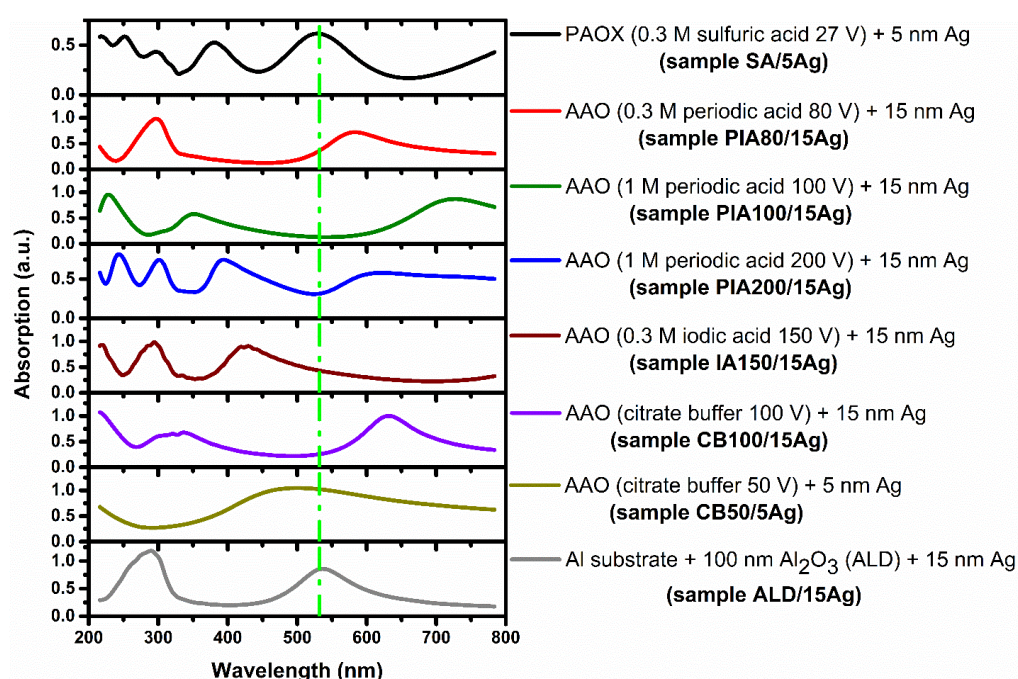


Figure 5. Comparison of UV-VIS DRS spectra of aluminum supported PAOX membrane from sulfuric acid sputtered with 5 nm Ag with various aluminum supported barrier-type AAO films sputtered with Ag and an aluminum substrate coated with 100 nm Al₂O₃ from ALD and sputtered with a 15 nm Ag. The green dash-dotted line at 532 nm indicates the laser wavelength used for Raman measurements.

3.1.5. X-ray photoelectron spectroscopic (XPS) characterization

In order to get an insight in the chemical composition of the different barrier-type AAO films in the near surface region and to determine the presence of any anionic impurities XPS was performed. In aluminum anodization it is well known that there is always a small percentage of anionic impurities coming mainly from the used electrolyte which are incorporated into the AAO film during anodization.^{78–81} Comparison of the XPS survey spectra of barrier-type AAO films from periodic acid, iodic acid and citrate buffer (Figure 6a) show the presence of the elements aluminum, oxygen and carbon, however in case of AAO films from periodic acid and iodic acid the incorporation of iodine presumably originating from the electrolyte is detected in the spectra. High resolution XPS spectra of the I 3d valence state (Figure 6b) show the absence of any iodine species in AAO film from citrate buffer while a mixture of iodine species could be found in the AAO films from periodic and iodic acid. In the samples AAO (1 M periodic acid 100 V) and AAO (0.3 M iodic acid 150 V) the deconvoluted high resolution XPS spectra for I 3d show a doublet at 624.7 eV and 636.1 eV with a doublet splitting of 11.4 eV corresponding to the I 3d_{5/2} and I 3d_{3/2}, respectively and which can be assigned to periodate (IO₄⁻) species.⁸² A further doublet is observed at 622.4 eV and 633.9 eV with a doublet splitting of 11.5 eV which corresponds to the I 3d_{5/2} and I 3d_{3/2} of iodate (IO₃⁻).^{83,84} Finally, a third doublet at 620.1 eV and 631.8 eV with a doublet splitting of 11.7 eV was observed and is most probably assigned to the I 3d_{5/2} and I 3d_{3/2} of molecular iodine I₂^{82,83} or a polyiodide species such as pentaiodide I₅⁻.⁸⁵ The formation of different iodine species which are incorporated in the AAO films could be explained through the occurrence of complex redox chemistry of the anionic iodine species present in the electrolyte during anodization. Interestingly, the periodate anion impurity is dominant compared to the other iodine species in both AAO films from periodic and iodic acid. The favored formation of the periodate IO₄⁻ species in case of the iodic acid (HIO₃) electrolyte is due to the well-known oxidative solution behavior of iodate IO₃⁻ into periodates under oxidative electrochemical conditions.⁸⁶ Nevertheless, it is noteworthy that in the AAO barrier layer obtained from iodic acid electrolyte the iodate and molecular iodine or pentaiodide represent a higher fraction of the total amount of iodine species present when compared to the AAO film from periodic acid. In the AAO (0.3 M iodic acid 150 V), iodate corresponds to 8.2 % and molecular iodine or pentaiodide corresponds to about 7.8 % of the total iodine species compared to the AAO film (1 M periodic acid 100 V) where the iodate content is 7.3 % and molecular iodine or pentaiodide amounts to 5.1 % of the total iodine species.

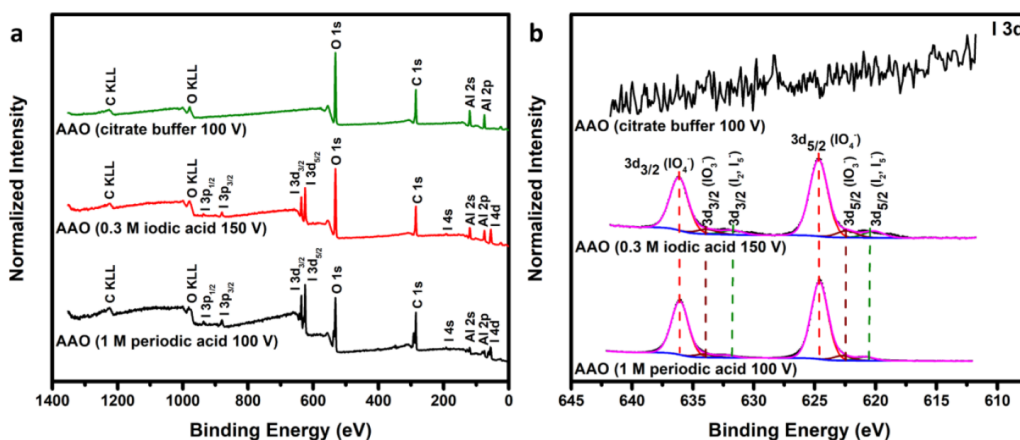


Figure 6. (a) XPS survey spectra and (b) high-resolution deconvoluted I 3d XPS spectra of AAO films prepared in 1M periodic acid at 100 V, 0.3 M iodic acid at 150 V and citrate buffer (pH = 5.8) at 100 V.

3.2. SERS performance of the silver sputtered alumina substrates

Rhodamine B (RhB) was used as model analyte to compare the SERS performance of the different SERS substrates. The SERS spectrum of RhB shows characteristic peaks in the region of 600-1700 cm^{-1} with the most prominent peaks found at 618 cm^{-1} , 1195 cm^{-1} , 1274 cm^{-1} , 1352 cm^{-1} , 1500 cm^{-1} and 1643 cm^{-1} which correlates well with the values found in literature.^{87,88} These Raman bands are mainly assigned to bending and stretching of C-C in the xanthene ring as well as C-H bending.^{87,88} Figure 7 shows a comparison of the SERS spectra obtained for 1 μM RhB on the different SERS substrates containing barrier-type AAO from periodic and iodic acid (Figure 7a), AAO from citrate buffer and ALD-deposited alumina (Figure 7b) as well as PAOX from sulfuric acid (Figure 7c) where the intensity scale range is kept constant to allow a direct comparison and a further comparison of the average SERS intensity at 1643 cm^{-1} with the corresponding standard deviation using a bar chart as it is found in Figure 7d. It can be clearly seen that the SERS spectra obtained from SERS substrates containing AAO films from periodic and iodic acid show significant higher enhancements (in case of PIA80/15Ag and IA150/15Ag) or at least comparable enhancements (in case of PIA100/15Ag and PIA200/15Ag) to SERS substrates containing the PAOX membrane. A comparison with SERS substrates containing barrier-type

AAO from citrate buffer or ALD-deposited alumina reveals a much better performance of the SERS substrates containing barrier-type AAO from iodine oxoacids especially when compared to the samples CB100/15Ag and ALD/15Ag. Only AAO from citrate buffer electrolyte obtained at 50 V and sputtered with 5 nm Ag (sample CB50/5Ag) shows high SERS activity which can be explained by the optimized thickness of the film leading to an absorption maximum near 532 nm which is an optimal condition for IERS. But still despite both, the SERS and IERS effect operating in that case, the resulting spectra from this substrate (sample CB50/5Ag) lie well below the SERS spectra obtained from all substrates prepared from periodic or iodic acid. At the same time, the SERS substrates containing AAO from periodic and iodic acid are still not optimized for the ideal conditions for IERS as all of them possess an absorption minimum or a low absorbance near an absorption minimum at 532 nm (as seen above in the corresponding absorption spectra, Figure 5). Although low absorbance is observed at that wavelength still high enhancement factors are obtained which rule out that interference effects are the underlying cause for the observed SERS enhancements observed with these substrates. Thus, if compared to the SERS substrate containing AAO from citrate buffer with similar absorption conditions at 532 nm (sample CB100/15Ag) a huge difference in the resulting SERS spectrum is observed. This shows the unique performance of the SERS substrates containing AAO films from periodic or iodic acid.

As the surface roughness is also an important factor to consider for the overall observed SERS enhancement, a comparison of the surface roughness of the silver sputtered AAO films from periodic acid and citrate buffer (see above, Figure 3) shows similar roughness if sample PA80/15Ag and CB100/15Ag are compared. Therefore, the surface roughness as a significant reason for the observed differences in the SERS performance can be ruled out here. The SERS substrate ALD/15Ag which was fabricated to allow for a comparison with the SERS substrates containing AAO from periodic and iodic acid as it meets the ideal IERS conditions due to its absorption maximum at 532 nm (see Figure 5) shows surprisingly low intensity SERS spectra. We attribute this to the very low surface roughness of ALD-deposited alumina (compare Figure 3) on one hand and to the amorphous nature of the ALD-deposited alumina⁸⁹ compared to the the AAO which is crystalline in nature (see FIB-TEM, Figure 4).

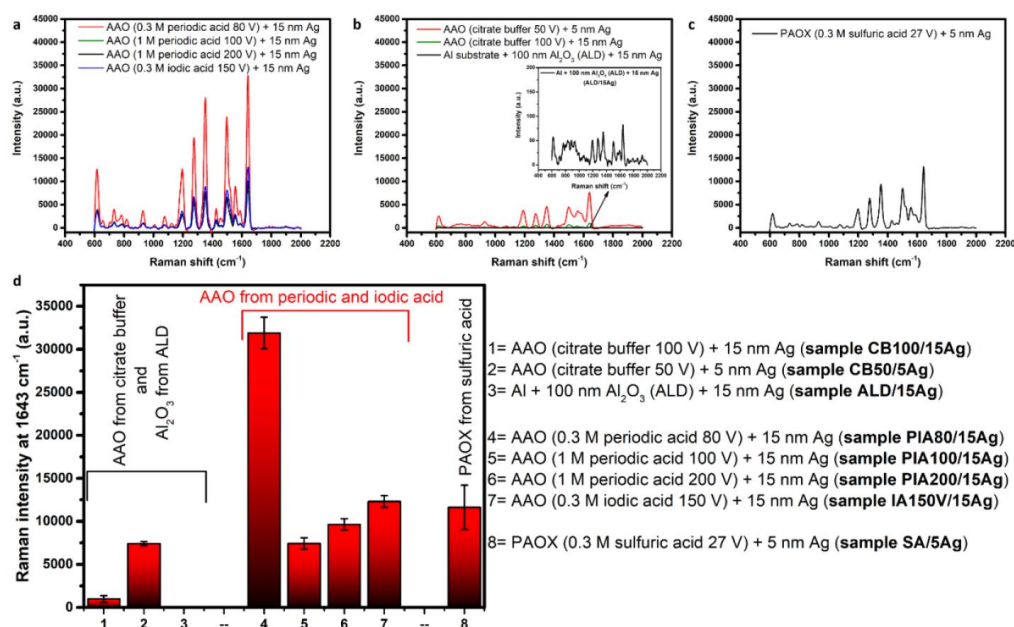


Figure 7. Comparison of the SERS spectra of 1 μM RhB on aluminum supported (a) AAO films from different periodic and iodic acid solutions and sputtered with 15 nm Ag, (b) AAO films from citrate buffer at different voltages and sputtered with silver as well as ALD-deposited Al₂O₃ on Al and sputtered with 15 nm Ag (magnified in inset) and (c) PAOX from sulfuric acid sputtered with 5 nm Ag. (d) Bar chart showing a direct comparison of the average SERS intensity of 1 μM RhB at 1643 cm⁻¹ on the different substrates presented under (a), (b) and (c).

A calculation of the enhancement factors (EF) for the different SERS substrates prepared in this work was performed using the formula

$$EF = \frac{I_{SERS}/C_{SERS}}{I_{RS}/C_{RS}}$$

where I_{SERS} and C_{SERS} are the measured SERS intensity at 1643 cm⁻¹ and the corresponding measured concentration of RhB (1 μM), respectively, and I_{RS} and C_{RS} are the normal Raman intensity measured for a concentration of 1 mM RhB drop-coated on a glass slide.^{34,90} A table with the calculated enhancement factors can be found in Table S2, Supporting information. For SERS substrates based on PAOX an enhancement factor of 1.52×10^5 was determined. In comparison an

enhancement factor of 3.90×10^5 was obtained for the best SERS substrate based on barrier-type AAO (PIA80/15Ag) which presents a 2.6-fold increase in the SERS enhancement compared to the PAOX-based SERS substrate.

All previous comparisons of the obtained differences in SERS enhancements between SERS substrates containing AAO from periodic or iodic acid and SERS substrates based on PAOX or other barrier-type AAO on the basis of physical factors such as surface roughness, refractive index or a possible IERS co-enhancement effect do not explain the observed differences which thus could indicate a chemical enhancement mechanism due to the presence of iodine species in the barrier-type AAO obtained from periodic or iodic acid (see for XPS spectra, Figure 6). Indeed, material compositions of dielectric and noble metals have also shown synergistic effects in SERS enhancement which was attributed to charge transfer (CT) effects and as such is based on a chemical enhancement effect.⁹¹ In order to follow this idea further, experiments have been performed where a 20 nm thick Al_2O_3 layer was deposited by ALD on top of the AAO films obtained from periodic acid as electrolyte. This layer should serve as a separator between the AAO film and the sputtered silver thus producing an iodine free region below the silver film. These new SERS substrates were then tested for their SERS performance showing a great decrease in the SERS enhancement when compared to their corresponding SERS substrates without ALD-deposited alumina as can be seen in Figure 8. This gives a further indication that the iodine species present in the AAO obtained from iodine oxoacid electrolytes as periodic or iodic acid could play a significant role in the observed SERS enhancements when using these barrier-type films as dielectrics below the sputtered silver film.

In summary of these combined studies a comparison of the difference observed in the SERS enhancement between SERS substrates based on the different films obtained from periodic and iodic acid electrolytes depends on several factors such as (i) the obtained film thickness, (ii) the resulting film roughness and most obviously (iii) the content and type of iodine species. Therefore, it is at that point not possible to reduce the comparison of the different film performances just to the content of iodine species in the film alone. This makes a direct explanation of the observed differences between the AAO films from periodic or iodic acid rather difficult.

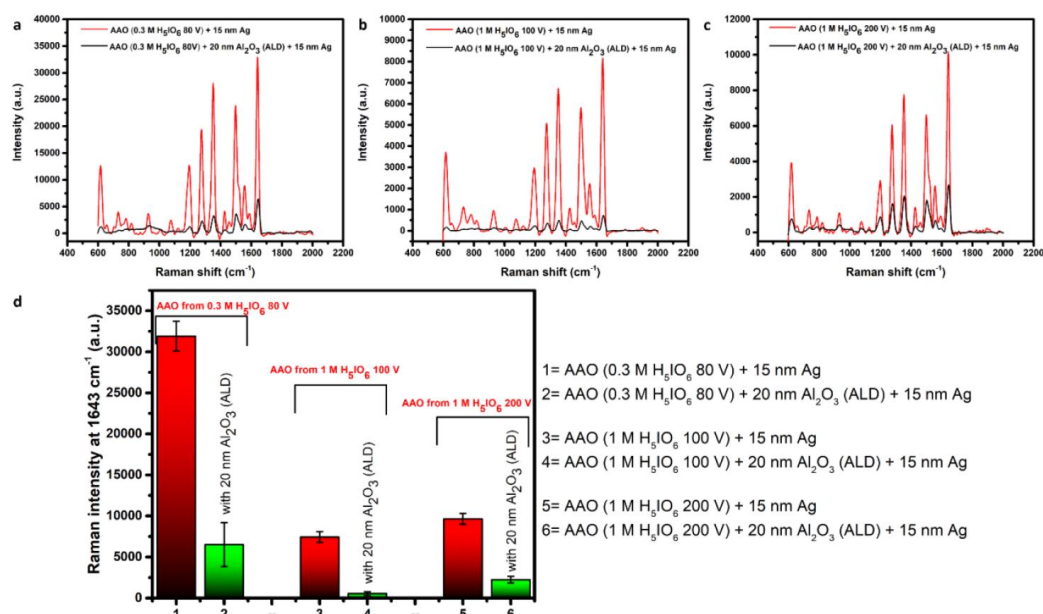


Figure 8. Comparison of the SERS spectra of 1 μM RhB on silver sputtered AAO prepared in (a) 0.3 M periodic acid at 80 V, (b) 1 M periodic acid at 100 V and (c) 1 M periodic acid at 200 V with and without 20 nm ALD-deposited alumina acting as a separator between the AAO film and the sputtered silver film. (d) Bar chart showing a direct comparison of the average SERS intensity of 1 μM RhB at 1643 cm^{-1} on the different substrates presented under (a), (b) and (c).

4. Conclusion

Silver sputtered dense barrier-type AAO is expected to yield much lower SERS enhancement factors than silver sputtered PAOX films due to the absence of nanopores which can act as centers for hot spots. However, herein we could show through comparison of silver sputtered PAOX with barrier-type AAO obtained from citrate buffer, periodic acid, iodic acid and ALD-deposited alumina, that especially SERS substrates based on barrier-type AAO obtained from iodine-based oxoacid electrolytes are able to yield high enhancement factors where physically derived factors such as increased surface roughness, increased refractive index or even an enhancement based on interference can be excluded. Thus, it is suggested that mainly the presence of various iodine species (periodate, iodate, iodine and pentaiodide) in these barrier-type films could contribute to the observed SERS enhancement and therefore point towards a possible chemical enhancement of the

SERS effect. In general, this study shows that the use of Al/AAO/Ag systems as SERS substrates is very interesting due to its straightforward fabrication. Furthermore, these systems can combine SERS enhancement, IERS enhancement and even chemical enhancement through the incorporation of iodine species during the electrochemical anodization process in the nonporous, dense AAO film which can even result in attractive enhancement factors. Further optimization bears the potential for the development of highly efficient SERS substrates for routine use.

Conflicts of interest

There are no conflicts to declare.

Supporting Information

Model used for fitting ellipsometry data, plots of variation the complex refractive indices with wavelength, table of complex refractive indices at specified wavelength, SEM image of silver sputtered PAOX, SEM image showing the thickness of AAO from citrate buffer, table with calculated enhancement factors

Acknowledgements

XPS measurements were carried out at the Karlsruhe Nano Micro Facility at KIT (M. Bruns) under the KNMF program. TEM studies were performed by J. Engstler (TUDa) under contract TUD1 at ERC Jülich. We thank Prof. R. Stark for the possibility of using the Raman spectrometer. M. Pashchanka thanks DFG (Deutsche Forschungsgemeinschaft) sincerely for financial support through the project PA 2713/1-1.

References

- (1) Stiles, P. L.; Dieringer, J. A.; Shah, N. C.; Van Duyne, R. P. Surface-Enhanced Raman Spectroscopy. *Annu. Rev. Anal. Chem* **2008**, *1*, 601–626.
- (2) Sharma, B.; Fernanda Cardinal, M.; Kleinman, S. L.; Greeneltch, N. G.; Frontiera, R. R.; Blaber, M. G.; Schatz, G. C.; Van Duyne, R. P. High-Performance SERS Substrates: Advances and Challenges. *MRS Bull.* **2013**, *38* (08), 615–624.
- (3) Lefrant, S.; Baltog, I.; Baibarac, M. Surface-Enhanced Raman Scattering Studies on

-
- Chemically Transformed Carbon Nanotube Thin Films. *J. Raman Spectrosc.* **2005**, *36* (6–7), 676–698.
- (4) Wang, C.; Meloni, M. M.; Wu, X.; Zhuo, M.; He, T.; Wang, J.; Wang, C.; Dong, P. Magnetic Plasmonic Particles for SERS-Based Bacteria Sensing: A Review. *AIP Adv.* **2019**, *9*, 010701.
- (5) Bruzas, I.; Lum, W.; Gorunmez, Z.; Sagle, L. Advances in Surface-Enhanced Raman Spectroscopy (SERS) Substrates for Lipid and Protein Characterization: Sensing and Beyond. *Analyst* **2018**, *143* (17), 3990–4008.
- (6) Zong, C.; Xu, M.; Xu, L.-J.; Wei, T.; Ma, X.; Zheng, X.-S.; Hu, R.; Ren, B. Surface-Enhanced Raman Spectroscopy for Bioanalysis: Reliability and Challenges. *Chem. Rev.* **2018**, *118* (10), 4946–4980.
- (7) Zheng, J.; He, L. Surface-Enhanced Raman Spectroscopy for the Chemical Analysis of Food. *Compr. Rev. Food Sci. Food Saf.* **2014**, *13* (3), 317–328.
- (8) Pilot, R. SERS Detection of Food Contaminants by Means of Portable Raman Instruments. *J. Raman Spectrosc.* **2018**, *49* (6), 954–981.
- (9) Tang, H.; Zhu, C.; Meng, G.; Wu, N. Review—Surface-Enhanced Raman Scattering Sensors for Food Safety and Environmental Monitoring. *J. Electrochem. Soc.* **2018**, *165* (8), B3098–B3118.
- (10) Álvarez-Puebla, R. A.; Liz-Marzán, L. M. Environmental Applications of Plasmon Assisted Raman Scattering. *Energy Environ. Sci.* **2010**, *3* (8), 1011–1017.
- (11) Fikiel, M. A.; Khandasammy, S. R.; Mistek, E.; Ahmed, Y.; Halámková, L.; Bueno, J.; Lednev, I. K. Surface Enhanced Raman Spectroscopy: A Review of Recent Applications in Forensic Science. *Spectrochim. Acta - Part A Mol. Biomol. Spectrosc.* **2018**, *197*, 255–260.
- (12) Dong, J.-C.; Zhang, X.-G.; Briega-Martos, V.; Jin, X.; Yang, J.; Chen, S.; Yang, Z.-L.; Wu, D.-Y.; Feliu, J. M.; Williams, C. T.; et al. In Situ Raman Spectroscopic Evidence for Oxygen Reduction Reaction Intermediates at Platinum Single-Crystal Surfaces. *Nat. Energy* **2019**, *4*, 60–67.

-
- (13) Tsai, M.-H.; Lin, Y.-K.; Luo, S.-C. Electrochemical SERS for in Situ Monitoring the Redox States of PEDOT and Its Potential Application in Oxidant Detection. *ACS Appl. Mater. Interfaces* **2019**, *11* (1), 1402–1410.
- (14) Moskovits, M. Surface-Enhanced Spectroscopy. *Rev. Mod. Phys.* **1985**, *57* (3), 783–826.
- (15) Lal, S.; Grady, N. K.; Kundu, J.; Levin, C. S.; Lassiter, J. B.; Halas, N. J. Tailoring Plasmonic Substrates for Surface Enhanced Spectroscopies. *Chem. Soc. Rev.* **2008**, *37* (5), 898–911.
- (16) Campion, A.; Kambhampati, P. Surface-Enhanced Raman Scattering. *Chem. Soc. Rev.* **1998**, *27*, 241–250.
- (17) Negri, P.; Dluhy, R. A. Ag Nanorod Based Surface-Enhanced Raman Spectroscopy Applied to Bioanalytical Sensing. *J. Biophotonics* **2013**, *6* (1), 20–35.
- (18) Su, Y.; Shi, Y.; Wang, P.; Du, J.; Raschke, M. B.; Pang, L. Quantification and Coupling of the Electromagnetic and Chemical Contributions in Surface-Enhanced Raman Scattering. *Beilstein J. Nanotechnol.* **2019**, *10*, 549–556.
- (19) Vo-Dinh, T. Surface-Enhanced Raman Spectroscopy Using Metallic Nanostructures. *TrAC - Trends Anal. Chem.* **1998**, *17* (8–9), 557–582.
- (20) Gu, X.; Trujillo, M. J.; Olson, J. E.; Camden, J. P. SERS Sensors: Recent Developments and a Generalized Classification Scheme Based on the Signal Origin. *Annu. Rev. Anal. Chem.* **2018**, *11* (1), 147–169.
- (21) Kahl, M.; Voges, E.; Kostrewa, S.; Viets, C.; Hill, W. Periodically Structured Metallic Substrates for SERS. *Sensors Actuators B Chem.* **1998**, *51* (1–3), 285–291.
- (22) Jensen, T. R.; Schatz, G. C.; Van Duyne, R. P. Nanosphere Lithography: Surface Plasmon Resonance Spectrum of a Periodic Array of Silver Nanoparticles by Ultraviolet - Visible Extinction Spectroscopy and Electrodynamics Modeling. *J. Phys. Chem. B* **1999**, *103* (13), 2394–2401.
- (23) Haynes, C. L.; Van Duyne, R. P. Nanosphere Lithography: A Versatile Nanofabrication Tool for Studies of Size-Dependent Nanoparticle Optics. *J. Phys. Chem. B* **2001**, *105* (24),

-
- 5599–5611.
- (24) Deng, X.; Braun, G. B.; Liu, S.; Sciortino, P. F.; Koefer, B.; Tombler, T.; Moskovits, M. Single-Order, Subwavelength Resonant Nanograting as a Uniformly Hot Substrate for Surface-Enhanced Raman Spectroscopy. *Nano Lett.* **2010**, *10* (5), 1780–1786.
- (25) Im, H.; Bantz, K. C.; Lindquist, N. C.; Haynes, C. L.; Oh, S. H. Vertically Oriented Sub-10-nm Plasmonic Nanogap Arrays. *Nano Lett.* **2010**, *10* (6), 2231–2236.
- (26) Ahn, H.-J.; Thiyagarajan, P.; Jia, L.; Kim, S.-I.; Yoon, J.-C.; Thomas, E. L.; Jang, J.-H. An Optimal Substrate Design for SERS: Dual-Scale Diamond-Shaped Gold Nano-Structures Fabricated via Interference Lithography. *Nanoscale* **2013**, *5* (5), 1836.
- (27) Suresh, V.; Ding, L.; Chew, A. B.; Yap, F. L. Fabrication of Large-Area Flexible SERS Substrates by Nanoimprint Lithography. *ACS Appl. Nano Mater.* **2018**, *1* (2), 886–893.
- (28) Shanmukh, S.; Jones, L.; Driskell, J.; Zhao, Y.; Dluhy, R.; Tripp, R. A. Rapid and Sensitive Detection of Respiratory Virus Molecular Signatures Using a Silver Nanorod Array SERS Substrate. *Nano Lett.* **2006**, *6* (11), 2630–2636.
- (29) He, Y.; Fu, J.; Zhao, Y. Oblique Angle Deposition and Its Applications in Plasmonics. *Front. Phys.* **2014**, *9* (1), 47–59.
- (30) Yang, K. H.; Liu, Y. C.; Yu, C. C. Enhancements in Intensity and Stability of Surface-Enhanced Raman Scattering on Optimally Electrochemically Roughened Silver Substrates. *Journal of Materials Chemistry*. 2008, pp 4849–4855.
- (31) Yang, K. H.; Liu, Y. C.; Yu, C. C. Simple Strategy to Improve Surface-Enhanced Raman Scattering Based on Electrochemically Prepared Roughened Silver Substrates. *Langmuir* **2010**, *26* (13), 11512–11517.
- (32) Kinnan, M. K.; Kumbhar, A.; Chumanov, G. Plasma Reduction of Silver Compounds for Fabrication of Surface-Enhanced Raman Scattering Substrates. *Appl. Spectrosc.* **2008**, *62* (7), 721–726.
- (33) Ma, C.; Trujillo, M. J.; Camden, J. P. Nanoporous Silver Film Fabricated by Oxygen Plasma: A Facile Approach for SERS Substrates. *ACS Appl. Mater. Interfaces* **2016**, *8*

-
- (36), 23978–23984.
- (34) Okeil, S.; Schneider, J. J. Controlling Surface Morphology and Sensitivity of Granular and Porous Silver Films for Surface-Enhanced Raman Scattering, SERS. *Beilstein J. Nanotechnol.* **2018**, *9* (1), 2813–2831.
- (35) Schwartzberg, A. M.; Grant, C. D.; Wolcott, A.; Talley, C. E.; Huser, T. R.; Bogomolni, R.; Zhang, J. Z. Unique Gold Nanoparticle Aggregates as a Highly Active Surface-Enhanced Raman Scattering Substrate. *J. Phys. Chem. B* **2004**, *108*, 19191–19197.
- (36) Péron, O.; Rinnert, E.; Lehaitre, M.; Crassous, P.; Compère, C. Detection of Polycyclic Aromatic Hydrocarbon (PAH) Compounds in Artificial Sea-Water Using Surface-Enhanced Raman Scattering (SERS). *Talanta* **2009**, *79* (2), 199–204.
- (37) Stiufiuc, R.; Iacovita, C.; Lucaciu, C. M.; Stiufiuc, G.; Dutu, A. G.; Braescu, C.; Leopold, N. SERS-Active Silver Colloids Prepared by Reduction of Silver Nitrate with Short-Chain Polyethylene Glycol. *Nanoscale Res. Lett.* **2013**, *8* (1), 47.
- (38) Tang, J.; Chen, W.; Ju, H. Sensitive Surface-Enhanced Raman Scattering Detection of Atrazine Based on Aggregation of Silver Nanoparticles Modified Carbon Dots. *Talanta* **2019**, *201*, 46–51.
- (39) Mosier-Boss, P. Review of SERS Substrates for Chemical Sensing. *Nanomaterials* **2017**, *7* (6), 142.
- (40) Poinern, G. E. J.; Ali, N.; Fawcett, D. Progress in Nano-Engineered Anodic Aluminum Oxide Membrane Development. *Materials (Basel)*. **2011**, *4* (3), 487–526.
- (41) Lee, W.; Park, S.-J. Porous Anodic Aluminum Oxide: Anodization and Templated Synthesis of Functional Nanostructures. *Chem. Rev.* **2014**, *114* (15), 7487–7556.
- (42) Masuda, H.; Fukuda, K. Ordered Metal Nanohole Arrays Made by a Two-Step Replication of Honeycomb Structures of Anodic Alumina. *Science (80-.)*. **1995**, *268* (5216), 1466–1468.
- (43) Masuda, H.; Satoh, M. Fabrication of Gold Nanodot Array Using Anodic Porous Alumina as an Evaporation Mask. *Jpn. J. Appl. Phys.* **1996**, *35* (1 B), L126–L129.

-
- (44) Zhang, S.; Wang, Y.; Tan, Y.; Zhu, J.; Liu, K.; Zhu, J. Anodic Aluminum Oxide with Fine Pore Size Control for Selective and Effective Particulate Matter Filtering. *Mater. Res. Express* **2016**, *3*, 074004.
- (45) Ma, Y.; Kaczynski, J.; Ranacher, C.; Roshanghias, A.; Zauner, M.; Abasahl, B. Nano-Porous Aluminum Oxide Membrane as Filtration Interface for Optical Gas Sensor Packaging. *Microelectron. Eng.* **2018**, *198*, 29–34.
- (46) Choi, D.; Choi, Y.; Hong, S.; Kang, T.; Lee, L. P. Self-Organized Hexagonal-Nanopore SERS Array. *Small* **2010**, *6* (16), 1741–1744.
- (47) Das, G.; Patra, N.; Gopalakrishnan, A.; Zaccaria, R. P.; Toma, A.; Thorat, S.; Di Fabrizio, E.; Diaspro, A.; Salerno, M. Fabrication of Large-Area Ordered and Reproducible Nanostructures for SERS Biosensor Application. *Analyst* **2012**, *137* (8), 1785–1792.
- (48) Lee, S. J.; Morrill, A. R.; Moskovits, M. Hot Spots in Silver Nanowire Bundles for Surface-Enhanced Raman Spectroscopy. *J. Am. Chem. Soc.* **2006**, *128* (7), 2200–2201.
- (49) Luo, Z.; Peng, A.; Fu, H.; Ma, Y.; Yao, J.; Loo, B. H. An Application of AAO Template: Orderly Assembled Organic Molecules for Surface-Enhanced Raman Scattering. *J. Mater. Chem.* **2008**, *18* (1), 133–138.
- (50) Kartopu, G.; Es-Souni, M.; Sapelkin, A. V.; Dunstan, D. Large-Scale, Reliable and Robust SERS-Active Nanowire Substrates Prepared Using Porous Alumina Templates. *J. Nanosci. Nanotechnol.* **2008**, *8* (2), 931–935.
- (51) Huang, Z.; Meng, G.; Huang, Q.; Chen, B.; Zhu, C.; Zhang, Z. Large-Area Ag Nanorod Array Substrates for SERS: AAO Template-Assisted Fabrication, Functionalization, and Application in Detection PCBs. *J. Raman Spectrosc.* **2013**, *44* (2), 240–246.
- (52) Ko, H.; Tsukruk, V. V. Nanoparticle-Decorated Nanocanals for Surface-Enhanced Raman Scattering. *Small* **2008**, *4* (11), 1980–1984.
- (53) Ji, N.; Ruan, W.; Wang, C.; Lu, Z.; Zhao, B. Fabrication of Silver Decorated Anodic Aluminum Oxide Substrate and Its Optical Properties on Surface-Enhanced Raman Scattering and Thin Film Interference. *Langmuir* **2009**, *25* (19), 11869–11873.

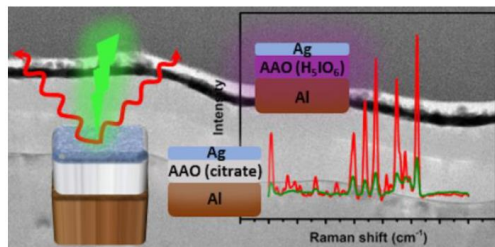
-
- (54) Chang, S.; Combs, Z. A.; Gupta, M. K.; Davis, R.; Tsukruk, V. V. In Situ Growth of Silver Nanoparticles in Porous Membranes for Surface-Enhanced Raman Scattering. *ACS Appl. Mater. Interfaces* **2010**, 2 (11), 3333–3339.
- (55) Walsh, R. J.; Chumanov, G. Silver Coated Porous Alumina as a New Substrate for Surface-Enhanced Raman Scattering. *Appl. Spectrosc.* **2001**, 55 (12), 1695–1700.
- (56) Qiu, T.; Zhang, W.; Lang, X.; Zhou, Y.; Cui, T.; Chu, P. K. Controlled Assembly of Highly Raman-Enhancing Silver Nanocap Arrays Templated by Porous Anodic Alumina Membranes. *Small* **2009**, 5 (20), 2333–2337.
- (57) Terekhov, S. N.; Mojzes, P.; Kachan, S. M.; Mukhurov, N. I.; Zhvavyi, S. P.; Panarin, A. Y.; Khodasevich, I. A.; Orlovich, V. A.; Thorel, A.; Grillon, F.; et al. A Comparative Study of Surface-Enhanced Raman Scattering from Silver-Coated Anodic Aluminum Oxide and Porous Silicon. *J. Raman Spectrosc.* **2011**, 42 (1), 12–20.
- (58) Wang, J.; Huang, L.; Yuan, L.; Zhao, L.; Feng, X.; Zhang, W.; Zhai, L.; Zhu, J. Silver Nanostructure Arrays Abundant in Sub-5 nm Gaps as Highly Raman-Enhancing Substrates. *Appl. Surf. Sci.* **2012**, 258 (8), 3519–3523.
- (59) Dongming, L.; Shuhai, J.; Jun, W.; Yang, J. Ordered Silver Nanoparticle Arrays as Surface-Enhanced Raman Spectroscopy Substrates for Label-Free Detection of Vitamin C in Serum. *Sensors Actuators A Phys.* **2013**, 201, 416–420.
- (60) Shan, D.; Huang, L.; Li, X.; Zhang, W.; Wang, J.; Cheng, L.; Feng, X.; Liu, Y.; Zhu, J.; Zhang, Y. Surface Plasmon Resonance and Interference Coenhanced SERS Substrate of AAO/Al-Based Ag Nanostructure Arrays. *J. Phys. Chem. C* **2014**, 118 (41), 23930–23936.
- (61) Sui, C.; Wang, K.; Wang, S.; Ren, J.; Bai, X.; Bai, J. SERS Activity with Tenfold Detection Limit Optimization on a Type of Nanoporous AAO-Based Complex Multilayer Substrate. *Nanoscale* **2016**, 8 (11), 5920–5927.
- (62) Celik, M.; Altuntas, S.; Buyukserin, F. Fabrication of Nanocrater-Decorated Anodic Aluminum Oxide Membranes as Substrates for Reproducibly Enhanced SERS Signals. *Sensors Actuators B Chem.* **2018**, 255, 2871–2877.

-
- (63) Hutter, T.; Elliott, S. R.; Mahajan, S. Interaction of Metallic Nanoparticles with Dielectric Substrates: Effect of Optical Constants. *Nanotechnology* **2013**, *24* (3), 035201.
- (64) Wang, T.; Zhang, Z.; Liao, F.; Cai, Q.; Li, Y.; Lee, S.-T.; Shao, M. The Effect of Dielectric Constants on Noble Metal/Semiconductor SERS Enhancement: FDTD Simulation and Experiment Validation of Ag/Ge and Ag/Si Substrates. *Sci. Rep.* **2014**, *4*, 4052.
- (65) Sinha, G.; Depero, L. E.; Alessandri, I. Recyclable SERS Substrates Based on Au-Coated ZnO Nanorods. *ACS Appl. Mater. Interfaces* **2011**, *3* (7), 2557–2563.
- (66) Li, X.; Hu, H.; Li, D.; Shen, Z.; Xiong, Q.; Li, S.; Fan, H. J. Ordered Array of Gold Semishells on TiO₂ Spheres: An Ultrasensitive and Recyclable SERS Substrate. *ACS Appl. Mater. Interfaces* **2012**, *4* (4), 2180–2185.
- (67) Zou, X.; Silva, R.; Huang, X.; Al-Sharab, J. F.; Asefa, T. A Self-Cleaning Porous TiO₂–Ag Core–Shell Nanocomposite Material for Surface-Enhanced Raman Scattering. *Chem. Commun.* **2013**, *49* (4), 382–384.
- (68) Zang, Y.; Yin, J.; He, X.; Yue, C.; Wu, Z.; Li, J.; Kang, J. Plasmonic-Enhanced Self-Cleaning Activity on Asymmetric Ag/ZnO Surface-Enhanced Raman Scattering Substrates under UV and Visible Light Irradiation. *J. Mater. Chem. A* **2014**, *2* (21), 7747–7753.
- (69) Prakash, J. Fundamentals and Applications of Recyclable SERS Substrates. *Int. Rev. Phys. Chem.* **2019**, *38* (2), 201–242.
- (70) Nemanich, R. J.; Tsai, C. C.; Connell, G. A. N. Interference-Enhanced Raman Scattering of Very Thin Titanium and Titanium Oxide Films. *Phys. Rev. Lett.* **1980**, *44* (4), 273–276.
- (71) Connell, G. A. N.; Nemanich, R. J.; Tsai, C. C. Interference Enhanced Raman Scattering from Very Thin Absorbing Films. *Appl. Phys. Lett.* **1980**, *36* (1), 31–33.
- (72) Pahlow, S.; Mayerhöfer, T.; Van Der Loh, M.; Hübner, U.; Dellith, J.; Weber, K.; Popp, J. Interference-Enhanced Raman Spectroscopy as a Promising Tool for the Detection of Biomolecules on Raman-Compatible Surfaces. *Anal. Chem.* **2018**, *90* (15), 9025–9032.

-
- (73) Evangelisti, F.; Stiefel, M.; Guseva, O.; Nia, R. P.; Hauert, R.; Hack, E.; Jeurgens, L. P. H.; Ambrosio, F.; Pasquarello, A.; Schmutz, P.; et al. Electronic and Structural Characterization of Barrier-Type Amorphous Aluminium Oxide. *Electrochim. Acta* **2017**, *224*, 503–516.
- (74) Kruth, M.; Meertens, D.; Tillmann, K. FEI Helios NanoLab 400S FIB-SEM. *J. large-scale Res. Facil.* **2016**, *2*, A59.
- (75) Lee, C.; Robertson, C. S.; Nguyen, A. H.; Kahraman, M.; Wachsmann-Hogiu, S. Thickness of a Metallic Film, in Addition to Its Roughness, Plays a Significant Role in SERS Activity. *Sci. Rep.* **2015**, *5*, 11644.
- (76) Shoute, L. C. T.; Bergren, A. J.; Mahmoud, A. M.; Harris, K. D.; McCreery, R. L. Optical Interference Effects in the Design of Substrates for Surface-Enhanced Raman Spectroscopy. *Appl. Spectrosc.* **2009**, *63* (2), 133–140.
- (77) De Laet, J.; Terryn, H.; Vereecken, J.; Vanhellefont, J. Spectroscopic Ellipsometry Characterization of Anodic Films on Aluminium Correlated with Transmission Electron Microscopy and Auger Electron Spectroscopy. *Surf. Interface Anal.* **1992**, *19*, 445–449.
- (78) Thompson, G. E.; Wood, G. C. Porous Anodic Film Formation on Aluminium. *Nature* **1981**, *290*, 230–232.
- (79) Yamamoto, Y.; Baba, N.; Tajima, S. Coloured Materials and Photoluminescence Centres in Anodic Film on Aluminium. *Nature* **1981**, *289*, 572–574.
- (80) Mukhurov, N. I.; Zhvavyi, S. P.; Terekhov, S. N.; Panarin, A. Y.; Kotova, I. F.; Pershukevich, P. P.; Khodasevich, I. A.; Gasenkova, I. V.; Orlovich, V. A. Influence of Electrolyte Composition on Photoluminescent Properties of Anodic Aluminum Oxide. *J. Appl. Spectrosc.* **2008**, *75* (2), 214–218.
- (81) Li, D.; Zhao, L.; Jiang, C.; Lu, J. G. Formation of Anodic Aluminum Oxide with Serrated Nanochannels. *Nano Lett.* **2010**, *10* (8), 2766–2771.
- (82) Sherwood, P. M. A. X-Ray Photoelectron Spectroscopic Studies of Some Iodine Compounds. *J. Chem. Soc. Faraday Trans. 2 Mol. Chem. Phys.* **1976**, *72*, 1805–1820.

-
- (83) Du, T.; Tamboli, D.; Luo, Y.; Desai, V. Electrochemical Characterization of Copper Chemical Mechanical Planarization in KIO₃ Slurry. *Appl. Surf. Sci.* **2004**, *229*, 167–174.
- (84) Ding, J.; Yuan, Y.; Xu, J.; Deng, J.; Guo, J. TiO₂ Nanopowder Co-Doped with Iodine and Boron to Enhance Visible-Light Photocatalytic Activity. *J. Biomed. Nanotechnol.* **2009**, *5* (5), 1–7.
- (85) Yao, Z.; Nie, H.; Yang, Z.; Zhou, X.; Liu, Z.; Huang, S. Catalyst-Free Synthesis of Iodine-Doped Graphene via a Facile Thermal Annealing Process and Its Use for Electrocatalytic Oxygen Reduction in an Alkaline Medium. *Chem. Commun.* **2012**, *48* (7), 1027–1029.
- (86) Holleman, A. F.; Wiberg, N.; Wiberg, E. *Lehrbuch Der Anorganischen Chemie*, 102nd ed.; Walter de Gruyter: Berlin, New York, 2007.
- (87) Sun, C. H.; Wang, M. L.; Feng, Q.; Liu, W.; Xu, C. X. Surface-Enhanced Raman Scattering (SERS) Study on Rhodamine B Adsorbed on Different Substrates. *Russ. J. Phys. Chem. A* **2015**, *89* (2), 291–296.
- (88) Lin, S.; Hasi, W. L. J.; Lin, X.; Han, S. Q. G. W.; Lou, X. T.; Yang, F.; Lin, D. Y.; Lu, Z. W. Rapid and Sensitive SERS Method for Determination of Rhodamine B in Chili Powder with Paper-Based Substrates. *Anal. Methods* **2015**, *7* (12), 5289–5294.
- (89) Miikkulainen, V.; Leskelä, M.; Ritala, M.; Puurunen, R. L. Crystallinity of Inorganic Films Grown by Atomic Layer Deposition: Overview and General Trends. *J. Appl. Phys.* **2013**, *113*, 021301.
- (90) Zhou, X.; Zhou, F.; Liu, H.; Yang, L.; Liu, J. Assembly of Polymer–Gold Nanostructures with High Reproducibility into a Monolayer Film SERS Substrate with 5 nm Gaps for Pesticide Trace Detection. *Analyst* **2013**, *138* (19), 5832–5838.
- (91) Jiang, X.; Li, X.; Jia, X.; Li, G.; Wang, X.; Wang, G.; Li, Z.; Yang, L.; Zhao, B. Surface-Enhanced Raman Scattering from Synergistic Contribution of Metal and Semiconductor in TiO₂/MBA/Ag(Au) and Ag(Au)/MBA/TiO₂ Assemblies. *J. Phys. Chem. C* **2012**, *116* (27), 14650–14655.

Table of contents (TOC) image



3 Summary

This work dealt with two different topics, namely the development of nanomaterials for effective photocatalytic water remediation and the development of efficient SERS substrates for trace analysis.

Section 2.1 dealt with a new approach for the preparation of various nanoparticle@CNT nanocomposites which enable efficient photocatalysis as they combine a number of advantages for photocatalysis including extended light absorption and spatial charge separation. In the presented approach ZnO nanoparticles were successfully deposited through atomic layer deposition (ALD) on a forest of VACNTs where the size of the particles could be carefully tuned by the number of ALD cycles. Through a gas phase sulfidation procedure, where thioacetamide was used as a precursor for the production of hydrogen sulfide gas, it was possible to convert the ZnO@CNT nanocomposites to a variety of ZnS/ZnO@CNT, sphalerite-based ZnS@CNT and wurtzite-based ZnS@CNT nanocomposites by controlling the temperature and time of the gas phase conversion process. Heating the ZnS@CNT nanocomposite during the sulfidation process for prolonged time at high temperatures even results in the formation of sulfur vacancies which turned out to be beneficial for the photocatalytic process. The different nanocomposites showed good photocatalytic activity towards the degradation of methyl orange which was used as model pollutant under simulated sunlight where the wurtzite-based ZnS@CNT nanocomposites with sulfur vacancies formed at 950 °C for 30 min showed the highest activity.

In **Section 2.2** a different class of materials was investigated for their photocatalytic activity, namely two-dimensional titanium chalcogenides. Through a chemical vapor transport method different layered titanium chalcogenides were synthesized through using different chalcogens (S, Se and Te) in different ratios to the titanium. As titanium selenide and titanium telluride did not show any significant photocatalytic activity, the study concentrated mainly on titanium sulfides. By changing the starting element ratios and synthesis conditions it was possible to obtain a series of titanium sulfides which are titanium trisulfide TiS_3 , titanium disulfide TiS_2 , low-temperature titanium monosulfide lt-TiS synthesized at 450 °C and high-temperature titanium monosulfide ht-TiS synthesized at 900 °C. While TiS_3 and TiS_2 represent stoichiometric compounds, it was found out that the different “titanium monosulfides” only represent highly defective titanium disulfides where excess titanium is incorporated in the interstitials. Testing their photocatalytic activity towards the degradation of methyl orange as model pollutant under simulated sunlight it turned out that especially TiS_3 and the defect-rich titanium monosulfides show high photocatalytic activities which even outperform the previously synthesized ZnS@CNT nanocomposites which shows their high activity. Furthermore, it was found out that

these active titanium sulfide photocatalysts are active in the dark which indicates their thermocatalytic activity. Thus, these materials represent combined photothermal catalyst which also explains its high activity in water remediation. On top, these materials also were found to show excellent recyclability which was found to be a result of the surface oxidation of these titanium sulfides, spontaneously forming a titanium sulfide/titanium oxide heterostructure which enables spatial separation of the photo-induced charge carriers further enhancing the photothermal catalytic activity of these materials.

Section 2.3 dealt with the investigation of different plasma treatments for the effective plasma-assisted preparation of silver SERS substrates. Different plasma treatments using single gases as hydrogen, nitrogen and argon all turned out to increase the surface roughness of the sputtered silver by various degrees depending on the type of plasma gas used, the plasma power, the gas flow rate and the plasma treatment time. Thus, plasma treatment enabled an increase in the SERS enhancement produced by these SERS substrates. Also, the use of combinations of plasma treatments was tested where an initial oxidative plasma treatment of thick silver films (200 nm thickness) by oxygen or air plasma followed by a reductive plasma treatment by hydrogen, nitrogen or argon resulted in different complex porous silver networks with high enhancement factors. Furthermore, this study shows the ability of mild argon plasma treatment in cleaning the surface of silver SERS substrates by effectively removing the previous applied analyte, thus enabling the re-use of these substrates. Even surface oxidation of these silver SERS substrates which results from the long-term storage of these substrates decreasing their SERS performance could be effectively eliminated by this mild argon plasma treatment proposed in this work.

In **Section 2.4**, a new system for the use as effective SERS substrate was investigated. This system is composed of aluminum/anodic aluminum oxide/silver (Al/AAO/Ag) where this system is interesting for SERS applications due to the influence of the dielectric underlying the noble metal and due to the possibility of interference co-enhancement effect. Investigating barrier-type AAO prepared in iodine oxoacid electrolytes (periodic acid and iodic acid) revealed the formation of barrier-type AAO doped with different iodine species as shown by the XPS investigation performed in our study. When these substrates were sputtered with silver and used as SERS substrates, they showed an unusual high SERS enhancement compared to other barrier-type AAO prepared in citrate buffer, ALD-deposited alumina and also PAOX which contains a nanostructuring enabling the formation of hot spots upon sputtering with silver. In depth investigation and comparison of the different systems pointed towards a possible chemical enhancement by the different iodine species. This main finding could be used for the design of more efficient SERS substrates in the future.

4 Conclusion and outlook

The work presented in this thesis suggests new approaches for the preparation of hybrid nanomaterial photocatalysts and facile methods for the preparation of SERS substrates which could enable large scale production. Hybrid nanomaterial photocatalysts based on VACNTs using gas phase deposition presented in this work showed the ability to produce a variety homogenous and ordered nanocomposites suitable for efficient photocatalysis. Two-dimensional titanium chalcogenides (especially titanium trisulfide and highly defective titanium disulfide) showed a combined photothermal catalytic activity. These titanium sulfides spontaneously formed titanium sulfide/titanium oxide heterostructures further enhancing their activity. On the other hand, plasma treatment presented a facile method for the surface roughening of sputtered silver thin films increasing their SERS enhancement factors depending on the treatment conditions. Finally, the use of barrier-type AAO doped with different iodine species in Al/AAO/Ag SERS substrates showed high SERS enhancement which could be attributed to a chemical enhancement besides the trivial electromagnetic enhancement opening the door for new SERS substrates which could be even analyte specific.

Taking the ideas of this thesis one step further, a combination of plasmonic substrates with semiconductor photocatalysts could offer an appropriate immobilization of the semiconductor photocatalysts on one hand and a further improvement of the photocatalytic activity on the other hand as they will act as plasmonic photocatalysts where better charge separation can result in an appropriate increase in the photocatalytic activity. Such combinations could be even useful as self-cleaning SERS substrates where the measured analyte can then be removed by photocatalysis, thus being a dual-functional material.

5 Appendix

All necessary reproduction rights and permissions for the figures obtained from third-party publications as well as the first author publications were obtained from the corresponding publisher. In the following the reproduction rights and permissions for the first author publications presented in this work are shown.

ZnS/ZnO@CNT and ZnS@CNT nanocomposites by gas phase conversion of ZnO@CNT. A systematic study of their photocatalytic properties

S. Okeil, J. Krausmann, I. Dönges, S. Pflieger, J. Engstler and J. J. Schneider, *Dalton Trans.*, 2017, **46**, 5189
DOI: 10.1039/C7DT00407A

If you are not the author of this article and you wish to reproduce material from it in a third party non-RSC publication you must [formally request permission](#) using Copyright Clearance Center. Go to our [Instructions for using Copyright Clearance Center page](#) for details.

Authors contributing to RSC publications (journal articles, books or book chapters) do not need to formally request permission to reproduce material contained in this article provided that the correct acknowledgement is given with the reproduced material.

Reproduced material should be attributed as follows:

- For reproduction of material from NJC:
Reproduced from Ref. XX with permission from the Centre National de la Recherche Scientifique (CNRS) and The Royal Society of Chemistry.
- For reproduction of material from PCCP:
Reproduced from Ref. XX with permission from the PCCP Owner Societies.
- For reproduction of material from PPS:
Reproduced from Ref. XX with permission from the European Society for Photobiology, the European Photochemistry Association, and The Royal Society of Chemistry.
- For reproduction of material from all other RSC journals and books:
Reproduced from Ref. XX with permission from The Royal Society of Chemistry.

If the material has been adapted instead of reproduced from the original RSC publication "Reproduced from" can be substituted with "Adapted from".

In all cases the Ref. XX is the XXth reference in the list of references.

If you are the author of this article you do not need to formally request permission to reproduce figures, diagrams etc. contained in this article in third party publications or in a thesis or dissertation provided that the correct acknowledgement is given with the reproduced material.

Reproduced material should be attributed as follows:

- For reproduction of material from NJC:
[Original citation] - Reproduced by permission of The Royal Society of Chemistry (RSC) on behalf of the Centre National de la Recherche Scientifique (CNRS) and the RSC
- For reproduction of material from PCCP:
[Original citation] - Reproduced by permission of the PCCP Owner Societies
- For reproduction of material from PPS:
[Original citation] - Reproduced by permission of The Royal Society of Chemistry (RSC) on behalf of the European Society for Photobiology, the European Photochemistry Association, and RSC
- For reproduction of material from all other RSC journals:
[Original citation] - Reproduced by permission of The Royal Society of Chemistry

If you are the author of this article you still need to obtain permission to reproduce the whole article in a third party publication with the exception of reproduction of the whole article in a thesis or dissertation.

Section 2.1 ZnS/ZnO@CNT and ZnS@CNT nanocomposites by gas phase conversion of ZnO@CNT. A systematic study of their photocatalytic properties

Photothermal catalytic properties of layered titanium chalcogenide nanomaterials

S. Okeil, S. Yadav, M. Bruns, A. Zintler, L. Molina-Luna and J. J. Schneider, *Dalton Trans.*, 2020, **49**, 1032

DOI: 10.1039/C9DT03798E

If you are not the author of this article and you wish to reproduce material from it in a third party non-RSC publication you must [formally request permission](#) using Copyright Clearance Center. Go to our [Instructions for using Copyright Clearance Center page](#) for details.

Authors contributing to RSC publications (journal articles, books or book chapters) do not need to formally request permission to reproduce material contained in this article provided that the correct acknowledgement is given with the reproduced material.

Reproduced material should be attributed as follows:

- For reproduction of material from NJC:
Reproduced from Ref. XX with permission from the Centre National de la Recherche Scientifique (CNRS) and The Royal Society of Chemistry.
- For reproduction of material from PCCP:
Reproduced from Ref. XX with permission from the PCCP Owner Societies.
- For reproduction of material from PPS:
Reproduced from Ref. XX with permission from the European Society for Photobiology, the European Photochemistry Association, and The Royal Society of Chemistry.
- For reproduction of material from all other RSC journals and books:
Reproduced from Ref. XX with permission from The Royal Society of Chemistry.

If the material has been adapted instead of reproduced from the original RSC publication "Reproduced from" can be substituted with "Adapted from".

In all cases the Ref. XX is the XXth reference in the list of references.

If you are the author of this article you do not need to formally request permission to reproduce figures, diagrams etc. contained in this article in third party publications or in a thesis or dissertation provided that the correct acknowledgement is given with the reproduced material.

Reproduced material should be attributed as follows:

- For reproduction of material from NJC:
[Original citation] - Reproduced by permission of The Royal Society of Chemistry (RSC) on behalf of the Centre National de la Recherche Scientifique (CNRS) and the RSC
- For reproduction of material from PCCP:
[Original citation] - Reproduced by permission of the PCCP Owner Societies
- For reproduction of material from PPS:
[Original citation] - Reproduced by permission of The Royal Society of Chemistry (RSC) on behalf of the European Society for Photobiology, the European Photochemistry Association, and RSC
- For reproduction of material from all other RSC journals:
[Original citation] - Reproduced by permission of The Royal Society of Chemistry

If you are the author of this article you still need to obtain permission to reproduce the whole article in a third party publication with the exception of reproduction of the whole article in a thesis or dissertation.

License and Terms

This is an Open Access article under the terms of the Creative Commons Attribution License (<http://creativecommons.org/licenses/by/4.0>). Please note that the reuse, redistribution and reproduction in particular requires that the authors and source are credited.

The license is subject to the *Beilstein Journal of Nanotechnology* terms and conditions:

(<https://www.beilstein-journals.org/bjnano>)

The definitive version of this article is the electronic one which can be found at:

[doi:10.3762/bjnano.9.263](https://doi.org/10.3762/bjnano.9.263)

6 References

- 1 V. R. Posa, V. Annavaram, J. R. Koduru, V. R. Ammireddy and A. R. Somala, *Korean J. Chem. Eng.*, 2016, **33**, 456–464.
- 2 Y. Li, H. Zhao and M. Yang, *J. Colloid Interface Sci.*, 2017, **508**, 500–507.
- 3 R. Cai, B. Zhang, J. Shi, M. Li and Z. He, *ACS Sustain. Chem. Eng.*, 2017, **5**, 7690–7699.
- 4 B. Xu, Y. Li, Y. Gao, S. Liu, D. Lv, S. Zhao, H. Gao, G. Yang, N. Li and L. Ge, *Appl. Catal. B Environ.*, 2019, **246**, 140–148.
- 5 Z. Tong, D. Yang, J. Shi, Y. Nan, Y. Sun and Z. Jiang, *ACS Appl. Mater. Interfaces*, 2015, **7**, 25693–25701.
- 6 C. Chen, W. Cai, M. Long, B. Zhou, Y. Wu, D. Wu and Y. Feng, *ACS Nano*, 2010, **4**, 6425–6432.
- 7 K. Woan, G. Pyrgiotakis and W. Sigmund, *Adv. Mater.*, 2009, **21**, 2233–2239.
- 8 D. J. Babu and J. J. Schneider, *Chemie-Ingenieur-Technik*, 2017, **89**, 1273–1287.
- 9 M. N. Chong, B. Jin, C. W. K. Chow and C. Saint, *Water Res.*, 2010, **44**, 2997–3027.
- 10 R. Saravanan, F. Gracia and A. Stephen, in *Nanocomposites for Visible Light-induced Photocatalysis. Springer Series on Polymer and Composite Materials.*, eds. M. Khan, D. Pradhan and Y. Sohn, Springer, 2017, pp. 19–40.
- 11 R. Ameta and S. C. Ameta, *Photocatalysis: Principles and Applications*, CRC Press, Taylor & Francis Group, 2017.
- 12 H. Ibach and H. Lüth, *Solid-State Physics: An Introduction to Principles of Materials Science*, Springer-Verlag Berlin Heidelberg, 2009.
- 13 J. H. Davies, *The Physics of Low-Dimensional Semiconductors: An Introduction*, Cambridge University Press, 1998.
- 14 A. Pfitzner, S. Dankesreiter, A. Eisenhofer and M. Cherevatskaya, in *Chemical Photocatalysis*, ed. B. König, Walter de Gruyter, 2013, pp. 211–245.
- 15 H. A. Foster, I. B. Ditta, S. Varghese and A. Steele, *Appl. Microbiol. Biotechnol.*, 2011, **90**, 1847–1868.
- 16 J. You, Y. Guo, R. Guo and X. Liu, *Chem. Eng. J.*, 2019, **373**, 624–641.
- 17 S. Kumar, S. Karthikeyan and A. F. Lee, *Catalysts*, 2018, **8**, 74.
- 18 G. Rammohan and M. Nadagouda, *Curr. Org. Chem.*, 2013, **17**, 2338–2348.
- 19 R. Vinu and G. Madras, *J. Indian Inst. Sci.*, 2010, **90**, 189–230.
- 20 W. Wu, C. Jiang and V. A. L. Roy, *Nanoscale*, 2015, **7**, 38–58.
- 21 A. Kudo and Y. Miseki, *Chem. Soc. Rev.*, 2009, **38**, 253–278.
- 22 A. I. Ekimov, A. L. Efros and A. A. Onushchenko, *Solid State Commun.*, 1985, **56**, 921–924.
- 23 H. Zhang, M. Bayne, S. Fernando, B. Legg, M. Zhu, R. L. Penn and J. F. Banfield, *J. Phys. Chem. C*, 2011, **115**, 17704–17710.

-
- 24 M. R. Hoffmann, S. T. Martin, W. Choi and D. W. Bahnemann, *Chem. Rev.*, 1995, **95**, 69–96.
- 25 S. Földner, P. Pohla, H. Bartling, S. Dankesreiter, R. Stadler, M. Gruber, A. Pfitzner and B. König, *Green Chem.*, 2011, **13**, 640–643.
- 26 S. Linic, P. Christopher and D. B. Ingram, *Nat. Mater.*, 2011, **10**, 911–921.
- 27 H. Zhou, Y. Qu, T. Zeid and X. Duan, *Energy Environ. Sci.*, 2012, **5**, 6732–6743.
- 28 C. A. Bignozzi, Ed., *Topics in Current Chemistry: Photocatalysis*, 2011.
- 29 L. Wang and T. Sasaki, *Chem. Rev.*, 2014, **114**, 9455–9486.
- 30 A. L. Linsebigler, G. Lu and J. T. Yates, *Chem. Rev.*, 1995, **95**, 735–758.
- 31 R. Asahi, T. Morikawa, H. Irie and T. Ohwaki, *Chem. Rev.*, 2014, **114**, 9824–9852.
- 32 R. A. P. Ribeiro, S. R. de Lazaro and C. R. de Oliveira, *Curr. Phys. Chem.*, 2016, **6**, 22–27.
- 33 E. Borgarello, J. Kiwi, M. Grätzel, E. Pelizzetti and M. Visca, *J. Am. Chem. Soc.*, 1982, **104**, 2996–3002.
- 34 X. Fan, X. Chen, S. Zhu, Z. Li, T. Yu, J. Ye and Z. Zou, *J. Mol. Catal. A Chem.*, 2008, **284**, 155–160.
- 35 M. I. Litter and J. A. Navío, *J. Photochem. Photobiol. A Chem.*, 1996, **98**, 171–181.
- 36 C. Y. Wang, C. Böttcher, D. W. Bahnemann and J. K. Dohrmann, *J. Mater. Chem.*, 2003, **13**, 2322–2329.
- 37 Y. Yalçın, M. Kiliç and Z. Çınar, *Appl. Catal. B Environ.*, 2010, **99**, 469–477.
- 38 R. Chauhan, A. Kumar and R. P. Chaudhary, *Spectrochim. Acta - Part A Mol. Biomol. Spectrosc.*, 2013, **113**, 250–256.
- 39 M. Shamsipur and H. R. Rajabi, *Spectrochim. Acta - Part A Mol. Biomol. Spectrosc.*, 2014, **122**, 260–267.
- 40 V. Etacheri, R. Roshan and V. Kumar, *ACS Appl. Mater. Interfaces*, 2012, **4**, 2717–2725.
- 41 S. H. Mohamed, *J. Phys. D. Appl. Phys.*, 2010, **43**, 035406.
- 42 R. Ullah and J. Dutta, *J. Hazard. Mater.*, 2008, **156**, 194–200.
- 43 W. Li, Y. Wang, H. Lin, S. I. Shah, C. P. Huang, D. J. Doren, S. A. Rykov, J. G. Chen and M. A. Barteau, *Appl. Phys. Lett.*, 2003, **83**, 4143–4145.
- 44 J. Shi, J. Zheng, Y. Hu and Y. Zhao, *Environ. Eng. Sci.*, 2008, **25**, 489–496.
- 45 J. Xu, Y. Ao, D. Fu and C. Yuan, *Colloids Surfaces A Physicochem. Eng. Asp.*, 2009, **334**, 107–111.
- 46 A. W. Xu, Y. Gao and H. Q. Liu, *J. Catal.*, 2002, **207**, 151–157.
- 47 X. Chen, S. Shen, L. Guo and S. S. Mao, *Chem. Rev.*, 2010, **110**, 6503–6570.
- 48 W. Choi, A. Termin and M. R. Hoffmann, *J. Phys. Chem.*, 1994, **98**, 13669–13679.
- 49 R. Asahi, T. Morikawa, T. Ohwaki, K. Aoki and Y. Taga, *Science (80-.)*, 2001, **293**, 269–271.
- 50 X. Chen and C. Burda, *J. Phys. Chem. B*, 2004, **108**, 15446–15449.
- 51 H. Irie, Y. Watanabe and K. Hashimoto, *J. Phys. Chem. B*, 2003, **107**, 5483–5486.

-
- 52 S. U. M. Khan, M. Al-Shahry and W. B. Ingler, *Science (80-.)*, 2002, **297**, 2243–2245.
- 53 C. Di Valentin, E. Finazzi, G. Pacchioni, A. Selloni, S. Livraghi, M. C. Paganini and E. Giamello, *Chem. Phys.*, 2007, **339**, 44–56.
- 54 W. Yu, J. Zhang and T. Peng, *Appl. Catal. B Environ.*, 2016, **181**, 220–227.
- 55 Y. Zhou, G. Chen, Y. Yu, Y. Feng, Y. Zheng, F. He and Z. Han, *Phys. Chem. Chem. Phys.*, 2015, **17**, 1870–1876.
- 56 S. Rehman, R. Ullah, A. M. Butt and N. D. Gohar, *J. Hazard. Mater.*, 2009, **170**, 560–569.
- 57 J. Zhao, C. Chen and W. Ma, *Top. Catal.*, 2005, **35**, 269–278.
- 58 J. Moon, C. Y. Yun, K. W. Chung, M. S. Kang and J. Yi, *Catal. Today*, 2003, **87**, 77–86.
- 59 R. Abe, K. Hara, K. Sayama, K. Domen and H. Arakawa, *J. Photochem. Photobiol. A Chem.*, 2000, **137**, 63–69.
- 60 D. Chatterjee and A. Mahata, *Catal. Commun.*, 2001, **2**, 1–3.
- 61 D. Chatterjee and A. Mahata, *J. Photochem. Photobiol. A Chem.*, 2002, **153**, 199–204.
- 62 S. Kaur and V. Singh, *Ultrason. Sonochem.*, 2007, **14**, 531–537.
- 63 X. Chen, L. Liu, P. Y. Yu and S. S. Mao, *Science (80-.)*, 2011, **331**, 746–750.
- 64 G. Wang, H. Wang, Y. Ling, Y. Tang, X. Yang, R. C. Fitzmorris, C. Wang, J. Z. Zhang and Y. Li, *Nano Lett.*, 2011, **11**, 3026–3033.
- 65 Z. Wang, C. Yang, T. Lin, H. Yin, P. Chen, D. Wan, F. Xu, F. Huang, J. Lin, X. Xie and M. Jiang, *Energy Environ. Sci.*, 2013, **6**, 3007–3014.
- 66 N. Liu, C. Schneider, D. Freitag, M. Hartmann, U. Venkatesan, J. Müller, E. Spiecker and P. Schmuki, *Nano Lett.*, 2014, **14**, 3309–3313.
- 67 H. Lu, B. Zhao, R. Pan, J. Yao, J. Qiu, L. Luo and Y. Liu, *RSC Adv.*, 2014, **4**, 1128–1132.
- 68 F. Teng, M. Li, C. Gao, G. Zhang, P. Zhang, Y. Wang, L. Chen and E. Xie, *Appl. Catal. B Environ.*, 2014, **148–149**, 339–343.
- 69 A. Sinhamahapatra, J. P. Jeon and J. S. Yu, *Energy Environ. Sci.*, 2015, **8**, 3539–3544.
- 70 S. Ghosh, Ed., *Visible-Light-Active Photocatalysis: Nanostructured Catalyst Design, Mechanisms, and Applications*, Wiley-VCH, 2018.
- 71 R. C. Pawar and C. S. Lee, *Heterogeneous Nanocomposite-Photocatalysis for Water Purification*, Elsevier, 2015.
- 72 J. Low, J. Yu, M. Jaroniec, S. Wageh and A. A. Al-Ghamdi, *Adv. Mater.*, 2017, **29**, 1601694.
- 73 J. Ge, Y. Zhang, Y. J. Heo and S. J. Park, *Catalysts*, 2019, **9**, 122.
- 74 R. Marschall, *Adv. Funct. Mater.*, 2014, **24**, 2421–2440.
- 75 H. Wang, L. Zhang, Z. Chen, J. Hu, S. Li, Z. Wang, J. Liu and X. Wang, *Chem. Soc. Rev.*, 2014, **43**, 5234–5244.
- 76 S. J. A. Moniz, S. A. Shevlin, D. J. Martin, Z. X. Guo and J. Tang, *Energy Environ. Sci.*, 2015, **8**,

- 731–759.
- 77 J. C. Yu, L. Wu, J. Lin, P. Li and Q. Li, *Chem. Commun.*, 2003, **9**, 1552–1553.
- 78 M. Zhou, J. Yu, S. Liu, P. Zhai and L. Jiang, *J. Hazard. Mater.*, 2008, **154**, 1141–1148.
- 79 C. Wang, C. Shao, X. Zhang and Y. Liu, *Inorg. Chem.*, 2009, **48**, 7261–7268.
- 80 M. Shang, W. Wang, L. Zhang, S. Sun, L. Wang and L. Zhou, *J. Phys. Chem. C*, 2009, **113**, 14727–14731.
- 81 P. Deák, B. Aradi and T. Frauenheim, *J. Phys. Chem. C*, 2011, **115**, 3443–3446.
- 82 R. Su, R. Bechstein, L. Sør, R. T. Vang, M. Sillassen, B. Esbjörnsson, A. Palmqvist and F. Besenbacher, *J. Phys. Chem. C*, 2011, **115**, 24287–24292.
- 83 D. O. Scanlon, C. W. Dunnill, J. Buckeridge, S. A. Shevlin, A. J. Logsdail, S. M. Woodley, C. R. A. Catlow, M. J. Powell, R. G. Palgrave, I. P. Parkin, G. W. Watson, T. W. Keal, P. Sherwood, A. Walsh and A. A. Sokol, *Nat. Mater.*, 2013, **12**, 798–801.
- 84 T. Ohno, K. Sarukawa, K. Tokieda and M. Matsumura, *J. Catal.*, 2001, **203**, 82–86.
- 85 J. Yu, W. Wang and B. Cheng, *Chem. - An Asian J.*, 2010, **5**, 2499–2506.
- 86 Y. S. Fu, J. Li and J. Li, *Nanomaterials*, 2019, **9**, 359.
- 87 N. Wu, *Nanoscale*, 2018, **10**, 2679–2696.
- 88 X. Zhang, Y. L. Chen, R. S. Liu and D. P. Tsai, *Reports Prog. Phys.*, 2013, **76**, 046401.
- 89 H. Li, Z. Bian, J. Zhu, Y. Huo, H. Li and Y. Lu, *J. Am. Chem. Soc.*, 2007, **129**, 4538–4539.
- 90 P. Wang, B. Huang, X. Qin, X. Zhang, Y. Dai, J. Wei and M. H. Whangbo, *Angew. Chemie - Int. Ed.*, 2008, **47**, 7931–7933.
- 91 Y. Bi, H. Hu, S. Ouyang, Z. Jiao, G. Lu and J. Ye, *J. Mater. Chem.*, 2012, **22**, 14847–14850.
- 92 W. Lu, X. Qin, H. Li, A. M. Asiri, A. O. Al-Youbi and X. Sun, *Part. Part. Syst. Character.*, 2013, **30**, 67–71.
- 93 K. Rajeshwar, N. R. De Tacconi and C. R. Chenthamarakshan, *Chem. Mater.*, 2001, **13**, 2765–2782.
- 94 M. O. Ansari, M. M. Khan, S. A. Ansari and M. H. Cho, *New J. Chem.*, 2015, **39**, 8381–8388.
- 95 H. Zhang, R. Zong, J. Zhao and Y. Zhu, *Environ. Sci. Technol.*, 2008, **42**, 3803–3807.
- 96 Y. Zhu, S. Xu and D. Yi, *React. Funct. Polym.*, 2010, **70**, 282–287.
- 97 D. Pathania, D. Gupta, A. H. Al-muhtaseb and G. Sharma, *J. Photochem. Photobiol. A Chem.*, 2016, **329**, 61–68.
- 98 M. Faisal, F. A. Harraz, A. A. Ismail, A. M. El-Toni, S. A. Al-Sayari, A. Al-Hajry and M. S. Al-Assiri, *Sep. Purif. Technol.*, 2018, **190**, 33–44.
- 99 R. Leary and A. Westwood, *Carbon N. Y.*, 2011, **49**, 741–772.
- 100 N. Syed, J. Huang, Y. Feng, X. Wang and L. Cao, *Front. Chem.*, 2019, **7**, 713.
- 101 B. H. Nguyen, V. H. Nguyen and D. L. Vu, *Adv. Nat. Sci. Nanosci. Nanotechnol.*, 2015, **6**, 033001.

-
- 102 A. Alwash, H. Adil, Z. Hussain and E. Yousif, *Arch. Nanomedicine Open Access J.*, 2018, **1**, 65–70.
- 103 Z. J. Shi, M. G. Ma and J. F. Zhu, *Catalysts*, 2019, **9**, 20.
- 104 X. Sui, X. Li, T. Ni, F. Lin and G. Li, *J. Mater. Sci.*, 2020, **55**, 2725–2740.
- 105 S. Wang and S. Zhou, *J. Hazard. Mater.*, 2011, **185**, 77–85.
- 106 K. Zhang, F. J. Zhang, M. L. Chen and W. C. Oh, *Ultrason. Sonochem.*, 2011, **18**, 765–772.
- 107 S. M. Miranda, G. E. Romanos, V. Likodimos, R. R. N. Marques, E. P. Favvas, F. K. Katsaros, K. L. Stefanopoulos, V. J. P. Vilar, J. L. Faria, P. Falaras and A. M. T. Silva, *Appl. Catal. B Environ.*, 2014, **147**, 65–81.
- 108 S. M. Lam, J. C. Sin, A. Z. Abdullah and A. R. Mohamed, *Fullerenes Nanotub. Carbon Nanostructures*, 2014, **22**, 471–509.
- 109 A. Miribangul, X. Ma, C. Zeng, H. Zou, Y. Wu, T. Fan and Z. Su, *Photochem. Photobiol.*, 2016, **92**, 523–527.
- 110 K. Byrappa, A. S. Dayananda, C. P. Sajan, B. Basavalingu, M. B. Shayan, K. Soga and M. Yoshimura, *J. Mater. Sci.*, 2008, **43**, 2348–2355.
- 111 L. P. Zhu, G. H. Liao, W. Y. Huang, L. L. Ma, Y. Yang, Y. Yu and S. Y. Fu, *Mater. Sci. Eng. B Solid-State Mater. Adv. Technol.*, 2009, **163**, 194–198.
- 112 M. Ahmad, E. Ahmed, Z. L. Hong, W. Ahmed, A. Elhissi and N. R. Khalid, *Ultrason. Sonochem.*, 2014, **21**, 761–773.
- 113 G. Zhu, H. Wang, G. Yang, L. Chen, P. Guo, L. Zhang and 5, *RSC Adv.*, 2015, **5**, 72476–72481.
- 114 S. A. Feng, J. H. Zhao and Z. P. Zhu, *New Carbon Mater.*, 2008, **23**, 228–234.
- 115 H. Wu, Q. Wang, Y. Yao, C. Qian, X. Zhang and X. Wei, *J. Phys. Chem. C*, 2008, **112**, 16779–16783.
- 116 Z. Fang, Y. Fan and Y. Liu, *Front. Optoelectron. China*, 2011, **4**, 121–127.
- 117 Z. Da Meng, S. Sarkar, L. Zhu, K. Ullah, S. Ye and W. C. Oh, *Synth. React. Inorganic, Met. Nano-Metal Chem.*, 2015, **45**, 1373–1379.
- 118 Y. Tang, J. Tian, T. Malkoske, W. Le and B. Chen, *J. Mater. Sci.*, 2017, **52**, 1581–1589.
- 119 A. Sharifi, L. Montazerghaem, A. Naeimi, A. R. Abhari, M. Vafaei, G. A. M. Ali and H. Sadegh, *J. Environ. Manage.*, 2019, **247**, 624–632.
- 120 Q. Liao, J. Sun and L. Gao, *Colloids Surfaces A Physicochem. Eng. Asp.*, 2008, **312**, 160–165.
- 121 V. K. Gupta, R. Kumar, A. Nayak, T. A. Saleh and M. A. Barakat, *Adv. Colloid Interface Sci.*, 2013, **193–194**, 24–34.
- 122 F. Yu, J. Ma and S. Han, *Sci. Rep.*, 2014, **4**, 5326.
- 123 Ihsanullah, A. Abbas, A. M. Al-Amer, T. Laoui, M. J. Al-Marri, M. S. Nasser, M. Khraisheh and M. A. Atieh, *Sep. Purif. Technol.*, 2016, **157**, 141–161.
- 124 W. Wang, P. Serp, P. Kalck and J. L. Faria, *J. Mol. Catal. A Chem.*, 2005, **235**, 194–199.

-
- 125 W. C. Oh and M. L. Chen, *Bull. Korean Chem. Soc.*, 2008, **29**, 159–164.
- 126 K. Rajasekar, S. Thennarasu, R. Rajesh, R. Abirami, K. Balkis Ameen and A. Ramasubbu, *Solid State Sci.*, 2013, **26**, 45–52.
- 127 W. De Zhang, B. Xu and L. C. Jiang, *J. Mater. Chem.*, 2010, **20**, 6383–6391.
- 128 X. Peng, J. Chen, J. A. Misewich and S. S. Wong, *Chem. Soc. Rev.*, 2009, **38**, 1076–1098.
- 129 S. Banerjee and S. S. Wong, *Nano Lett.*, 2002, **2**, 195–200.
- 130 S. Ravindran, K. N. Bozhilov and C. S. Ozkan, *Carbon N. Y.*, 2004, **42**, 1537–1542.
- 131 W. Li, C. Gao, H. Qian, J. Ren and D. Yan, *J. Mater. Chem.*, 2006, **16**, 1852–1859.
- 132 M. Olek, T. Büsgen, M. Hilgendorff and M. Giersig, *J. Phys. Chem. B*, 2006, **110**, 12901–12904.
- 133 L. Han, W. Wu, F. L. Kirk, J. Luo, M. M. Maye, N. N. Kariuki, Y. Lin, C. Wang and G. J. Zhong, *Langmuir*, 2004, **20**, 6019–6025.
- 134 X. Li, Y. Liu, L. Fu, L. Cao, D. Wei and Y. Wang, *Adv. Funct. Mater.*, 2006, **16**, 2431–2437.
- 135 D. M. Guldi, G. M. A. Rahman, V. Sgobba, N. A. Kotov, D. Bonifazi and M. Prato, *J. Am. Chem. Soc.*, 2006, **128**, 2315–2323.
- 136 L. Zhao and L. Gao, *J. Mater. Chem.*, 2004, **14**, 1001–1004.
- 137 F. Gu, C. Li and S. Wang, *Inorg. Chem.*, 2007, **46**, 5343–5348.
- 138 B. H. Juárez, C. Klinke, A. Kornowski and H. Weller, *Nano Lett.*, 2007, **7**, 3564–3568.
- 139 S. M. George, *Chem. Rev.*, 2010, **110**, 111–131.
- 140 R. W. Johnson, A. Hultqvist and S. F. Bent, *Mater. Today*, 2014, **17**, 236–246.
- 141 K. Pfeiffer, U. Schulz, A. Tünnermann and A. Szeghalmi, *Coatings*, 2017, **7**, 118.
- 142 J. W. Elam, D. Routkevitch, P. P. Mardilovich and S. M. George, *Chem. Mater.*, 2003, **15**, 3507–3517.
- 143 M. Kariniemi, J. Niinistö, M. Vehkamäki, M. Kemell, M. Ritala, M. Leskelä and M. Putkonen, *J. Vac. Sci. Technol. A Vacuum, Surfaces, Film.*, 2012, **30**, 01A115.
- 144 X. L. Li, C. Li, Y. Zhang, D. P. Chu, W. I. Milne and H. J. Fan, *Nanoscale Res. Lett.*, 2010, **5**, 1836–1840.
- 145 Y.-H. Lin, P.-S. Lee, Y.-C. Hsueh, K.-Y. Pan, C.-C. Kei, M.-H. Chan, J.-M. Wu, T.-P. Perng and H. C. Shih, *J. Electrochem. Soc.*, 2011, **158**, K24–K27.
- 146 Y. Zhang, I. Utke, J. Michler, G. Ilari, M. D. Rossell and R. Erni, *Beilstein J. Nanotechnol.*, 2014, **5**, 946–955.
- 147 C. Marichy, N. Donato, M. Latino, M. G. Willinger, J. P. Tessonier, G. Neri and N. Pinna, *Nanotechnology*, 2015, **26**, 024004.
- 148 Y. Zhang, C. Guerra-Núñez, I. Utke, J. Michler, M. D. Rossell and R. Erni, *J. Phys. Chem. C*, 2015, **119**, 3379–3387.
- 149 L. Acauan, A. C. Dias, M. B. Pereira, F. Horowitz and C. P. Bergmann, *ACS Appl. Mater.*

-
- Interfaces*, 2016, **8**, 16444–16450.
- 150 A. Szabó, L. P. Bakos, D. Karajz, T. Gyulavári, Z. R. Tóth, Z. Pap, I. M. Szilágyi, T. Igricz, B. Parditka, Z. Erdélyi and K. Hernadi, *Materials (Basel)*, 2019, **12**, 1095.
- 151 S. Bai, N. Zhang, C. Gao and Y. Xiong, *Nano Energy*, 2018, **53**, 296–336.
- 152 H. Fujiwara, H. Hosokawa, K. Murakoshi, Y. Wada, S. Yanagida, T. Okada and H. Kobayashi, *J. Phys. Chem. B*, 1997, **101**, 8270–8278.
- 153 H. Fujiwara, H. Hosokawa, K. Murakoshi, Y. Wada and S. Yanagida, *Langmuir*, 1998, **14**, 5154–5159.
- 154 X. Chen, L. Liu and F. Huang, *Chem. Soc. Rev.*, 2015, **44**, 1861–1885.
- 155 M. Kong, Y. Li, X. Chen, T. Tian, P. Fang, F. Zheng and X. Zhao, *J. Am. Chem. Soc.*, 2011, **133**, 16414–16417.
- 156 J. Yan, G. Wu, N. Guan, L. Li, Z. Li and X. Cao, *Phys. Chem. Chem. Phys.*, 2013, **15**, 10978–10988.
- 157 Z. Fang, B. Bueken, D. E. De Vos and R. A. Fischer, *Angew. Chemie - Int. Ed.*, 2015, **54**, 7234–7254.
- 158 M. K. Nowotny, L. R. Sheppard, T. Bak and J. Nowotny, *J. Phys. Chem. C*, 2008, **112**, 5275–5300.
- 159 X. Pan, M. Q. Yang, X. Fu, N. Zhang and Y. J. Xu, *Nanoscale*, 2013, **5**, 3601–3614.
- 160 J. Nowotny, M. A. Alim, T. Bak, M. A. Idris, M. Ionescu, K. Prince, M. Z. Sahdan, K. Sopian, M. A. Mat Teridi and W. Sigmund, *Chem. Soc. Rev.*, 2015, **44**, 8424–8442.
- 161 T. Bak, M. K. Nowotny, L. R. Sheppard and J. Nowotny, *J. Phys. Chem. C*, 2008, **112**, 13248–13257.
- 162 M. Long and L. Zheng, *Chinese J. Catal.*, 2017, **38**, 617–624.
- 163 S. Wang, L. Pan, J. J. Song, W. Mi, J. J. Zou, L. Wang and X. Zhang, *J. Am. Chem. Soc.*, 2015, **137**, 2975–2983.
- 164 J. Nowotny, T. Bak, M. K. Nowotny and L. R. Sheppard, *Int. J. Hydrogen Energy*, 2007, **32**, 2630–2643.
- 165 M. K. Nowotny, T. Bak and J. Nowotny, *J. Phys. Chem. B*, 2006, **110**, 16302–16308.
- 166 J. Nowotny, T. Bak and T. Burg, *Ionics (Kiel)*, 2007, **13**, 79–82.
- 167 G. Liu, L. Wang, H. G. Yang, H. M. Cheng and G. Q. Lu, *J. Mater. Chem.*, 2010, **20**, 831–843.
- 168 J. Schneider, M. Matsuoka, M. Takeuchi, J. Zhang, Y. Horiuchi, M. Anpo and D. W. Bahnemann, *Chem. Rev.*, 2014, **114**, 9919–9986.
- 169 F. Peng, L. Cai, H. Yu, H. Wang and J. Yang, *J. Solid State Chem.*, 2008, **181**, 130–136.
- 170 J. Wang, D. N. Tafen, J. P. Lewis, Z. Hong, A. Manivannan, M. Zhi, M. Li and N. Wu, *J. Am. Chem. Soc.*, 2009, **131**, 12290–12297.

-
- 171 G. Liu, Y. Zhao, C. Sun, F. Li, G. Q. Lu and H. M. Cheng, *Angew. Chemie - Int. Ed.*, 2008, **47**, 4516–4520.
- 172 T. Sun, J. Fan, E. Liu, L. Liu, Y. Wang, H. Dai, Y. Yang, W. Hou, X. Hu and Z. Jiang, *Powder Technol.*, 2012, **228**, 210–218.
- 173 N. Feng, Q. Wang, A. Zheng, Z. Zhang, J. Fan, S. Bin Liu, J. P. Amoureux and F. Deng, *J. Am. Chem. Soc.*, 2013, **135**, 1607–1616.
- 174 Z. Wu, S. Cao, C. Zhang and L. Piao, *Nanotechnology*, 2017, **28**, 275706.
- 175 S. Xiong, B. Xi, C. Wang, G. Xi, X. Liu and Y. Qian, *Chem. - A Eur. J.*, 2007, **13**, 7926–7932.
- 176 P. Pichat, Ed., *Photocatalysis and Water Purification: From Fundamentals to Recent Applications*, Wiley-VCH, 2013.
- 177 Y. Li, Y. L. Li, B. Sa and R. Ahuja, *Catal. Sci. Technol.*, 2017, **7**, 545–559.
- 178 K. Ariga and M. Ebara, Eds., *Materials Nanoarchitectonics*, Wiley-VCH, 2018.
- 179 F. Haque, T. Daeneke, K. Kalantar-zadeh and J. Z. Ou, *Nano-Micro Lett.*, 2018, **10**, 23.
- 180 X. Dong and F. Cheng, *J. Mater. Chem. A*, 2015, **3**, 23642–23652.
- 181 J. Xiong, J. Di, J. Xia, W. Zhu and H. Li, *Adv. Funct. Mater.*, 2018, **28**, 1801983.
- 182 M. Chhowalla, H. S. Shin, G. Eda, L. J. Li, K. P. Loh and H. Zhang, *Nat. Chem.*, 2013, **5**, 263–275.
- 183 H. Zhang, *ACS Nano*, 2015, **9**, 9451–9469.
- 184 B. Luo, G. Liu and L. Wang, *Nanoscale*, 2016, **8**, 6904–6920.
- 185 A. V. Kolobov and J. Tominaga, *Springer Series in Materials Science, Vol. 239: Two-dimensional Transition-metal Dichalcogenides*, Springer International Publishing Switzerland, 2016.
- 186 C. Hawkins and L. Whittaker-Brooks, *ACS Appl. Nano Mater.*, 2018, **1**, 851–859.
- 187 R. R. Chianelli and M. B. Dines, *Inorg. Chem.*, 1975, **14**, 2417–2421.
- 188 S. K. Srivastava and B. N. Avasthi, *J. Mater. Sci.*, 1992, **27**, 3693–3705.
- 189 J. Dai, M. Li and X. C. Zeng, *Wiley Interdiscip. Rev. Comput. Mol. Sci.*, 2016, **6**, 211–222.
- 190 S. Okeil, S. Yadav, M. Bruns, A. Zintler, L. Molina-Luna and J. J. Schneider, *Dalt. Trans.*, 2020, **49**, 1032–1047.
- 191 A. J. Molina-Mendoza, M. Barawi, R. Biele, E. Flores, J. R. Ares, C. Sánchez, G. Rubio-Bollinger, N. Agrait, R. D'Agosta, I. J. Ferrer and A. Castellanos-Gomez, *Adv. Electron. Mater.*, 2015, **1**, 1500126.
- 192 J. Kang, H. Sahin, H. D. Ozaydin, R. T. Senger and F. M. Peeters, *Phys. Rev. B - Condens. Matter Mater. Phys.*, 2015, **92**, 075413.
- 193 F. A. Rasmussen and K. S. Thygesen, *J. Phys. Chem. C*, 2015, **119**, 13169–13183.
- 194 J. Kang and L. W. Wang, *Phys. Chem. Chem. Phys.*, 2016, **18**, 14805–14809.
- 195 M. Barawi, E. Flores, I. J. Ferrer, J. R. Ares and C. Sánchez, *J. Mater. Chem. A*, 2015, **3**, 7959–

-
- 7965.
- 196 E. Flores, J. R. Ares, I. J. Ferrer and C. Sánchez, *Phys. Status Solidi - Rapid Res. Lett.*, 2016, **10**, 802–806.
- 197 F. Lévy, Ed., *Crystallography and crystal chemistry of materials with layered structures*, D. Reidel Publishing Company: Dordrecht, Holland, 1976.
- 198 J. L. Murray, *Bull. Alloy Phase Diagrams*, 1986, **7**, 156–163.
- 199 J. Benard and Y. Jeannin, in *Nonstoichiometric Compounds*, American Chemical Society, 1963, pp. 191–203.
- 200 E. Smith and G. Dent, *Modern Raman Spectroscopy - A Practical Approach*, John Wiley & Sons Ltd, 2005.
- 201 H. A. . Szymanski, Ed., *Raman Spectroscopy: Theory and Practice*, Plenum Press, New York, 1967.
- 202 D. C. Harris and M. D. Bertolucci, *Symmetry and Spectroscopy: An Introduction to vibrational and electronic spectroscopy*, Dover, 1978.
- 203 P. J. Larkin, *Infraed and Raman Spectroscopy: Principles and Spectral Interpretations*, Elsevier, 2011.
- 204 A. Jorio, R. Saito, G. Dresselhaus and M. S. Dresselhaus, *Raman Spectroscopy in Graphene Related Systems*, Wiley-VCH, 2011.
- 205 P. Vandenabeele, *Practical Raman Spectroscopy: An Introduction*, John Wiley & Sons, Ltd, 2013.
- 206 M. Fleischmann, P. J. Hendra and A. J. McQuillan, *Chem. Phys. Lett.*, 1974, **26**, 163–166.
- 207 D. L. Jeanmaire and R. P. VAN Duyne, *J. Electroanal. Chem. Interfacial Electrochem.*, 1977, **84**, 1–20.
- 208 M. G. Albrecht and J. A. Creighton, *J. Am. Chem. Soc.*, 1977, **99**, 5215–5217.
- 209 A. Campion and P. Kambhampati, *Chem. Soc. Rev.*, 1998, **27**, 241–250.
- 210 M. Fan, G. F. S. Andrade and A. G. Brolo, *Anal. Chim. Acta*, 2011, **693**, 7–25.
- 211 S. Lefrant, I. Baltog and M. Baibarac, *J. Raman Spectrosc.*, 2005, **36**, 676–698.
- 212 K. Kneipp, H. Kneipp, I. Itzkan, R. R. Dasari and M. S. Feld, *J. Phys. Condens. Matter*, 2002, **14**, R597–R624.
- 213 I.-H. Chou, M. Benford, H. T. Beier, G. L. Coté, M. Wang, N. Jing, J. Kameoka and T. A. Good, *Nano Lett.*, 2008, **8**, 1729–1735.
- 214 K. Kneipp, H. Kneipp, I. Itzkan, R. R. Dasari and M. S. Feld, *Curr. Sci.*, 1999, **77**, 915–924.
- 215 T. Vo-Dinh, F. Yan and M. B. Wabuyeleye, *J. Raman Spectrosc.*, 2005, **36**, 640–647.
- 216 R. A. Álvarez-Puebla and L. M. Liz-Marzán, *Energy Environ. Sci.*, 2010, **3**, 1011–1017.
- 217 H. Tang, C. Zhu, G. Meng and N. Wu, *J. Electrochem. Soc.*, 2018, **165**, B3098–B3118.
- 218 J. D. Jackson, *Classical Electrodynamics*, John Wiley & Sons, Inc., Hoboken, NJ, USA, 3rd ed., 1999.

-
- 219 E. Le Ru and P. Etchegoin, *Principles of Surface Enhanced Raman Spectroscopy and related plasmonic effects*, Elsevier B.V., 2009.
- 220 K. A. Willets and R. P. Van Duyne, *Annu. Rev. Phys. Chem.*, 2007, **58**, 267–297.
- 221 M. Pelton and G. Bryant, *Introduction to Metal-Nanoparticle Plasmonics*, John Wiley & Sons, Inc., and Science Wise Publishing, Hoboken, New Jersey, 2013.
- 222 P. L. Stiles, J. A. Dieringer, N. C. Shah and R. P. Van Duyne, *Annu. Rev. Anal. Chem.*, 2008, **1**, 601–626.
- 223 A. J. Haes and R. P. Van Duyne, *Anal. Bioanal. Chem.*, 2004, **379**, 920–930.
- 224 S. Schlücker, Ed., *Surface Enhanced Raman Spectroscopy: Analytical, Biophysical and Life Science Applications*, Wiley-VCH, Weinheim, Germany, 2011.
- 225 Y. Li, in *Plasmonic Optics: Theory and Applications*, 2017, pp. 1–39.
- 226 A. Derkachova, K. Kolwas and I. Demchenko, *Plasmonics*, 2016, **11**, 941–951.
- 227 S. A. Maier, *Plasmonics: Fundamentals and Applications*, Springer, Bath, United Kingdom, 2007.
- 228 G. P. Wiederrecht, Ed., *Handbook of Nanoscale Optics and Electronics*, Elsevier B.V., 2010.
- 229 R. P. Feynman, R. B. Leighton and M. Sands, 1964.
- 230 D. Saeedkia, Ed., *Handbook of terahertz technology for imaging, sensing and communications*, Woodhead Publishing Limited, 2013.
- 231 W. Cai and V. Shalaev, *Optical Metamaterials: Fundamentals and Applications*, Springer, New York, 2010.
- 232 E. J. Zeman and G. C. Schatz, *J. Phys. Chem.*, 1987, **91**, 634–643.
- 233 M. A. Ordal, R. J. Bell, R. W. Alexander, L. L. Long and M. R. Querry, *Appl. Opt.*, 1985, **24**, 4493–4499.
- 234 P. R. West, S. Ishii, G. V. Naik, N. K. Emani, V. M. Shalaev and A. Boltasseva, *Laser Photonics Rev.*, 2010, **4**, 795–808.
- 235 M. Procházka, *Surface-Enhanced Raman Spectroscopy: Bioanalytical, Biomolecular and Medical Applications*, Springer International Publishing, 2016.
- 236 D. O. Sigle, E. Perkins, J. J. Baumberg and S. Mahajan, *J. Phys. Chem. Lett.*, 2013, **4**, 1449–1452.
- 237 G. Demirel, H. Usta, M. Yilmaz, M. Celik, H. A. Alidagi and F. Buyukserin, *J. Mater. Chem. C*, 2018, **6**, 5314–5335.
- 238 Y.-C. Liu, C.-C. Yu and S.-F. Sheu, *J. Mater. Chem.*, 2006, **16**, 3546.
- 239 K. H. Yang, Y. C. Liu and C. C. Yu, *J. Mater. Chem.*, 2008, **18**, 4849–4855.
- 240 P. Cao, R. Gu and Z. Tian, *J. Phys. Chem. B*, 2003, **107**, 769–777.
- 241 K. H. Yang, Y. C. Liu and C. C. Yu, *Langmuir*, 2010, **26**, 11512–11517.
- 242 M. K. Kinnan, A. Kumbhar and G. Chumanov, *Appl. Spectrosc.*, 2008, **62**, 721–726.

-
- 243 C. Ma, M. J. Trujillo and J. P. Camden, *ACS Appl. Mater. Interfaces*, 2016, **8**, 23978–23984.
- 244 S. Okeil and J. J. Schneider, *Beilstein J. Nanotechnol.*, 2018, **9**, 2813–2831.
- 245 G. Barbillon, V. E. Sandana, C. Humbert, B. Bélier, D. J. Rogers, F. H. Teherani, P. Bove, R. McClintock and M. Razeghi, *J. Mater. Chem. C*, 2017, **5**, 3528–3535.
- 246 F. Shao, Z. Lu, C. Liu, H. Han, K. Chen, W. Li, Q. He, H. Peng and J. Chen, *ACS Appl. Mater. Interfaces*, 2014, **6**, 6281–6289.
- 247 S. M. Asiala, J. M. Marr, G. Gervinskas, S. Juodkazis and Z. D. Schultz, *Phys. Chem. Chem. Phys.*, 2015, **17**, 30461–30467.
- 248 C. Zhang, S. Z. Jiang, C. Yang, C. H. Li, Y. Y. Huo, X. Y. Liu, A. H. Liu, Q. Wei, S. S. Gao, X. G. Gao and B. Y. Man, *Sci. Rep.*, 2016, **6**, 25243.
- 249 Z. Zuo, K. Zhu, C. Gu, Y. Wen, G. Cui and J. Qu, *Appl. Surf. Sci.*, 2016, **379**, 66–72.
- 250 D. Choi, Y. Choi, S. Hong, T. Kang and L. P. Lee, *Small*, 2010, **6**, 1741–1744.
- 251 Y. Zhao, X. Liu, D. Y. Lei and Y. Chai, *Nanoscale*, 2014, **6**, 1311–1317.
- 252 J. W. Jeong, M. M. P. Arnob, K. M. Baek, S. Y. Lee, W. C. Shih and Y. S. Jung, *Adv. Mater.*, 2016, **28**, 8695–8704.
- 253 R. C. Maher, in *Raman Spectroscopy for Nanomaterials Characterization*, ed. C. S. S. R. Kumar, Springer, Berlin, Heidelberg, 2012, pp. 215–260.
- 254 P. G. Etchegoin and E. C. Le Ru, *Phys. Chem. Chem. Phys.*, 2008, **10**, 6079–6089.
- 255 D. Radziuk and H. Moehwald, *Phys. Chem. Chem. Phys.*, 2015, **17**, 21072–21093.
- 256 S. L. Kleinman, R. R. Frontiera, A. I. Henry, J. A. Dieringer and R. P. Van Duyne, *Phys. Chem. Chem. Phys.*, 2013, **15**, 21–36.
- 257 A. M. Schwartzberg, C. D. Grant, A. Wolcott, C. E. Talley, T. R. Huser, R. Bogomolni and J. Z. Zhang, *J. Phys. Chem. B*, 2004, **108**, 19191–19197.
- 258 O. Péron, E. Rinnert, M. Lehaitre, P. Crassous and C. Compère, *Talanta*, 2009, **79**, 199–204.
- 259 R. Stiufiuc, C. Iacovita, C. M. Lucaciu, G. Stiufiuc, A. G. Dutu, C. Braescu and N. Leopold, *Nanoscale Res. Lett.*, 2013, **8**, 47.
- 260 J. Tang, W. Chen and H. Ju, *Talanta*, 2019, **201**, 46–51.
- 261 P. Mosier-Boss, *Nanomaterials*, 2017, **7**, 142.
- 262 D. K. Lim, K. S. Jeon, J. H. Hwang, H. Kim, S. Kwon, Y. D. Suh and J. M. Nam, *Nat. Nanotechnol.*, 2011, **6**, 452–460.
- 263 N. H. Kim, S. J. Lee and M. Moskovits, *Adv. Mater.*, 2011, **23**, 4152–4156.
- 264 L. A. Dick, A. D. McFarland, C. L. Haynes and R. P. Van Duyne, *J. Phys. Chem. B*, 2002, **106**, 853–860.
- 265 J. A. Dieringer, A. D. McFarland, N. C. Shah, D. A. Stuart, A. V. Whitney, C. R. Yonzon, M. A. Young, X. Zhang and R. P. Van Duyne, *Faraday Discuss.*, 2006, **132**, 9–26.

-
- 266 J. C. Hulteen, D. A. Treichel, M. T. Smith, M. L. Duval, T. R. Jensen and R. P. Van Duyne, *J. Phys. Chem. B*, 1999, **103**, 3854–3863.
- 267 J. P. Camden, J. A. Dieringer, J. Zhao and R. P. Van Duyne, *Acc. Chem. Res.*, 2008, **41**, 1653–1661.
- 268 T. Atay, J. H. Song and A. V. Nurmikko, *Nano Lett.*, 2004, **4**, 1627–1631.
- 269 J. Theiss, P. Pavaskar, P. M. Echternach, R. E. Muller and S. B. Cronin, *Nano Lett.*, 2010, **10**, 2749–2754.
- 270 S. J. Lee, A. R. Morrill and M. Moskovits, *J. Am. Chem. Soc.*, 2006, **128**, 2200–2201.
- 271 T. Qiu, W. Zhang, X. Lang, Y. Zhou, T. Cui and P. K. Chu, *Small*, 2009, **5**, 2333–2337.
- 272 B. Sharma, M. Fernanda Cardinal, S. L. Kleinman, N. G. Greeneltch, R. R. Frontiera, M. G. Blaber, G. C. Schatz and R. P. Van Duyne, *MRS Bull.*, 2013, **38**, 615–624.
- 273 K. F. Domke, D. Zhang and B. Pettinger, *J. Am. Chem. Soc.*, 2006, **128**, 14721–14727.
- 274 M. D. Sonntag, J. M. Klingsporn, L. K. Garibay, J. M. Roberts, J. A. Dieringer, T. Seideman, K. A. Scheidt, L. Jensen, G. C. Schatz and R. P. Van Duyne, *J. Phys. Chem. C*, 2012, **116**, 478–483.
- 275 K. L. Kelly, E. Coronado, L. L. Zhao and G. C. Schatz, *J. Phys. Chem. B*, 2003, **107**, 668–677.
- 276 P. Negri and R. A. Dluhy, *J. Biophotonics*, 2013, **6**, 20–35.
- 277 Y. Su, Y. Shi, P. Wang, J. Du, M. B. Raschke and L. Pang, *Beilstein J. Nanotechnol.*, 2019, **10**, 549–556.
- 278 L. Guerrini and D. Graham, *Chem. Soc. Rev.*, 2012, **41**, 7085–7107.
- 279 H. K. Lee, Y. H. Lee, C. S. L. Koh, G. C. Phan-Quang, X. Han, C. L. Lay, H. Y. F. Sim, Y. C. Kao, Q. An and X. Y. Ling, *Chem. Soc. Rev.*, 2019, **48**, 731–756.
- 280 E. C. Le Ru, E. Blackie, M. Meyer and P. G. Etchegoin, *J. Phys. Chem. C*, 2007, **111**, 13794–13803.
- 281 X. M. Lin, Y. Cui, Y. H. Xu, B. Ren and Z. Q. Tian, *Anal. Bioanal. Chem.*, 2009, **394**, 1729–1745.
- 282 Y. Han, R. Lupitskyy, T. M. Chou, C. M. Stafford, H. Du and S. Sukhishvili, *Anal. Chem.*, 2011, **83**, 5873–5880.
- 283 S. Yüksel, M. Ziegler, S. Goerke, U. Hübner, K. Pollok, F. Langenhorst, K. Weber, D. Cialla-May and J. Popp, *J. Phys. Chem. C*, 2015, **119**, 13791–13798.
- 284 G. Sinha, L. E. Depero and I. Alessandri, *ACS Appl. Mater. Interfaces*, 2011, **3**, 2557–2563.
- 285 X. Li, H. Hu, D. Li, Z. Shen, Q. Xiong, S. Li and H. J. Fan, *ACS Appl. Mater. Interfaces*, 2012, **4**, 2180–2185.
- 286 X. Zou, R. Silva, X. Huang, J. F. Al-Sharab and T. Asefa, *Chem. Commun.*, 2013, **49**, 382–384.
- 287 Y. Zang, J. Yin, X. He, C. Yue, Z. Wu, J. Li and J. Kang, *J. Mater. Chem. A*, 2014, **2**, 7747–7753.
- 288 J. Prakash, *Int. Rev. Phys. Chem.*, 2019, **38**, 201–242.
- 289 U. Huebner, R. Boucher, H. Schneidewind, D. Cialla and J. Popp, *Microelectron. Eng.*, 2008, **85**,

-
- 1792–1794.
- 290 B. Yan, A. Thubagere, W. R. Premasiri, L. D. Ziegler, L. D. Negro and B. M. Reinhard, *ACS Nano*, 2009, **3**, 1190–1202.
- 291 X. Deng, G. B. Braun, S. Liu, P. F. Sciortino, B. Koefer, T. Tombler and M. Moskovits, *Nano Lett.*, 2010, **10**, 1780–1786.
- 292 H. Im, K. C. Bantz, N. C. Lindquist, C. L. Haynes and S. H. Oh, *Nano Lett.*, 2010, **10**, 2231–2236.
- 293 U. S. Dinish, F. C. Yaw, A. Agarwal and M. Olivo Malini, *Biosens. Bioelectron.*, 2011, **26**, 1987–1992.
- 294 H.-J. Ahn, P. Thiyagarajan, L. Jia, S.-I. Kim, J.-C. Yoon, E. L. Thomas and J.-H. Jang, *Nanoscale*, 2013, **5**, 1836–1842.
- 295 R. Gillibert, M. Sarkar, J.-F. Bryche, R. Yasukuni, J. Moreau, Mondher Besbes, G. Barbillon, B. Bartenlian, M. Canva and M. L. de la Chapelle, *Nanotechnology*, 2016, **27**, 115202.
- 296 R. Alvarez-Puebla, B. Cui, J. P. Bravo-Vasquez, T. Veres and H. Fenniri, *J. Phys. Chem. C*, 2007, **111**, 6720–6723.
- 297 S. Krishnamoorthy, S. Krishnan, P. Thoniyot and H. Y. Low, *ACS Appl. Mater. Interfaces*, 2011, **3**, 1033–1040.
- 298 T. R. Jensen, M. D. Malinsky, C. L. Haynes and R. P. Van Duyne, *J. Phys. Chem. B*, 2000, **104**, 10549–10556.
- 299 C. L. Haynes and R. P. Van Duyne, *J. Phys. Chem. B*, 2001, **105**, 5599–5611.
- 300 C. L. Haynes and R. P. Van Duyne, *J. Phys. Chem. B*, 2003, **107**, 7426–7433.
- 301 X. Zhang, C. R. Yonzon, M. A. Young, D. A. Stuart and R. P. Van Duyne, *IEE Proc. - Nanobiotechnology*, 2005, **152**, 195–206.
- 302 W. C. Lin, L. S. Liao, Y. H. Chen, H. C. Chang, D. P. Tsai and H. P. Chiang, *Plasmonics*, 2011, **6**, 201–206.
- 303 W. G. Yan, J. W. Qi, Z. Bin Li and J. G. Tian, *Plasmonics*, 2014, **9**, 565–571.
- 304 Z. Zhu, Q. Li, B. Bai and S. Fan, *Nanoscale Res. Lett.*, 2014, **9**, 25.
- 305 X. Zhou, F. Zhou, H. Liu, L. Yang and J. Liu, *Analyst*, 2013, **138**, 5832–5838.
- 306 H. Liang, Z. P. Li, W. Wang, Y. Wu and H. Xu, *Adv. Mater.*, 2009, **21**, 4614–4618.
- 307 C. Farcau, M. Potara, C. Leordean, S. Boca and S. Astilean, *Analyst*, 2013, **138**, 546–552.
- 308 E. A. Tastekova, A. Y. Polyakov, A. E. Goldt, A. V Sidorov, A. A. Oshmyanskaya, I. V Sukhorukova, D. V Shtansky, W. Grünert and A. V Grigorieva, *Beilstein J. Nanotechnol.*, 2018, **9**, 880–889.
- 309 S. B. Chaney, S. Shanmukh, R. A. Dluhy and Y. P. Zhao, *Appl. Phys. Lett.*, 2005, **87**, 031908.
- 310 S. Shanmukh, L. Jones, J. Driskell, Y. Zhao, R. Dluhy and R. A. Tripp, *Nano Lett.*, 2006, **6**, 2630–2636.

-
- 311 Y. He, J. Fu and Y. Zhao, *Front. Phys.*, 2014, **9**, 47–59.
- 312 Y. C. Chen, R. J. Young, J. V Macpherson and N. R. Wilson, *J. Phys. Chem. C*, 2007, **111**, 16167–16173.
- 313 A. O. Altun, T. C. Bond and H. G. Park, *Proc. SPIE - Int. Soc. Opt. Eng.*, 2014, **9168**, 1–9.
- 314 J. Zhang, X. Zhang, C. Lai, H. Zhou and Y. Zhu, *Opt. Express*, 2014, **22**, 21157–21166.
- 315 K. Zhang, J. Ji, X. Fang, L. Yan and B. Liu, *Analyst*, 2015, **140**, 134–139.
- 316 Y. Jin, Y. Wang, M. Chen, X. Xiao, T. Zhang, J. Wang, K. Jiang, S. Fan and Q. Li, *ACS Appl. Mater. Interfaces*, 2017, **9**, 32369–32376.
- 317 C. Srichan, M. Ekpanyapong, M. Horprathum, P. Eiamchai, N. Nuntawong, D. Phokharatkul, P. Danvirutai, E. Bohez, A. Wisitsoraat and A. Tuantranont, *Sci. Rep.*, 2016, **6**, 23733.
- 318 J. Chen, G. Qin, Q. Chen, J. Yu, S. Li, F. Cao, B. Yang and Y. Ren, *J. Mater. Chem. C*, 2015, **3**, 4933–4944.
- 319 G. Seniutinas, G. Gervinskas, R. Verma, B. D. Gupta, F. Lapierre, P. R. Stoddart, F. Clark, S. L. McArthur and S. Juodkazis, *Opt. Express*, 2015, **23**, 6763.
- 320 M. Schierhorn, S. J. Lee, S. W. Boettcher, G. D. Stucky and M. Moskovits, *Adv. Mater.*, 2006, **18**, 2829–2832.
- 321 H.-H. Wang, C.-Y. Liu, S.-B. Wu, N.-W. Liu, C.-Y. Peng, T.-H. Chan, C.-F. Hsu, J.-K. Wang and Y.-L. Wang, *Adv. Mater.*, 2006, **18**, 491–495.
- 322 G. Das, N. Patra, A. Gopalakrishnan, R. P. Zaccaria, A. Toma, S. Thorat, E. Di Fabrizio, A. Diaspro and M. Salerno, *Analyst*, 2012, **137**, 1785–1792.
- 323 E. P. Hoppmann, W. W. Yu and I. M. White, *Methods*, 2013, **63**, 219–224.
- 324 L. Polavarapu, A. La Porta, S. M. Novikov, M. Coronado-Puchau and L. M. Liz-Marzán, *Small*, 2014, **10**, 3065–3071.
- 325 F. F. Chen and J. P. Chang, *Lecture Notes on Principles of Plasma Processing*, Springer US, 2003.
- 326 C. Tendero, C. Tixier, P. Tristant, J. Desmaison and P. Leprince, *Spectrochim. Acta - Part B At. Spectrosc.*, 2006, **61**, 2–30.
- 327 R. A. Jelil, *J. Mater. Sci.*, 2015, **50**, 5913–5943.
- 328 E. M. Liston, *J. Adhes.*, 1989, **30**, 199–218.
- 329 C. S. Wong and R. Mongkolnavin, *Elements of Plasma Technology*, Springer, 2016.
- 330 E. M. Liston, L. Martinu and M. R. Wertheimer, *J. Adhes. Sci. Technol.*, 1993, **7**, 1091–1127.
- 331 D. G. Petlin, S. I. Tverdokhlebov and Y. G. Anissimov, *J. Control. Release*, 2017, **266**, 57–74.
- 332 H.-J. Tiller, U. Demme, D. Lenke, P. Bühner and K. Meyer, *Krist. und Tech.*, 1975, **10**, K103–K108.
- 333 S. Y. Kim, K. Hong, K. Kim, H. K. Yu, W.-K. K. Kim and J.-L. L. Lee, *J. Appl. Phys.*, 2008, **103**, 76101.

-
- 334 H. Kim, K. Y. Shin, H. S. Kang, S. H. Lee and J. M. Kim, *Microsyst. Technol.*, 2016, **22**, 1135–1142.
- 335 S. Shanmugan, D. Mutharasu and I. Kamarulazizi, *Eur. Phys. J. Appl. Phys.*, 2012, **58**, 10802.
- 336 T. Hutter, S. R. Elliott and S. Mahajan, *Nanotechnology*, 2013, **24**, 035201.
- 337 T. Wang, Z. Zhang, F. Liao, Q. Cai, Y. Li, S.-T. Lee and M. Shao, *Sci. Rep.*, 2014, **4**, 4052.
- 338 W. Lee and S.-J. Park, *Chem. Rev.*, 2014, **114**, 7487–7556.
- 339 H. Masuda and K. Fukuda, *Science (80-.)*, 1995, **268**, 1466–1468.
- 340 H. Masuda and M. Satoh, *Jpn. J. Appl. Phys.*, 1996, **35**, L126–L129.
- 341 S. Zhang, Y. Wang, Y. Tan, J. Zhu, K. Liu and J. Zhu, *Mater. Res. Express*, 2016, **3**, 074004.
- 342 Y. Ma, J. Kaczynski, C. Ranacher, A. Roshanghias, M. Zauner and B. Abasahl, *Microelectron. Eng.*, 2018, **198**, 29–34.
- 343 J. W. Diggle, Downie T.C. and C. W. Goulding, *Chem. Rev.*, 1969, **69**, 365–405.
- 344 R. J. Nemanich, C. C. Tsai and G. A. N. Connell, *Phys. Rev. Lett.*, 1980, **44**, 273–276.
- 345 G. A. N. Connell, R. J. Nemanich and C. C. Tsai, *Appl. Phys. Lett.*, 1980, **36**, 31–33.
- 346 D. Shan, L. Huang, X. Li, W. Zhang, J. Wang, L. Cheng, X. Feng, Y. Liu, J. Zhu and Y. Zhang, *J. Phys. Chem. C*, 2014, **118**, 23930–23936.
- 347 J. Wang, L. Huang, L. Yuan, L. Zhao, X. Feng, W. Zhang, L. Zhai and J. Zhu, *Appl. Surf. Sci.*, 2012, **258**, 3519–3523.
- 348 R. J. Walsh and G. Chumanov, *Appl. Spectrosc.*, 2001, **55**, 1695–1700.

7 Curriculum Vitae

Personal information

Name: Sherif Mahmoud El-Sayed Okeil Ibrahim
Date of birth: 05/07/1986
Place of birth: Bonn, Germany
Address: Siemensstraße 3
64289 Darmstadt
Germany

Education

10/2014 - present
Dr.rer.nat
Dept. of Inorganic Chemistry
Technische Universität Darmstadt, Germany

01/2010 - 04/2013
Master of Science (Pharmaceutical Analytical
Chemistry)
Faculty of Pharmacy
Ain Shams University, Cairo, Egypt

10/2004 - 05/2009
Bachelor of Pharmaceutical Science
Faculty of Pharmacy
Ain Shams University
Cairo, Egypt

06/2004
Abitur
Deutsche Evangelische Oberschule
Cairo, Egypt

Sherif Okeil